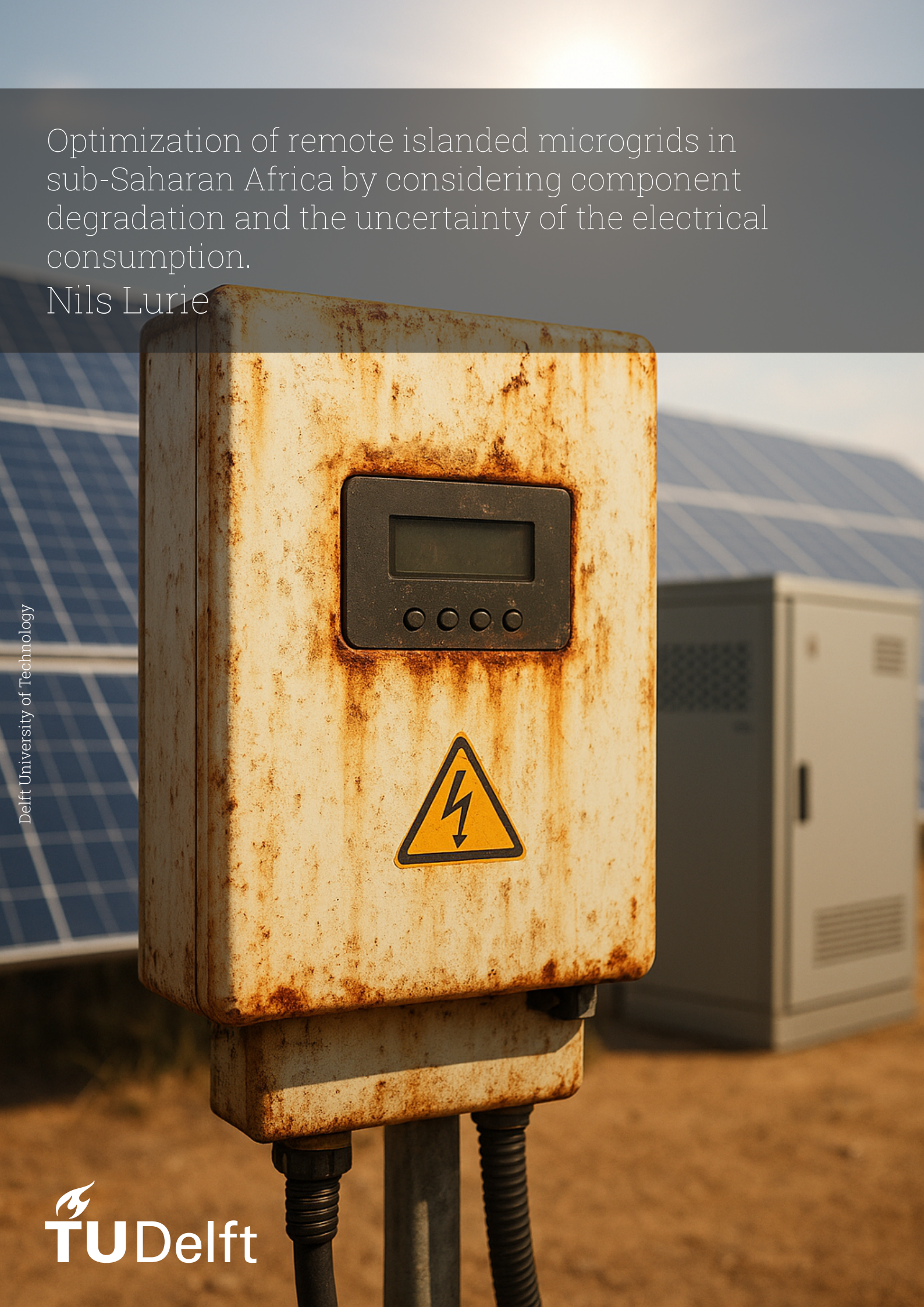
Optimization of remote islanded microgrids in sub-Saharan Africa by considering component degradation and the uncertainty of the electrical consumption.

Nils Lurie



Delft University of Technology

TU Delft

Optimization of remote islanded microgrids in sub-Saharan Africa by considering component degradation and the uncertainty of the electrical consumption.

by

Nils Lurie

Main Supervisor:	Laura Ramirez Elizondo
Daily Supervisors:	Joel Alpízar-Castillo
	Qobad Shafiee
External Supervisor	Sergio Balderrama Subieta
Project Duration:	August, 2024 - September, 2025
Faculty:	Electrical Engineering, Mathematics & Computer Science, TU Delft

Thesis Committee:	Laura Ramirez Elizondo	TU Delft: EEMCS - DCE&S
	Mohamad Ghaffarian Niasar	TU Delft: EEMCS - HVT
	Francesco Lombardi	TU Delft: TPM - ESS
	Sergio Balderrama Subieta	University of San Simon

TU Delft

Abstract

It is estimated that 600 million people will still lack access to electricity by 2030, most of whom live in the rural regions of sub-Saharan Africa. One of the main technical challenges with rural electrification is the high associated costs with the expansion of the existing grids to remote locations. The most promising alternative to main grid extension is an off-grid microgrid. Off-grid microgrids do not require a connection to the main grid and they are modular allowing to adjust the design for the needs of the specific location. Nevertheless, off-grid microgrids are still very expensive and it is necessary to continue the efforts in reducing the associated costs of microgrid design and operation.

The microgrid topology considered in this thesis project consists of a solar panel array as the primary energy generation source in combination with a battery electrical storage system to help tackle the issue of intermittency of solar energy. In addition, a backup diesel generator is present to generate electricity during the moments when there is no electricity available from the solar panel array and no energy is left in the battery. The microgrid also has an inverter, which allows to convert the different voltage levels of the PV array, the battery, and diesel generator to a suitable voltage for the distribution lines, which leads to consumers.

When designing a particular microgrid, it is necessary to determine the capacity of the microgrid components such that it is not oversized, which would result in wasted resources, but also must not be undersized since then electricity cannot be provided at all times. In the literature, many micorgrid sizing approaches have been proposed to find the optimal capacities of the microgrid components and to reduce the total cost of the system. However, the proposed optimization strategies are always accompanied by different types of assumptions, some of which include fixed weather and electrical load curves and simplified component degradation models. It would not be possible to create an all-encompassing model since then the computational time would drastically increase. However, the literature that proposes new optimization strategies often lacks motivation regarding the choices made for one level of detail over another.

There are three main goals to this thesis project. Firstly, the effect on the microgrid configuration and cost is investigated between two different dispatch optimization algorithms - rule-based dispatch (RB) and particle swarm optimization (PSO). Secondly, the influence of choosing between two different battery degradation models is investigated - an energy throughput model and a semi-empirical model. Finally, the impact of including inverter degradation is investigated. Since inverter degradation has not been previously considered in microgrid sizing optimization models, an experimental investigation of a theoretical inverter degradation model by Alpízar et al. has been performed.

The inverter degradation model assumes that the switch inside the boost converter is the primary reason for the degradation as all the curtailed power is redirected through the switch. To experimentally investigate the switch degradation depending on the current profile a testing setup was designed which allowed to determine the junction temperature which is the main variable influencing the lifetime of the switch. The experimental results were compared with simulations performed in the LTspice circuit simulation software. The experimental results show that improper solar panel curtailment strategies can reduce the switch lifetime by more than 60%, which is in line with the conclusions of the study by Alpízar-Castillo et al.

With the obtained knowledge that the selected dispatch strategy has a direct effect on the inverter degradation, the degradation model is included in the sizing optimization model. Therefore, sizing optimization has been done for different combinations of degradation models for both sizing optimization

algorithms. The optimization algorithms have been programmed in Python programming language. The obtained results indicate that the selection of the specific combination of degradation models mostly influences the final capacity of the solar panel array with a maximum relative difference of 30% between the different combinations of degradation models. It is also shown that the battery capacity is marginally influenced by the selection of the degradation models. However, when choosing the energy throughput model, a choice has to be made for the total number of cycles, which has a direct impact on the total degradation of the battery and consequently the total price of the system. However, it does not significantly influence the dispatch decisions.

When comparing the sizing optimization algorithm coupled with PSO dispatch against the optimization coupled with RB dispatch it is shown that the former algorithm is more flexible upon different capacity configurations of microgrid components. However, the PSO dispatch algorithm has an issue with consistency that results in a difference in the estimated OPEX of up to 20% within five consecutive runs of dispatch for the same microgrid configuration. When applied to sizing optimization PSO performs slightly better than the RB-based optimization when switch degradation is considered, however, the results are inconclusive due to the presented inconsistency. However, it was shown that the proposed nested PSO algorithm performs significantly better when switch degradation is not considered by improving the scheduling of the backup diesel generator. Finally, it is shown that the algorithm based on two nested PSO optimization algorithms is more than 1000 times slower than the optimization algorithm, which uses RB dispatch. However, given that the algorithm is not run real-time it does not present a direct challenge. Nevertheless, this presents a trade-off between the computational time and the performance in the capability of finding a cheaper solution.

Preface

With a high confidence (more than 60%) I can say that with the rapid rise of AI compute power in a few years parts of my thesis that I have been struggling to put together for months will be easily made within a few hours. I think I now understand how the researchers felt before the rise of commercial computers.

Nevertheless, I think that being a good researcher does not mean being skillful in a specific software or knowledgeable about a specific topic. To the best of my understanding a good researcher is capable of asking the right questions. I am too modest to say that I have been asking the right questions (which in itself might not be modest). But throughout my thesis I have been trying to question other people's questions, beliefs, and assumptions. And the essence of this thesis is to see what happens when one starts to question everything. While the time restrictions eventually forced me to drop some of my endless questions and replace them with assumptions of my own I hope that the reader of my thesis will still be able to appreciate my effort.

Nils Lurie
Delft, September 2025

Acknowledgements

Throughout my academic journey if the form of my Master thesis project there have been many people that I need to thank. My largest gratitude goes to my daily supervisor Joel Alpízar-Castillo. He has been actively supporting me from the very first day of my thesis project. He has always had an extremely positive attitude both when I came to his office to share some new insights or when I came with ”I think everything is wrong” as the first words coming from my mouth. A large thank you also to my supervisors Laura Ramirez Elizondo, Qobad Shafiee and Sergio Luis Balderrama. All of them have given me full freedom on exploring the directions wherever the project has lead me and given me suggestions on finding my way back when I have gone off-road too much. I also have to say a big thanks to Filip Simjanoski without whom the experimental part of my thesis would not have been possible (also I would not have seen the amazing event of SMD resistors flying into the horizon from an applied heatgun). And finally, of course, thank you to my family and to all of my friends who have been supporting me no matter on which part of the mental sine-wave I was at the time.

Contents

Abstract i

Preface iii

Acknowledgements iv

1 Introduction 1

1.1 Electrification in the past and in the present . . . 1

1.2 Impact of electrification . . . 4

1.3 Types of solutions for rural electrification . . . 5

1.4 Problem Formulation . . . 6

2 Theoretical Background 10

2.1 Overview of microgrids . . . 10

2.1.1 Definition of a microgrid . . . 10

2.1.2 Microgrid Components . . . 11

2.1.3 Microgrid Topologies . . . 11

2.1.4 Microgrid Control . . . 13

2.2 Battery Technology . . . 15

2.2.1 Overview of battery chemistries . . . 15

2.2.2 Physical structure . . . 17

2.2.3 Working Principles . . . 18

2.2.4 Degradation Mechanisms . . . 19

2.2.5 Stress factors . . . 20

2.3 Switch Lifetime . . . 23

2.3.1 Switch Degradation Mechanisms . . . 23

2.3.2 Overview of the lifetime models . . . 26

3 Literature Review 28

3.1 Load Modeling . . . 29

3.2 Microgrid Sizing Optimization . . . 33

3.2.1 Optimization Approaches . . . 33

3.2.2 Common Trends and Trade-offs . . . 38

3.2.3 Current Research . . . 40
3.3 EMS Optimization . . . 42
3.3.1 Additional Optimization Approaches . . . 42
3.3.2 Common Trends and Trade-offs . . . 45
3.4 Battery Degradation Modelling . . . 46
3.4.1 Linear Models . . . 47
3.4.2 Models accounting for partial charge/discharge cycles . . . 48
3.4.3 Semi-empirical and empirical models . . . 49
3.4.4 Trade-off between the level-of-detail, computational power and the cost of the final product . . . 49

4 Methodology **52**
4.1 Experimental Investigation of the Switch Lifetime Model . . . 53
4.1.1 Existing Work on the Impact of Curtailment on Switch Lifetime . . . 54
4.1.2 Tools Used to Determine Switch Lifetime . . . 56
4.1.3 Approaches for Determining Junction Temperature . . . 58
4.1.4 Experimental Implementation of the Switching Loss Estimation via the Double-Pulse Test . . . 63
4.1.5 Experimental Implementation of junction temperature estimation during an operation of a boost converter . . . 69
4.2 Optimization of Microgrid Sizing . . . 74
4.2.1 Load Curve Generation . . . 74
4.2.2 Weather Curve Generation . . . 81
4.2.3 Battery Degradation Models . . . 81
4.2.4 Proposed Optimization Algorithm . . . 84
4.2.5 Performance Evaluation . . . 96

5 Experimental Results of Switch Lifetime Testing **99**
5.1 Double-Pulse Test . . . 99
5.2 Junction Temperature Experiments . . . 102

6 Results of Microgrid Sizing Optimization **110**
6.1 Use Case: Samionta Microgrid . . . 110
6.2 Impact of Battery Degradation Models . . . 113
6.3 Impact of switch degradation . . . 116
6.4 Dispatch Optimization . . . 119
6.4.1 Comparison between RB and PSO dispatch optimization . . . 119
6.4.2 OPEX changes over the years . . . 122
6.5 Sizing Optimization Results . . . 123
6.6 Environmental Cost . . . 128

7 Conclusions and Suggested Future Improvements **131**

7.1 Conclusions 131

7.2 Future Improvements 132

References **134**

List of Figures

1.1 Urban and rural electrification rates of Western-African countries[5]. 2
1.2 Map of world population density [7]. 3
1.3 Microgrid layout of the type of microgrids considered in the thesis project. 6
1.4 Yearly number of publications on Scopus between the years of 2005 and 2024 for the prompt ”Microgrid AND Optimization AND Siz*” [23] 7

2.1 An example of an AC microgrid topology [38]. 12
2.2 An example of a DC microgrid topology [38]. 12
2.3 An example of a DC/AC microgrid topology [38]. 13
2.4 A visual overview of the implementations of centralized, decentralized and distributed control architectures [40]. 14
2.5 Ragone plot of battery power density versus energy density [42]. 16
2.6 LCOE of different energy storage technologies [43]. 16
2.7 Schematic of the main components of a lithium-ion (Li-ion) cell [44]. 17
2.8 Simplified diagram of a Li-ion battery cell [45]. 19
2.9 Degradation mechanisms in Li-ion batteries[45]. 19
2.10 An example of a capacity fade in a Li-ion battery depending on the number of cycles [49]. 21
2.11 The cell capacity loss map under room temperature as a function of cycle aging at various C-rates [45]. 22
2.12 Battery cycle life as a function of temperature [50]. 22
2.13 Battery cycle life as a function of DoD [51]. 23
2.14 Failure modes within a SiC MOSFET (a) chip (b) package [52]. 24
2.15 Layout of and IGBT chip [53]. 25

3.1 General workflow for microgrid sizing optimization and the outline of the chapter. 28
3.2 Comparison of the LoadProGen and RAMP models in predicting the electrical load as described in [61]. 30
3.3 Procedure for load profile generator based on SOM [66]. 31
3.4 Causal-loop diagram representing the dynamics between electricity demand and IGAs [74]. 32
3.5 Summary of the microgrid sizing optimization approaches. 36

3.6 Distribution of the optimization approaches proposed in the review articles by Akbas et al. in [95]. . . . 38
3.7 Overview of the EMS optimization approaches. . . . 44
3.8 Analysis of different optimization techniques based on the number of publications during 2010–2020 [129]. . . . 45
3.9 Pictorial representation of the analysis of three commonly used optimization techniques [129]. . . . 46
3.10 Overview of the battery degradation models found in the literature included into microgrid optimization algorithms. . . . 47
3.11 Identification and addition of partial cycles for battery degradation modelling [138]. . . . 48
3.12 Optimized amounts of the total costs, purchase cost from the grid and replacement cost of the ESS under different degradation models [34]. . . . 51

4.1 Flowchart of the proposed microgrid sizing optimization algorithm and the overview of the chapter contents. . . . 52
4.2 Flowchart of the method used to investigate switch degradation dependency on the chosen mission profile. . . . 53
4.3 Overview of the converter studied in [102]. . . . 54
4.4 Normalized expected lifetime of the switch inside the boost converter depending on the solar panel array curtailment threshold [102]. . . . 55
4.5 System LCOE as a function of the curtailment threshold of the solar panel array [102]. . . . 55
4.6 An arbitrary temperature profile of a switch over time (on the left), which has been rotated by 90 degrees for a better visualization of the algorithm (on the right) [58]. . . . 56
4.7 Visualization of the Rainflow counting algorithm according to the implementation by Infineon in their application note in [58]. . . . 57
4.8 Example of an equivalent thermal model of a power electronic device. . . . 58
4.9 Foster and Cauer thermal models [153]. . . . 59
4.10 Thermal impedance curves of the C3M0045065K SiC MOSFET [151]. . . . 59
4.11 Cauer network containing the RC elements and a current source, which has a current value equivalent to the switch losses. . . . 60
4.12 Thermocouple implementation inside a SiC MOSFET [161]. . . . 61
4.13 An example of an infrared measurement of the switch temperature during testing by using a thermal camera [160]. . . . 62
4.14 Basic circuit diagram of experimental DPT testing [167]. . . . 64
4.15 Gate-source voltage, drain-source voltage and the switch current waveforms during the DPT test [167]. . . . 64
4.16 Operation of a DPT circuit during the on and off periods of the pulses [167]. . . . 65
4.17 Wolfspeed SpeedVal kit motherboard and daughter card. . . . 66
4.18 The experimental setup used to perform the DPT test. . . . 67
4.19 Points of alignment of V_{ds} and I_d waveforms during post-processing of the measurement data [168]. . . . 68
4.20 Visual overview on the settings for the determination of switching loss [169]. . . . 69

4.21 SpeedVal Kit Buck/Boost Accessory Board 190uH 40A connected to the SpeedVal Motherboard [173]. . . . 70
4.22 An electrical circuit diagram of a Boost converter. . . . 70
4.23 Example waveforms of the V_{gs}, V_{ds}, I_{sw} and I_{diode} for the boost converter. . . . 71
4.24 Original and modified configuration of the switches of the Wolfspeed daughter card. . . . 72
4.25 Junction temperature dependance on the on-resistance of the C3M0045065K switch [151]. 72
4.26 Overview of the load profile generation process. . . . 74
4.27 The layer structure of the RAMP model [61]. . . . 75
4.28 RAMP layer structure applied to an example. . . . 75
4.29 Visualization of the stochastic modeling of two random appliance turn-ons and turn-offs during 24-hour interval. The different appliances have been represented with green and red colours while purple indicates the accumulative load. ”S” and ”E” indicates start and end points of operation windows. . . . 76
4.30 Visualization of the working principles of the RAMP multi-year feature. . . . 77
4.31 Visualization of the clustering process . . . 79
4.32 General dendrogram for hierarchical clustering [181]. . . . 80
4.33 SSE as a function of representative days for the Samionta use-case. . . . 81
4.34 Energy throughput calculation for a simple degradation model. . . . 82
4.35 CC and CV charging stages of a battery [189]. . . . 83
4.36 Visualization of the particle swarm consisting of four particles. The positions and velocities of the first iteration are in white while the ones of the second iteration are in blue. . . . 86
4.37 Overview of the nested sizing/EMS PSO algorithm. . . . 88
4.38 Example diesel consumption of a diesel generator [193] . . . 90
4.39 Different types of PSO Neighbourhood Topologies [196]. . . . 92
4.40 High-level flowchart of the dispatch algorithm introduced in [124]. . . . 97

5.1 Simulated and measured drain current and drain-source voltage waveforms of the DPT. 99
5.2 Simulated and measured drain current and drain-source voltage waveforms during turn-off and turn-on of the SiC MOSFET. . . . 100
5.3 Simulated and measured dissipated power of the switch during the turn-off and turn-on. 101
5.4 Relative $R_{\text{DS-on}}$ increase depending on the RMS current flowing through the switch for a duty cycle of 0.65. . . . 102
5.5 Relative $R_{\text{DS-on}}$ curves depending on the RMS current for different duty cycles. . . . 103
5.6 A second-order polynomial fit of the stacked $R_{\text{DS-on}}$ curves. . . . 103
5.7 Junction temperature dependence on the RMS switch current extracted by combining the junction temperature calibration curve and the polynomial fit of the R_{DS-on} curves. . . 104
5.8 Extrapolated fit of the current-temperature curve from the current data points from the reference mission profile with a curtailment threshold of -1.1 kW. . . . 105
5.9 Junction temperature fits for three different thresholds in the reference model. . . . 105
5.10 Current-temperature lookup-curves corresponding to the three results - reference model (threshold of -2.0 kW), experimental results and the simulation. . . . 106

5.11 Degradation curves at different curtailment thresholds - the original curve from the paper by Alpizar-Castilo et al. in [102], the curve produced from the junction temperatures of the measurements, and the simulation of the performed measurements. 107

5.12 Histogram of the encountered RMS currents durin a mission profile for two different curtailment thresholds. 108

6.1 Solar Panel Array built in Samionta. 111

6.2 Base load curve, which has been generated by using RAMP model. 111

6.3 Modeled load profile of electrical consumption in Samionta village by using the newly-introduce multi-year feature of RAMP. 112

6.4 Comparison of the semi-empirical battery degradation with the energy-throughput model by considering different number of cycles. 114

6.5 Comparison of total degradation and NPC between different battery degradation models while using RB dispatch and considering switch degradation. 115

6.6 Calendar and cyclic degradation for the SE-SD case. 116

6.7 PV dispatch comparison between the cases when switch degradation has not been considered and when it has been considered. 117

6.8 Dispatched and maximum possible dispatchable PV power in SE-NSD and SE-SD cases.117

6.9 Battery SOC for the SE-NSD and SE-SD cases of RB dispatch optimization. 118

6.10 Switch temperature comparison between the cases when switch degradation has not been considered and when it has been considered. 118

6.11 PV and diesel generator dispatch for RB and PSO optimization for SE-SD case with oversized solar panel array. 121

6.12 Dispatched battery power and the corresponding SOC curves for RB and PSO optimization. 121

6.13 Yearly normalized OPEX changes over 10 years. 122

6.14 Yearly normalized changes in generator and battery throughput. 122

6.15 Yearly normalized changes in OPEX and generator throughput for another optimization case. 123

6.16 PV and battery capacities for different cases of PSO and RB sizing optimization 124

6.17 Daily curtailment and the switch degradation for different cases of PSO and RB optimization124

6.18 Battery degradation after 10 years for different cases of PSO and RB sizing optimization. 125

6.19 CAPEX and daily OPEX for different cases of RB and PSO sizing optimization. 126

6.20 Daily energy throughput for different cases of RB and PSO dispatch algorithms inside sizing optimization. 126

6.21 NPC for different cases of PSO and RB sizing optimization. 127

6.22 Sizing by introducing a ”carbon tax” in case of RB dispatch, semi-empirical battery degradation model and switch degradation considered. 129

List of Tables

1.1 Percentages of urban and rural population served by electrification in low- and middle-income countries by region in 1970 and 1990 [3]. 2

1.2 Urbanization in different parts of the world and some countries in Africa expressed as a percentage of population living in or near cities or urban areas. 3

1.3 Types of assumptions made in microgrid sizing optimization and corresponding examples. 7

2.1 Overview of the timescales and functions of the control levels in hierarchical control of microgrids [39]. 14

2.2 Different anode materials and their characteristics [45]. 17

2.3 Different cathode materials and their characteristics [45]. 18

3.1 Comparison of the load forecasts between the LoadProGen and RAMP models [61]. . . 31

3.2 Research progress overview for the microgrid sizing optimization with the ”x” indicating whether a certain feature has been implemented in the optimization algorithm. 41

4.1 Comparison of TSEPs in SiC MOSFETs and Si IGBTs [163]. 63

4.2 Summary of the main characteristics of the C3M0045065K SiC switch [151]. 66

4.3 Overview of the supplementary equipment for the DPT and Boost converter measurements. 67

4.4 Testing conditions for the experimental Double-Pulse Test. 67

4.5 Example of a table that allows define new appliances to be added to specific user types. 78

5.1 Summary of the simulations and experimental measurements of the DPT. 101

6.1 Microgrid components used in Samionta. 112

6.2 Modeled costs of the components in Samionta microgrid. 113

6.3 Overview of the cases studied for the microgrid sizing optimization. 113

6.4 Dispatch optimization results for a run of a rule-based optimization and for five runs of the PSO-based optimization for the SE-SD case. 119

6.5 Comparison of the optimization solutions between RB and PSO dispatch for PV capacity of 6.5 kWp and battery capacity of 30.0 kWh. 120

6.6 Comparison of the optimization solutions between RB and PSO dispatch for PV capacity of 7.8 kWp and battery capacity of 30.0 kWh. 120

6.7 Comparison of the optimization solutions between RB and PSO dispatch for PV capacity of 5.2 kWp and battery capacity of 30.0 kWh. 120
6.8 Overview of switch degradation for RB and PSO optimization for the four considered cases. 125
6.9 Comparison between the OPEX of 6 representative days and 40 representative days. . 127
6.10 Comparison of computation time for different cases for RB and PSO dispatch and sizing. 128
6.11 Sizing and fuel fraction for different applied carbon tax amounts. 129

Chapter 1

Introduction

During the UN Sustainable Development Summit in 2015, ”Transforming our world: the 2030 Agenda for Sustainable Development” was adopted, which includes 17 sustainable development goals (SDGs). ”Ensure access to affordable, reliable, sustainable, and modern energy for all” is one of these SDGs (Goal 7) [1]. Although this goal is among those that have made the greatest progress since 2015 only 40% of the targets have been met or are on track to be met. The rest of the targets for the goal have been classified as having ”Marginal or moderate progress” [2]. It is therefore estimated that by 2030 more than 600 million people will still lack access to electricity (over 80% of whom live in sub-Saharan Africa) and 1.8 billion people will not have access to clean cooking appliances [2]. Hence, it is crucial to increase the work related to rural electrification in low– and middle-income countries.

This chapter explores the challenge of electrification in both the past and the present day, presenting the reasons why so many people nowadays still lack access to electricity. The importance of electrification is then explained supported by scientific evidence of the impacts of introduction of electricity to rural communities. Following, a brief introduction is given to the solutions of electrification in rural areas portraying both the advantages and disadvantages. Finally, the problem definition of the thesis is done and an overview of the report is given.

1.1 Electrification in the past and in the present

Before a potential future solution to the previously identified problem is proposed, a context for the past has to be established. Thus, in this section, the highlights of the world’s electrification processes are provided.

Electricity has been an essential tool in economic and technological advancement as it is needed in both light and heavy industries - starting from the production of home appliances to the production of airplanes [3]. Electricity emerged as a commercially available commodity in the 1880s in the USA. It took 70 years to complete the urban and rural electrification for the USA, meaning that the USA was fully electrified around the 1950s. European countries also finalized their electrification by the end of the first half of the 20th century [3].

Meanwhile, electrification in South Asia, South America, and Africa (especially sub-Saharan Africa) moved slower. Table 1.1 shows a comparison of electrification as a percentage of the population in these regions [3].

Table 1.1: Percentages of urban and rural population served by electrification in low- and middle-income countries by region in 1970 and 1990 [3].

Region	Urban		Rural	
	1970	1990	1970	1990
North Africa and Middle East	65	81	14	35
Latin America and Caribbean	67	82	15	40
Sub-Saharan Africa	28	50	4	8
South Asia	39	67	12	25
East Asia and Pacific	51	82	25	45
All developing countries	52	76	18	33
Total served (in millions)	320	1100	340	820

It can be seen that in 1970 the proportion of people served in urban regions was between 25% and 70%, while less than 30% of rural regions had access to electricity and less than 50% of rural regions were electrified in 1990. The electrification rates are especially low in sub-Saharan Africa and South Asia [3].

However, South Asia has taken a significant turn in progress in the last few decades. Between 1993 and 2012 the percentage of the total population with access to electricity grew from 46.7 % to 79.5% and in 2021 it reached 98.8%, thus electrifying almost the entire population. In comparison, electricity access in sub-Saharan Africa has increased from 28.4% in 1994 to 51.4% in 2020, showing a significantly slower pace [4]. However, it is also important not to generalise all countries into a single continent, therefore, Fig. 1.1 gives an overview of the electrification rates in different countries in the western African region [5]. It can be noted that electrification rates differ significantly from country to country, while for the vast majority rural electrification is significantly lower than urban electrification.

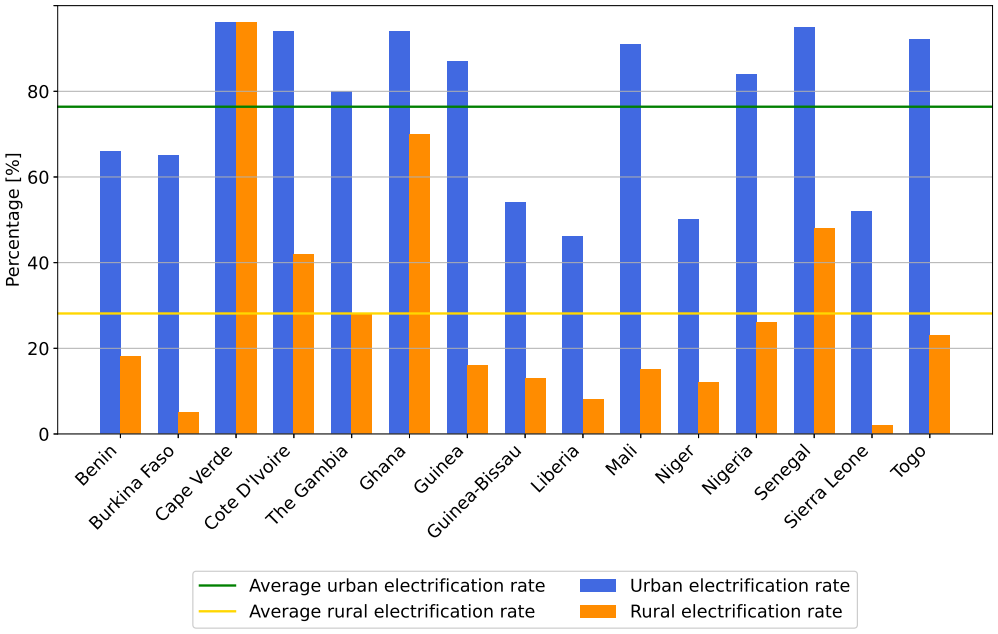


Figure 1.1: Urban and rural electrification rates of Western-African countries[5].

One of the reasons for the slower progress in access to electricity in sub-Saharan Africa is related to population density [6]. As can be seen in Figure 1.2, the population density is noticeably higher in southern Asia than in most of Africa. Specifically, most South Asian countries exceed 60 people per square kilometer, with many exceeding 100 people. In contrast, with some exceptions such as Egypt,

Nigeria, Ethiopia, and a few others, most African countries have a population density of less than 50 people per square kilometer [7]. In addition, it is also important to consider the urbanization rates. The percentages of the population living in urban areas in different parts of the world have been summarized in Table 1.2.

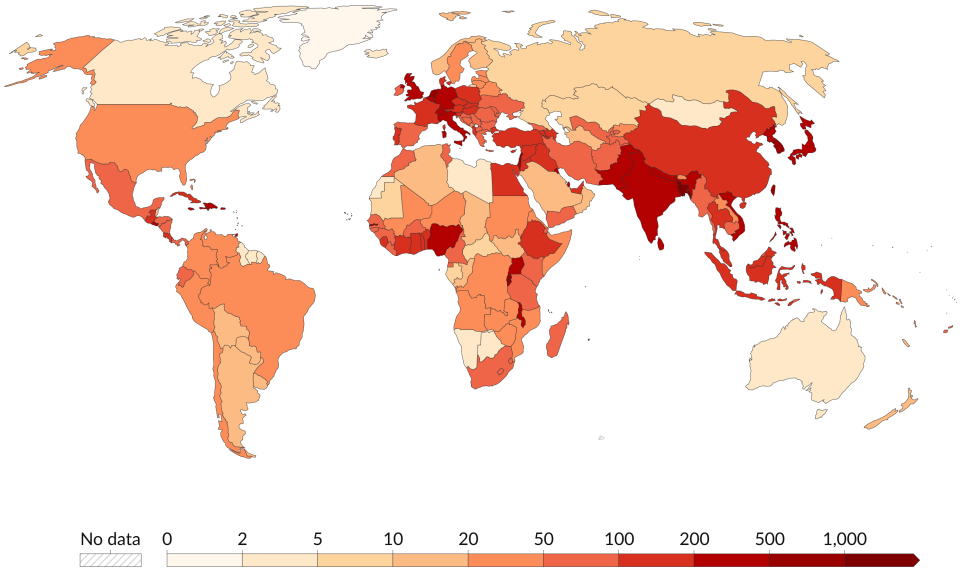


Figure 1.2: Map of world population density [7].

Table 1.2: Urbanization in different parts of the world and some countries in Africa expressed as a percentage of population living in or near cities or urban areas.

Region or country	Percentage of urban population [%]
European Union	76
North America	83
Middle East and North Africa	63
South Asia	36
Sab-Saharan Africa	43
Benin	50
Cape Verde	68
Ghana	59
Nigeria	54
Senegal	50
Togo	44

It can be seen that the European Union, North America, and the Middle East together with North Africa have urbanization rates above 60%. This means that at least two thirds of the population in these regions live in highly dense areas, making electrification easier due to the large number of connections. On the other hand, Sub-Saharan Africa has an urbanization rate of only 43%, meaning that the population is distributed throughout the country significantly more. However, one can see that the urbanization rate in southern Asia is even lower (36%), while rural electrification is significantly higher. This could be related to Figure 1.2. Although urbanization is lower, the density of people is significantly higher, meaning that even though most of the people do not live in areas that are considered urban, the density of rural areas is higher on average.

Population density plays a role in electrification speed because it determines which type of electrification is more cost-effective to use [8]. Specifically, in population-dense regions, it is most sensible to

extend the main grid as it allows to connect great number of users without running into capacity issues. However, in remote regions with low population density, it can be significantly more expensive to run cables to remote locations than it is in urban areas. The study by Mentis et al. in [8] has used OnSSET software to create a map of Sub-Saharan Africa depicting that in different regions different types of electrification solution are applicable.

The low cost-effectiveness of rural electrification is an issue that most countries face or have faced in the past, including the United States. Rural regions in the USA had to wait much longer before they could be connected to an electricity grid in part due to technological restrictions and the cost of rural electrification [3].

However, the low population density in rural regions is only one of the reasons for the difficulties of rural electrification. Four reasons could potentially be distinguished as pointed out by Pellegrini et al. in [3]:

- Rurality
- Cost
- Cultural differences
- Institutional challenges

Rurality and the cost of rural electrification have already been discussed previously. In addition Pellegrini et al. have distinguished the aspect of cultural differences between rural and urban areas of the twentieth century USA. For example, farmers in the USA living in the countryside looked at electricity with suspicion as it was a new and unknown technology. Finally, lack of coordination between different institutions and organizations can be the reason for the failure of a project even when financial difficulties have been resolved [9].

However, cost is the critical deciding factor for electrification. In rural areas, both the system costs more to build and the inhabitants have less money to spare than it is in urban areas. The costs have often been the reason for the villagers not connecting to the grid even when one has already been made [3], [9].

1.2 Impact of electrification

There is little doubt about the positive impact of giving someone access to electricity, such as increased comfort and productivity simply based on what types of appliances can be powered by electricity. Nevertheless, there is still a discussion on the extent to which rural electrification increases economic growth and improves healthcare. Duran and Sahinyazan [10] have shown in their study that there are both social and environmental benefits to connecting a community to a microgrid, for example, the creation of jobs, an increase in well-being and quality of life, as well as a reduction in fossil emissions. Similar findings have been found in other studies [11], [12]. However, the health benefits are not always found to correlate with the introduction of an electricity supply, [13], [14] while others do find a positive correlation [11],[12]. There are also studies that bring doubt on the economical benefits of electrification. Some studies have shown that the economical growth was not increased upon introduction of connection to the grid/microgrid [13], [15]. One of the reasons is the fact that the employment rate for rural communities is often low due to small population, therefore, it is hard to create a trade-market and electrification does not help with that. Even if some income-generating activities can be created based on electrification, there are no consumers that could spend their money on them due to the unemployment.

It also has to be taken into account that there are limitations to which it is possible to objectively assess the impacts of the electrification. It is hard to find two comparable households or villages and take one as a base case, since it is possible that the household that decided to connect to the grid was more dynamic and hence more significant differences could be seen after the connection to the grid. But this household might also have improved without the connection [11]. Similarly, the economic potential of the region should be taken into account when evaluating the impact of electrification. Regions that have less economic opportunities and in which the inhabitants potentially travel somewhere else for

work might show smaller economic growth than the areas in which electricity directly allows to create new businesses or expand the existing ones.

Although the exact correlations between electrification and certain economic, health, and general welfare aspects might not be entirely clear, electrification is certainly part of the equation for socio-economic development of a region. Although electrification of a remote village does not necessarily mean a good healthcare system, it does allow for introduction of refrigerators, which are necessary for a doctor's practice in order to store certain medicaments. For some this conclusion might look obvious, however, the author of the thesis finds it important to take a step back and reflect on what role the electrification plays in the society.

1.3 Types of solutions for rural electrification

Three general electrification strategies have often been distinguished - grid connection, microgrid connection, and solar home system (SHS) [8]. The three types represent three different scales, with the main grid being the largest representing a global approach and the SHS being the smallest representing a local approach. The remainder of this section provides a brief summary of each one.

Main Grid Extension
Grid extension as the name suggests, implies a connection to the main grid. This type of connection is common in most high-income countries - both in urban and rural neighborhoods - and in the urban areas of the middle and low-income countries. Grid connection is a necessity if electricity consumption is high, since microgrids or solar-home systems usually have significantly less generation per consumer connected to the grid/house [8]. Grid extension also allows to deal with the load peaks well since traditional grids are connected to flexible fossil fuel-based generators that can react well to load changes [16].

Microgrid
An extensive description of a microgrid can be found in Chapter 2, but to briefly describe it, a microgrid is a small electrical grid that consists of generation, consumption, and interconnections between the two with an optional electricity storage unit. While microgrids often operate directly connected to the main grid they are know for their capability to operate independently or also known as islanded operation [17]. Some microgrids are designed to switch between modes depending on the grid stability, while others are designed to function only off-grid. Off-grid microgrids are often used as a means of remote rural electrification and less so in urban electrification [18]. Off-grid microgrids can often be cheaper to construct than to create a connection with the main grid, as depicted by Mentis et al. [8]. However, given the smaller size of the microgrids and the local generation of electricity, one of the main disadvantages is the limitation in dealing with unplanned load peaks. Firstly, unplanned load peaks can cause stability issues since microgrids have limited inertia [19]. Secondly, unplanned load peaks are hard to design because they require overdesigning of the microgrid, which can drastically increase costs, hence in some situations load curtailment is issued [20].

Solar Home System (SHS)
Solar home systems are energy generation systems made for individual households and usually consist of a rooftop solar panel system, an electrical storage element, and a control system [21]. Solar home systems are most often used in remote locations, with one or a few households, where it is not profitable to build an entire microgrid [9]. However, the amount of generation of SHS might often not be enough to cover consumption, or it might be too expensive for the household to pay for enough capacity. SHS has the advantage that theoretically a group of SHSs can be transformed into a microgrid if the necessary capital is available. Alternatively, in case a microgrid or the main grid is nearby, a connection can be made.

1.4 Problem Formulation

Microgrids are expected to play a crucial role in rural electrification as evaluated by different industry experts and committees. In the report 'Lights, Power, Action' by the Africa Progress Panel it was estimated that 45% of the electricity connections in rural areas of Africa will be made by the use of mini-grids. The report classifies a microgrid as a subset of minigrids, where it is defined as a minigrid working in islanded mode and having a capacity between 100 kW and 1 MW [22]. And some estimates even predict that up to 60% of the new generation of electricity to provide universal access will be introduced through the implementation of microgrids [18]. Hence, one of the motivations for the thesis project is to contribute to the research and development of microgrids, as it is one of the main tools for the elimination of energy poverty.

A general diagram of the type of microgrids considered in this thesis can be seen in Fig. 1.3.

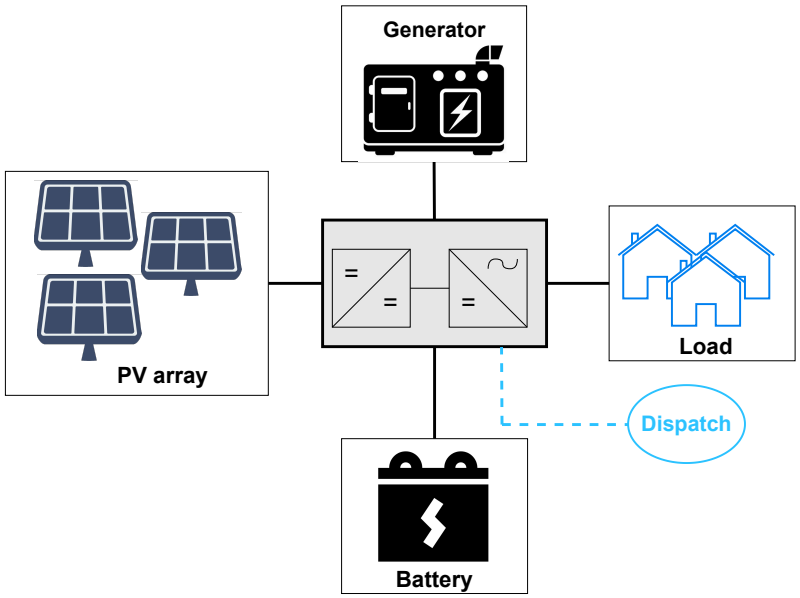


Figure 1.3: Microgrid layout of the type of microgrids considered in the thesis project.

The considered microgrids are meant for rural communities in sub-Saharan Africa, therefore they are not connected to the main grid and are fully self-sustaining. Moreover, it is considered that the climate is in general dry, however, there is a distinction between a dry season and a rainy season, specifically for the use case introduced in Chapter 6. As shown in Fig. 1.3, the considered microgrid case is a single-bus system with PV solar panel array as the main generation unit and an additional diesel generator as a secondary source of energy. In addition, an electricity storage system is installed to compensate for the intermittency of solar energy. Together with the load, the electrical components are connected to an inverter that allows to make the necessary energy conversion steps. The inverter also takes care of the energy dispatch. It is also important to note that the thesis project does not consider an electricity market as the electricity price in the considered microgrids is determined by the microgrid operator. Therefore, the goal of the optimization problem is to reduce the total cost of the microgrid or specifically net-present cost (NPC), since it allows to account for the inflation rate and the discount rate along the years.

In recent years, the number of research articles published on microgrid optimization has increased significantly, as can be seen in Fig. 1.4. Nevertheless, the current optimization strategies tend to make many assumptions that often lead to a suboptimal microgrid design. Table 1.3 provides a summary of the types of assumptions made in the literature.

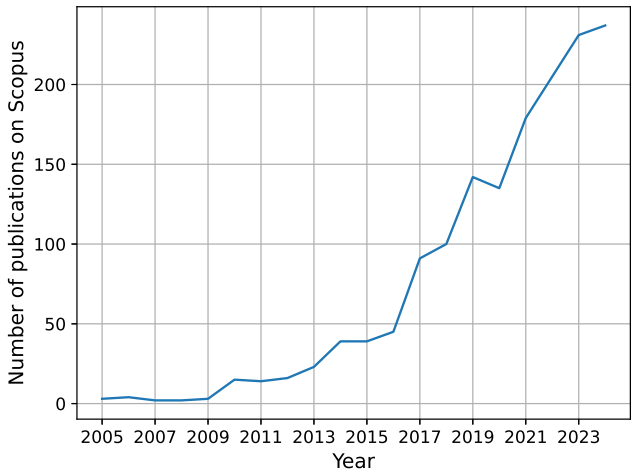


Figure 1.4: Yearly number of publications on Scopus between the years of 2005 and 2024 for the prompt ”Microgrid AND Optimization AND Siz*” [23] .

Table 1.3: Types of assumptions made in microgrid sizing optimization and corresponding examples.

Type of assumptions	**Examples**
System-level Assumptions	Independent modeling of sizing and energy dispatch No capacity limits in power lines No losses in electrical transmission
Environmental assumptions	Deterministic weather profile No environmental effects on the system
Electrical load assumptions	Deterministic electrical consumption No growth/changes in electrical consumption over the years
Component modeling assumptions	No/simplified component degradation Constant component energy conversion efficiencies

The first type of assumptions is related to system-level considerations. An example is that the literature often lacks holistic sizing optimization strategies that account for energy dispatch. Sometimes, the energy dispatch is significantly simplified. For example, many of the optimization strategies for the size of the microgrid assume a simple load-following strategy [24], which uses a priority-based approach where renewable generation sources are dispatched first, followed by battery storage and finally the backup generator. Load-following often does not lead to an optimal dispatch of resources because the same logic is applied regardless of the weather and electrical load. In contrast, optimized economic dispatch makes sure that the dispatch costs are minimized by calculating the optimal dispatch schedule depending on the available generation and expected load. In addition, some assumptions are often made at the technical system level. For example, system capacity limits and electrical losses are most often ignored. To prevent that, one would need to run an optimal power flow in addition to energy dispatch.

The second set of assumptions considers the environment. A common example is the use of fixed weather profiles (temperature, irradiation, wind profile) of a single year. The simplest approach is to use data of a historical year from the area of study. This approach can result in varying system performance across the years depending on how similar a particular year is to the chosen historical year. To account for the variations in weather over the years, a common method is to use typical metheorological years (TMY). TMYs are synthetic weather curves generated by combining representative months that have been derived from multiple years of weather data [25]. Although this approach provides a statistically more probable weather time series, the curve still presents only one scenario. Multi-scenario analysis is

sometimes done to evaluate the system's performance in extreme conditions, however, a more robust method is to use Monte Carlo analysis. However, even though the Monte Carlo method considers a large number of possible scenarios, it is significantly more computationally intense [26]. Similarly, rarely environmental effects on the components are taken into account when sizing the system. An example, is the dusting of solar panels. In countries with dry weather, it is common for sand layers to form on solar panels, which when not cleaned can significantly reduce the efficiency of the solar panels [27].

Thirdly, it has to be acknowledged that the systems are always designed based on assumptions about consumer behavior. However, it is extremely difficult to predict the exact pattern of the consumed energy, hence often the reality differs significantly from the model. It has even been shown that consumers themselves cannot accurately predict their own consumption patterns [28]. Similarly as with weather profile generation, using a historical load curve might not be the most accurate method. Additionally, some microgrids fail to account for load growth leading to undersized microgrids [29].

The fourth and final type of assumptions include assumptions related to the level-of-detail in microgrid component modeling. It can be found that across a variety of studies there are large differences in how the component degradation has been modeled. Some studies use simple or no degradation models, while others use select some components for which to use complex degradation models that are partially or fully based on the physical degradation phenomena. Moreover, designs sometimes assume a constant efficiency for the solar panels [30], [31], however, the efficiency of the solar panels depends on the module temperature, which in turn depends on the ambient temperature, irradiance and even wind speed [32], [33]. Therefore, the resulting system can outperform or not perform well enough depending on the assumptions made.

One of the main reasons why so many assumptions are made is directly related to the computational cost of the optimization algorithm. One could design a model which does not make any of the previously mentioned assumptions, however, in all likelihood the model would take too long to run to be practical. There is always a trade-off between the level of complexity and the computational time. Therefore, it is necessary to evaluate the impact of different simplifications in system modeling. Such an evaluation would help to understand which assumptions are reasonable to make and which assumptions could significantly change the design decisions if made. The literature has provided some comparisons of the impact of the modeling assumptions. For example, Wang et al. in [34] compared the impact of different battery degradation models on the LCOE of a microgrid and Dakir et al. in [35] compared the effect of using a rule-based dispatch versus an optimization-based controller on the Net Present Cost of a microgrid system. Nevertheless, a comprehensive comparison is still lacking. Therefore, the main goal of this thesis project is to provide a detailed comparison of the trade-offs between the model complexity and the impact on the final design and cost. Additionally, the thesis explores modeling the inverter degradation within the microgrid sizing optimization, which has not been done before to the knowledge of the author of the thesis. However, due to the time constraints, it was decided to limit the scope of the thesis to the assumptions related to optimization strategy and component degradation, hence the effect of weather uncertainty and distribution line capacity limits are not investigated in this thesis project.

The following core research question has been identified for the thesis project based on the identified gaps in the literature:

How to optimally size a microgrid in sub-Saharan Africa under dry climate with high irradiation while considering consumer behaviour uncertainty and component degradation?

The core research question has been split into several subquestions:

- How does the inclusion of the battery and solar panel inverter switch degradation influence the solution of the sizing and EMS optimization problem(s) and the computation time?
- How do the results of the microgrid sizing optimization compare between a nested microgrid sizing-dispatch optimization with a non-nested optimization?
- How to experimentally test the influence of the solar power curtailment strategy on the switch degradation inside the inverter without the need of doing long-term power cycling experiments?

The following is a list of contributions that this thesis has made to the scientific work of rural microgrid sizing optimization:

- Development of a nested PSO microgrid sizing algorithm that uses a stochastic load profile and accounts for degradation of battery electrical storage and the inverter.
- A comparison and overview of the effects of the degradation of battery electrical storage, inverter.
- A comparison and analysis of the trade-offs between using a nested sizing optimization and non-nested sizing optimization.
- Development of an experimental test setup for the investigation of the effects of power curtailment on microgrid inverter switch degradation.

The report consists of a total of five core chapters. Chapter 2 provides background information on some of the core concepts that a reader might find useful to make the reading of the rest of the chapters easier. Specifically, Chapter 2 provides an overview of the types of microgrids and the types of control used in microgrids. In addition, an overview of the main battery chemistries and the degradation mechanisms of batteries has been given. Chapter 3 shows the progress in optimization approaches for microgrid sizing and dispatch and presents the research gaps in the state-of-the-art optimization strategies. It also gives an overview of the current load modeling tools and battery degradation models. Next, Chapter 4 explains in detail the methodology for the proposed optimization strategy of this thesis project and introduces the design and methodology for the experiments performed to investigate switch degradation under different control strategies. In the following, Chapter 5 presents the results of the experimental investigation. Finally, Chapter 6 describes the use case of the Samionta microgrid showing how the optimization strategy can be used to optimize the sizing and dispatch of a microgrid and provides a comparison with a reference dispatch strategy from the literature.

Chapter 2

Theoretical Background

This chapter is meant to provide the reader with some background knowledge that can be useful in understanding the subsequent chapters. If, however, the reader already is familiar with the concepts covered in this chapter they can directly continue with Chapter 3, which describes the state-of-the-art research in the microgrid sizing optimization. In this chapter, Section 2.1 provides an overview of what exactly defines a microgrid and how microgrids are classified. Section 2.2 provides a brief overview of the battery working principles and their degradation mechanisms. Finally, Section 2.3 introduces the switch degradation mechanisms and the lifetime estimation model.

2.1 Overview of microgrids

2.1.1 Definition of a microgrid

The definitions of microgrids vary in the literature. One of the more known definitions of a microgrid is written by the US Department of Energy Microgrid Exchange Group: ”A microgrid is a group of interconnected loads and distributed energy resources within clearly defined electrical boundaries that acts as a single controllable entity with respect to the grid. A microgrid can connect and disconnect from the grid to enable it to operate in both grid-connected and islanded modes” [36].

There are four properties that can be extracted from this definition:

- A group of interconnected loads and distributed energy resources
- Clearly defined electrical boundaries
- Acts as a single controllable entity with respect to the grid
- Can be operated in both grid-connected and islanded-mode

Firstly, a microgrid consists of a group of interconnected loads and distributed energy resources (DERs). DERs also do not have a common definition, nevertheless, US Federal Energy Regulatory Commission (FERC) [37] defines it as: ”A DER is any resource located on the distribution system, any subsystem thereof or behind a consumer’s meter. DERs may include electric storage resources, distributed generation, demand response, energy efficiency, thermal storage, and electric vehicles and their supply equipment. ” Secondly, microgrid has clearly defined electrical boundaries. This means that there is a clear point of interconnection for the microgrid with the main grid which is where the switch is located that connects or disconnects the microgrid from the main grid. Thirdly, the microgrid acts as a single controllable entity. It does not mean that all the loads and DER’s are controlled by a single controller, but rather that the microgrid as a whole is controlled together as a unified system. Finally, a microgrid has two operational modes. Microgrids can be operated both in connection to the main grid and in a disconnected manner, which means that they have independence.

2.1.2 Microgrid Components

Microgrids consist of several main components:

- Generation Units - typical examples of electricity generation units include roof-top solar panels or small solar panel arrays, small wind turbines, diesel generators, and sometimes hydropower generators as well as a mix between any of the mentioned units.
- Electrical loads - electrical loads can include both residential consumption as well as industrial loads depending on the location of the microgrid.
- Storage Units - nowadays many of the existing microgrids consists of renewable energy power plants which struggle with the intermittency of the weather. Hence, storage units such as batteries help to even out the inconsistencies of the generated power both within a day and sometimes between several days.
- Converters - microgrids often consist of both AC and DC loads as well as AC and DC generation units (for example, solar panels and diesel generators). In order to distribute the power within the microgrid it is necessary to convert it to a single type of voltage. To achieve that different types of converters can be used - DC-to-AC, AC-to-DC or DC-to-DC. To convert AC to a different level of AC, a transformer is needed, or lately AC-to-DC-to-AC converters have been used.
- Distribution network - to connect the generation units with the electrical loads, a distribution system is needed. Examples of distribution system elements include cabling and protection, as long as previously mentioned converters.

2.1.3 Microgrid Topologies

It is very common to distinguish three microgrid topologies based on the types of generation sources and the main bus(es) of the grid. These topologies are AC microgrids, DC microgrids, and DC/AC or hybrid microgrids. A description of the types of components within a microgrid as well as the microgrid topologies is given in this subsection.

AC microgrid
As shown in Fig. 2.1, an AC microgrid has a central AC bus to which all the generation units (DERs) and consumers are connected. DC loads, solar panels, and batteries are connected via inverters to transform DC voltage into AC voltage, while AC loads can be connected directly. Wind turbines are connected via an AC/AC converter, which in practice is an AC/DC/AC converter. AC microgrids are the most common microgrid topology, because most of the loads and generation units for the time being use AC. However, AC microgrids have the disadvantage that connection to the main grid can cause difficulties because the frequency and phase of the voltage have to be synchronized [38]. Additionally, electrical losses can be higher for AC microgrids than for DC or hybrid microgrids.

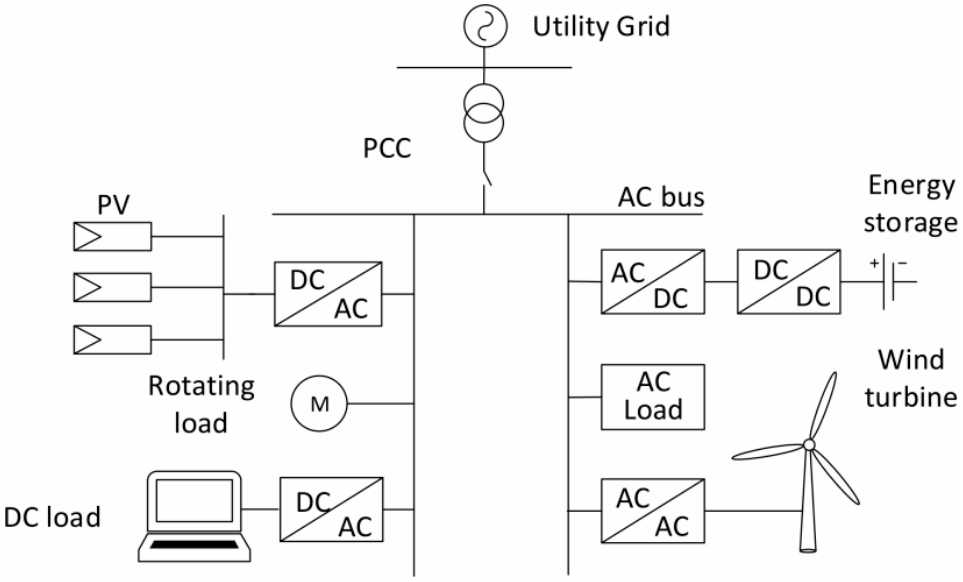


Figure 2.1: An example of an AC microgrid topology [38].

DC microgrids

An example of a DC microgrid has been shown in Fig. 2.2. Instead of an AC bus in this topology all the loads, the DERs and battery have been connected to a DC bus, which is then connected to the main grid via a DC/AC converter. DC/DC converters are used for storage, photovoltaic arrays and DC loads, while AC/DC converters are used for AC loads and wind turbine. DC microgrid topology is becoming more common as more PV arrays, batteries, and electric vehicles are used. An advantage of this topology is that DC/DC converters are more efficient than DC/AC converters, and hence more energy is saved in conversion. The disadvantages of DC microgrids include more complex protection schemes and difficulties in reconstructing existing AC networks [38].

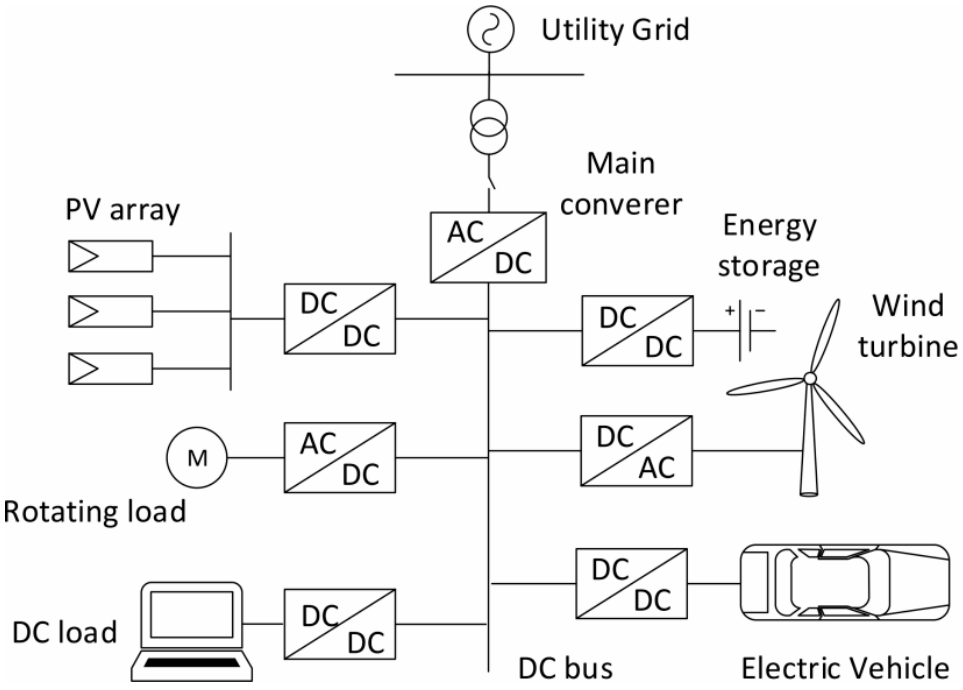


Figure 2.2: An example of a DC microgrid topology [38].

AC/DC microgrids (Hybrid microgrids)
AC/DC microgrid topology has been depicted in Fig. 2.3. As the name suggests, it is a mix of AC and DC microgrid topologies. It can be seen in the figure that there is both an AC bus and a DC bus. The DC loads, and PV array are connected to the DC bus via a DC/DC converter while the AC rotating load is connected directly to the bus and the wind turbine is connected via an AC/AC converter as before. The two buses are connected with an AC/DC bidirectional converter thus allowing the power flow to go in both directions [38]. This topology allows for the most efficient configuration as the most efficient converters (if needed at all) can be used for each type of DER and load.

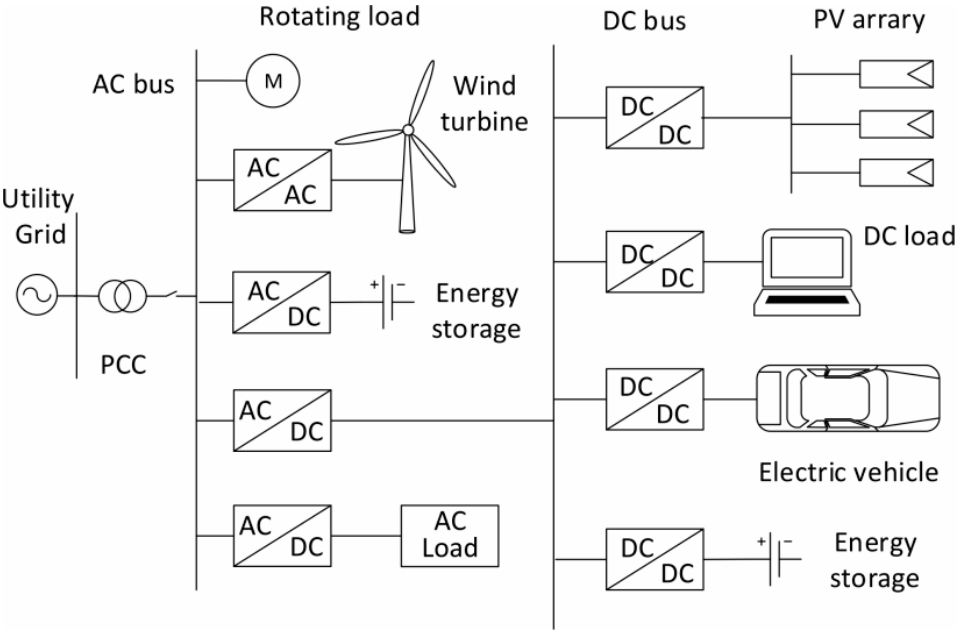


Figure 2.3: An example of a DC/AC microgrid topology [38].

2.1.4 Microgrid Control

There are two aspects of microgrid control that are addressed in this subsection - the control hierarchy and the distinction between centralized, decentralized, and distributed control.

The hierarchical control scheme usually distinguishes three levels - primary, secondary, and tertiary control - while in some cases only two control levels are present [39], [38]. The three levels correspond to the timescales the corresponding controls need to operate within. Primary control needs to react within milliseconds to seconds, secondary control needs to react within a few seconds to a few minutes but sometimes also up to an hour, and tertiary control operates within the hour-to-day range [39]. Primary control is responsible for regulating the output power of the DERs by controlling the corresponding converters. It involves regulating the output voltage and current as well as islanding detection ensuring active and reactive power sharing [39], [40].

The secondary control level includes functions like secondary voltage and frequency control, power quality control, and load shedding. Finally, tertiary control is related to the functions related with the interaction with the main grid such as power exchange, energy markets, and optimal operating points in respect to the main grid. It deals with the economic dispatch problem which allows to schedule which generation units should be used based on load and weather prediction as well as choice can be made how the storage unit should be used. However, there is no agreement among researchers whether the tertiary control should be related to the microgrid control or to the main grid control [39]. Nonetheless, the thesis deals with islanded microgrids where it is needed to perform economic dispatch without the presence of a main grid. Hence, it could be argued that these types of microgrids have a tertiary control. An overview of the control levels has been provided in Table 2.1

Table 2.1: Overview of the timescales and functions of the control levels in hierarchical control of microgrids [39].

Control Level	Timescale	Functions
Primary Control	Miliseconds to seconds	Primary voltage and frequency control Ensuring power balance
Secondary Control	Seconds to one hour	Secondary voltage and frequency control Demand side management and load shedding
Tertiary Control	Minutes to days	Economical Dispatch Ancillary services

There are three main implementations of hierarchical control - centralized, decentralized and distributed control. A visual overview has been provided in Fig. 2.4

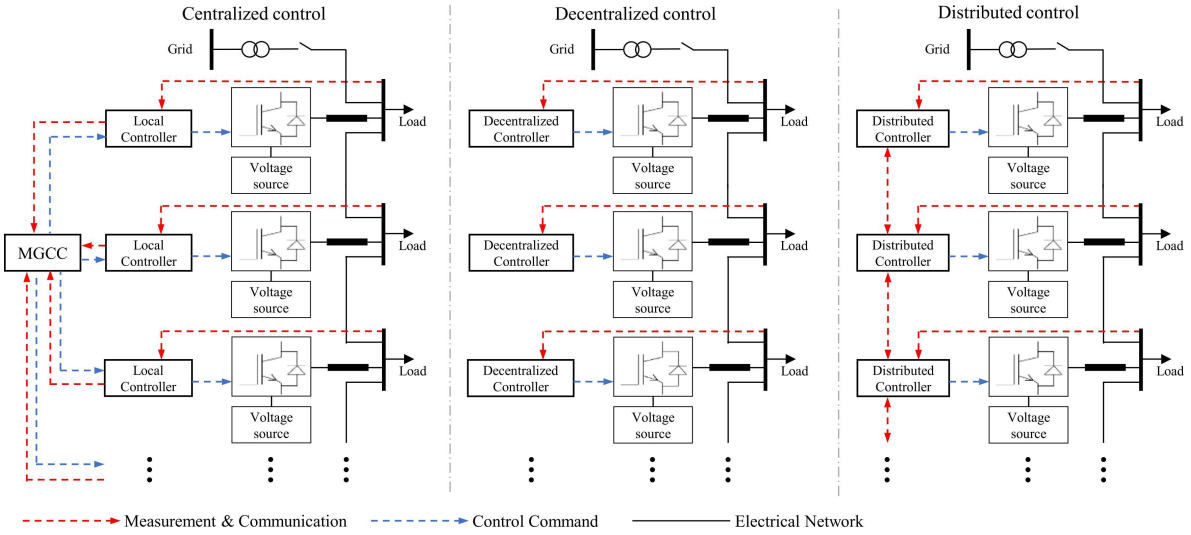


Figure 2.4: A visual overview of the implementations of centralized, decentralized and distributed control architectures [40].

Centralized control architecture as the name suggests consists of a single control unit (microgrid central controller), which takes care of the generation and load set points. Centralized control allows for an excellent overview of the microgrid and simple synchronization of frequency since there are communication channels between each local controller and the microgrid central controller. However, it comes with a high computation cost. Since system-wide optimization can take a long time, it can influence microgrid stability since centralized control cannot react to disturbances that require quick decision. Therefore, sufficient reserves need to be installed in a centralized control scheme to deal with disturbances, which ultimately increases the price of the microgrid [40].

A fully decentralized control architecture includes having a local controller for each unit in the microgrid. There is no central control unit, and there is no communication between each local controller. The operation points of the unit connected to the local controller are set based on the local information of the voltage and frequency. This type of operation straight away implies the issue of synchronization. Without communication channels between local controllers, it is very difficult to ensure that each of them provides the same frequency and phase shift [41]. However, decentralized control is significantly less computationaly expensive than centralized control and results in higher stability and reliability since the reaction time to disturbances is very fast.

Distributed control architecture provides a balance between the centralized and decentralized control architectures. As can be seen in Fig. 2.4 there are communication channels between the neighboring controllers while there is still no central controller. This architecture sacrifices some of the computational speed with respect to decentralized control but still ensures reliable and stable operation [41]. This type

of control resolves the issue of synchronization present in decentralized control, as all the neighboring controllers can communicate their frequency setpoints with each other.

This section has provided an overview of the different topologies and control architectures of microgrids. It is meant to provide a general picture to the reader on how the microgrids differ from one another and what the trade-offs are when making a choice for a certain topology or control scheme, which will be introduced at the start of the next chapter.

2.2 Battery Technology

This section first provides an overview of the battery chemistries after which the physical structure and working principles of a Lithium-ion batteries are explained. Finally, an overview of the degradation mechanisms inside lithium-ion batteries is provided.

2.2.1 Overview of battery chemistries

Given the intermittency of renewable generation sources, such as the sun or the wind, a secondary source of electricity is needed to guarantee continuous supply. There are several ways of implementing a secondary source in microgrids - it can be a renewable source, such as hydropower or geothermal power; it can be a carbon-neutral energy, for example, biofuels and it can be an energy source based on fossil fuels, such as a diesel generator. However, there is a solution that can use a delayed supply of the same primary source (solar or wind) by storing the electrical energy for later use.

The two main implementations of energy storage in this context are batteries and hydrogen storage. Hydrogen storage has a higher energy density than batteries, but it also has higher losses and requires additional infrastructure such as electrolyzers, fuel cells, and possibly hydrogen pipelines, making the investment costs very high. Hence, hydrogen storage is better suited for long-term large-scale storage [42]. Battery storage on the other hand has a higher power density and significantly lower energy density while the losses are also lower, making it suitable for short-term energy storage. Since the focus of the thesis project is on locations that have a relatively stable supply of solar energy throughout the year, battery energy storage is sufficient.

There are a variety of different types of batteries that can be used for electricity storage, however, different battery technologies have different advantages and disadvantages. The ratios between the cost and power and the energy densities are one of the most important characteristics to compare. An overview of battery technologies and how they compare with the ratios between power and energy densities can be seen in Fig. 2.5 [42].

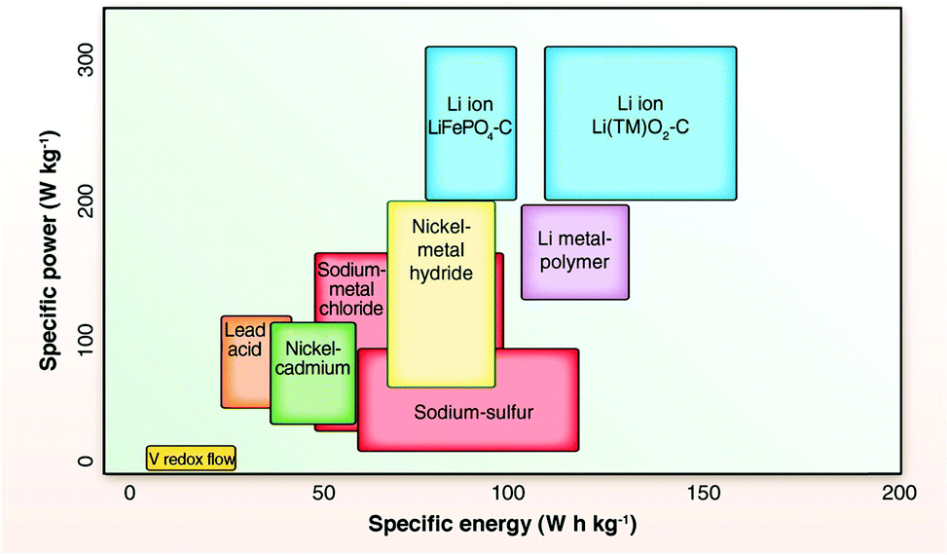


Figure 2.5: Ragone plot of battery power density versus energy density [42].

It can be seen that Li-ion batteries have noticeably higher power densities and/or energy densities depending on the technology, which means that they are the most compact battery technology in terms of W/kg and Wh/kg.

The cost comparison of different energy storage technologies including different battery technologies can be seen in Fig. 2.6 [43].

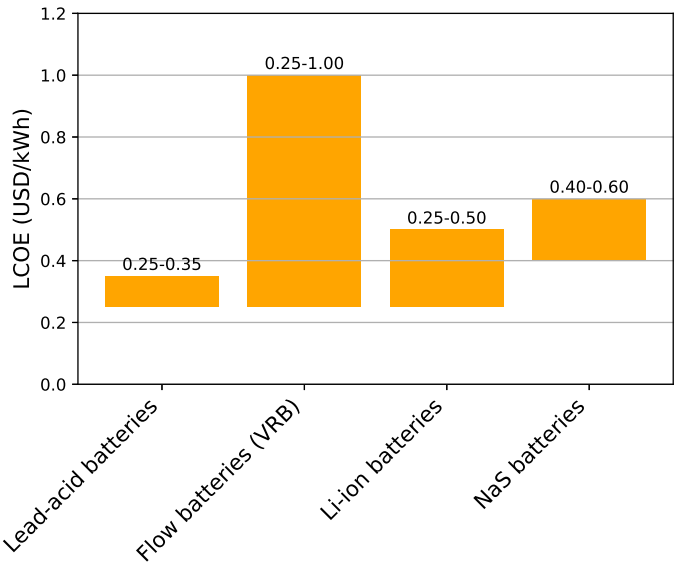


Figure 2.6: LCOE of different energy storage technologies [43].

It can be seen that the LCOE of the Li-ion batteries is slightly lower than that of NaS batteries, while being slightly more expensive than lead acid batteries depending on the exact chemistry. As can be seen, flow battery technology has a very wide variability in LCOE, which could be both because of different possible chemistries and applications. Therefore, given that Li-ion batteries have better performance in power and energy density, and the cost is comparable with other battery technologies, they have become as one of the more widely used battery technologies especially in the electric vehicle industry.

2.2.2 Physical structure

The general structure of a Li-ion cell can be seen in Fig. 2.7 [44].

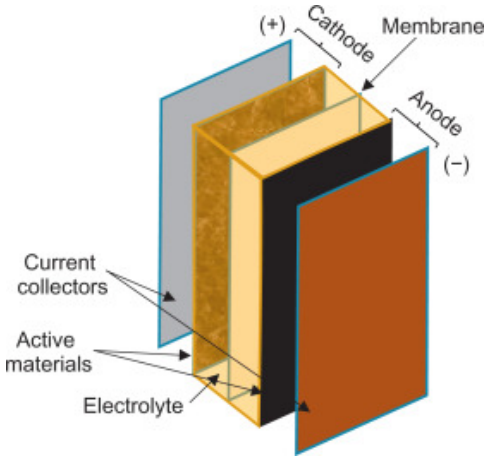


Figure 2.7: Schematic of the main components of a lithium-ion (Li-ion) cell [44].

It consists of an anode, a cathode, an electrolyte, and a separating membrane. The anode and cathode (electrodes) have two sections, the active material and the current collectors. Active material is the part that participates in the electrochemical reactions, while current collectors are used for the collection of electrons. The current collectors are also connected to the external circuit, which is not depicted in this figure. The electrolyte between the anode and cathode allows the transport of ions, whereas the separating membrane makes sure that only specific types of ions can pass through to allow the necessary electrochemical reactions [44].

An overview of the main anode and cathode materials along with the advantages and disadvantages have been given in Table 2.2 and Table 2.3 [44].

Table 2.2: Different anode materials and their characteristics [45].

Material	Theoretical capacity [mAh/g]	Average potential [V]	Advantages	Issues
Li metal	3800	0	Energy density	High reactivity, dendrite growth, and fires, explosions
Graphite	372	~ 0.1	Mature technology	Outside electrolyte stability
Cokes	-	~ 0.15	High capacity and cycle life	High consumption of Li
$\mathrm{Li}_x\mathrm{Si}_y$	4200	~ 0.16	High capacity, low cost	Volume changes, nanostructures
$\mathrm{Li}_x\mathrm{Sn}_y$	790	~ 0.4	High capacity, low cost	Volume changes, nanostructures
$\mathrm{Li}_4\mathrm{Ti}_5\mathrm{O}_{12}$	170	~ 1.55	Low volume expansion, chemical, and thermal stability	Low specific capacity, and high voltage

Table 2.3: Different cathode materials and their characteristics [45].

Material	Theoretical capacity [mAh/g]	Average potential [V]	Advantages	Issues
LCO	274	3.9	Field-tested operation	High cost, low thermal stability
NCA	200	3.6	Long calendar life	Fast aging at high T
LMO	48	4.0	Price, environmentally friendly	Reduced cycle life
NMO	280	3.8	Energy density, cost	Low Li diffusivity
NMC	278	3.7	High capacity	Relatively high price
LFP	170	3.4	Low cost, safety and environmental compatibility	Low electronic conductivity, and potential

The overview tables are provided to give a sense of how many different factors have to be taken into account when choosing a proper combination of an anode and cathode. It should be noted that the average potentials in Table 2.2 are listed in comparison to the average voltage of the pure lithium anode. Lithium theoretically is the best material for the anode due to the most negative potential of (-3.05 V) since the highest voltage for the cell can be achieved by combining the material with the most positive potential as a cathode and the material with most negative potential as anode. However, due to lithium plating, which increases the cell resistance and development of dendrites that could cause a short circuit, it is not used that commonly [45]. Graphite is more often used. Graphite anode allows for high insertion/removal rates. Lithium cobalt oxide (LCO) is one of the more commonly used cathodes, however, cobalt is not widely available and it is toxic [45]. Lithium manganese oxide (LMO) and lithium iron phosphate (LFP) are commonly used alternatives.

The electrolyte in a Li-ion battery should have the following characteristics: high ionic conductivity, high chemical and electrochemical stability towards electrodes, an operation range between (-20 °C) and (+60 °C), high safety, and low cost. The four main types of electrolytes are liquid, ionic liquid, solid polymer, and gel polymer electrolytes. Each type of electrolyte has its advantages and disadvantages, for example, liquid electrolytes have ionic conductivity, while their thermal stability is quite poor. It is the opposite for solid electrolytes for which the ionic conductivity is poor, but the thermal stability is high [44]. The choice of the electrolyte depends on the specific application.

The membrane serves as a separator to ensure that only specific ions cross it while the electrons are not transported. The membrane itself does not participate in the electrochemical reactions [44],[46]. Examples of separator membrane materials include polymeric polyethylene or polypropylene membrane and a non-woven fabric mat [46].

Given the requirement for high electric conductivity, metals are generally used as current collectors. Usually, copper is used as the anode collector, while aluminum is used as the cathode collector [44].

2.2.3 Working Principles

In this section, the basic working principles of a Li-Ion cell are explained. Fig. 2.8 shows a simplified diagram of a Li-ion cell.

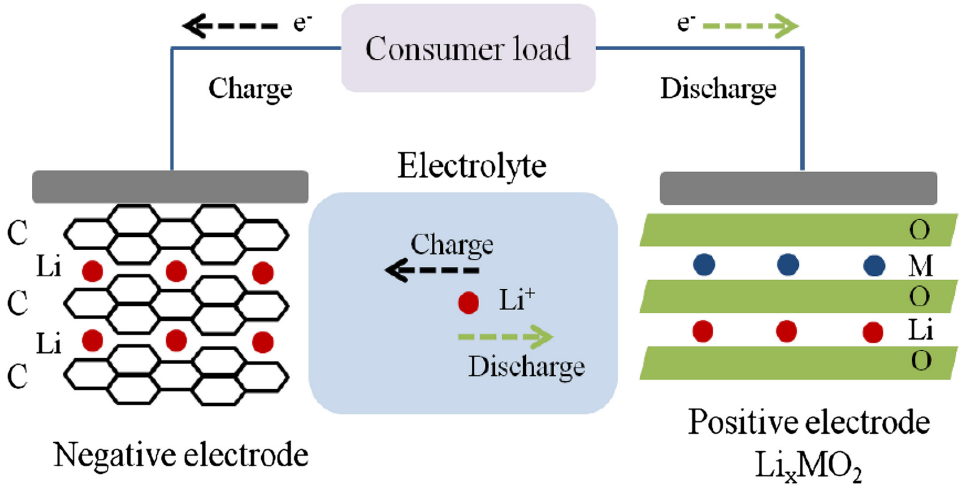


Figure 2.8: Simplified diagram of a Li-ion battery cell [45].

As depicted in the figure, at the moment when an external circuit is connected to the current collectors of the anode and cathode the charging or discharging starts taking place. Upon connection, electrons start flowing from the negative electrode (anode) to the positive electrode (cathode) and the lithium ions flow in the same direction via the electrolyte. The directions in case of charging and discharging are opposite. In such a way, chemical energy is converted into electrical energy (discharging) and vice versa [45].

2.2.4 Degradation Mechanisms

This sub-section gives an overview of the main degradation mechanisms in Li-ion cells. The degradation or aging of a battery can be characterized as energy loss, power loss, or both simultaneously. There are many degradation mechanisms that contribute to battery aging, which involve interaction between different battery components. An overview of the degradation mechanisms has been shown in Fig. 2.9 [45].

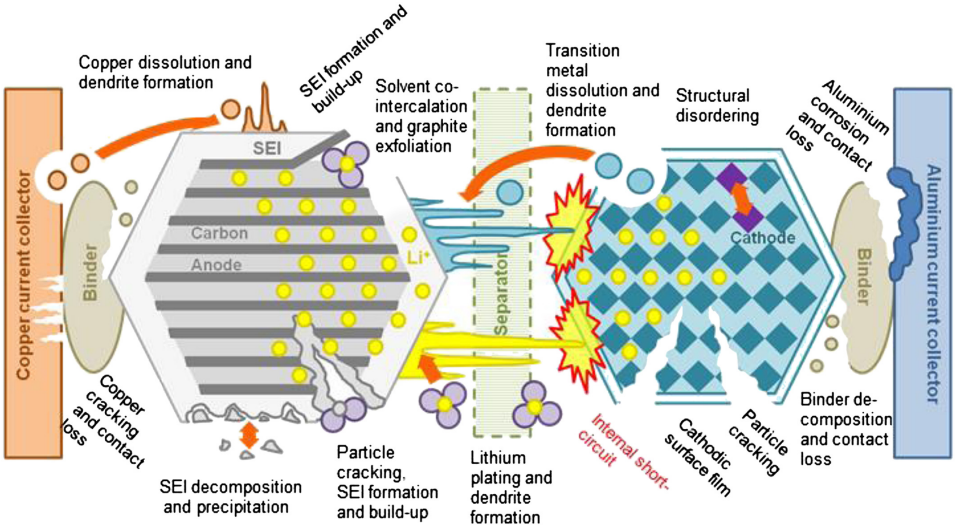


Figure 2.9: Degradation mechanisms in Li-ion batteries[45].

Next, the most important degradation mechanisms will be described.

Formation of solid electrolyte interphase (SEI)

SEI is often considered as the dominant reason for anode aging. The side reaction between the anode and the electrolyte leads to a decomposition of the electrolyte, whose products form an SEI layer between the anode and the electrolyte. The formation of the SEI is significantly more rapid during the initial stages than in the later stages. The formation of SEI increases the internal resistance and results in a capacity fade [45].

Lithium plating

Another degradation mechanism that connected with anode is lithium plating. It takes place if the anode potential exceeds 0 V. This causes capacity fade since active material is consumed. Additionally, dendrites form that can rip the separation layer, causing a short circuit, which destroys the battery [45].

Separator Degradation

In addition to the previously mentioned tearing due to dendrite growth, the separator also contributes to battery aging due to clogging of the pores due to electrolyte decomposition and mechanical changes due to high temperatures (if applicable) [45]. Separator degradation contributes to the power fade.

Current collector degradation

When the cell is not operated under the intended conditions, inappropriate voltages, temperatures, or charge/discharge currents, current collectors (aluminum or copper) are prone to oxidation[45]. The pitting corrosion on the aluminum current collector describes the process in which the aluminum surface is corroded in pin-like holes. It can decrease the calendar life of the battery [47]. Corrosion of the copper current collector has a direct effect on the battery capacity [45].

Mechanical deformation

During the charging and discharging of the battery, both the anode and cathode change volume as the reactants are inserted or extracted. This can cause loss of electrical contact with the anode and cathode and formation of cracks (thereby increasing the internal resistance) [45].

2.2.5 Stress factors

Besides physical phenomena that accelerate battery degradation due to impurities in battery construction, there are several reasons why battery degrades faster, which are caused by operating conditions (stress factors) of the battery. Typically, battery aging is split into two types: calendar aging and cyclic aging [48].

Calendar Degradation

Calendar degradation considers the degradation during the times when the battery is not in use. As described in [48] calendar aging depends on three variables - the time spent in the idle state, the ambient temperature, and the State-of-Charge (SOC) of the idle state.

Time
During idle state side reactions and SEI growth continue [48].

Ambient Temperature
Temperature can be seen as a catalyst for side reactions - the higher the temperature, the higher the reaction rate, and the larger the SEI growth [48].

SOC

Higher SOC correlates with higher degradation. This is because a lower anode potential has a relationship with a higher SEI growth. Additionally, for NMC batteries, a higher cathode potential has a relationship with a higher transition metal dissolution due to oxidation of lattice oxygen [48].

Cyclic Degradation

Cyclic degradation is related to all the degradation mechanisms that occur during active use of the battery. The stress factors of cyclic degradation include the charge / discharge rate (C-rate), the number of cycles, the mean state of charge (mSOC), the depth of discharge (DoD), the ambient temperature, and the moisture [45], [48].

Number of cycles and C-rate
Fig. 2.10 shows an example of a capacity fade curve for a lithium-ion battery [49].

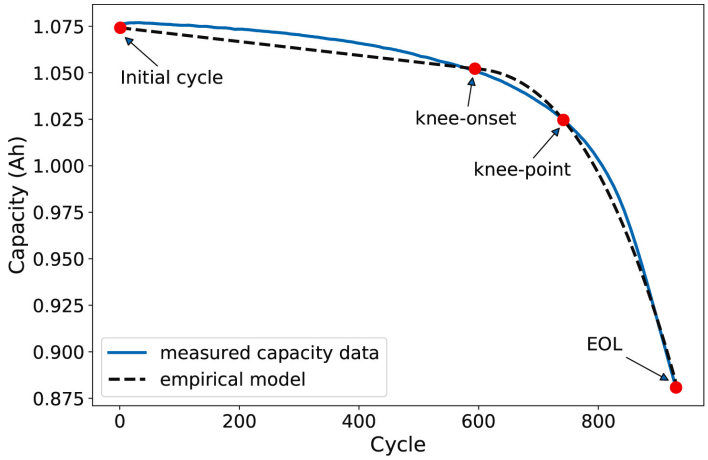


Figure 2.10: An example of a capacity fade in a Li-ion battery depending on the number of cycles [49].

It can be seen that the capacity decreases over the lifetime of the battery. When the battery reaches the knee point, the degradation increases rapidly soon after which the battery reaches its end-of-life (EOL). Furthermore, the capacity fade for different charge / discharge rates is depicted in Fig. 2.11. It can be observed that higher c-rates lead to more rapid capacity fade.

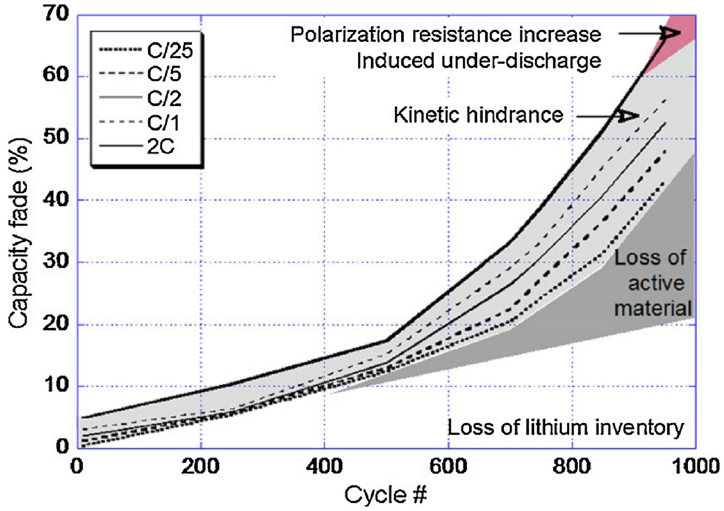


Figure 2.11: The cell capacity loss map under room temperature as a function of cycle aging at various C-rates [45].

Temperature

There is a certain operating range of temperatures that the battery is intended to be used within. In addition, a difference has to be noted between the ambient temperature and the cell temperature. Since cells are stacked, the temperature in the inner-most cell is usually different from the outer-most cell that is in contact with the frame and the environment. In addition, charging and discharging of the battery increases the temperature of the cells, and hence it can be higher than the one of the environment. The environment, therefore, can be used as a coolant. Figure 2.12 shows an example of a curve depicting cycle life dependency on the cell temperature. It can be seen that there is a certain temperature range for which the cycle life stays constant, but outside this range the cycle life starts to rapidly drop [50]. If the temperature is too low, lithium plating can be caused. In contrast, if the temperature is too high, SEI growth, particle cracking, and transition metal dissolution are accelerated [48]. There is an additional trade-off to be considered when choosing the operation temperature between the capacity and the rate of degradation, as an increased temperature increases the reaction rate, which in turn increases the cell capacity, however, it also increases the degradation rate. This relationship is described by the Arrhenius law [45].

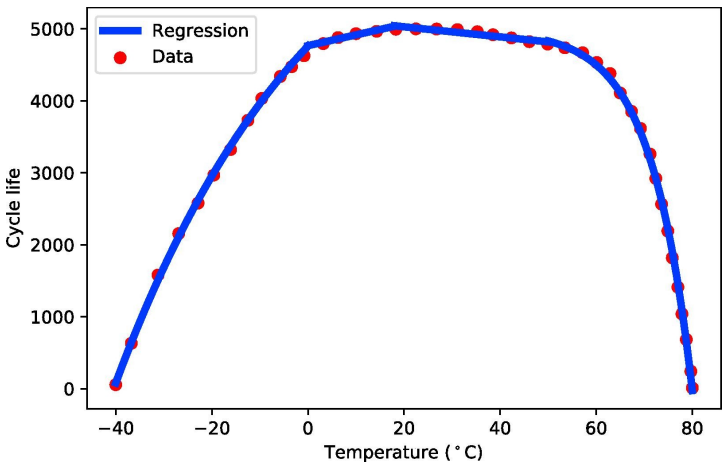


Figure 2.12: Battery cycle life as a function of temperature [50].

Mean-State-of-Charge (mSoC) and Depth-of-Discharge

It has been shown that mSOC has an effect on the cyclic age. Specifically, mSOC between 45 and

55% has been shown to give the highest cycle life, while an mSOC of 90% to 95% gives the lowest cycle life. This behavior is related to different stages of lithiation of the graphene anode [48].

Fig. 2.13 shows the cycle life of different charge / discharge ranges or DoDs [51]. It can be seen that lower DoDs correlate with longer cycle life. In general, this correlation is attributed to the volume changes due to charge/discharge cycles that cause cracks in the anode - the higher the DoD, the larger are the volume changes, the more likely cracks will be caused [45].

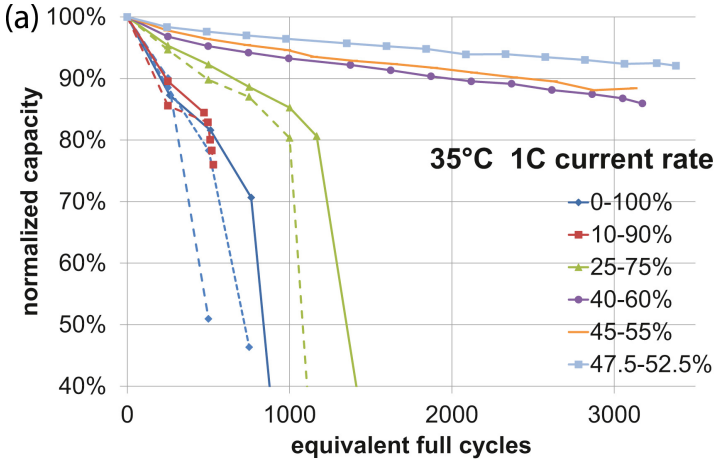


Figure 2.13: Battery cycle life as a function of DoD [51].

2.3 Switch Lifetime

This section first gives a brief introduction into the SiC and Si IGBT degradation mechanisms, after which the most common switch lifetime models have been described. The reason for reviewing both the SiC and Si IGBT switch degradation mechanisms is because in the later chapters a reference model is introduced, which makes use of the Si IGBT switch while the available switch type in the realized experimental setup is SiC.

2.3.1 Switch Degradation Mechanisms

A cross-section diagram of a SiC along with the failure modes for the chip and the package is shown in Fig. 2.14 as depicted in [52].

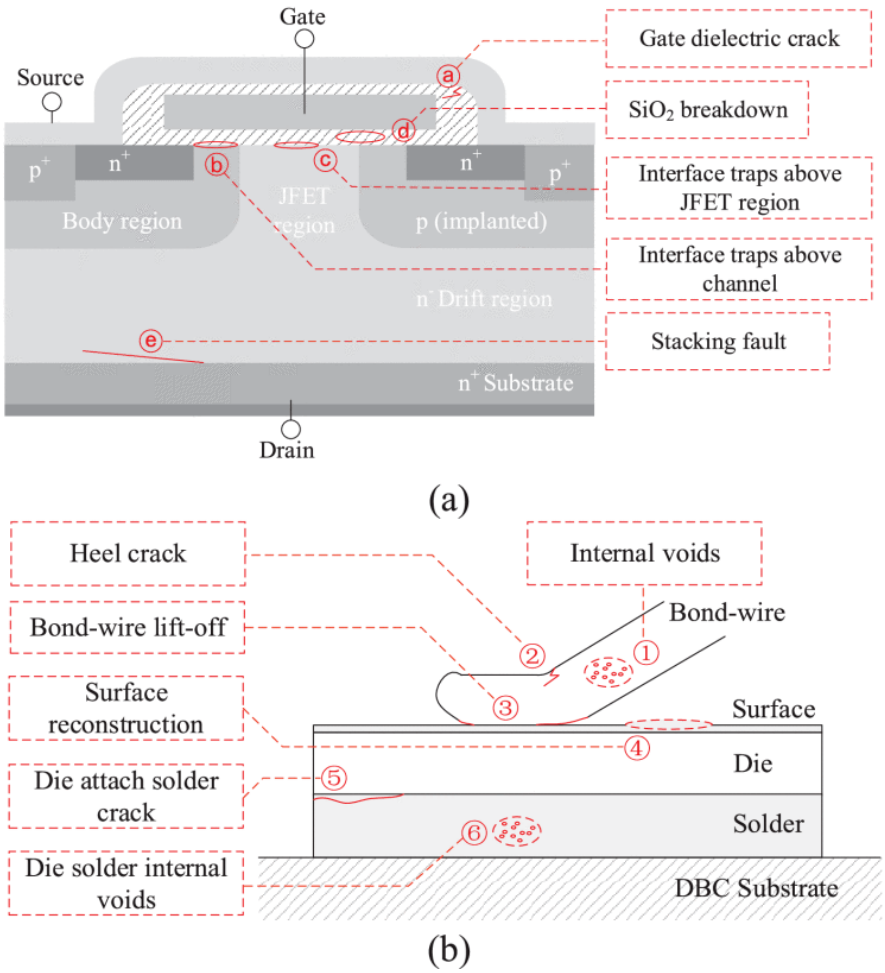


Figure 2.14: Failure modes within a SiC MOSFET (a) chip (b) package [52].

The figure depicts three major degradation mechanisms on the chip level - gate oxide reliability, stacking fault, and gate dielectric cracks. Gate oxide reliability encompases SiO_2 breakdown, interface traps above the JFET region, and interface traps above the channel. In order to keep the threshold voltage and transconductance values within reasonable ranges, it is necessary to reduce the thickness of the gate oxide layer in comparison to Si devices. Hence, the lifetime of the gate oxide for SiC devices is noticeably lower than that of Si devices [52].

The energy band offset between the SiC and SiO_2 layers inside the SiC MOSFET is lower than that for a Si device, making it easier for the electrons to tunnel between the two layers. A tunneling current is created that goes through the SiO_2 layer, breaking the bonds between Si and O_2 and eventually creating defects in the layer. Over time, a path between the gate and the source may be created that causes large gate leakage currents [52]. Another gate oxide reliability issue is the interface quality between the SiC and SiO_2 layers due to inherent challenges in the manufacturing process where the carbon atoms complicate the formation of an abrupt SiO_2 layer. Traps are created by the local concentrations of carbon atoms that are charged and discharged during the switching operation. Therefore, the threshold voltage can be shifted. These traps grow over time not only decreasing the lifetime of the device but also reducing the channel mobility [52].

The second degradation category, stacking faults, is related to the internal reverse body diode of the SiC MOSFET. Without going into the mechanisms of the stacking fault, the resulting effect is a gradual increase of the drain-source leakage current, which in turn can cause power loss increase and voltage blocking capability decrease. Finally, the gate dielectric cracking needs to be mentioned. The main reason for gate dielectric cracking is the large temperature swings that occur during extreme operational

conditions. If the coefficient of thermal expansion (CTE) differs between different points of the SiC chip, it can cause excessive stress on the dielectric material resulting in cracks [52].

Package-related degradation mechanisms also have three subcategories - bond-wire fatigue, surface reconstruction, and die solder fatigue. Bond-wire fatigue is among the most common package-related failure modes not only for SiC devices but also in other types of power electronic switches. The general reason for bond-wire fatigue is the difference in CTE in different parts of the package. The average temperature and the temperature changes are established to have a direct impact on the speed of the bond-wire degradation [52]. The result of bond-wire degradation is an increase in the $R_{\text{ds-on}}$ of the device, which can be used to estimate the level of degradation, as will be covered in later sections of this chapter.

There are two more negative effects caused by the differences in CTE. Firstly, cracking of the Aluminum surface of the source is caused. Cracking leads to a further increase in the on-resistance of the device. Secondly, cracks are caused in the die attachment solder during long-term thermochemical cycling. The effect is more prevalent in SiC devices than in Si devices because of the higher Young modulus leading to lower elasticity, making the device more susceptible to cracking [52].

The degradation mechanisms of Si IGBTs are now covered. For reference, an overview of the layout of an IGBT has been provided in Fig. 2.15.

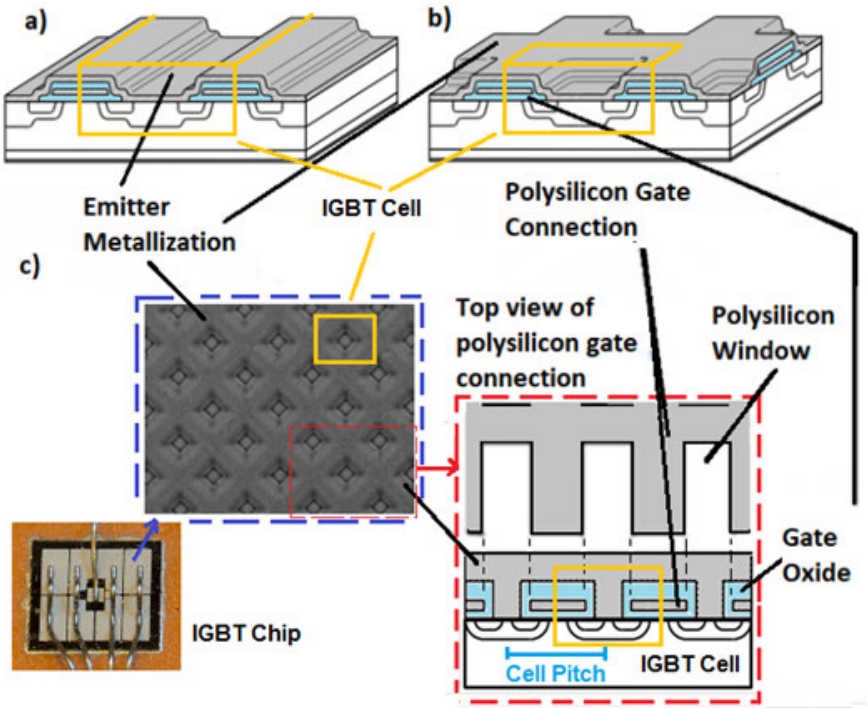


Figure 2.15: Layout of and IGBT chip [53].

Similarly as for the SiC devices chip-related and package-related failure modes can be distinguished. The two categories of chip-related failure modes as described in [53] are the overstress failure modes and wear-out fatigue modes. Overstress fatigue modes are related to extreme events such as overvoltages and overcurrents. Extreme conditions can lead to bond-wire lift-off or rupture, latch-up, loss of blocking capability, and secondary breakdown in the BJT structure. Wear-out failure modes are related to the deterioration of the gate oxide, however, this type of failure mode is not as frequent in the newest generations of IGBT devices. Another chip-related failure mode is electrochemical migration present in humid conditions under high voltage and temperature. Electrochemical migration at the chip passivation layer can lead to increased leakage currents and gradual loss of blocking capabilities [53].

Similarly as for SiC the differences in CTEs can lead to bond-wire cracking and liftoff, delamination,

and cracking of the solder layers and degradation of the chip metalization. Creation of voids due to high currents can also be caused [53].

Theory has shown that there are both similarities and differences in the degradation mechanisms between SiC MOSFETs and Si IGBTs, however, it is hard to judge the actual performance of the switch performance in the operation. Chen et al in [54] have therefore made a direct comparison of the performance of two 1.2 kV devices - SiC MOSFET and Si IGBT - under the same power cycling conditions. Physical analysis was done after the power cycling tests both on the chip level and on the package level. The results of the study show that the degradation undergone by the SiC MOSFET switches is significantly greater than that of the Si IGBTs. After 7000 cycles the electrical and thermal parameters noticeably change for the SiC switches, while it starts taking place in the IGBTs only after 38,000 cycles. Based on the physical inspection by using optical and x-ray microscopy the difference in the degradation speed is mainly attributed to the difference in the Young's modulus causing greater cracking in the solder layer. It is also concluded that chip-level degradation takes place much later than package-level degradation both for SiC MOSFETs and Si IGBTs [54].

2.3.2 Overview of the lifetime models

Lifetime prediction models of Si IGBT switches have been studied for a long time. In 1997 Held et al. in **HeldFastApplication** proposed a switch lifetime model that predicts the average number of cycles that an IGBT switch would withstand under fixed cycling conditions as:

$$N_f = A \cdot \Delta T_j^{\alpha} \exp\left(\frac{Q}{R \cdot T_m}\right), \tag{2.1}$$

where ΔT_j is the junction temperature swing of an IGBT, α is the Coffin-Manson exponent where $\alpha = 5$, Q corresponds to the bandgap energy $Q = 0.8\ eV$, R stands for the gas constant, and T_m is the case (medium) temperature [55].

This model was made as part of the LESIT project and was later adjusted to:

$$N_f = A \cdot \Delta T_j^{\alpha} \exp\left(\frac{E_g}{k_b \left(T_{\mathrm{j,min}} + \frac{\Delta T_j}{2}\right)}\right) \tag{2.2}$$

where k_b is the Boltzmann constant [56]. Both the LESIT model and the subsequent models are based on the Coffin-Manson law, which relates plastic (as opposed to elastic) deformation for the bond wire with the dependency on the junction temperature swings. LESIT project in addition makes use of the Arhenius relationship to consider the dependency on the medium temperature. Therefore, these models focus mainly on package-level degradation rather than chip-level degradation, which is consistent with the study in [54], which as mentioned in Section 2.3.1 found that package-level degradation occurs faster than chip-level degradation.

One of the most commonly used lifetime models is a more advanced version of the LESIT model. It was developed by Bayerer et al. in [57]. In their study, they showed that the switch lifetime depends on additional parameters such as heating time of the thermal cycles (t_{on}), maximum bond-wire current (I), switch voltage rating (V) and the bond-wire diameter (D). Therefore, the resulting empirical model was defined as follows:

$$N_f = K \cdot \Delta T_j^{\beta_1} \exp\left(\frac{\beta_2}{T_j}\right) t_{\mathrm{on}}^{\beta_3} I^{\beta_4} V^{\beta_5} D^{\beta_6}, \tag{2.3}$$

where $\beta_1 - \beta_6$ are empirical parameters. The model is also referred to as CIPS08 model. Later an additional factor was defined by Infineon to improve the CIPS08 model that depends on the heating time of the thermal cycles, as described in their application note. The correction factor is defined as follows [58], [59]:

$$\frac{N_f\left(t_{\mathrm{on}}\right)}{N_f(1.5)} = \begin{cases} 2.25 & t_{\mathrm{on}} \leq 0.1s \\ \left(\frac{t_{\mathrm{on}}}{1.5}\right)^{-0.3} & 0.1s \leq t_{\mathrm{on}} \leq 60s \\ 0.33 & t_{\mathrm{on}} \geq 60s \end{cases} \tag{2.4}$$

Finally, it is worth noting that another iteration of the LESIT lifetime model was done by the SEMIKRON company based on the testing the company did on their own switches. The model adds two additional terms that more accurately predict the lifetime at low junction temperature swings [60]. The model is called SKIM63 and models the lifetime of an IGBT as:

$$N_f = A_0 A_1^{\beta} \Delta T_j^{-\beta} \Delta T_j^{\alpha} \exp\left(\frac{E_g}{k_B T_{jm}}\right) \frac{C + t_{\text{on}}^{\gamma}}{C + 2^{\gamma}} k_t, \tag{2.5}$$

where β is expressed as $\beta = \exp\left(\frac{-(\Delta T_j - T_0}{\lambda}\right)$ and A_0 is the technology coefficient, A_1 is the factor of the low temperature swing extension, λ is the drop constant of the low junction temperature swing extension, α is the Coffin-Manson exponent, γ is the time exponent, and k_t is the thickness factor of the chip. All of the mentioned constants can be found in the SEMIKRON application note in [60].

Chapter 3

Literature Review

Microgrid sizing can generally be described as a process of choosing the capacity (size) of different components of the microgrid. Usually, it is done in such a way as to minimize the cost of the microgrid while simultaneously making sure that the consumers are satisfied. To make sure that consumers do not lose access to electricity while keeping the microgrid power balance, it is necessary to properly control the energy flows of the microgrid for the expected load and generation levels. The control decisions include the decisions of, for example, when to charge and discharge the battery, when to start and stop the diesel generator, and when to curtail the power generated by the solar panel array. The energy management decisions made to control the energy flows determine the operational costs of the microgrid. Hence, the cost of the microgrid can be split in two main parts - the investment cost determined by the size of the components and the operational costs determined by the energy management decisions. While investment costs are paid only at the start of the microgrid lifetime, operational costs are paid throughout its lifetime.

Therefore, a commonly used workflow of microgrid sizing optimization and the outline of this chapter is shown in Fig. 3.1.

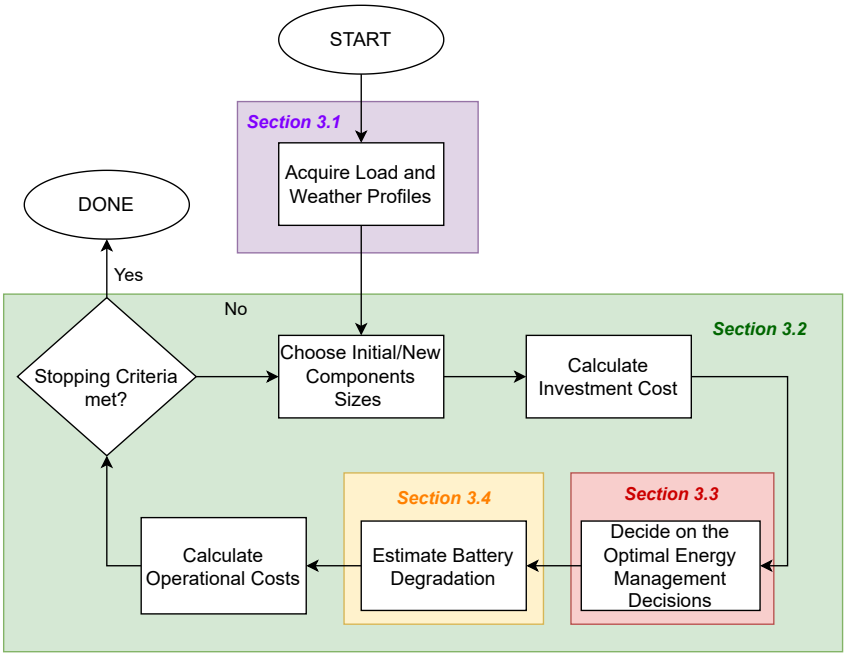


Figure 3.1: General workflow for microgrid sizing optimization and the outline of the chapter.

After acquiring the load and weather data of the specific use-case the process iterates over a loop where a certain component size is chosen and the investment costs are calculated followed by an evaluation of the microgrid operation. When a certain dispatch strategy is chosen, the degradation of the battery storage is evaluated and subsequently the operational costs are calculated. If certain stopping criteria are met, for example, the algorithm cannot find a cheaper solution anymore or a certain cost threshold is found, the optimization can be stopped. Otherwise, a new size of the components is tested, and the process is repeated.

Following the process diagram in Fig. 3.1, first, Section 3.1 shows different methods for modeling the electrical consumption. Weather curve extraction has not been introduced in this chapter, as it is not the focus of this thesis project. Section 3.2 provides an overview of the algorithmic approaches that can be used to implement the general sizing optimization. Next, an overview of EMS optimization approaches has been provided in Section 3.3 and finally, the various existing methods on how to model battery degradation have been explained in Section 3.4.

3.1 Load Modeling

In order to size the system and design the control strategies, it is necessary to know the load profile of the system. Clearly, it is impossible to know the load profile exactly unless it is already fixed beforehand, which is not the case for most use cases. The exact load profile is unknown, however, methods exist that help to estimate the load profile. The control system is then responsible for making sure that the system still works properly even if the actual load does not match the estimates.

A plethora of methods for load forecasting have been developed as the need for load forecasting arose with the introduction of electric grids. However, the vast majority of them are concerned with the load prediction of urban areas consisting of large distribution grids [61]. Furthermore, most of the methods make use of the past data to predict the future data [62], [63]. This is a solid approach as past consumption is directly related to future consumption of a specific area. In addition, data from other comparable locations can be used to make the predictions even stronger. The large availability of data, which only increases due to smart-meter systems, makes machine learning a suitable tool for performing the load predictions.

This project, however, deals with rural communities that are located far from the main grid, which usually makes it too expensive to make a grid extension leading to the use of microgrids. The communities that are connected to a microgrid usually have not had electricity connection, therefore, there is no historical consumption data. It could be argued that microgrids have been around for several decades, which allows to use historical data of other microgrids to try to estimate the consumption of a newly implemented one. The challenge with this approach is that usually communities tend to differ from each other depending on the country, geographical location, and culture, thus influencing load patterns, making it harder to use past data from other microgrids since, for example, school holidays and local holidays, as well as local work patterns, must be taken into account [61].

Nonetheless, given the relatively smaller size of the system, more rudimentary approaches can be used in sizing and control. Surveys can be done with the communities and the load profile can be estimated from the user estimations of the appliance use. However, in some cases, it has unfortunately resulted in frequent power shortages or not enough power generation [28]. The mismatches and the loss of load bring about a need for more advanced techniques in estimating the loads without access to historical data.

Mandelli et al. came to this conclusion in their paper: ”Novel procedure to formulate load profiles for off-grid rural areas” in year 2016 [64]. In order to fill this gap in tools, they developed a tool that can generate daily load profiles from the survey data. This model can be classified as a bottom-up model, meaning that microscopic data (household or appliance level) is used to approximate the load profile. In contrast, the top-down approach uses macroscopic data (distribution or transmission system level) to then split it down to a household level and then estimate the load profile [62]. The algorithm made by Mandeli et al., called LoadProGen, has the following five steps:

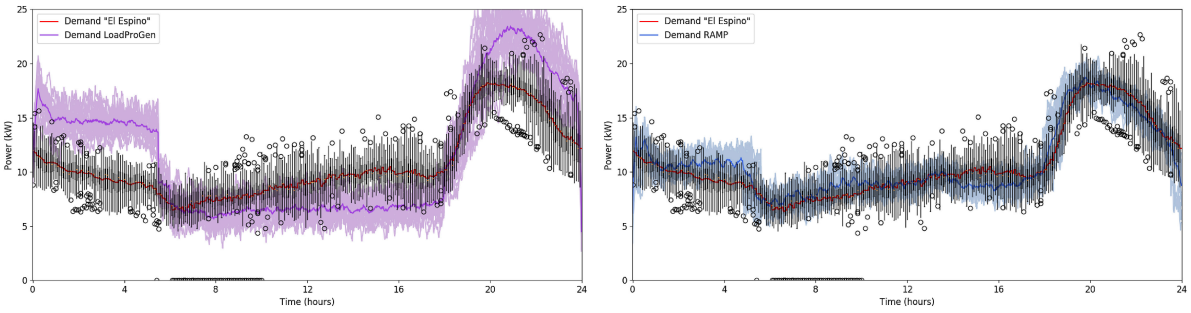
- Input data aggregation - the data from the surveys is aggregated and transformed into a common format that can then be used to generate the load profile
- Peak window estimation - the peak time window, peak power and energy within that window is calculated along additional performance indicators
- Load curve estimation - probability distributions are used to calculate the load curve by randomizing the consumption within the allowed time intervals.
- The process continues till the peak power matches the one denoted by the user
- Previous steps are repeated for each user class and the results are aggregated into a final profile.

LoadProGen has been used in other studies to generate load profiles. For example, Mandelli [65] et al. used it to size a microgrid in a village in Uganda and Zheng et al. used the model to size a biomass-integrated microgrid [30].

LoadProGen has been a good first step in generating load profiles without historical data on electricity consumption, however, there were still improvements to be made, for example, the degree of stochasticity could have been increased and it could have been extended to other energy systems besides electricity, such as heat. Lombardi et al. were aware of these gaps in the model and hence created a new model, inspired by LoadProGen, called RAMP or Remote-Areas Multi-energy systems load Profiles [61].

RAMP model was built upon the idea of LoadProGen to try to formulate the load curves for locations with no historical data on the load consumption. The general approach is comparable with the one of LoadProGen - the survey data is used to create stochastic load profiles. The survey data includes the appliance types, total usage over a day, the windows of the possible functioning time among many more parameters. The layered approach of ” user type - use - appliance ” as well as the detail of the surveys are two aspects that have been improved from LoadProGen. In addition, the stochasticity of the model has also been improved.

The comparison of the two models can be seen in Fig. 3.2 [61]. The forecasts of the LoadProGen and RAMP models are depicted in purple and blue colours while the actual consumption of the village El Espino is depicted in grey. It can be easily seen that the RAMP model performs significantly better than LoadProGen. The quantitative comparison can be seen in Table 3.1, where LF denotes the load factor representing the ratio between the average load and the peak load, CF denotes capacity factor representing the ratio between the peak load and the maximum possible load and NRMSE represents the normalized root mean square error [61]. NRMSE of the RAMP model is just under 10% while it is roughly 30% for LoadProGen.



(a) Load Profile Forecast by using LoadProGen model **(b)** Load Profile Forecast by using RAMP model

Figure 3.2: Comparison of the LoadProGen and RAMP models in predicting the electrical load as described in [61].

Table 3.1: Comparison of the load forecasts between the LoadProGen and RAMP models [61].

	Measured data	LoadProGen	RAMP	Err% LoadProGen	Err% RAMP
Peak Load [W]	18222	23466	18751	28.8 %	2.9%
LF [-]	0.585	0.491	0.578	16.1%	1.2%
CF[-]	0.114	0.147	0.117	28.9%	2.6%
Aggregate Demand [kWh]	256	269	260	5.1%	1.6%
NRMSE [%]	-	30.6%	9.6%	-	-

A different approach has been established by Llanos et al. [66]. They have used self-organizing maps to generate the load profile. The procedure of generating the load profile by the use of SOM can be seen in Fig. 3.3

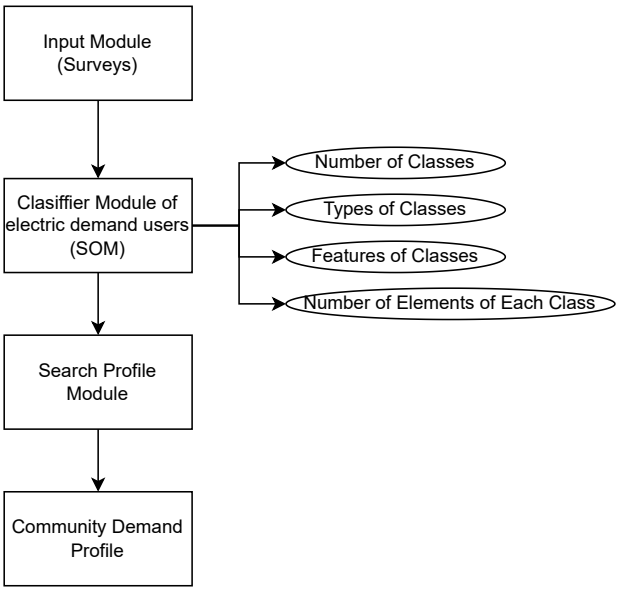


Figure 3.3: Procedure for load profile generator based on SOM [66].

It consists of three modules. The input module is responsible for acquiring the surveys by making house visits. The information that is collected contains the number of inhabitants, the type of appliances, and the time intervals when the appliances are used. The Classifier Module extracts the features that characterize each class in an unsupervised manner. The search module contains a heuristic model to find houses with similar characteristics. Since no historical data is available a different comparable community can be used to perform the classification, and later a metering system can be installed and the database can be updated [66].

Since the paper by Llanos et al. was published there have been several attempts to try to apply this method for load profile generation [67], [68]. It is hard to judge the performance of this model at the moment. The relative error levels reported in [67] lie between 7% and 34%, while for [69] the maximum absolute percentage errors lie between 10% and 35% and [68] reports the errors in absolute values and not relative values.

A similar comparison between LoadProGen, RAMP and SOMs has also been done by Takalani and Bekker [70]. However, some more bottom-up methods have been developed that should be mentioned but will not be discussed in detail. Yuan et al. in [71] developed a model that formulates load curves for rural households in China. The model has a relative error of 4% to 11% depending on the season, an

average error of 5.4%, and a peak error of 12% to 15%. Bottom-up models have also been developed by Ashetehe et al. [72] and Narayan [73], however, the papers where the models have been introduced lack validation. The former model compares the generated waveform to the ones of LoadProGen and HOMER, however, given that these softwares do not produce fully accurate load curves, it is not possible to do a proper comparison. The latter model compares only the relative error of the total generated energy (2.9%) and the load factor.

The final aspect that has to be addressed is the generation of a load curve for multiple years. The vast majority of research papers consider only one year, since it covers all seasons. However, it is not satisfactory if such load curves are desired to be used for system sizing because usually the load grows over the years. From the previously mentioned models, only one of them was specifically improved for this purpose, which has been described in [29] by Stevanato et al. In this paper, the Microgridspy-MYCE model is used for the optimization of microgrid sizing. The load generation in this method is done by a modified version of RAMP, which randomly models the load growth depending on the user input. Unfortunately, this feature has not been kept in the RAMP model in the following versions.

Some other works that delve into multi-year optimization have used easier approaches. For example, Fioriti et al. made use of several load growth scenarios with different probabilities where the load grows linearly over the years with different rates [24].

The two mentioned multi-year load forecasting models are rather simple. Riva et al. in [74] argue that the approaches simply increasing the load (number of users and/or appliances) based on uniform or normal distributions or increasing it linearly does not capture the complex socio-economical dynamics present in the rural communities. Hence, using these simple approaches in microgrid optimization could lead to improperly sized systems. Riva et al. present that the socio-economical relationship could be represented by using causal-loop diagrams [74]. An example of such a diagram is shown in Fig. 3.4. It presents the dynamics between electricity demand and income-generating activities (IGAs). In between the two are several levels that show more detailed aspects that explain the dynamics. The arrows with a ”+” or a ”-” represent whether there is a positive or a negative relationship.

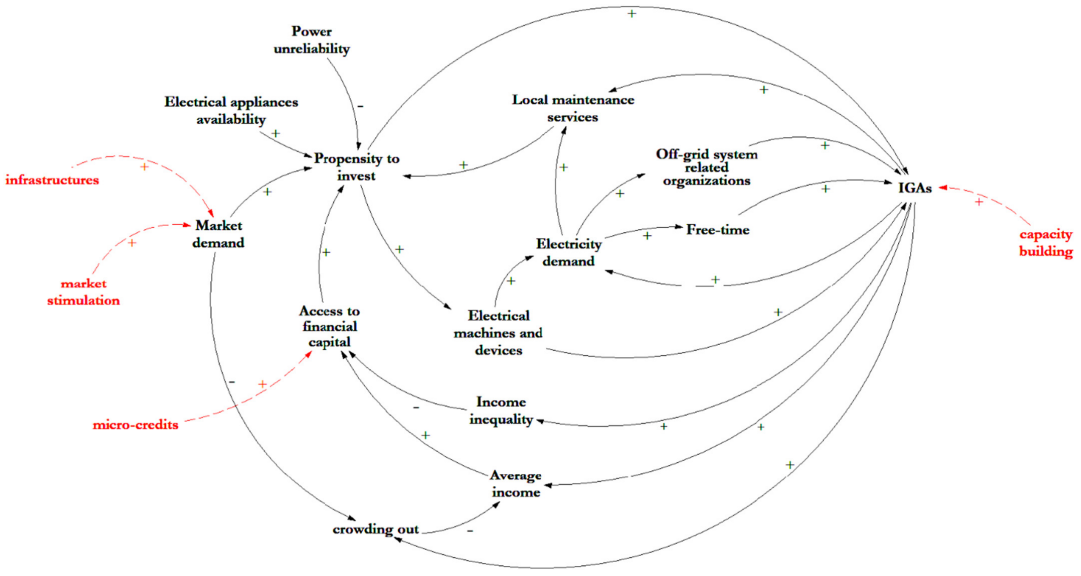


Figure 3.4: Causal-loop diagram representing the dynamics between electricity demand and IGAs [74].

Causal loop diagrams are often used in a method called system dynamics that combines control theory and system design [75]. Hartvigsson et al. were one of the first to try to apply system dynamics in multi-year load forecasting in microgrid context. System dynamics models for microgrids are usually coupled with bottom-up models for appliance modeling and an optimization tool(s) for sizing and dispatching the microgrid [75]. In fact, the LoadProGen model has been used together with system dynamics by Riva et al. to model the energy consumption of a village of Ikondo in Tanzania [76].

3.2 Microgrid Sizing Optimization

In this section, first an overview of the optimization approaches is provided, followed by a summary of common trends, and finally, the literature on the existing work on different microgrid sizing methodologies is provided.

3.2.1 Optimization Approaches

In general, microgrid sizing optimization approaches can be divided in two main groups - mathematical approaches and metaheuristics.

Mathematical Approaches

Mathematical approaches (also called classical approaches) are based on analytical optimization. Analytical optimization refers to an approach in which the solution space is defined by a set of equalities and/or inequalities referred to as constraints. Unless some constraints are let go (relaxed), the proposed solution will always abide by the defined constraints, as every solution within the solution space takes into account the constraints. Several different mathematical approaches exist with varying complexities, most popular of which are further explained in this sub-section.

Linear Programming (LP) and Mixed-Integer Linear Programming (MILP)
Linear programming is the simplest of the mathematical optimization approaches. The constraints are exclusively linear, which can often lead to a simplification of the problem. Examples of linear constraints include the maximum capacities of the microgrid components or power balance equality. Depending on the specific project, the use of LP can lead to different degrees of inaccuracy in the results. Nevertheless this approach is very efficient in terms of the necessary computational power [77]. If the optimization problem is relatively simple in its design, then LP can prove to be the best approach to be used.

A special case of LP is Mixed-Integer Linear Programming (MILP). In addition to linear constraints, binary constraints are introduced as well, for example, turning on/off a generator. While seemingly binary constraints do not change much in the problem definition, the complexity of the optimization problem is significantly increased. This is because the solution space is no longer continuous. In order to solve the MILP problem, it is necessary to build a decision tree with all the binary constraints and iteratively solve LP problems for each possible combination of binary values. While the necessary computation power is significantly higher for MILP in comparison to LP, MILP can provide a good balance between the level-of-detail in representing the reality and the computational speed.

Nonlinear Programming (NLP)
Nonlinear programming is a type of mathematical optimization where variables and constraints are nonlinear. This optimization method allows to replicate the real-world phenomena via the nonlinearities. For example, battery degradation can be expressed by using non-linear functions of time, which is much more realistic as batteries degrade relatively more at the beginning of their lifetime than during the rest of their operation time. The problem definition of NLP is similar to that for LP and MILP with the difference in the equations used to define the constraints. However, the solving process is significantly different from the solving of LP and MILP problems. NLP is very expensive in terms of computational power and the result often depends on the initial guess [77]. These types of algorithms are very complex, hard to implement, and are still an active field of research.

Robust Optimization and Stochastic Optimization
Robust and stochastic optimization deal with optimization under uncertainty. Specifically, robust optimization approaches account for the worst-case scenarios by considering a range of different possible parameter values in an uncertainty set. These approaches, however, tend to be conservative resulting in oversizing the systems so that the worst case scenarios can be facilitated even if they happen very rarely [78], [79].

Stochastic programming can be used to try to accommodate this problem by defining probability distributions for the uncertainty sets [79]. However, that in itself is a very difficult task as it encounters the complexity of trying to predict the likelihoods of weather, consumer behaviour energy markets etc..

Metaheruistic Tools

In contrast to mathematical approaches, metaheuristic approaches solve optimization numerically. These approaches start by covering as large of a part of the solution space as possible, however, very quickly the exploration is targeted towards regions of the solution space that give more promising results. Hence, if the optimal solution lies in a region which is surrounded by significantly worse solutions, there is a chance that it will be missed. This subsection introduces the most widely used metaheuristic optimization approaches, however, there exist many more.

Genetic algorithms (GA)
Genetic algorithm is a type of optimization technique that mimics the natural evolution processes found in nature. The basic idea of the GA is as follows: first all the relevant input parameters are fed in such as the environmental data, economical data, optimization constraints, and the fitness function. Based on these, a random initial population is made. It then enters a feedback loop where the fitness of the solution is first evaluated followed by reproduction, crossover, and mutation after which the next generation is selected. Reproduction and crossover stages involve creating new solutions that are based on the some of the previous ones correlating with the parents and children in the nature. The best new solutions (children) can then be selected for the next generation and reproduction. This general process represents evolution. In addition, the mutation action is added, which randomly changes some of the solutions which helps to avoid falling into local optimums. Without the mutations best children solutions would continuously be selected and reproduced, and the final solution would be directly dependent on the initialization of the algorithm [80],[81].

Particle Swarm Optimization (PSO)
PSO is a metaheuristic optimization approach that is based on the intelligence of swarms. A particle swarm is a structure of basic units that make up a group to have a common task. Each potential solution in PSO is called a particle. The coordinates of each particle are associated with the decision variables of the solution that have a position and a velocity vector. Based on the position coordinates of the particles, the fitness function is evaluated. The results of the fitness function for each particle are used to calculate the velocity vectors of each particle, which then determine the next position of each particle in the swarm. The process is continued until the swarm finds an optimum or a certain amount of iterations has been reached set by the user. Similarly as for genetic algorithms, PSO adds randomness to the movement of particles to facilitate a better exploration of the solution space and avoid falling into local optima, however, it is impossible to completely avoid it [80], [82].

Simulated Annealing (SA)
SA is a Monte Carlo-based optimization approach. The name comes from similarities with the iron annealing process [83]. The idea of SA is that each candidate solution is compared with the current best solution. If it is better, it is accepted and if it is worse, it can be accepted with a certain probability, which is determined by some criteria that can be chosen by the user. The annealing procedure allows for wide area searches with a faster temperature decrease at the beginning of the iterative process, then local area searches around the best solutions in the wide area search steps with a slower temperature decrease [81]. The temperature is related to the probability of accepting a suboptimal solution. As time goes on, the temperature decreases and suboptimal solutions are accepted less and less often. High temperatures at the beginning allow for better exploration, while lower temperatures at the end allow for convergence.

Ant colony (AC)
The optimization technique is inspired by the observation of an ant colony, as the name suggests. The algorithm makes use of ”a smell of the path” which vanishes with time, representing the pheromones

that ants leave behind them. If the path is no longer used, the chance that it is used by another ant decreases [81]. In the context of optimization, the food that the ants are looking for represents the constraints of the optimization problem (the final destination is fixed). The paths that the ants take to the food represent the potential solutions, and the shortest or quickest path would represent the optimal solution. Exploration of the solution space is encouraged by the vanishing smell of the path - ants start to explore different paths corresponding to different solutions. At the same time, convergence (exploitation) is facilitated by the increased likelihood of using a path that is already being used.

Grey-wolf optimization (GWO)
Similarly as GA and PSO and AC the inspiration for Grey-wolf optimization comes from nature, particularly, from wolf packs. The algorithm makes use of the hierarchy of wolf packs where four levels are distinguished - alpha, beta, delta, and gamma where alpha is the dominant wolf and gamma has the least say [84]. The levels of the wolf pack represent the fitness levels of a particular solution in the context of optimization. Alpha level represents the fittest solution while beta and gamma are the second and third fittest solutions. The rest of the solutions are depicted as omega or the lowest level. Hunting and encircling the prey by the pack represents exploration, while attacking the prey represents exploitation. The positions of the alpha, beta, and delta wolves represent the decision variables of the three best solutions. The positions change as the prey (best value of the fitness function) is hunted, encircled, and finally attacked [84].

Comparison of different metaheuristic approaches
While for mathematical approaches there is usually a clear trade-off between the complexity, accuracy and the computational time, a comparison between different metaheuristic approaches is more difficult to make. The difficulty of comparison comes from the fact that the general underlying working principles of different metaheuristic approaches is the same. They start with an initialization phase where the aim is to cover the solution space as well as possible. After the fitness function is evaluated for the initial possible solutions, a process consisting of exploration and exploitation begins. Usually exploration is dominant at the beginning, while exploitation gradually becomes more dominant over the iterations. The differences between different metaheuristic approaches come from the differences in updating the decision variables while performing the search for the global optimum, implementation of randomness in the search, and how the exploration and exploitation processes are implemented.

In principle, the details of the exploration and exploitation processes determine which of the metaheuristic approaches is more suitable for which optimization problem. However, given the wide variety of different approaches in the current state of research, it is not possible to test all of them for each problem. Moreover, it is not obvious before testing whether one approach is more suitable than the other without being an expert in all of them (or at least having used the approaches). Hence, some approaches that are the most general and allow for easy modifications of the problem setup have experienced higher popularity than some of the others even if they might not be the most appropriate for a specific problem.

An overview of the microgrid sizing optimization approaches has been provided in Fig. 3.5.

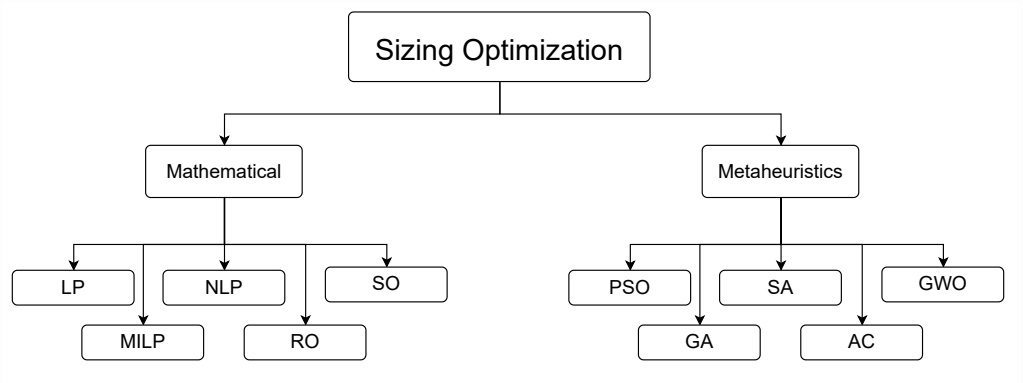


Figure 3.5: Summary of the microgrid sizing optimization approaches.

Optimization Software

Even though a great variety of optimization approaches exist, it can be time-consuming to implement one from scratch. There is a wide variety of ready-to-use software tools with a user interface that perform microgrid optimization. This subsection describes some of the more popular tools and some that are the best fitted for the rural microgrid sizing optimization.

HOMER Pro
HOMER Pro is one of the most well-known commercial microgrid optimization software tools. Despite its popularity, however, the modeling of the system and the optimization procedure is simpler than many alternative software tools. The core optimization algorithm is based on grid-search meaning that the algorithm checks for all possible configurations in a brute-force manner [85]. For problems with a large solution space, it becomes infeasible to rigorously check all the options quite quickly. Therefore, the provided solution can be far from the global optimum. HOMER Pro developers claim to have designed a new optimization algorithm as an alternative, however, it is not disclosed how exactly the algorithm works and on what optimization approach it is based upon.

The energy dispatch is implemented based on popular rule-based strategies, namely, load-following or cycle charging, which are further explained in Section 3.3. Furthermore, the software uses an energy-throughput battery degradation model. Finally, the software is not flexible in the inputs that the user can provide, such as component technology and degradation models. It is also not possible to model load changes over years. However, it should be mentioned that HOMER Pro allows the modeling of hydrogen fuel cells and electrolysers as well as compressed air storage, which is not possible with many other optimization software tools [85].

As has been mentioned previously, HOMER has been very popular in the academic community. Upon the search query of ”microgrid AND optimization AND HOMER” Scopus database provides 445 articles that have been published with the number of articles published each year rising. From the list of the provided articles 75 were published both in 2023 and 2024.

DER-CAM
DER-CAM is a decision support tool developed by the Lawrence Berkeley National Laboratory allowing to find the optimal distributed energy resource portfolio, placement, and dispatch. DER-CAM is free to use and the source code is available for free for academic use [86].

DER-CAM makes use of the MILP optimization approach. The features include empirical battery degradation model which considers calendar and cyclic degradation, use of MILP to solve the dispatch problem, and possibility to perform multi-objective optimization to minimize the emissions and costs simultaneously. DER-CAM also provides flexibility in defining load profiles and solar generation profiles [86].

DER-CAM software has been extensively used in academic research for different purposes, including microgrid optimization, performing economic analysis of distribution grid systems, or optimization of distribution heating and cooling networks. To mention two examples, Jaesung Jung and Michael Villaran in [87] use DER-CAM software to determine the optmal capacity and location for distributed energy resources, as well as the dispatch of an electric grid of the Brookhave National Laboratory. The study analyses the influence of geographical location on electrical performance and the economic effects on the selected microgrid. Another study by Kang et al. in [88] uses DER-CAM to optimize a microgrid on Lombok Island in Indonesia with the focus on resiliency. The software allows to consider N-1 contingency planning while performing the optimization.

MycroGridsPy
MicroGridsPy is an open-source microgrid sizing and dispatch optimization model developed in Python and based on the *Pyomo* library. It is a two-stage stochastic model where the first stage addresses the sizing problem, while the second stage addresses the dispatch. Both stages are executed by using the MILP optimization approach. The model was originally developed by Sergio Balderrama and Sylvain Quoilin at the University of Liege in 2016, however, many updates have been made since then and the model is currently being maintained and developed by the SESAM group in the Politecnico di Milano [89].

The model stands out with its focus on the microgrids sizing in specifically remote locations, and hence the optimization of off-grid microgrids. It is also one of the rare models that takes into account load growth over the years and allows for the grid component capacity expansion instead of optimizing for the conditions at the end of microgrid lifetime. It is also admirable that the model performs stochastic optimization instead of a deterministic one as often done in the literature. Furthermore, the model also allows for multi-objective optimization by taking into account, for example, the emissions and not only the cost [89].

One of the drawbacks that must be mentioned is that the model also uses an energy-throughput battery degradation model. Moreover, given that the model is solving a nested MILP optimization problem, it requires an external solver. While there are some open-source solvers, they can be significantly slower than the commercially available ones. [89]

MicroGridsPy has been used in academic research to explore different aspects of rural microgrid sizing optimization problems. For example, Balderrama et al. in [32] compared the results of the sizing problem between deterministic optimization and stochastic optimization for the village of El Espino in Bolivia. Furthermore, Stevanato et al. in [89] used MicrogridsPy to address the planning of third-generation microgrids in Rwanda by performing multiobjective optimization between NPC and CO2 emissions. Finally, MicroGridsPy was used by Stevanato et al. in [29] to compare the optimization results with and without expansion of microgrid capacity during its lifetime.

iHOGA
iHOGA is a hybrid renewable system optimization software developed by Rodolfo Dufo López. It is based on two nested genetic algorithms of which the first stage addresses component sizing, while the second stage addresses the dispatch similarly to the MicroGridsPy [90]. However, the second stage is a hybrid of genetic algorithm and the load-following strategy, hence the dispatch is not guaranteed to be at the global optimum [90].

The software has two versions - a free version and a commercial software. The main differences include differences in the dispatch optimization, more advanced features in battery modeling, and possibility to optimize for the system lifetime instead of just one year. However, the concidered load growth over the years is linear. Neither of the versions is open source and therefore does not allow for modifications of the code [90].

Similarly as the other mentioned softwares, iHOGA has been extensively used in academic research. An example includes an article by Hoarcă et al. in [91] where a comparison is made between the optimization results of iHOGA and HOMER for a sizing of an off-grid hybrid renewable system in Romania. Another example is an article by Heman Shamachurn in [92] in which a sizing optimization of an off-grid

hybrid energy system is performed for a case study in suburban Paris.

Other Optimization Software Tools
This subsection has described four popular software tools for rural microgrid sizing optimization, however, it is a very small sample of the readily available tools. Dorian Höffner and Sebastian Glombik have performed a comprehensive meta-review of the academic literature by analysing software tools for microgrid optimization [93]. They ended up distinguishing over 500 optimization software tools. Although the study focused on optimization software meant for urban energy settings, a good portion can also be used for rural microgrid sizing optimization. Some examples include software tools such as Offgridders, INSEL, RETScreen, and many more [93],[94].

3.2.2 Common Trends and Trade-offs

A study done by Akbas et al. in [95] reviewed more than a hundred articles that focus on microgrid sizing optimization. It should be noted that articles using optimization software were not included in the review. Fig. 3.6 shows the distribution of the optimization approaches utilized in these studies. It can be seen that the split between the mathematical and metaheuristic approaches is roughly equal and comprises around 85% of the total. The remainder is covered by a type of approaches called heuristics. The paper refers to heuristics as approaches that are tailored to the specific use-case and meant to quickly solve large-scale non-differentiable problems by providing ”acceptable” solutions. Since heuristics are not generalizable and provide only an approximate optimum they are not further discussed in this chapter.

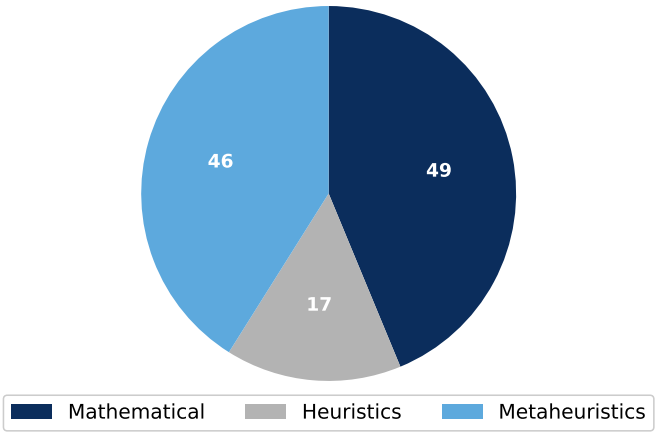


Figure 3.6: Distribution of the optimization approaches proposed in the review articles by Akbas et al. in [95].

Another study by Mohseni and Brent in [96] analysed more than 500 scientific articles covering microgrid energy planning optimization. Among this set, almost two thirds used mathematical optimization algorithms, while the rest used metaheuristic algorithms. The most popular optimization algorithms included linear programming, mixed-integer linear programming as well as genetic algorithms, and particle swarm optimization. This provides a similar trend with the review of Akbas et al.

In addition to the reviews by Akbas et al. and Mohseni et al., there have been other reviews that also acknowledge the fact that neither mathematical nor metaheuristic algorithms provide universally better performance in microgrid sizing optimization [81], [97]. Sometimes the suitability of the algorithm is use-case dependent, while other times both types of algorithms are able to find a similar optimum solution.

Nevertheless, there are some inherent advantages and disadvantages to mathematical and metaheuris-

tic algorithms that are not possible to avoid. Mathematical and metaheuristic algorithms can be compared on 3 main criteria:

- Convergence to a global optimum
- Computation time
- Performance on non-linear problems

Convergence to a global optimum
For the discussion of convergence, MILP has been taken as an example from the spectrum of mathematical approaches, since it is among the most used mathematical approaches for microgrid sizing optimization. Similar conclusions can be reached with other types of mathematical approaches, however, the solving methods of other mathematical algorithms differ.

The general approach of MILP solvers is to first solve the problem while relaxing the binary constraints into linear constraints. The solution to this relaxed problem is the lower bound of the possible solution (in case the cost is being minimized). This means that the solutions to the actual problem will at best reach the lower bound. After solving the relaxed problem, a decision tree is created with all the possible binary constraints. If there is enough time and the problem is small enough, it is possible to run a new optimization for each leaf of the tree, thus covering the entire solution space. However, if it is not possible to test all the leaves, it is still possible to compare the best found solution with the solution of the relaxed problem. If there is a difference between the two in the fitness function (for example cost), it is called the optimality gap. The approach described here is called branch-and-bound [98]. Since usually MILP problems are set up in such a way that they are convex, it is known that the solution of the relaxed problem is the bound of a global optimum.

In contrast, in the case of the metaheuristic algorithms, it is usually not possible to know how far from the global optimum the found solution is and whether the solution that has been found has not fallen into a local optimum. This is because these algorithms do not have a point of reference. These algorithms usually compare the quality of a particular solution with respect to the other solutions tested [81].

Computation Time
In terms of computation time, mathematical approaches take significantly longer to solve, which is related to the previously explained example of convergence. Mathematical methods are based on analytical equations and the entire solution space is methodically investigated, which makes the computation times very large. For that reason, it is often not possible to solve the optimization problem with conventional coding. Dedicated solvers have been developed to assist with solving the optimization problems, the most popular of which are only commercially available such as Gurobi, CMPLX or GAMS.

Metaheuristic algorithms, however, cover only the most promising parts of the solution space. If a specific region of a solution space is not promising, that region is usually excluded from further investigation. In case of sensitive fitness functions, this can lead to an exclusion of a global optimum solution. Nevertheless, smart selection of the solution space is what allows metaheuristic algorithms to keep the computation times generally lower than for mathematical methods.

Even when the state-of-the-art optimization solvers are used, the optimization time is significantly larger when using MILP in contrast to metaheuristics. Comparison between computation times between the two has been done in several studies, for example, in the study by Fioriti et al. [99] it was shown that metaheuristics performed the optimization almost twice as fast as the MILP optimization for the same optimization problem.

Performance with non-linear problems
Previously, the example of MILP was used which deals only with linear constraints in combination with binary constraints. On the other hand, the approach becomes significantly more complex when nonlinear problems are considered. In some cases, it is possible to translate the non-linear constraints into a

set of linear constraints [95]. The process of linearization, however, can misrepresent the actual problem as a simplification is done. Mathematical methods for non-linear problems have been developed as well, for example, non-linear programming, however, it even further increases the computation time and they are significantly harder to implement [95].

In contrast, metaheuristics deal well with non-linear problems. Since they are not bound to the underlying physical concepts of the problem, the solving process does not change. However, depending on the type of problem, the chance of falling into a local optimum can vary drastically. For different problem set-ups the tuning of the hyperparameters can also become more difficult [97].

3.2.3 Current Research

So far in this section, different sizing optimization approaches that can theoretically be used have been covered. This subsection offers an overview of a selection of papers in order to observe the spectrum of the features included in different research articles.

Table 3.2 provides a comparison of which *features* have or have not been implemented in a non-exhaustive sample of articles. Due to the scope of the thesis, it is not possible to analyse an exhaustive list since it would include hundreds of articles. However, this list has been assembled to give a feeling of the differences rather than to give a comprehensive overview of all the existing literature on sizing methodologies. Additionally, optimization approaches that have been used both for the sizing and specifically for the EMS have been listed.

The four features that have been reviewed include:

- PV Generation Uncertainty - the feature indicates whether the author of the research has used a deterministic weather profile or taken into consideration the uncertainty of the weather profile.
- Load Uncertainty - the feature indicates whether the author has used a historical load curve or taken into account the uncertainty of the electrical load consumption. The feature has also been indicated with an ”x” if the author accounted for the uncertainty by generating a synthetic load curve that is based on probabilistic distributions of the consumer behavior.
- Load growth - the feature indicates whether the author has considered the electrical load changes over long time spans, for example, over several years.
- Battery Degradation - the feature indicates whether the author has considered battery degradation over time in any type of manner.

Additionally, two more aspects were checked for, but not found to be described or modeled in an extensive manner:

- Distribution line losses and capacity limits - in the vast majority of the microgrid sizing optimization research it is assumed that any decision of the EMS can be executed. However, in some cases, it might not be the case as in the reality distribution lines have capacity limits. If a certain distribution line has reached its maximum limit, the dispatch decision might need to be adjusted. This in turn would potentially lead to higher operation costs and possibly a different sizing solution.

  As an exception, two articles were found that have indeed considered the impact of distribution line limits on the sizing, namely, Mashayekh et al. in [100] and Rousis et al. in [101] in which they used MILP and genetic algorithms, respectively, to solve the optimization problems. However, the inclusion of optimal power flow, which was the main focus of their research, and load and weather uncertainties as well as battery degradation were not considered.
- Inverter degradation - as shown by Alpízar-Castillo et al. in [102] solar power curtailment decisions have a significant impact on the inverter lifetime. To the extent of the knowledge of the author of this thesis project, this influence on the inverter lifetime has not been considered in the microgrid sizing optimization problems.

A note has to be made, however, that the features are still quite general. For example, there are many different load uncertainty models that can be implemented, where some are much more detailed than others. Hence, even though a certain row might be fully filled with ”x” indicating that all the features have been covered, it can potentially mean that the model is less detailed or it has lower time resolution.

The abbreviations in the columns of ”Sizing Optimization Approach” and ”EMS Optimization Approach” correspond to the approaches introduced in the previous subsections. The only exception is ”RB”, which indicated a ”Rule-Based” EMS approach. Detailed explanation has been provided in Section 3.3. Briefly, rule-based dispatch approaches include a subset of dispatch approaches that rely on ”if-else” statements that are very computationally cheap to execute, but rely on the experience of the designer and in most cases are not the optimal manner in dispatching the resources. Additionally, ”DP” corresponds to Dynamic Programming and ”FL” corresponds to fuzzy logic, which are optimization approaches used more often specifically for EMS optimization and are also introduced in Section 3.3.

Table 3.2: Research progress overview for the microgrid sizing optimization with the ”x” indicating whether a certain feature has been implemented in the optimization algorithm.

Paper	PV Generation Uncertainty	Load Uncertainty	Load Growth	Battery Degradation	Sizing Optimization Approach	EMS Optimization Approach
[103]					GA	GA
[104]		x		x	PSO	MILP
[99]					PSO/MILP	RB/MILP
[105]					MILP	MILP
[106]					GA	MILP
[107]					MILP	MILP
[108]					MILP	MILP
[109]		x			MILP	MILP
[110]	x	x			MILP	FL
[111]	x	x	x		MILP	MILP
[112]	x	x		x	MILP	MILP
[113]		x	x	x	MILP	MILP
[114]	x	x			PSO	RB/MILP
[29]		x	x	x	MILP	MILP
[100]					MILP	MILP
[115]				x	GS	DP
[35]				x	GS	MILP
[116]	x	x			PSO	RB
[117]					GA	GA
[118]	x	x			GA	MILP
[119]					MILP	MILP
[26]	x	x			PSO	RB
[120]					PSO	RB
[24]	x	x	x	x	PSO	RB
[121]	x				GA	GA
[122]		x		x	GA	RB
[123]	x	x			MFO	RB
[124]		x			PSO	RB

There is a spectrum in the number of features that have been included in sizing optimization problems. Some of the papers are, however, worth analysing in more detail. Firstly, the work by Fioriti et al. in [24] has managed to cover all the features that were compared. The system has been simulated with an hourly resolution. The solar generation profile has been generated using the Graham model, which includes a two-step ARMA methodology that captures the random deviation of the solar irradiance and the temperature. A multi-year growth has been implemented. The load demand is modeled with a constant increase over the years supplemented with Gaussian noise with 20% standard deviation. Historical data from a microgrid in Kenya is used as the basis [24]. A serious downside to the work is the use of rule-based dispatch strategy, which can lead to suboptimal dispatch decisions and hence influence the sizing results. Furthermore, the battery degradation model is among the more simplified ones, which does not necessarily reflect the real-life behavuor of the battery.

The optimization model by Stevanato et al. presented in [29] is also worth distinguishing. It has been one of the inspirations for the focus of this thesis project. The motivation for the work was to try to tackle the assumptions that the academic literature had often relied upon. In particular, they combined the RAMP load prediction model and proposed an extension to the then existing MicroGridsPy software, which allowed to model load evolution over several years and allowed for microgrid component capacity extension which was not possible before in the model [29]. Although the optimization model still assumes a deterministic weather profile and a simple battery model, it is one of the rare (if not the only) papers that has addressed the possibility of component capacity expansion in the context of rural microgrid sizing optimization. A detailed analysis of the effects of these considerations was performed and a comparison with a model without capacity expansion was made.

The article by Atia et al. in [112] proposes a nested MILP model that optimizes the size and operation of a grid-tied microgrid in Okinawa, Japan. Stochastic weather patterns are used to create weather data for three years. For example, the Weibull distribution is used to construct the wind speed data. The load data is divided into controllable and uncontrollable data. A demand-side management strategy is implemented for the controllable load. The uncontrollable load data is generated based on historical data and Gaussian distribution to stochasticity [112]. A simple linear battery degradation model is used. The model considers long-term load and weather changes however it is limited to 3 years, which limits the analysis when it comes to the microgrid lifetime .

Finally, Dakir et al. in [35] have made a comparison between the cases of having a nested optimization versus having a MILP-based sizing optimization in combination with a rule-based EMS strategy. The comparison between mathematical and metaheuristic approaches is not done often in academic literature when performing rural microgrid optimization. It was concluded that there is a great influence on the final result between the two cases for a grid-tied microgrid. A less significant difference was observed in the isolated microgrid case, as there were no market interactions with the main grid [35]. Nevertheless, the research could be expanded as the microgrid model in the research done by Dakir et al. makes use of a simplistic battery degradation model and does not consider weather and load uncertainties.

Therefore, it can be identified that there is still a scientific gap in the topic of rural microgrid sizing optimization. There is no research paper that has managed to implement an optimization algorithm for rural microgrid optimization while taking into account all the mentioned features and implementing an optimization-based power dispatch. Furthermore, degradation of power converters was not found to be included in microgrid sizing optimization in the covered literature.

3.3 EMS Optimization

The aim of this section is to introduce some additional optimization approaches that are more specifically used in the optimization of the microgrid energy management systems. Similarly as for microgrid sizing, both mathematical and metaheuristic approaches are used. Two additional approaches have been introduced in the category of mathematical approaches. In contrast, given the generalizable nature of metaheuristic approaches, all of the mentioned approaches in Section 3.2 can also be used to optimize energy dispatch. Section 3.3.2 provides an overview and reflection on the most popular EMS optimization approaches.

3.3.1 Additional Optimization Approaches

This subsection introduces *additional* optimization approaches that are often used for the optimization of EMS specifically. Nonetheless, most of the optimization approaches introduced in Section 3.2 are also used for the optimization of EMS.

Rule-Based Approaches

The rule-based method is the simplest type of energy management system. It is represented by a list of ”if-else” statements which determine the charging/discharging of the battery, controlling the generator,

or curtailing the renewable generation. For example, an energy system could check whether there is more generation or consumption and in the case there is more generation, it could charge the battery and discharge the battery when there is too much load. Additional rules are usually introduced to keep to the component capacity limits and the SOC limits of the battery.

The two most popular rule-based energy dispatch approaches are the load-following and cycle-charging approaches. The load-following approach prioritizes the use of renewable energy. For a given load, it would first dispatch all the solar (or wind) energy followed by the battery storage and only if needed turn on the diesel generator. In case there is too much renewable power, the battery is charged [99]. The cycle charging approach has a similar idea with the exception that the generator is also turned on whenever the battery SOC drops below a certain threshold [99].

Mathematical Approaches

Dynamic Programming (DP)
DP relies on splitting the main problem into series of sub-problems which can be optimized by using the most suitable method [77]. For example, Mishra et al. in [125] have performed cost optimization of an electric storage system within electrical grids by the use of DP. The algorithm splits the optimization horizon into series of intervals and makes use of the solutions of the previous horizons to optimize the dispatch of the current interval rather than starting the search for a solution from scratch. Another example of dynamic programming has been shown in [115]. In the paper DP was used to optimize the energy dispatch by first solving the dispatch of each year individually and calculating the ”transition costs” after which the transition states (intermediate years) are connected. Dynamic programming increases the efficiency of the solver, but it requires a high level of expertise to decide on the most suitable optimization approach for each sub-problem, and the general implementation in itself is significantly more complex than for many other optimization approaches.

Model Predictive Control (MPC)
MPC is a type of control approach that compares the actual output of a system process (microgrid) and the outputs of a modeled process of that system. The difference of both is sent to a prediction block, which predicts the output of the next step. Those are then used to choose a suitable control action. One of the greatest challenges of MPC is the high computational time, which means that powerful hardware is required to keep it within reasonable margins. Nevertheless, MPC is a promising method that can provide solutions to problems in stability, power quality, and energy management [126].

Metaheuristic Approaches

The most commonly used metaheuristic methods match with the ones used for microgrid sizing, namely, genetic algorithms (or more generally evolutionary algorithms) as well as particle swarm optimization. For further details on metaheuristic approaches Section 3.2 can be checked.

Other Approaches

Fuzzy Logic Approaches
Fuzzy logic approaches allow for a more natural implementation of constraints. Instead of assigning hard constraints for the battery SOC limits, for example, between 20% and 80% it is possible to assign a *preference* for the SOC to lie in that range. However, it is possible that the SOC leaves the range if it is possible to acquire a significant improvement in the objective function. It is still possible to define a hard limit, for example, that the battery SOC should not exceed 100% and should not go below 0% since it is not physically possible. The advantage of fuzzy logic is that it allows for soft constraints instead of only hard constraints [127]. However, implementation of Fuzzy Logic can become quite complex for large optimization problems.

Game Theory -based Approaches (GT)
Game theory can be defined as ”the branch of applied mathematics which is dedicated to study and analyze the interactions between rational independent decision makers called players [128]” The two main types of game theory games are cooperative and non-cooperative games. The former describes

games where the players have the ability to coordinate with other players with the goal of symbiotically increasing everyone's profits. The latter types of game include players who are not interested in cooperation, but instead operate independently from each other [128].

Game-theory approaches are particularly useful when the demand response is in place. The EMS in such a case plays a mixed-strategy noncooperative game till it reaches the Nash equilibrium. It has been shown that GT can be used to minimize the cost and emissions of the microgrid by applying a smart control strategy [129].

Multi-agent Systems (MAS)
Multi-agent systems is an alternative for the commonly used SCADA system for the control of large electrical power systems. MAS is well suited for the management of DERs, as it can better deal with the uncertainty that comes from the intermittency of renewable energy resources [130]. As the name suggests, MAS consists of several agents each taking care of their sub-system within the overall system. There is a communication network between the agents, and they work together to achieve the goals of the general system. At the same time, they have complete autonomy over their actions [130].

An overview of the EMS optimization approaches is provided in Fig. 3.7

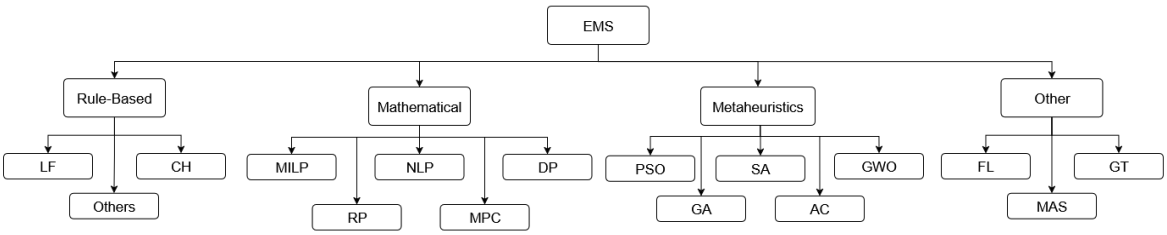


Figure 3.7: Overview of the EMS optimization approaches.

3.3.2 Common Trends and Trade-offs

A study by Thirunavukkarasu et al. has reviewed and grouped more than 500 research articles. Fig. 3.8 shows the distribution of the articles along different optimization techniques.

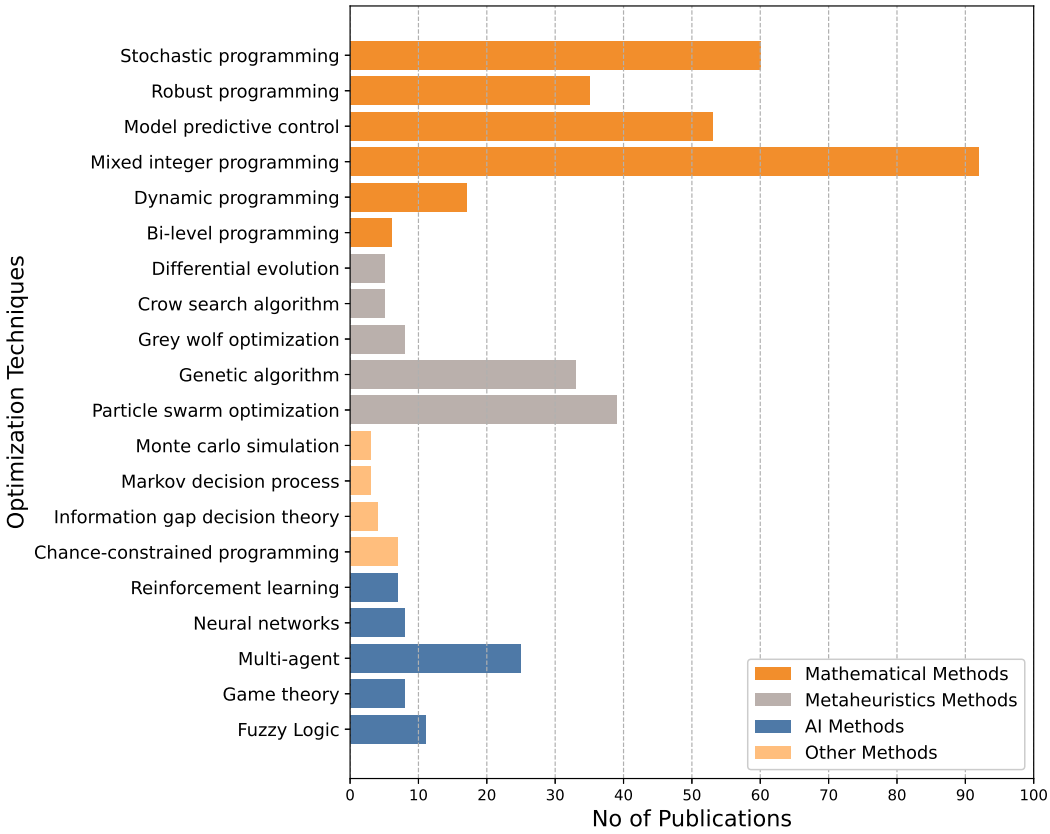


Figure 3.8: Analysis of different optimization techniques based on the number of publications during 2010–2020 [129].

More than 50% of the articles have used mathematical approaches for the optimization of EMS, with MILP and stochastic programming being the most widely used. Genetic algorithms and particle swarm optimization also stand out as being more often used than most of the other approaches. Finally, the multi-agent systems approach has also been used more often than the other AI-based techniques. However, MAS is used mostly for the EMS of systems that make use of decentralized control strategies [129].

It can be seen that MILP and Stochastic Programming approaches dominate the optimization of the energy dispatch. However, similarly as for the microgrid sizing optimization, there is still a wide variety of approaches being used. It could be explained by a similar reasoning as in Section 3.2.2 since the same trade-offs of convergence, computation time, and ability to solve non-linear problems exist when optimizing the dispatch of the microgrid.

The study by Thirunavukkarasu et al. also provided an analysis of the trade-offs of three popular optimization approaches shown in Fig. 3.9.

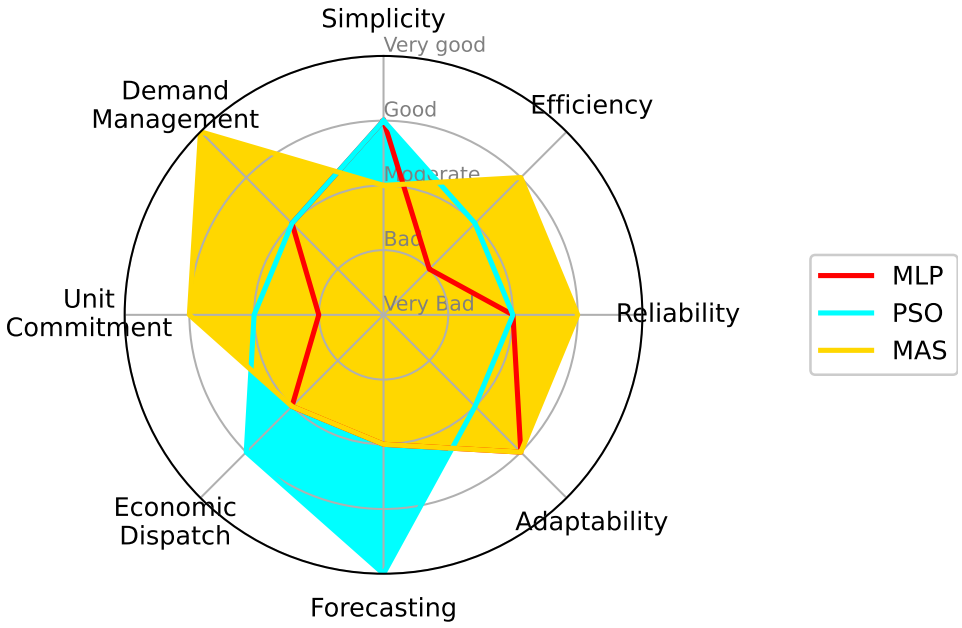


Figure 3.9: Pictorial representation of the analysis of three commonly used optimization techniques [129].

Besides comparing the simplicity, efficiency, reliability and adaptability, a comparison is given on the performance on the previously mentioned aspects. It can be seen that while MILP is a relatively simple and adaptable method, it is not very efficient and performs badly with unit commitment problems and optimization, including demand-side management. PSO is almost as good or better than MILP in almost all aspects except for adaptability. While PSO is better than MILP with unit commitment and economic dispatch problems it performs similarly in problems containing demand-side management. PSO also performs great with problems that include forecasting. MAS has significantly different performance in optimization problems. It outperforms both PSO and MILP in efficiency and reliability as well as greatly deals with demand-side management problems, however, it is significantly more complex and same as MILP does not deal well with economic dispatch or problems including forecasting of future load or generation.

Together, the analysis in Section 3.2.2 and the analysis by Thirunavukkarasu et al. provide an explanation of why there is no consensus on which optimization approaches are the best to use. It is still the case that the objectively best approach will depend from case to case if it is even to find an objectively best approach. Whenever choosing a specific approach over another, a trade-off is made and it will depend on the user what performance aspect is easier to sacrifice.

3.4 Battery Degradation Modelling

In this section, different approaches for modeling battery degradation in microgrid optimization problems will be shown. Various methods are used in research for battery degradation modeling for long-term microgrid sizing and energy management system design. The methods differ by the level of detail that is taken into account. The level of detail modeled has a direct effect on the computational time and accuracy. The higher the level of detail, the higher the accuracy, while the computation time also increases. However, often there is a threshold after which the gain in accuracy does not outweigh the increase in computational time.

In general, battery degradation models can be divided into four broad categories, as depicted in Fig. 3.10: linear models, models that account for partial charge/discharge cycles, semi-empirical and empirical models, and finally, physics-based models. This section does not provide an explanation of phisycs-based models, as they are very complex and require extensive information about the chemical

and physical interactions and hence are very computationally expensive [131]. At the end of the section the trade-offs between the computational cost, level-of detail and the solution accuracy are discussed in more detail.

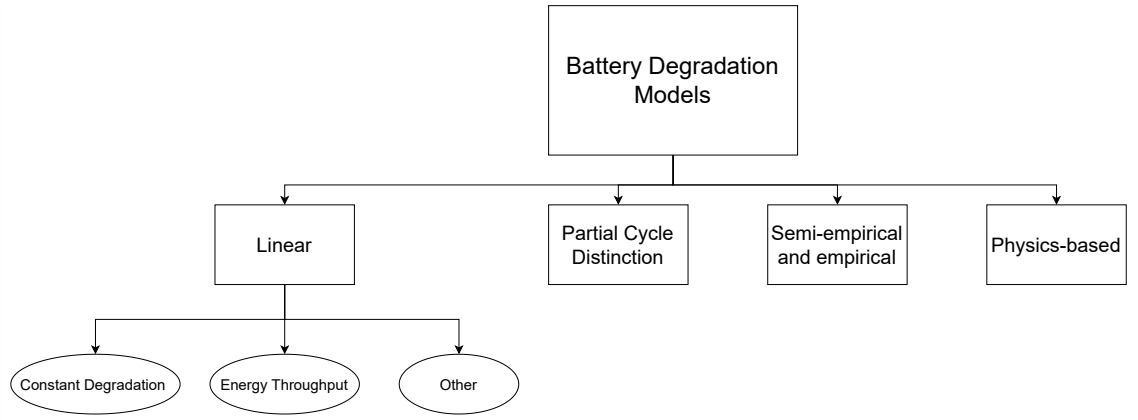


Figure 3.10: Overview of the battery degradation models found in the literature included into microgrid optimization algorithms.

Before the explanations of different degradation models are provided it is important to note two definitions of battery parameters. Firstly, the battery state of health (SOH) is defined as

$$SOH = \frac{Q_a}{Q_n} \cdot 100\%, \tag{3.1}$$

where Q_a is the actual capacity and Q_n is the nominal capacity [132]. SOH is often used as a measure of the degree of battery degradation. An SOH of 80% is often considered the end-of-life of the battery [132], [133]. Secondly, there are several definitions of battery depth-of-discharge (DoD). In the context of this thesis project, DoD is defined as:

$$DoD = SOC^{\text{max}} - SOC^{\text{min}}, \tag{3.2}$$

where SOC^{max} and SOC^{min} are the maximum and minimum states of charge of particular cycles. This definition was used by Boennec et al. in [134].

3.4.1 Linear Models

The simplest way to implement battery degradation in the optimization problem is to apply a constant degradation rate as a percentage of the total capacity at the start of its lifetime as has been done in [112] and [122]. Hence, the battery capacity is decreased by the same rate every year.

A slightly more advanced approach is to use the energy throughput of the battery as has been done in [104]. The energy throughput every day is calculated according to the following equation:

$$E_{\text{th}}(d_t) = \sum_{d=1}^{d_t} \sum_{h=1}^{24} (p_{\text{dis}}(d,h) + p_{\text{ch}}(d,h)), \tag{3.3}$$

where p_{dis} and p_{ch} are the discharge and charge powers, respectively, as functions of the day and hour. Once the energy throughput is obtained, the new capacity of the battery can be calculated as:

$$Q_{\text{bss,deg}}(d_t) = Q_{\text{bss}} - k_{\text{deg}} E_{\text{th}}(d_t), \tag{3.4}$$

where k_{deg} is a constant degradation factor, which differs for different battery chemistries [104]. The energy throughput method has also been used in [113] and [24]. They additionally consider the efficiency of the battery as a variable instead of a constant. A similar approach is applied by Dakir and Cornelusse in [35] and by Stevanato et al. in [29] where they count the number of cycles over the lifetime instead of the energy throughput. The degradation rate as a function of the number of cycles has also been presented in [135].

3.4.2 Models accounting for partial charge/discharge cycles

Zia et al. in [136] use a custom model that uses a relatively simple relationship that correlates the level of SOH with SOC and DoD that has been originally developed in [137]. This method models SOH as a reciprocal of the number of lifecycles N_{cycles}. The model also assumes that partial discharges are additive and together make up a full discharge. It neglects the temperature effects since they consider a system with good climate control, and hence the battery unit temperature is kept constant. It is also assumed that the charge and discharge levels stay below 1 C, hence the effects of charging/discharging rate on the lifetime can be neglected as well. The SOH is determined as:

$$\Delta SOH(Q_{t0}, Q_{t1}, I) = \Delta SOH(Q^{\text{max}}, Q_{t1}, I) - \Delta SOH(Q^{\text{max}}, Q_{t0}, I) = \frac{1}{N_{\text{cycle}}(Q_{t1}, I)} - \frac{1}{N_{\text{cycle}}(Q_{t0}, I)}, \tag{3.5}$$

where $Q^{\text{MAX}} - Q_{t1}$ and $Q_{t1} - Q_{t0}$ are partial discharges

A more advanced method is used by Amini et al. in [138]. The model considers that partial cycles have a different influence on the degradation than a full cycle. Fig. 3.11 shows an example of two partical cyles with identified peaks and valleys. The degradation of the battery according to the figure is then calculated as:

$$AG_{\text{T}}^{\text{cyc}} = \sum_{DOD} (AG_{\text{T,DOD}}^{\text{cyc,compl}} + AG_{\text{T,DOD}}^{\text{cyc,incompl}}), \tag{3.6}$$

where AG represent the aging terms of complete and incomplete cycles as functions of temperature and depth-of-discharge and $AG_{\text{T,DOD}}^{\text{cyc,incompl}}$ can be calculated as:

$$AG_{\text{T,DOD}}^{\text{cyc,incompl}} = AG_{\text{T,DOD = valley}}^{\text{cyc,compl}} - AG_{\text{T,DOD = peak}}^{\text{cyc,compl}} = \frac{Q^{\text{init}}(1 - EOL)}{N_{\text{T,DOD=valley}}^{\text{fail}}} - \frac{Q^{\text{ins}}(1 - EOL)}{N_{\text{T,DOD=peak}}^{\text{fail}}}, \tag{3.7}$$

where $N_{(\text{T,DOD})}^{\text{fail}}$ is the cycle life and Q^{init} is the initial capacity. The cycle life and the aging terms are calculated by using empirically derived equations based on the work done by Swierczynsky et al. in [139]. Moreover, the model by Amini et al. also takes into account calendar aging.

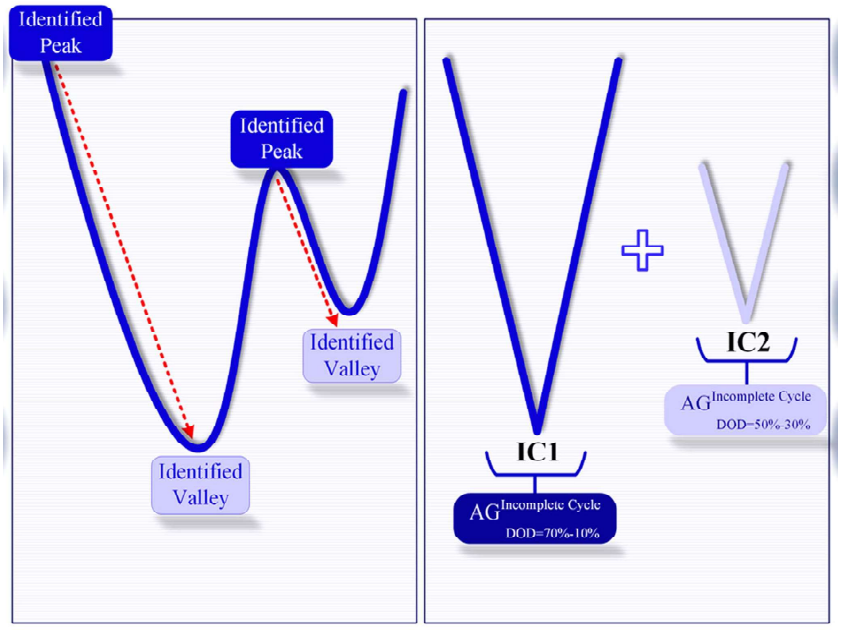


Figure 3.11: Identification and addition of partial cycles for battery degradation modelling [138].

A similar approach utilizing partial cycles has been used by Masaud et al. in [140] and Wang et al. in [141] once again utilizing the model from the work of Swierczynsky et al. [139].

Finally, it is worth mentioning the rainflow count algorithm, which is similar to the the partial cycle model introduced previously by [138]. The rainflow count model calculates the ”fatigue” of the battery by taking into account the DoD at each time interval. Fatigue is determined every month by using the following equation:

$$\Delta_{\text{cyc}}(m) = \sum_{i=1}^{|\overrightarrow{DoD}|} \frac{1}{2 \cdot NCF(\overrightarrow{DoD}_i)}, \tag{3.8}$$

where factor 2 represents the counting of half-cycles instead of full cycles, $\overrightarrow{DoD}$ is the vector containing the time series of DoD values of the corresponding month and the NCF function provides the number of cycles achievable for a particular DoD value. In addition, calendar aging has also been implemented in this model [134]. SoH is then calculated as:

$$SoH_{m+1} = SoH_m - \Delta_{\text{cyc}}(m) - \Delta_{\text{cal}}(m), \tag{3.9}$$

where $\Delta_{\text{cyc}}(m)$ and $\Delta_{\text{cal}}(m)$ are the cyclic and calendar fatigue, respectively.

3.4.3 Semi-empirical and empirical models

A semi-empirical model combines the physical and empirical parameters into a single model. Although theoretical models are usually hard to implement due to many non-linear relationships and empirical models usually are applicable only for very specific conditions, semi-empirical models combine the strengths of both [133]. Hence, empirical models are not explicitly explained in this subsection.

The reason for using one semi-empirical model over the other depends on the battery chemistry and the specific application for which the optimization is done. Some semi-empirical models are more general and can be used for different battery chemistries by adjusting certain parameters in the model, such as those made by Fallahifar and Kalantar in [142] or by Xu et al. in [133]. However, many models have been derived for specific battery chemistries such as the one in [143].

Next, an example of a semi-empirical model is given. The model has been derived by Xu et al. in [133]. The SOH in this model is calculated by using the following equation, which makes use of empirical parameters:

$$SoH_t = \alpha_{\text{sei}} \cdot e^{-\beta_{\text{sei}} \cdot fd_t} + (1 - \alpha_{\text{sei}}) e^{-fd_t}, \tag{3.10}$$

where α_{sei} and β_{sei} are empirical parameters that describe the formulation of SEI, fd is a variable describing the global stress on the battery up to time t. The global stress depends on DoD, time, average SOC, and the temperature T. fd of a single half-cycle can be calculated as:

$$fd^{\text{unit}} = (0.5 \cdot S_{\text{DoD}}(DoD) + S_t(t)) \cdot S_{\text{SoC}}(SoC) \cdot S_T(T), \tag{3.11}$$

where S_{DoD}, S_{SoC}, S_t and S_T are the stress functions that are dependent on DoD, SoC, time, and temperature, respectively. These are associated with the stress factors described in Section 2.2.5. To give an example, the stress function for the temperature is defined as:

$$S_T(T) = e^{k_T(T - T_{\text{ref}}) \cdot \frac{T_{\text{ref}}}{T}}, \tag{3.12}$$

where k_T is the temperature stress coefficient and T_{ref} is the reference temperature that is often taken as 293K [133]. This example model considers four stress factors, however, different models account for different stress factors depending on which ones are applicable for the use case. For instance, if there is climate control for the battery storage system, then the stress factor from the temperature could potentially be neglected as is done by Boennec et al. in [134], where the example model by Xu et al has been simplified.

3.4.4 Trade-off between the level-of-detail, computational power and the cost of the final product

It has been established in this section that there is a wide range of level-of-detail to which the battery degradation can be modeled, however, the question still remains of which level of detail is sufficient

to accurately model battery degradation processes in the optimization problem. While greater level-of-detail might give more accuracy, it also brings greater computational time, and often increasing the level-of-detail further brings marginal benefits. Hence, this section inspects analysis of these trade-offs covered in the literature.

Many articles argue that it is important to use more detailed battery degradation models, while not giving explicit arguments on what benefits they bring beyond having a model that better represents reality, such as the ones in [142] or [144]. The latter paper in-detail analyses different aspects missing from the previously done research while missing a reference on what is the impact in the final result when higher level of detail is included in these optimization models. These papers are not the only ones lacking argumentation for the chosen level of detail.

Nevertheless, there are authors who have done the opposite and have done an analysis of the impact of the inclusion of a detailed battery degradation model. For example, Dakir et al. in [35] compare the resulting yearly cash flows for a grid-connected microgrid project between the cases where an energy-throughput degradation model for battery storage system is included versus the case when it is not. In the case where degradation of the components was included, the PV capacity was almost half, while for one of the control strategies the battery system was removed as a whole, thus increasing the size of the diesel generator (for the other control strategy the battery capacity decreased by around 40 %). Meanwhile, the net present value changed from negative 2.883 million euros to negative 3.292 million euros (a difference of 13.5 %) - similar results were obtained for both control strategies. This study shows the concrete effects of the inclusion of component degradation.

An even more elaborate analysis was performed by Wang et al. in [34], where the effects of five different battery degradation models were analysed. Fig. 3.12 shows a comparison of the total costs of the microgrid using different battery degradation models - J_{grid} is the electricity cost purchased from the utility grid, J_{ESS} is the replacement cost of the energy storage system, while J_{cost} is the sum of both. ”Linear”, ”PLET”, ”NREL”, and ”Arrhenius” represent different battery degradation models of varying complexity that address different stress factors, while ”CAPN” is the model that combines all the stress factors into one single model [34]. For example, a linear model is a version of the energy throughput models mentioned above. It can be seen that different models can either overestimate or underestimate the costs in the range of 40%, which is a significant difference.

Although the two presented examples do not evaluate the impact of all the possible details of different levels of detail for different degradation models, it can still be concluded that the effect of the degradation model has potentially serious effects on the final costs of the microgrid.

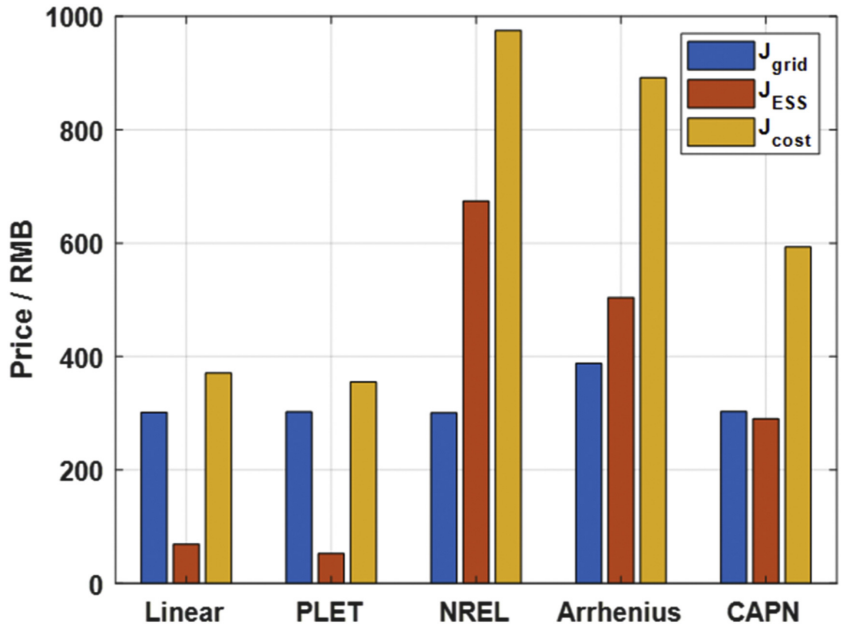


Figure 3.12: Optimized amounts of the total costs, purchase cost from the grid and replacement cost of the ESS under different degradation models [34].

Chapter 4

Methodology

This chapter provides a detailed explanation of all the tools and methods used to experimentally investigate switch degradation under different mission profiles and to perform microgrid optimization while considering load stochasticity and component degradation. Fig. 4.1 provides an overview of the proposed microgrid sizing optimization algorithm.

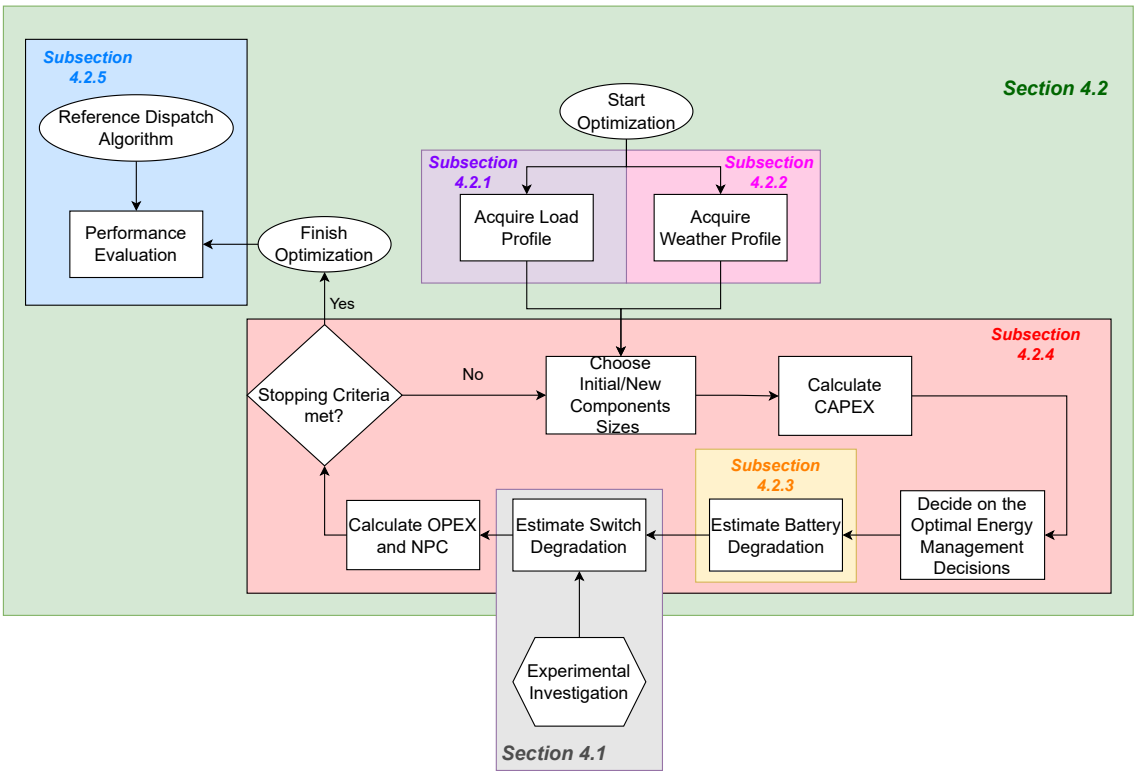


Figure 4.1: Flowchart of the proposed microgrid sizing optimization algorithm and the overview of the chapter contents.

It can be seen that the figure resembles Fig. 3.1 introduced in Chapter 3. However, a few differences can be identified. Firstly, the estimation of the switch degradation has been added inside the optimization loop, which is one of the main contributions of this thesis project. Secondly, it can be seen that load and weather acquisition have been treated separately. Finally, a performance evaluation block has been added after the completion of the optimization to understand how well the proposed algorithm

works.

To provide a brief overview of this chapter, section 4.1 describes in a detailed manner how the switch degradation can be estimated. It also describes how to experimentally investigate the dependency of degradation on the dispatch strategy. Section 4.2 delves into the details of the microgrid sizing optimization algorithm through five subsections. Subsection 4.2.1 and Subsection 4.2.2 describe how the load and weather profiles were acquired to be used as input for the sizing optimization. Subsection 4.2.3 delves into the details of the chosen battery degradation models. Subsection 4.2.4 explains all the steps of the core optimization algorithm and finally Subsection 4.2.5 provides an overview of how the performance of the algorithm is evaluated.

The reason for starting the chapter with the experimental investigation of switch degradation is that to better understand the final design of the proposed optimization algorithm it is necessary to understand the component models used to build up the model. Since the section of experimental investigation cannot be split and distributed across the chapter it was decided to start with the section on switch degradation even if it is not the start of the optimization algorithm in Fig. 4.1.

4.1 Experimental Investigation of the Switch Lifetime Model

This section introduces and explains the tools and methods used to carry out the experimental investigation of switch degradation inside the inverter of the solar panel array. An overview of the method and the content of this section is provided in Fig. 4.2.

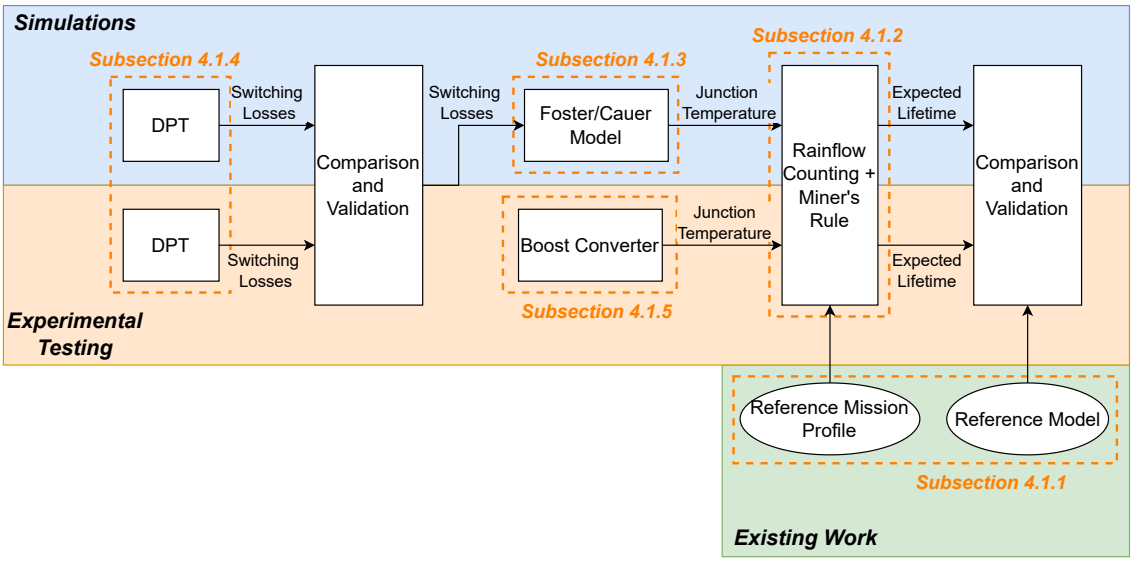


Figure 4.2: Flowchart of the method used to investigate switch degradation dependency on the chosen mission profile.

The section consists of four subsections: subsection 4.1.1 introduces the study by Alpízar-Castillo et al. [102] where the model of switch degradation is made depending on the amount of power curtailment. The study serves as a basis for the experimental investigation described in this section. Subsection 4.1.2 introduces the switch lifetime model that has been used in the reference study and the experimental investigation. It is shown that the degradation is strongly dependent on the switch junction temperature, which in turn depends on the switching losses inside the switch. The approaches for determining the junction temperature and the switching losses have been explained in Subsections 4.1.3 and 4.1.4, respectively. Finally, in Subsection 4.1.5 the experimental testing setup for determining the junction temperature dependency on the mission profile has been introduced.

It can be seen in Fig. 4.2 that the flowchart is split in two main parts - simulations and experimental

testing. The goal of the thesis project was not only to investigate how real-life measurements compare with the reference model in [102] but also to see how closely it is possible to simulate the model in circuit-based software such as LTSpice or PLECS. Hence, the double-pulse test (DPT) setup to determine switching loss was not only built in the lab setting but also simulated. After the comparison of the switching loss measurements and the simulations, the junction temperature of the switch during an operation of a Boost converter could be modeled. Junction temperature estimates consequently allowed to estimate the lifetime of the switch. The simulated junction temperatures were compared with the experimentally determined ones, and finally the extracted lifetime estimations were compared with the reference model.

4.1.1 Existing Work on the Impact of Curtailment on Switch Lifetime

The theme of this thesis is to explore different assumptions made in the microgrid sizing and dispatch optimization. One of the aspects that has been neglected in the research so far is considering the degradation of the switches inside PV inverters. While there are some optimal dispatch algorithms that take into account battery degradation when deciding on the optimal dispatch for a microgrid, there are none that would do the same for the PV inverters (to the author's knowledge of this thesis).

The impact on the reliability of PV inverter switches depending on weather and geographical location has been studied before in [145] and [146]. However, studies assume that solar panel arrays work at the maximum power point. This could be a valid assumption in case the arrays are connected to the main grid, however, in the case of microgrids, the EMS would often curtail the power generated by the array to ensure power balance.

The impact of different curtailment thresholds on the lifetime of the switch inside an inverter has however been shown before by Alpízar-Castillo et al. in [102]. They studied a PV converter consisting of a boost converter and an inverter shown in Fig. 4.3 . They argued that the critical part of the converter is the switch inside the boost converter, since operating outside maximum power point (MPP) puts additional stress on the switch on the DC side, which is not the case for the switches on the AC side which operate at a fixed AC voltage.

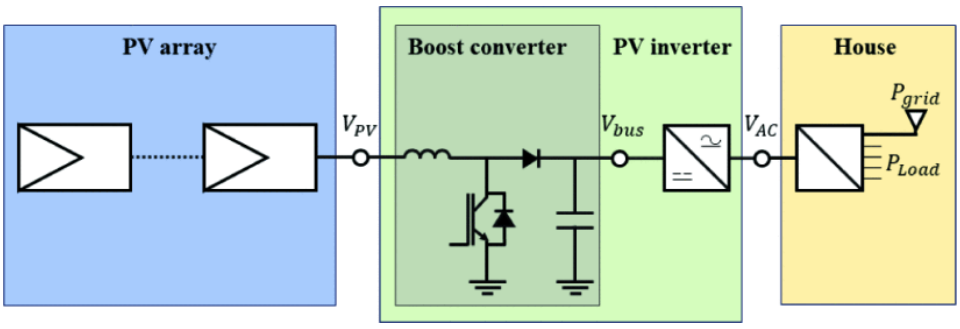


Figure 4.3: Overview of the converter studied in [102].

By modeling the switch degradation with the use of the Bayerer model, the study applied a mission profile of a residential home and simulated the effects of different curtailment thresholds of the converter. Similar methodology was also applied in [145] and [146]. The resulting lifetime dependency on the curtailment threshold is shown in Fig. 4.4. It can be seen that the curtailment threshold has a significant impact on the lifetime of the switch. The system is rated at 2 kW and it can be seen that for curtailment thresholds up to 1 kW, the switch lifetime varies between 20% and 90% of the normalized lifetime. It means that in case the curtailment threshold is set too low, the switch might fail significantly faster, thus increasing the cost of the system.

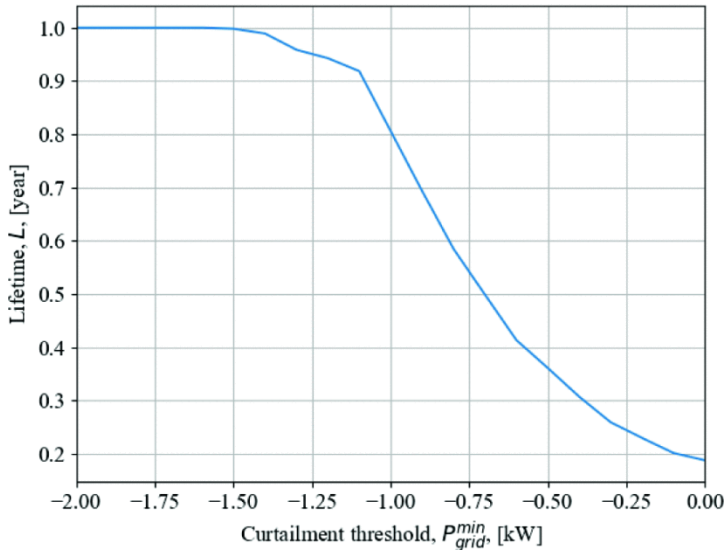


Figure 4.4: Normalized expected lifetime of the switch inside the boost converter depending on the solar panel array curtailment threshold [102].

The study in [102] also investigated the impact of the curtailment threshold on the LCoE of the system, as shown in Fig. 4.5. It can be seen that the LCoE correspondingly increases as the curtailment threshold decreases (in absolute value), corresponding to the decreased lifetime of a switch. The resulting change in replacement LCoE goes up to more than five times, while in the base LCoE it goes up to more than two times.

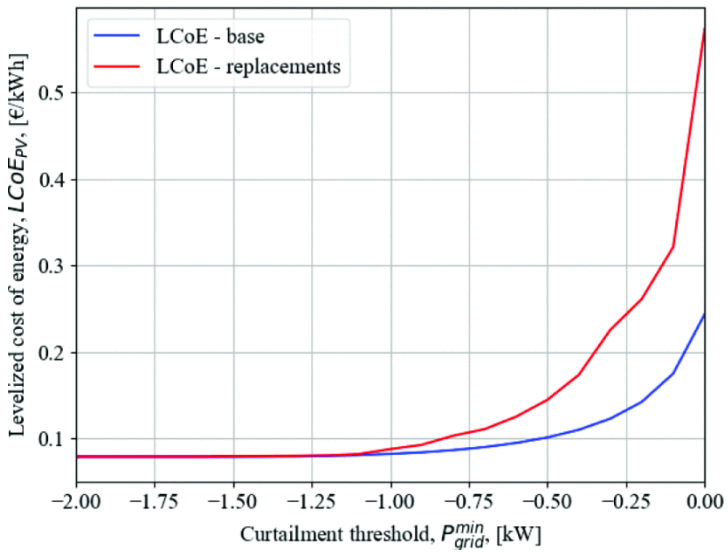


Figure 4.5: System LCOE as a function of the curtailment threshold of the solar panel array [102].

Thus, it was shown that the curtailment strategy, and hence the EMS of the microgrid can theoretically have a significant impact on the final cost of the system, meaning that it is important to model it while performing the sizing optimization of the microgrid. However, the results in [102] are based only on theoretical models and simulations, and no real-life tests of the switches were performed in the study. While the time constraints of the thesis do not allow to do power cycling to test the lifetime of the switches, the work in the remainder of the chapter describes the experimental investigation of the impact of the mission profile on the junction temperature of real switches. This is then the input for the theoretical degradation model which can then be combined with rainflow counting to estimate the

lifetime similarly to what has been done in [102].

4.1.2 Tools Used to Determine Switch Lifetime

To investigate the correlation presented in the work of Alpízar-Castillo et al. [102] shown in Fig. 4.4 the mission profile of the same study is used. The study in [102] uses Bayerer model to evaluate and compare switch lifetime under different curtailment thresholds. The formulation of the Bayerer model has been introduced in Section 2.3 and equation (2.3) is used for the calculations and is repeated here for convenience:

$$N_f = K \cdot \Delta T_j^{\beta_1} \exp\left(\frac{\beta_2}{T_j}\right) t_{\text{on}}^{\beta_3} I^{\beta_4} V^{\beta_5} D^{\beta_6}, \tag{4.1}$$

The equation is used in the experimental investigation to replicate the study as closely as possible. The only variable inside the equation that is measured during the experimental testing is the junction temperature of the semiconductor device (junction temperature swing and the minimum junction temperature). The rest of the parameters are fixed and depend on the manufacturing parameters as described in Section 2.3 except for t_{on}, which is determined by the mission profile. The approaches for the junction temperature estimation are described in the following subsection.

Equation (4.1) describes the switch lifetime in case of fixed cycling conditions, which means that the current flowing through the switch and the heating cycles are the same throughout the lifetime of the device. This is however often not the case for the converter at the output of the solar panel array as the irradiation and the electrical load are always changing. Therefore, rainflow-counting algorithm is used together with the Miner's rule to estimate the equivalent heating cycles of the switch and to calculate the lifetime of the switch under changing operational conditions.

Rainflow-counting method is a widely used method for calculating accumulative mechanical fatigue of a structure or a device based on stress-strain hysteresis loop [147].The method allows to count the accumulative damage to a device under changing stress/strain cycling conditions. The concept of rainflow-counting was introduced by Matsuishi and Endo in 1968 in [148]. Many variations of rainflow-counting have been developed since, however, the general idea has stayed the same [149]. The approach described by Infineon in [58] has been described here.

As an example, a temperature profile of a switch over time has been taken as shown in Fig. 4.6. The figure also shows the same profile with rotated axis to help visualize the method better.

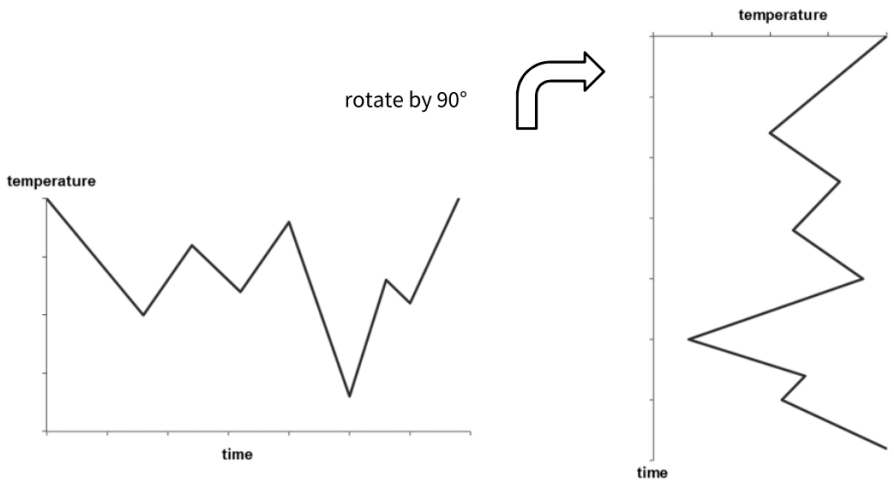
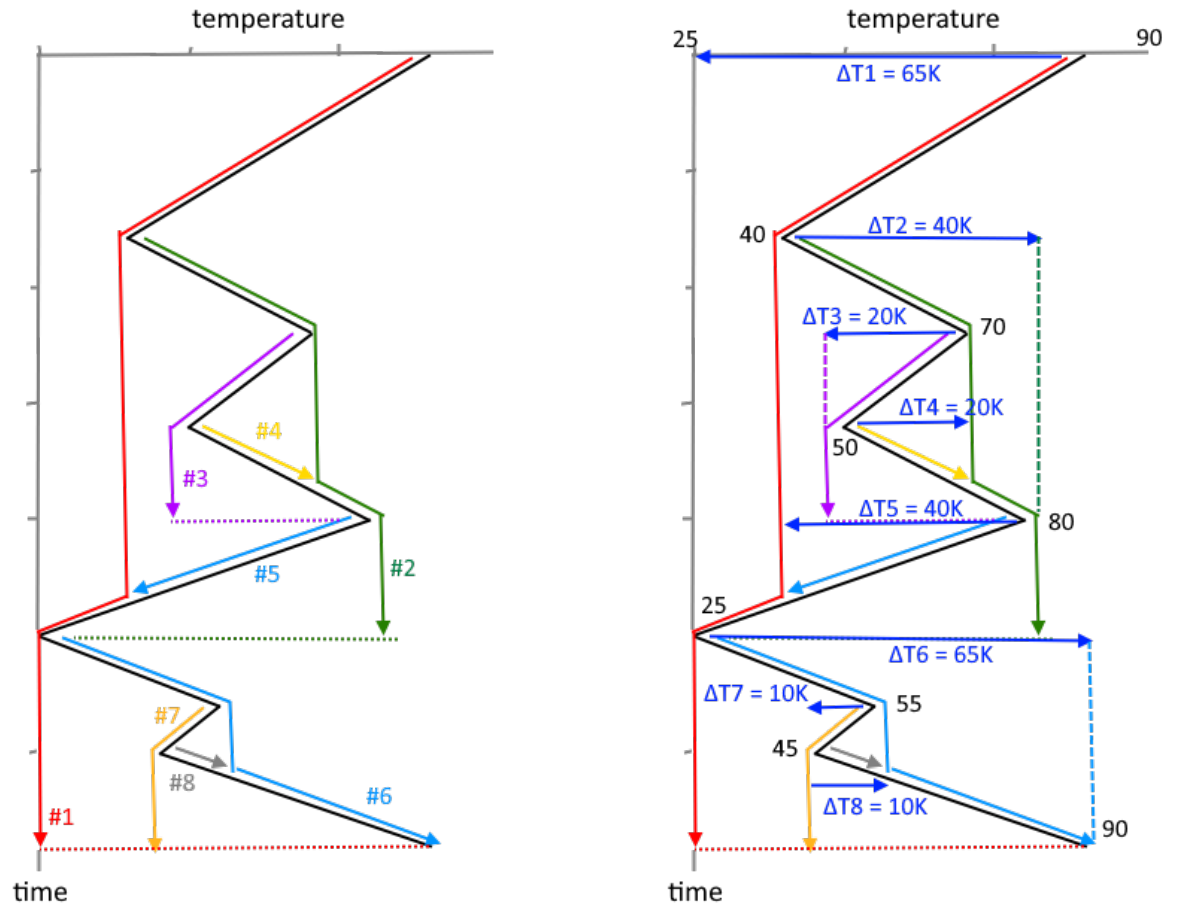


Figure 4.6: An arbitrary temperature profile of a switch over time (on the left), which has been rotated by 90 degrees for a better visualization of the algorithm (on the right) [58].

The general idea of rainflow-counting is to decompose the arbitrary cycling profile into smaller cycles that, added together, create the total profile. Fig. 4.7 visualizes the identification of the water droplet-

s/streams that ”flow down a roof” (Fig. 4.7a) and the corresponding identification of the thermal cycles (4.7b).



(a) Identification of ”water droplets/streams”

(b) Identification of the temperature cycles based on the ”water stream flows” and their termination criteria.

Figure 4.7: Visualization of the Rainflow counting algorithm according to the implementation by Infineon in their application note in [58].

A stream starts at every vertex (maximum or minimum) of the temperature profile. The counting is started from the top. The termination of the ”flow” is determined by several rules as follows [58]:

- A stream that has started at a maximum ”flows over” two minimums by touching them and vice versa (streams #1 and #2 in Fig. 4.7a)
- A stream that has started at a maximum passes a maximum that is higher than the one where it started from and vice versa (stream #3 in Fig. 4.7a)
- A stream reaches another stream that has been counted previously (stream #4, #5 and #8 in Fig. 4.7a.
- A stream ”falls off” from the analysed segment of the profile (stream #6 and #7 in Figure 4.7a).

Fig. 4.7b shows how the temperature differences for different thermal cycles are identified. The identified temperature differences ΔT_x come in pairs as can be seen in the figure. The pair of two partial cycles create one full cycle, which can then be used as the input for the next step in damage estimation.

The damage from the individual cycles is added together according to the Miner's rule introduced by Milton Miner in [150], which states that the accumulative damage of different stresses can be calculated as the linear sum of fractions of the number of cycles at a certain stress divided by the number of cycles till failure at such stress. Equation (4.2) shows the analytical expression of the Miner's rule.

$$D = \sum_{i=1}^{m} \frac{n_i}{N_i} \tag{4.2}$$

where n_i represents the number of cycles at a stress i and N_i represents the number of cycles till failure at a stress i [150].

4.1.3 Approaches for Determining Junction Temperature

One of the common factors present in the lifetime models is the junction temperature swing. Higher junction temperature swing corresponds with higher switch degradation. Before describing the approaches for determining the junction temperature, it is important to understand what is meant by the junction temperature. Fig. 4.8 shows the three main interfaces that need to be considered when estimating the junction temperature:

- Junction-Case
- Case-Heatsink
- Heatsink-Ambient Air

During power cycling, the temperature of the heatsink will be different from the one of the case of the discrete device, which in turn will be different from the junction temperature inside the discrete device. The simplest approach for modeling the different temperatures is to model them as being separated by thermal resistances, which describe the temperature increase per watt of power. At least some of the values for the thermal resistances can often be found in the datasheets of semiconductor devices [151].

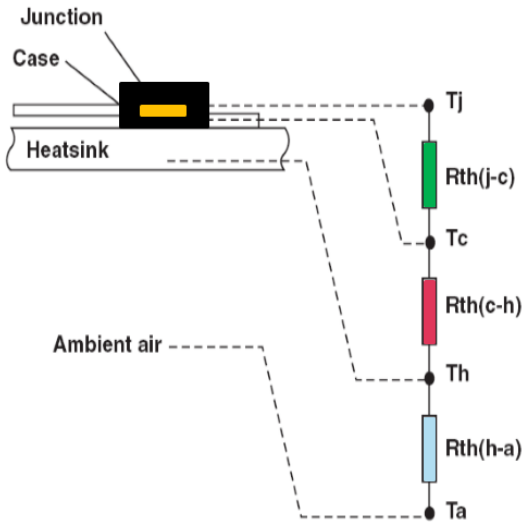
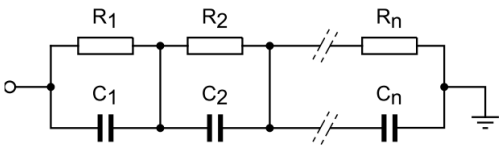
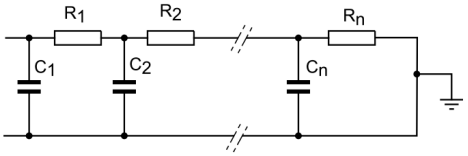


Figure 4.8: Example of an equivalent thermal model of a power electronic device.

As distinguished by Cao et al. in [152] there are three general types of approaches to determine the junction temperature of power semiconductor devices - model-based approaches, sensor-based approaches and approaches making use of the temperature-sensitive electrical parameters. The three types of approaches are next described in detail in this subsection.



(a) Foster thermal model of a semiconductor device.



(b) Cauer thermal model of a semiconductor device.

Figure 4.9: Foster and Cauer thermal models [153].

Model-based Approach: Foster-Cauer Model

A commonly used model to determine the junction temperature of a semiconductor device is the Foster-Cauer model. It has been used extensively in both industry [153], [154] and research [155]. Part of the appeal of the Foster-Cauer models comes from their simplicity as the thermal behaviour of the semiconductor device is modeled as simple RC networks. Foster and Cauer circuit models have been shown in Fig. 4.9.

Foster model can be acquired by creating a parametric fit of the thermal impedance curve of the specific semiconductor device. Such curves can usually be found in the device datasheets. An example of such a curve is given in Fig. 4.10.

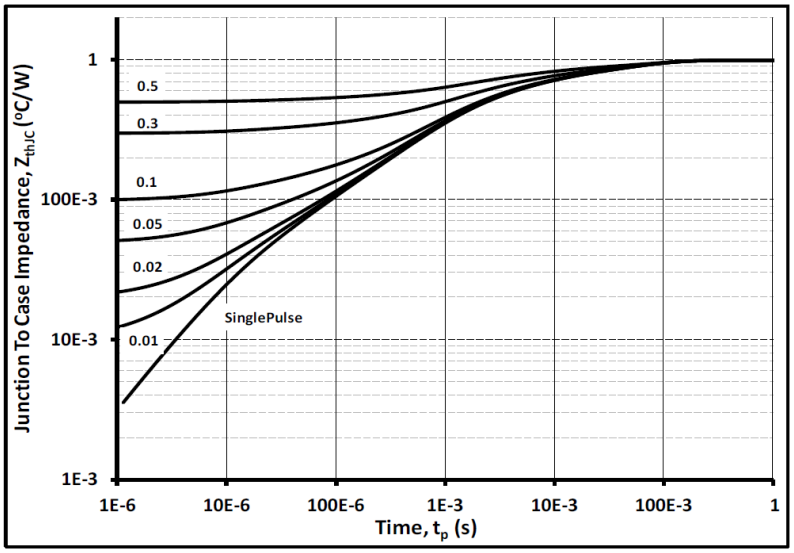


Figure 4.10: Thermal impedance curves of the C3M0045065K SiC MOSFET [151].

The curves show how the thermal impedance changes in degrees per watt depending on the duty cycle of the current flowing through the switch. A range of curves has been plotted for different duty cycles from a single pulse to a duty cycle of 50%. The parametric fit can be produced via the following equation:

$$Z_{\text{th}} = \sum R_i \cdot \left(1 - \exp\left(-\frac{t}{\tau_i}\right)\right), \tag{4.3}$$

where the time constant τ is calculated as $\tau_i = R_i C_i$, where R_i and C_i are the corresponding resistances and capacitances within the Foster model [153]. To ideally represent the behaviour of the device one would need to have an infinite number of stages, which is not practically possible to model, but usually three or four stages are deemed to be accurate enough for most modeling purposes [156]. Given that the resistances and capacitances in equation (4.3) are unknown, they have to be acquired empirically to find such a combination which fits the curve in Fig. 4.10. The simplest method to acquire the

parameter values is to try all the possible options until one is found with sufficient accuracy, however, that could be a very time-consuming method. Some more advanced methods have been developed, for example, there is an open-source PSO optimization algorithm that fits the 3rd order curve within 10 seconds developed by Bartlomiej Ufnalski, which can be found in [157]. In addition, PLECS software provides a tool that allows us to extract the values of the RC elements by importing the datasheet of the device and drawing the points of the selected curve.

It is important to note that Foster model is not based on real physical phenomena - the resistances and capacitances do not actually represent physical electrical elements, which means that the model cannot be used directly to estimate the junction temperature [153]. The solution is to transform the Foster model into the Cauer model, which also helps to represent the dimensionality of the device [158]. Foster-Cauer transformation is a well established mathematical method for acquiring the Cauer model from the Foster model, and implementations of it can be found in different software tools. The explanation of the transformation is emitted here, since it does not provide additional insights and is used as a black-box model within the scope of the thesis.

Finally, to complete the Cauer model, a current source has to be added at the input as shown in Fig. 4.11.

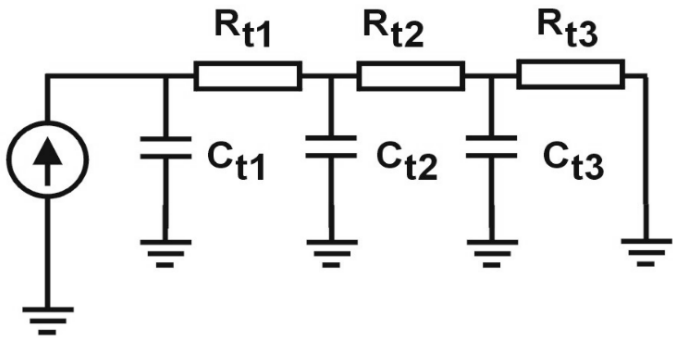


Figure 4.11: Cauer network containing the RC elements and a current source, which has a current value equivalent to the switch losses.

The instantaneous value of the current source is equal to the instantaneous losses of the switch. The voltage across the current source can then be interpreted as the increase in junction temperature in comparison to a reference steady-state temperature. If one desires to directly acquire the absolute temperature, a voltage source has to be added on the other end of the circuit with a value corresponding to the ambient temperature.

The instantaneous energy loss inside the switch can be determined as:

$$P_{\text{loss}} = V_{\text{switch}} I_{\text{switch}}, \tag{4.4}$$

where V_{switch} is the voltage drop across the switch while it is conducting and I_{switch} is the current flowing through the switch. When calculating the losses analytically as was done in [102] the total losses inside the switch can be split into conduction loss and switching loss:

$$\begin{aligned} P_{\text{total}} &= P_c + P_s \\ P_c &= V_0 I_{\text{av}} + R_{\text{CE}} I_{\text{rms}}^2 \\ P_s &= \frac{f_s E_s |V_s|}{V_{\text{nom}}} \end{aligned} \tag{4.5}$$

where V_0 is the on-state zero-current collector-emitter voltage, R_{CE} is the on-state resistance [159], f_s is the switching frequency, E_s is the switching energy, V_s is the instantaneous voltage and V_{nom} is the nominal voltage under test conditions [102].

The energy loss can be modeled using a quadratic fit as follows:

$$E_s = a_T + b_T |i_{\text{av}}| + c_T i_{\text{rms}}^2 \tag{4.6}$$

where a_T, b_T and c_T are the dynamic characteristic parameters that are usually obtained from the datasheet [102].

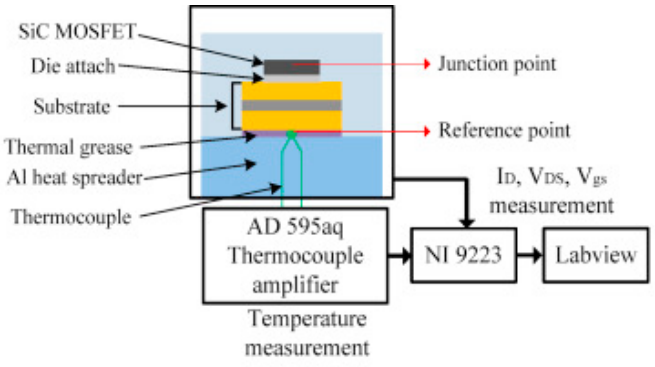
To simulate the junction temperature LTspice software has been used where the Cauer model has been modeled. The RC parameters have been extracted by uploading the datasheet of the studied switch on the PLECS software and using the automated tool, which extracts the parameters.

Sensor-based Approaches

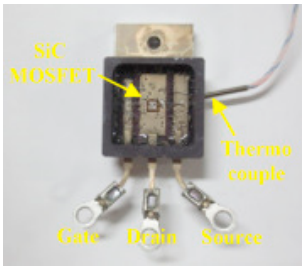
Sensor-based approaches allow for direct measurement of the junction temperature, however, there are technical limitations in acquiring accurate measurements of specifically the junction temperature as opposed to the case temperature. As described in [152] and [160] some sensor-based methods include thermocouples, optical fiber temperature probes, and infrared measurements. There are two distinct disadvantages with methods that require direct contact with the junction such as thermocouples (shown in Fig. 4.12). Direct measurements require opening up the chip package, which is not only impractical for implementation and reproducibility of results, but can also influence the thermal behaviour of the junction itself as there is a direct contact with the junction or the substrate [160].

There are also indirect sensor-based methods that make use of optical sensors, for example, infrared sensors as shown in Fig. 4.13. They are very straightforward to use as long as the device under-test is not obstructed by other objects or parts of the circuitry. Nonetheless, there is a serious drawback to this method. Firstly, since the chip package is not modified, temperature measurement can only be made at the surface of the package, and, as discussed before, the temperature of the package does not always correspond to the one of the junction. Hence, non-contact optical measurements can only be used at low switching frequencies, in which case the chip casing has enough time to reach the junction temperature [152].

During the experimental measurements of this thesis project, IR measurements and a temperature probe were used to monitor the heatsink temperature to prevent the circuit from reaching extreme temperatures, but were not used as means for a precise junction temperature estimation.



(a) Diagram of an implementation of a thermocouple.



(b) Practical implementation of a thermocouple for a SiC MOSFET.

Figure 4.12: Thermocouple implementation inside a SiC MOSFET [161].

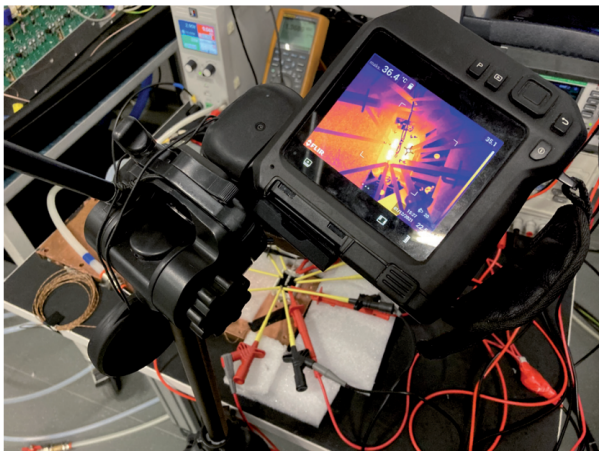


Figure 4.13: An example of an infrared measurement of the switch temperature during testing by using a thermal camera [160].

Temperature Sensitive Electrical Parameters

Temperature-Sensitive Electrical Parameters (TSEPs) can be defined as a set of electrical parameters that change in response to the junction temperature of the power semiconductor devices [162]. The main advantage of TSEPs is that they allow for online monitoring of device junction temperature without physical interventions to device packaging. However, the disadvantages include low sensitivity, which requires high accuracy and precision of measurement equipment. Another drawback is the need for calibration of the TSEP (sometimes multiple times during the mission profile). The calibration of TSEP is necessary due to manufacturing differences from one device to another (even for different devices of the same model).

The concept of TSEPs has been used for a long time in the context of IGBTs, however, the applications for the SiC MOSFETs are still being actively researched. Even though the reference model by Alpízar-Castillo makes use of IGBTs to align with the existing research in the universities facilities it was decided to use SiC MOSFETs to perform the experimental investigation. To show that a similar approach could be theoretically be used also for Si IGBT switches, TSEPs of both SiC and Si IGBTs were investigated.

The specific TSEPs that are often used for determining the online junction temperature inside IGBTs include on-state voltage, saturation current, threshold voltage among others [152]. However, not all of these are applicable for SiC MOSFETs. TSEPs that have been often used in previous research for junction temperature measurements in SiC devices include threshold voltage, on-state voltage, on-resistance, and gate voltage plateau [160] [162]. Each of the TSEPs presents a trade-off between the complexity of the measurement setup and the sensitivity of the measurement to noise and environmental conditions.

Yu et al. in their study made a comparison between different TSEPs for both Si IGBT and SiC MOSFET devices [163]. The purpose of the study was to assess the applicability of different TSEPs for online junction temperature monitoring. The results of the study are summarized in Table 4.1.

Table 4.1: Comparison of TSEPs in SiC MOSFETs and Si IGBTs [163].

Devices	TSEPs					
		R_{on}	V_{TH}	$t_{\text{d-off}}$	di/dt	V_{GP}
Si IGBT	Sensitivity	Low	High	High	Low	High
	Implementation	Easy to measure (using high voltage analog isolation circuit)	Difficult for online measurement	Easy to measure	Easy to measure	Easy to measure, but requires to measure DC bus voltage
SiC MOS	Sensitivity	High	Low	Low	High	Low
	Implementation	Easy to measure (using high voltage analog isolation circuit)	Difficult for online measurement	Easy to measure, but requires high bandwidth current sensor	Easy to measure, but requires high bandwidth current sensor	Difficult to measure

The table shows an overview of the sensitivity and ease of implementation for five different TSEPs for both the Si IGBTs and SiC MOSFETs, namely, the on-resistance R_{on}, threshold voltage V_{th}, turn-off delay $t_{\text{d-off}}$, slope of current rise di/dt and the gate plateu voltage V_{GP}. Threshold voltage is difficult to be used as a TSEP because it requires very high-bandwidth noiseless equipment both in the case of Si IGBT and SiC MOSFET. The gate plateu voltage can also cause some difficulties in measuring for SiC MOSFETs because of the low sensitivity.

The three best candidates not only in [163], but also often referenced in other studies are the on-resistance, turn-off delay, and the current rise slope [152], [164]. Since the available evaluation board in the lab allows testing primarily SiC MOSFETs the choice is made for the R_{on} (or specifically $R_{\text{ds-on}}$) as the TSEP to be used for junction temperature measurement. R_{on} is not only easy to measure but it also matches with other on-going research taking place in the lab.

There are two main factors contributing to the increase in $R_{\text{ds-on}}$ (drain-source resistance during conduction) of a silicon carbide MOSFET: self-heating of the device and saturation of charge mobility [165]. Firstly, self-heating of the device contributes to the rise in the temperature expressed as:

$$\Delta T = P \cdot Z_{\text{th}} \tag{4.7}$$

where P is the dissipated power and Z_{th} is the thermal impedance of the device [166]. Self-heating is more pronounced at temperatures up to 100°C and shows a linear relationship between R_{DSon} and junction temperature. Charge carrier saturation portrays a more nonlinear behaviour but is more pronounced at temperatures above 100°C [165].

4.1.4 Experimental Implementation of the Switching Loss Estimation via the Double-Pulse Test

As previously mentioned, the input for the Foster-Cauer model is the dissipated power inside the switch during its operation. To validate whether the simulation simulates the switch losses in a representative manner, the losses inside the switch are tested. This section focuses on the experimental implementation of the Double-Pulse Test (DPT) - a widely-used method for estimating switching loss.

Working Principles of the Double-Pulse Test

The basic circuit layout of the DPT is shown in Fig. 4.14.

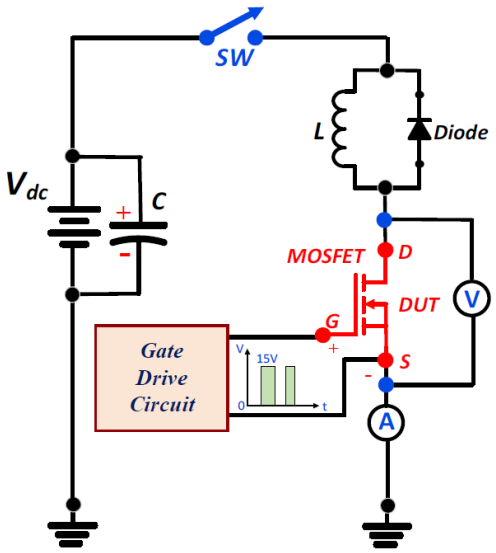


Figure 4.14: Basic circuit diagram of experimental DPT testing [167].

The circuit consists of a voltage source (V_{dc} inside the diagram), an inductor, a diode in parallel to the inductor, and the switch that is being tested (MOSFET in red in the diagram). The switch is supplied with two short pulses at its gate. An example of a V_{gs} waveform is shown in Fig. 4.15 (a).

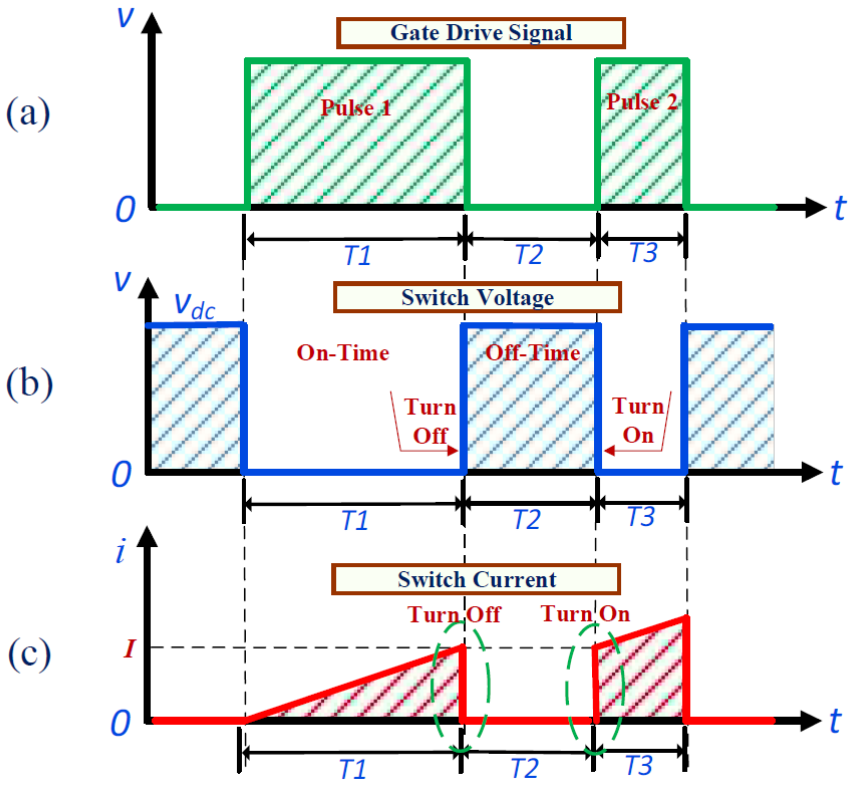


Figure 4.15: Gate-source voltage, drain-source voltage and the switch current waveforms during the DPT test [167].

The first pulse is usually longer than the second pulse as denoted in the figure. The current flow during the first pulse and during the off state of the switch have been shown in Fig. 4.16 (a) and Fig. 4.16 (b), respectively. The current flow during the second pulse is the same as during the first pulse as shown in Fig. 4.16 (a).

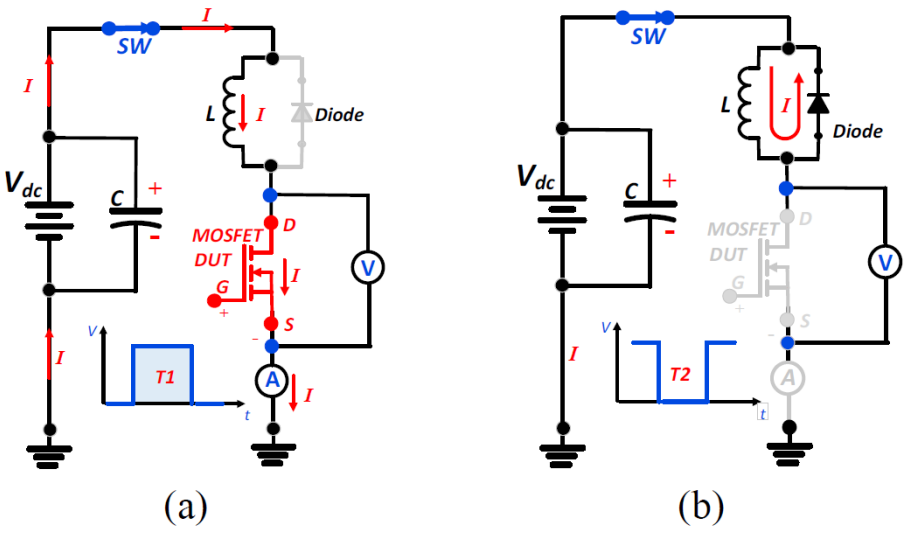


Figure 4.16: Operation of a DPT circuit during the on and off periods of the pulses [167].

While the switch is in the on state (during T1 and T3 as per Fig. 4.15), the current flows from the DC power source through the inductor and through the switch (also referred to as the device under test (DUT)). During the off-state (T2 in Fig. 4.15), the current cannot flow through the DUT, hence it circles through the loop of the inductor and the parallel diode. This loop allows to maintain the current at the value at which it rose during the first pulse. Upon the second pulse, the current continues to flow through the DUT at a magnitude that was maintained during the off-state. The current then continues to rise until the end of the second pulse. The resulting waveforms of the switch voltage and the switch current can be seen in Fig. 4.15 (b) and Fig. 4.15 (c).

It can be seen that the current increases during the first pulse (T1) and continues to rise from the same magnitude during the second pulse (T2). As indicated in Fig. 4.15 the measurement of the switching energy during the turn-off E_{off} is done at the end of the first pulse, while the energy during the turn-on is measured at the start of the second pulse. In this manner, the current during the measurements of E_{off} and E_{on} can be kept the same and allows for a better comparison between the two. This feature is the main motivation for the choice of having two pulses. The duration of the second pulse is shorter than that of the first pulse because there is no need to continue increasing the current after the measurement of the turn-on loss. Since the switch loss measurements might be done at high currents, the duration of the second pulse should be kept to a minimum to the extent that it does not influence the measurement of the on-energy.

The duration of the first pulse depends on the chosen inductor value and the desired current level for the switching loss measurement. However, too long of a pulse can cause self-heating of the device, which is undesired. Although the exact limitation of the pulse length will depend on testing setup, usually it is recommended to keep the first pulse in the order of tens of microseconds [168], [169].

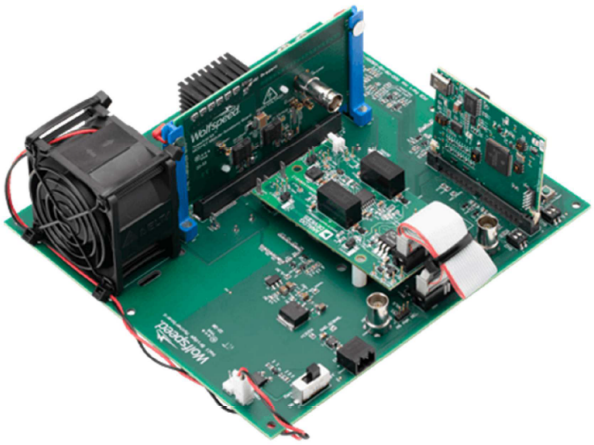
Experimental Testing Setup

The double pulse test has been implemented by using the Wolfspeed SpeedVal evaluation kit. MOD MBHB0900V40A motherboard has been used as a base. Testing has been performed on C3M0045065K SiC switches. A summary of the main characteristics of the C3M0045065K switch is provided in Table 4.2. 941PWRMMC3M0045065K power daughter card has been used, which contains two such

switches mounted on a heatsink. To drive the switch on the daughter card, the CGD1700HB2MUNA gate driver has been chosen. The motherboard and the daughter card can be seen in Fig. 4.17a and Fig. 4.17b respectively.

Table 4.2: Summary of the main characteristics of the C3M0045065K SiC switch [151].

Parameter	Symbol	Value
Maximum Drain-Source Voltage	V_{DS}	650 V
Operational Gate-Source Voltage	V_{GS}	-4/15 V
Maximum Continuous Drain Current $T_c = 25°C$	I_d^{25}	49 A
Maximum Continuous Drain Current $T_c = 175°C$	I_d^{175}	35 A
Typical on-resistance $T_j = 25°C$	$R_{\text{ds-on}}$	45 $m\Omega$
Turn-on Switching Energy	E_{on}	44 μJ
Turn-off Switching Energy	E_{off}	14 μJ
Diode Forward Voltage $T_j = 25°C$	V_{fwd}	4.8 V
Junction-Case Thermal Resistance	$R_{\theta JC}$	0.85$°C/W$
Junction-Ambient Thermal Resistance	$R_{\theta JC}$	40$°C/W$



(a) SpeedVal Kit HalfBridge Motherboard 900V 40A (941MODMBHB0900V40A) [169].



(b) Boards SpeedVal Kit HalfBridge Power Daughter Card 45mohm 650V TO2474 (941PWRMMC3M0045065K) [170]

Figure 4.17: Wolfspeed SpeedVal kit motherboard and daughter card.

An overview of the additional equipment for the testing setup has been provided in Table 4.3 and the implementation of the setup can be seen in Fig. 4.18.

Table 4.3: Overview of the supplementary equipment for the DPT and Boost converter measurements.

Device	Function
Keysight DC Power Supply N8950A	High-Voltage power supply
Aim TTi EL302RD dual power supply	12 V Power supply to power the evaluation board
Tektronix Waveform Generator AFG31251 (1 channel 250 MHz)	Generate pulses for the gate-driver
Tektronix MSO444-BW-1000 Mixed Signal Oscilloscope (1 GHz)	Display the output waveforms
Tektronix TEK-TIVP1 1 GHz galvanically isolated high impedance voltage probe	Measure the gate-source voltage
Tektronix TEK-TPP0850 High Voltage Probe	Measure the drain-source voltage
Tektronix TCP0150 Current Probe	Measure the drain current

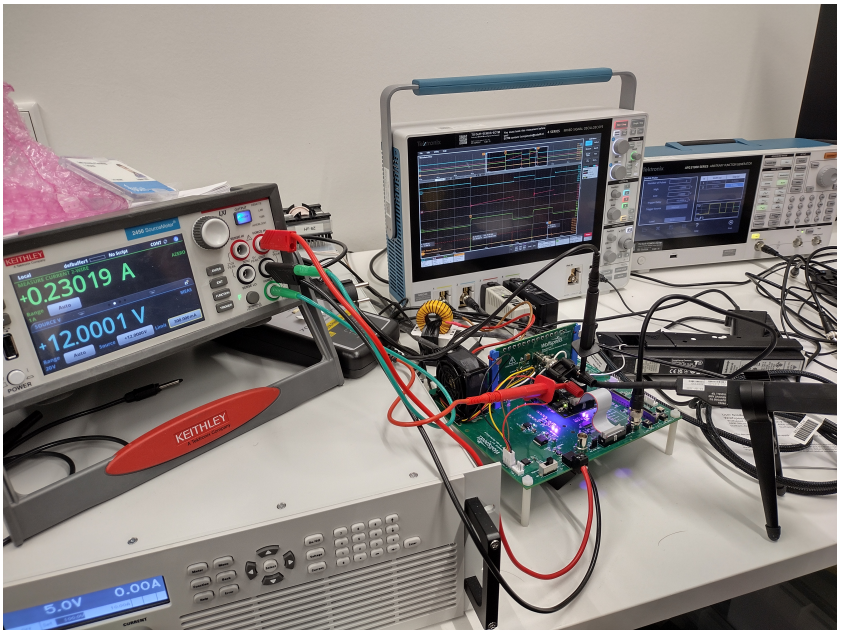


Figure 4.18: The experimental setup used to perform the DPT test.

The settings for the DPT were replicated to the datasheet such that a comparison with the expected values can be made. An overview of the testing conditions listed have been provided in Table 4.4. The steady-state junction temperature, drain voltage, drain-source current and gate-source voltages of the test match with the settings listed in the datasheet of the switch.

Table 4.4: Testing conditions for the experimental Double-Pulse Test.

Parameter	Symbol	Value
Junction Temperature	T_j	$25°C$
Drain voltage of the upper switch	V_{dd}	400 V
Drain-source current	I_{ds}	17.6 A
Gate-source voltage settings	V_{gs}	-4/+15 V
Load inductance	L	99 μH
Duration of the first pulse	t_{p1}	10.5 μs
Duration of the second pulse	t_{p2}	2 μs

The load inductor of 100 μH was used. The duration of the first pulse was selected to be 10.5 μs, while

the duration of the second pulse was 2 μs. The gap between pulses was set to 8 μs. The duration of the first pulse was fine-tuned such that a current of 17.6 A was achieved as listed by the datasheet. The results of the experimental test and a comparison with the simulations can be found in Chapter 5.

Deskewing and loss estimation

A notable aspect of DPT measurements is the deskewing procedure or proper alignment of the drain-source voltage and drain current waveforms used to calculate the switching losses. If not implemented properly, the measured turn-on and turn-off energies can lead to errors over 100% [169],[171]. Two possible post-processing methods of deskewing include the alignment of either the start of the V_{ds} drop with the start of the I_d rise or the alignment of the I_d maximum with the local maximum of the V_{ds} initial voltage drop across the parasitic stray inductances. The points of alignment are shown in Fig. 4.19.

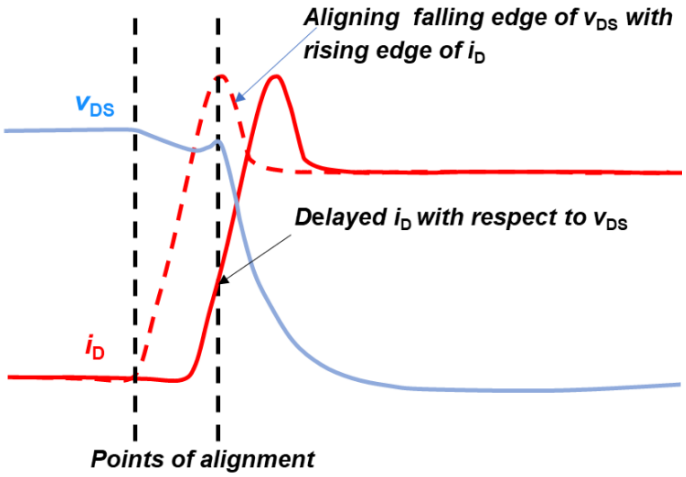


Figure 4.19: Points of alignment of V_{ds} and I_d waveforms during post-processing of the measurement data [168].

Alternatively, the load inductor can be replaced with a resistor and align the measurement waveforms before the measurement, since the resistor does not have a phase change [168], [169]. However, there can still be a parasitic inductance to the resistor, which can cause misalignment of the waveforms [168]. A more advanced option is proposed by Tektronix where the effects of the probe resistance, bias voltage of the on-voltage, and the effective loop inductance in the power loop are taken into account. The deskewing is performed automatically by the oscilloscope if the option is chosen [172]. Nevertheless, since the deskewing option has to be purchased as a separate license and is not available in the oscilloscope used for the measurements, the deskewing was performed by filtering the output waveforms and aligning the starting points of the voltage drop and the current rise.

As indicated in the Wolfspeed manual, the turn-off loss should be measured as the product of the current and voltage waveform by starting at the time instance when the drain-source voltage has reached 10% of its nominal voltage and ending when the current has reached 10% of its nominal value. Similarly, for the turn-on loss the dissipated power should be integrated between the time instance when the current has increased to 10% of its nominal value and the time instance when the voltage has dropped to 10% of its nominal value [169]. A visual overview taken from the Wolfspeed manual is provided in Fig. 4.20.

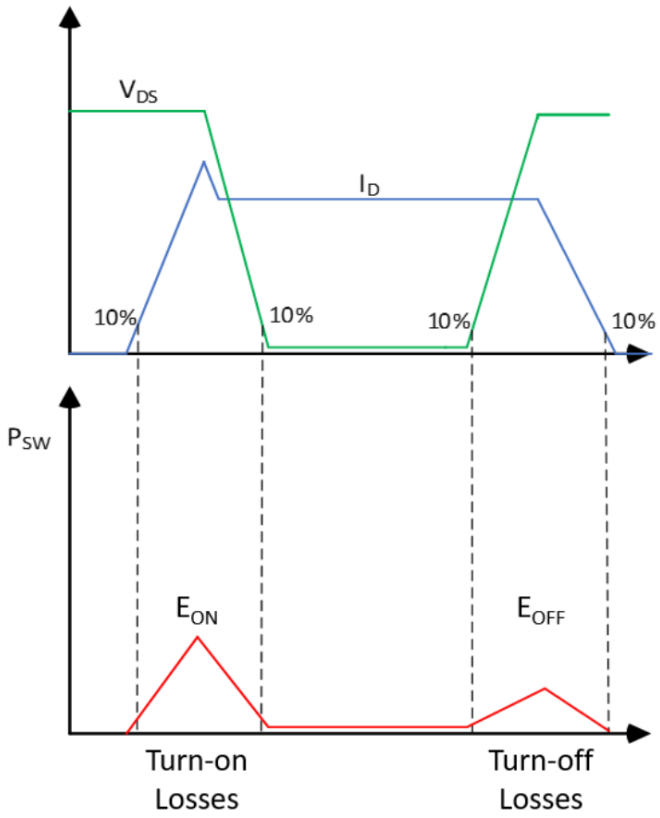


Figure 4.20: Visual overview on the settings for the determination of switching loss [169].

4.1.5 Experimental Implementation of junction temperature estimation during an operation of a boost converter

The objective of the experimental investigation of the switch degradation at different curtailment threshold voltages is to see whether a similar behaviour in the dependence of the switch degradation on the curtailment threshold can be found to the one shown in the study by Alpizar-Castillo et al. [102]. Since it is not possible to do (accelerated) power cycling tests due to the time constraints, the last two steps of rainflow-counting and Miner's rule as presented in the study will be done in the exact same manner. Therefore, the investigation is limited to determining the junction temperature of the semiconductor devices under a mission profile similar to that used in the study. The junction temperature profile is then used to determine the relative lifetime of the device for different curtailment thresholds.

For the implementation of the boost converter, the 941ACCBUCKBOST190UH Buck-Boost board has been used. The board is complementary to the SpeedVal Kit Motherboard and can be directly connected to it. The motherboard connected together with the Buck-Boost board can be seen in Fig. 4.21.

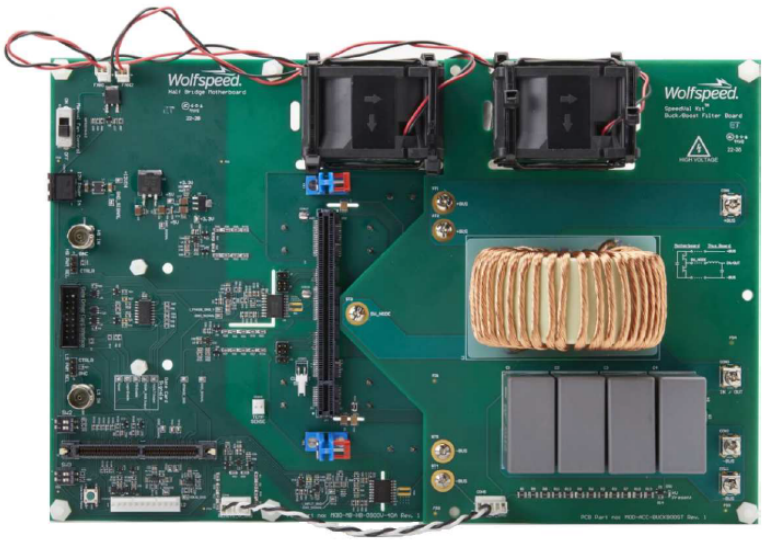


Figure 4.21: SpeedVal Kit Buck/Boost Accessory Board 190uH 40A connected to the SpeedVal Motherboard [173].

An electrical circuit diagram of the boost converter can be seen in Fig. 4.22. In the implementation of the setup the body-diode of the second SiC switch connected to the daughter card is used as the diode of the boost converter, similarly as the body-diode is used for the DPT.

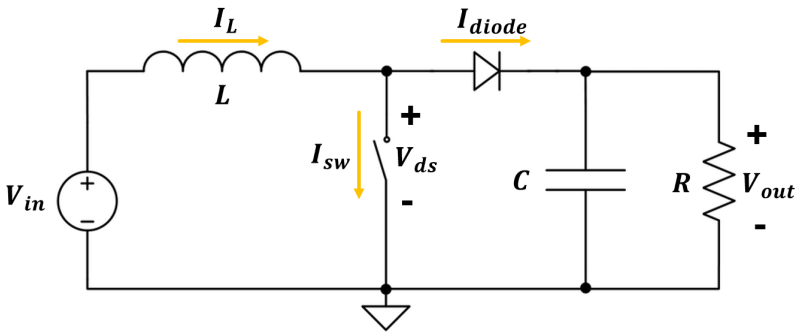


Figure 4.22: An electrical circuit diagram of a Boost converter.

The theoretical waveforms of the switch voltage V_{ds}, the switch current I_{switch}, and the diode current I_{diode} together with the control signal voltage V_{gs} have been provided in Fig. 4.23.

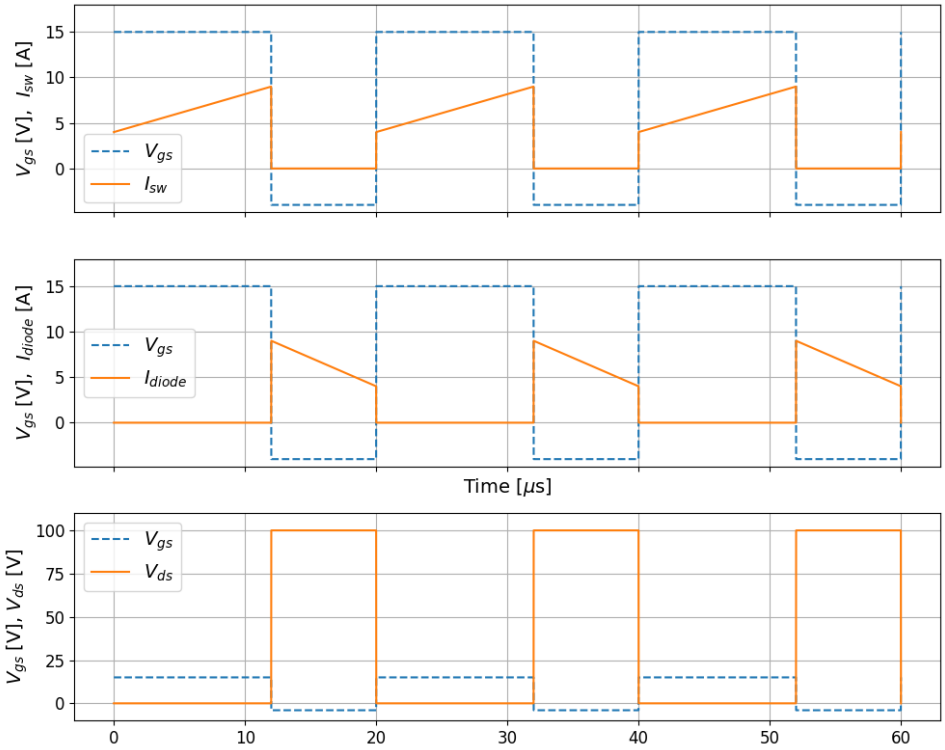
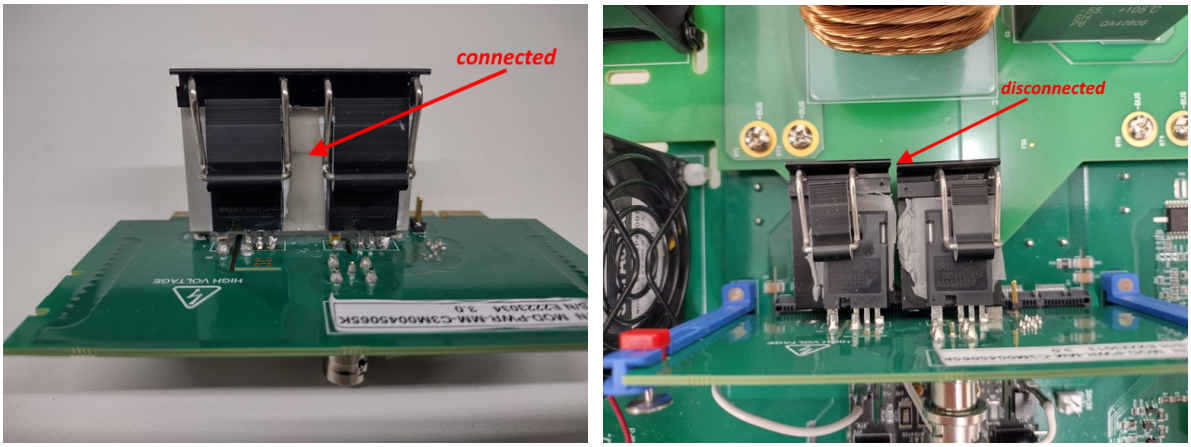


Figure 4.23: Example waveforms of the V_{gs}, V_{ds}, I_{sw} and I_{diode} for the boost converter.

The $R_{\text{ds-on}}$ measurements are made during the moments when the switch is turned on as the division between the corresponding voltage drop across the switch (in the range of 0.5-1V) and the corresponding current flowing through the switch.

During the design of the experiment, however, a crucial issue with the setup was discovered that would not allow one to acquire accurate junction temperature measurements if corrections were not made. As can be seen in Fig. 4.23 during the first part of the pulse, the current flows through the switch, while during the second part it flows through the diode. The problem lies in the design of the daughter card as shown in Fig. 4.24a, where it can be seen that both switches are connected to the same heatsink. This means that when the current flows through the body-diode of the second switch it heats up the heatsink and correspondingly the other switch even though it is in the off state. Therefore, the temperature of the switch increases both during the on and off operation.



(a) Original Wolfspeed daughter card - both switches connected to the same heatsink.

(b) Modified Wolfspeed daughter card - each switch connected to its own heatsink.

Figure 4.24: Original and modified configuration of the switches of the Wolfspeed daughter card.

To resolve the issue, the heatsink was replaced with two smaller heatsinks as shown in Fig. 4.24b so that each switch is heated separately. However, the body-diode of the SiC switch has a very large forward voltage (4.5 V), resulting in very large losses during conduction compared to the losses inside the switch. Hence, the reduction of the heatsink caused overheating of the second switch. To reduce the losses during the conduction of the diode, the second switch was replaced with a power diode: Infineon IDWD40G200C5. The power diode has a forward voltage drop of 1.5 V in addition to lower thermal impedance which means that it heats up less per every watt disipated [174]. The changes in the circuit resolved the issue and the measurements could be performed as planned.

The junction temperature lookup table has been generated in two steps. First, the boost converter was run at different input voltages and switch currents and the $R_{\text{ds-on}}$ values were extracted by measuring the drain-source voltage and drain current of the switch. Secondly, the curve relating $R_{\text{ds-on}}$ and junction temperature was used to correlate different switch currents with their corresponding junction temperatures. The curve found in the datasheet (Fig. 4.25) was used to correlate $R_{\text{ds-on}}$ and the junction temperature for the analysis of the final results.

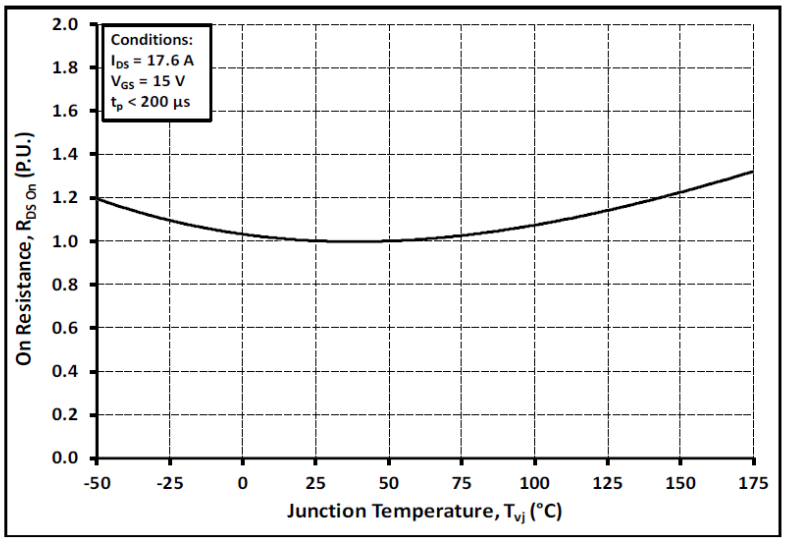


Figure 4.25: Junction temperature dependance on the on-resistance of the C3M0045065K switch [151].

The procedure for the $R_{\text{ds-on}}$ measurements at different settings is as follows:

1. Choose the input voltage and the corresponding duty cycle to reach 100 V at the output of the boost converter
2. Set a delay of 100 ms in the oscilloscope for the capture of the initial $R_{\text{ds-on}}$. A delay is set to avoid the initial transients after turning on the converter.
3. Turn on the boost converter
4. Save the V_{ds} and I_{ds} waveforms automatically captured by the oscilloscope
5. Wait 60 s for the switch to heat up
6. Manually stop and save the V_{ds} and I_{ds} waveforms containing a duration of 4 ms of data corresponding to 80 pulses
7. Let the converter cool till the temperature probe connected to the switch indicates that the room temperature has been reached (usually takes around two to three minutes)
8. Once the tests have been completed the $R_{\text{ds-on}}$ values for different settings can be calculated from the measured voltage and current waveforms. The average of the 80 measured pulses should be taken as the final value of $R_{\text{ds-on}}$.
9. The relative increase of $R_{\text{ds-on}}$ can be calculated by dividing the average $R_{\text{ds-on}}$ value of the measurement after 60 s by the measurement at the start of the test.

It must be emphasized that the relative $R_{\text{ds-on}}$ increase is not a comparison to an $R_{\text{ds-on}}$ value at a certain current set point. The curve shows how much the $R_{\text{ds-on}}$ changes after 60 seconds of sustained current at different currents set points. Therefore, if an RMS current of 13.5 A is set, then after 60 seconds $R_{\text{ds-on}}$ increases by 1.7% in comparison to the start of the measurement. However, the relative $R_{\text{ds-on}}$ value in comparison to a current of 5 A could be 5 to 10% higher, which is not what is plotted in the curve. The absolute value of $R_{\text{ds-on}}$ changes between different set points at the same temperature, as $R_{\text{ds-on}}$ has a slight current dependency. The datasheet of the C3M0045065K switches indicates that $R_{\text{ds-on}}$ increases by 5% between 10 and 20 A of applied current. Nevertheless, the designed test circumvents this dependency since only the increase of $R_{\text{ds-on}}$ over time is compared and not between different current set points. The measurements were repeated for input voltages of 25 V, 30 V, 35 V, 40 V, 50 V, and 60 V. As the input voltage increases, the maximum current that can be run through the switch decreases due to the decreasing duty cycle.

In summary, it has been shown how to both simulate and experimentally test the switch degradation curve presented in the study by Alpízar et al. It was shown that the simulation can be done by building a Cauer model in LTspice, which allows to simulate the junction temperature based on the dissipated power inside the switch of a boost converter. To ensure that the simulation aligns with the experimental setup, a double-pulse test is implemented to compare the simulated losses with the experimentally measured ones. A boost converter has been built to test different current settings, which are then used to make comparisons with the mission profile shown in the reference study. To determine the junction temperature of the switches inside the experimental boost converter, $R_{\text{ds-on}}$ is used as a temperature-sensitive electrical parameter indicating the junction temperature. Finally, a method has been proposed to determine the relative $R_{\text{ds-on}}$ change such that it is not influenced by any other factors than the heating of the switch. The extracted temperatures from the simulation and experimental setup can then be used as input for the Bayerer model and consequently the Miner's rule to determine the degradation at different control settings. If the experimental results show that switch degradation is indeed correlated to the microgrid dispatch decisions, then it motivates to include switch degradation model inside the dispatch and sizing optimization to explore its effects on the final solutions of the optimization problems.

There are two main scientific contributions presented in the methodology of this section:

- Experimental validation of the loss simulation through the DPT, which is often neglected in similar switch investigation studies. While DPT on its own is a very common method for estimating the switch losses
- Design of a method for extracting the $R_{\text{ds-on}}$ based on a time-based measurement of heating to exclude any other variables from influencing the result. Such an approach has not been observed by the author in the existing work. In addition, dynamic $R_{\text{ds-on}}$ measurements for the determination

of the junction temperature of converters are very rarely performed in general due to, for example, parasitics, which can easily prevent one from obtaining accurate $R_{\text{ds-on}}$ measurements. Usually, the switches are tested isolated from any other circuitry to minimize the external factors from influencing the measurements.

The next section provides a detailed explanation of how the proposed optimization algorithm is built, which includes both the battery and switch degradation models.

4.2 Optimization of Microgrid Sizing

Overview of this section can be found in Fig. 4.1. The first two subsections explain how the load and weather curves have been obtained, which are used as input for optimization. Next, the battery degradation models which have been used in the optimization have been explained followed by an overview of the optimization algorithm itself, and finally it is explained how the performance of the algorithm is evaluated.

4.2.1 Load Curve Generation

In this section, the process of obtaining the load profile is described. Fig. 4.26 shows the general flowchart of how the data acquired from the surveys is transformed into a load profile used as an input for the optimization.

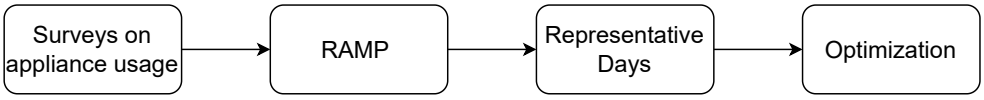


Figure 4.26: Overview of the load profile generation process.

First, RAMP model is used to produce a stochastic load profile of one year from the survey data on the planned appliance usage. To reduce the computation time clustering is used to create a set of representative days to reduce the profile of 365 days to a smaller number of days which still contain enough information about the load profile to be able to size the microgrid accurately. Therefore, this Subsection first explains the working principles of the RAMP model after which an overview of the approach used to acquire the representative days is provided.

RAMP: a Tool for the Generation of Stochastic Load Profiles

The optimization algorithm makes use of the RAMP model which was already briefly introduced in section 3.1. As previously mentioned, the model uses a layered approach. The layer structure is depicted in Fig. 4.27. The highest layer in the hierarchy is the User Type layer, which is usually used to define different high-level categories of users, for example, household, hospital, school, public lighting, etc. Each User type consists of Users, which represent the second layer in the hierarchical structure. Each User represents an instance of the specific user types. It is possible to simultaneously define a certain number of users of each type. Each User has been assigned with certain type of appliances. The behaviour of the appliances can again be defined independently of the User type. Hence, different User types can be characterized by Users who own certain types and certain number of specific appliances[61].

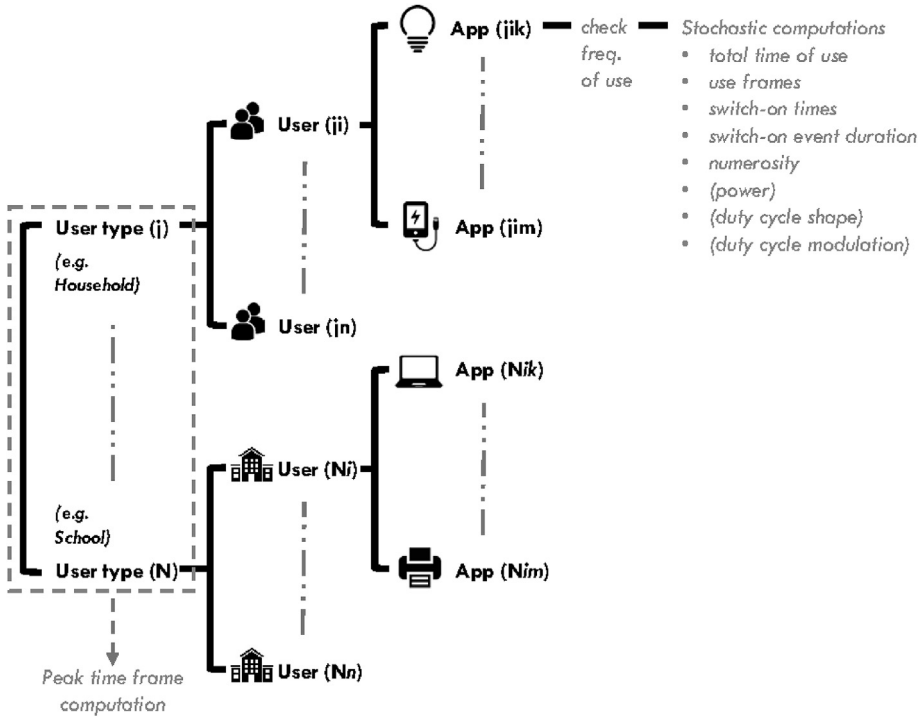


Figure 4.27: The layer structure of the RAMP model [61].

To further clarify the layer structure, the diagram in Fig. 4.28 has been created. It shows two User types: 2-room appartment and a 4-room house. The Users ”A_user X” and ”H_user X” show instances of the User types. Hence, each User represents another 2-room appartment or another 4-room house instead of being the actual ”users” or inhabitants of a single house. A specific User type is assigned with a certain portfolio of appliances. Therefore, to model a 3-room appartment a new User type has to be defined.

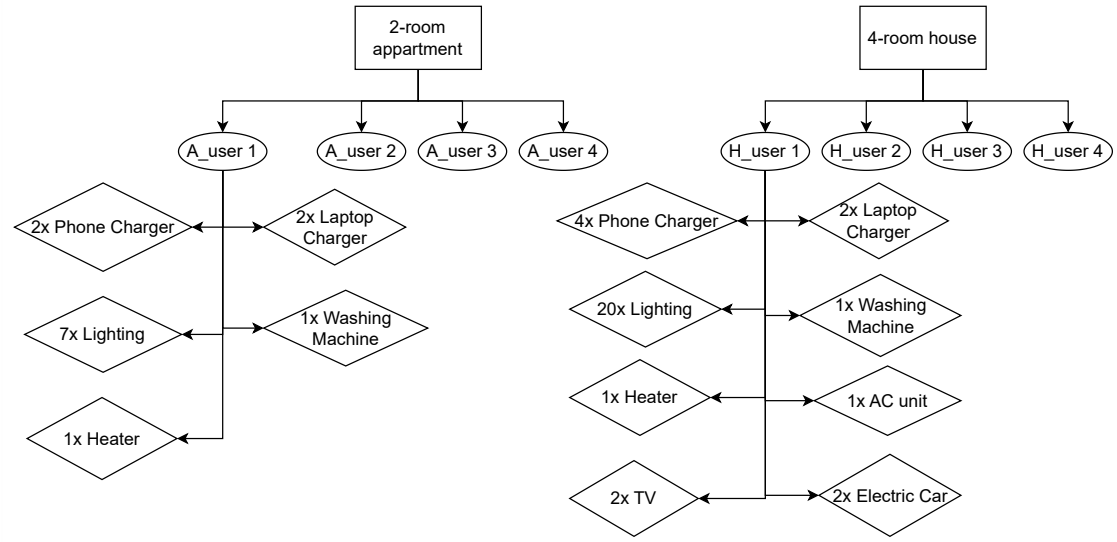


Figure 4.28: RAMP layer structure applied to an example.

Although the method assumes that all Users within a User type own the same types and numbers of appliances, which deviates from the reality, a User type is only meant to represent the average behavior.

If a higher accuracy is desired, more subcategories can be created. Nevertheless, the aim of the model is to generate an accumulative load curve instead of a detailed representation of each individual user.

Fig. 4.29 shows a visualization of the process of appliance schedule modeling within a 24-hour interval as modeled by Lombardi et al. in [61].

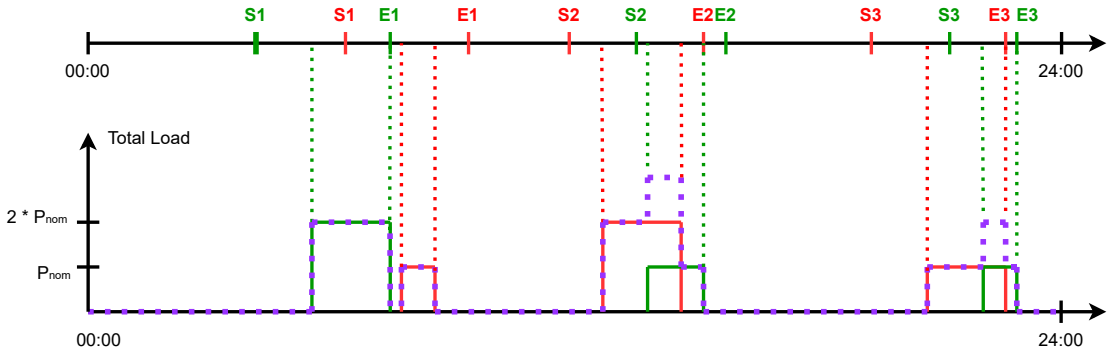


Figure 4.29: Visualization of the stochastic modeling of two random appliance turn-ons and turn-offs during 24-hour interval. The different appliances have been represented with green and red colours while purple indicates the accumulative load. ”S” and ”E” indicates start and end points of operation windows.

The figure shows an example of two random appliances with different possible windows of operation. The first appliance is represented with a green colour while the second appliance is drawn with red. The total load comprised of both appliances is coloured purple. In this example, both appliances have three possible windows of operation. The windows are usually chosen according to the user input from surveys. The starting points and the ending points of each operation window have been denoted with ”S” and ”E”, respectively. Hence, the first window for the appliance in green starts at the green ”S1” and ends at ”E1”. The same applies for the appliance in red and the other two windows of operation for both appliances. As can be seen in the figure, both appliances operate somewhere within the windows of operation. Both the exact starting time and the duration of operation are determined based on random distribution while having a specific minimum time operation for every appliance type.

In addition, it can be seen that appliances can operate at different power levels, which are determined on the basis of how many appliances of the same type operate at the corresponding moment. The number of appliances operating is also determined randomly. However, it is assumed that the appliances always operate at their nominal power, with some exceptions as in the case of fridges, whose operating power depends on the outside temperature and the amount of active use.

An aspect of the model that has not been portrayed in Fig. 4.29 is the selection of peak time frames and the randomization process. The model distinguishes between peak time frames and off-peak time frames as per [61]. The selection of the peak time frame follows the same approach as in the LoadProGen model explained in [64] where the peak time frame is the time window where the maximum power is found in an imaginary profile where all the appliances operate simultaneously at full power throughout their windows of operation. Peak time frames represent the time intervals during the day during which large amounts of electricity users tend to operate their appliances at the same time. For example, one such peak time frame often can be found in the early evening when the working population has come home and start cooking and using other home appliances.

The number of appliances per type and user is selected differently for off-peak and on-peak time frames. For off-peak time frames, the number of appliances is chosen according to a uniform distribution in range between zero and the maximum amount of appliances that can operate simultaneously. For on-peak time frames the number of appliances is chosen according to a Gaussian distribution centered around the mean of the the interval between zero and the maximum amount of appliances and the standard deviation reaching ends of the interval [61].

Therefore, the four main steps of the RAMP model can be summarized as follows:

1. Identify the peak time frame
2. Identify the operational windows of each appliance type for each user
3. Model random switch-on times with a random interval of operation
4. Calculate the total load profile

As mentioned, the description of the RAMP model is based on the paper by Lombardi et al. [61]. This section has covered the main working principles of the model, but some details have been left out, for example the modeling of refrigerators. Similarly, the model has evolved since the publication of the original paper and some implementation details have changed, nevertheless the general idea has stayed the same.

RAMP: Reintroduction of the Multi-Year Load Growth Feature

In this section, an additional feature to the RAMP model is introduced, whose development has been part of this thesis. As mentioned in Section 3.2, the article by Stevanato et al. [29] has shown the importance of considering time horizons in the range of the system lifetime. However, that requires a tool that allows to model the long-term changes in the electrical demand. A multi-year load growth option for the RAMP model was introduced to accommodate this possibility. However, the multi-year feature was not updated over the years with changes in the RAMP core code. Since long-term behaviour of the consumers is very important for microgrid sizing optimization it was decided to reintroduce the multi-year feature.

Fig. 4.30 gives a visual overview of the newly introduced multi-year feature.

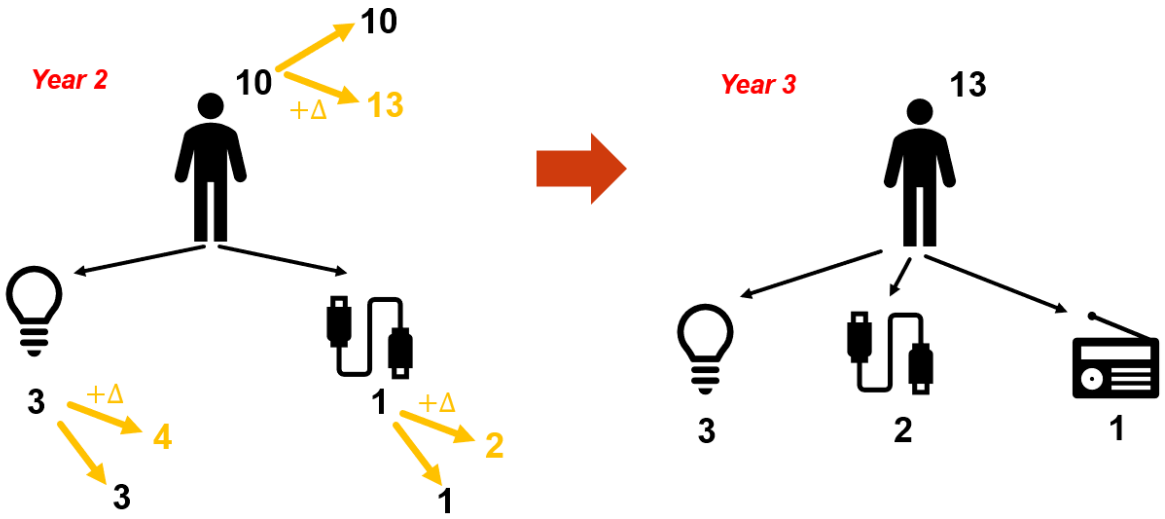


Figure 4.30: Visualization of the working principles of the RAMP multi-year feature.

The figure shows an evolution of appliances for an arbitrary user between two instances of time with respect to an arbitrary reference point, in this case year 2 and year 3. In year 2 the user owns two types of appliances that consume electricity - light bulbs and phone chargers. They have 3 light bulbs and one charger. In addition, there are 10 users of the same type who own the same types and numbers of appliances. In year 2, there is a possibility that both the number of users and the number of appliances will increase. The increase expressed as Δ is determined based on a uniform distribution with limits defined by the user of the model. However, there is a probability (for example 50%) that the number of users or the number of appliances will remain the same. An example of a resulting number of users and appliances can be seen on the right side of the figure. It can be seen that the number of users and the number of chargers increased while the number of lightbulbs remained the same. Upon

multiple runs of the same model, one would get different results as the increases are based on random distribution combined with an additional probability of successful increase. Finally, it can be seen that a new appliance has been added in year 4, namely, a radio. New appliances are added according to the input of the user of the RAMP model. They can be defined inside an Excel document according to a pre-defined format, and the table is imported inside the Python model. Table 4.5 shows an example of such a table.

Table 4.5: Example of a table that allows define new appliances to be added to specific user types.

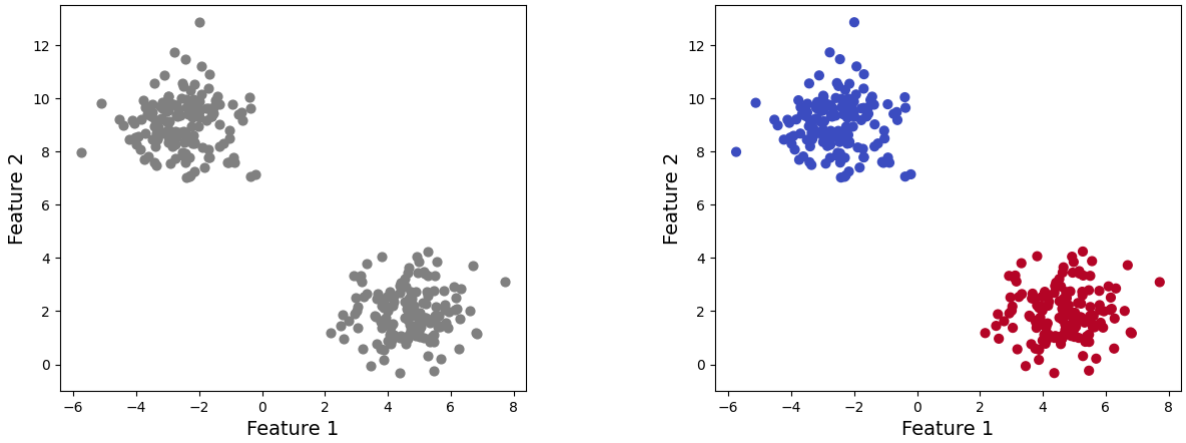
User type	Name of the appliance	Year the appliance to be added	Number of the newly introduced appliances
User Type 1	Radio	3	1
User Type 1	TV	5	1
User Type 2	Electric Toothbrush	2	2
User Type 2	Refrigerator 1	5	1
User Type 2	Refrigerator 2	7	1

Representative Days

One of the greatest bottlenecks for a nested optimization using metaheuristics is the computation time. One of the means to reduce it is the use of representative days. Representative days allow to extract the unique conditions that a system undergoes over an arbitrary time span. Often the time span to be used to extract the representative days is one year, since the system conditions tend to have a seasonal behavior. However, in the case of a changing consumer base, the time period could be extended.

As described in [175] by Pfenninger, there are three categories of methods to reduce the time resolution of a time series: heuristics, downsampling, and clustering. Heuristics involve choosing the representative days by hand. Usually, the extreme days are chosen to make sure that the system works under all conditions. The extreme days can be complemented with some more frequently encountered days. The second method of downsampling involves reducing the resolution of the time steps. For example, a resolution of 15 minutes can be reduced in hourly steps. The reduced resolution however can hide some dynamic behaviour of the system.

Finally, a more complex but often also more accurate method is clustering. Clustering is a type of unsupervised machine learning method that allows to simplify a dataset by assigning the data entries to smaller groups called clusters. Each cluster is represented by a centroid or the mean value of the data entries belonging to a certain cluster. Therefore, naturally, a certain data entry belongs to the cluster whose centroid is closest to [175]. The concept of clusters has been visualized in Fig. 4.31. First, Fig. 4.31a shows arbitrary data entries that have two dimensions. Second, Fig. 4.31b shows the classification into clusters.



(a) An example of an unclustered dataset.

(b) An example of a clustered dataset.

Figure 4.31: Visualization of the clustering process

Different types of clustering have been used in previous research to select representative days. Nahmacher et al. in [176] uses Ward's hierarchichal clustering to choose representative time slices that simultaneously account for both the electricity demand and variable renewable energy. Geraedts et al. in [177] makes use of the k-medoids approach to find the representative days for the demand in the context of optimization of fifth-generation heating networks. K-means clustering has been applied by Chen et al. in [178] to find representative days for optimization of a partially self-sufficient microgrid containing wind and solar power generation units.

Comparisons of the performance of different clustering methods for the selection of reperesentative days have been made in [179] and [180]. The first study compares heuristics, Ward's hierarchical clustering, random selection an optimization-based clustering, and a hybrid approach consisting of random selection combined with optimal weight selection. The second study makes performance comparison between k-means clustering, fuzzy c-means clustering, and Ward's hierarchical clustering. [179] uses Normalized Root Mean-Squared Error to compare the performance of different clustering methods while [180] uses Average Power Time Mismatch Index. The first study concludes that the optimization-based clustering performs the best with random selection giving surprisingly close results to Ward's hierarchical clustering. From the analyzed methods, the second study finds the k-means algorithm to be the most accurate. Nevertheless, both studies also show that the difference between different algorithms is often not significant, especially for a large number of representative days. An exception is optimization-based clustering, which performs better in all of the scenarios considered in [179], but optimization-based clustering is significantly harder to implement.

Hence, in the context of this thesis, Ward's hierarchical clustering is chosen because it provides a good balance between complexity and performance. Hierarchical clustering algorithms give the same assignment of clusters every time they are run, making the review process easier. They also make sure that the extreme data points are assigned to a cluster the last making it suitable for the application of representative day clustering [176]. A brief overview of the working principles of Ward's hierarchical clustering is provided in the remainder of this subsection.

Hierarchical clustering algorithms can be divided into two types - divisive hierarchical clustering and agglomerative hierarchical clustering. The difference between the two types is the initial assignment of clusters for the entire dataset. Divisive hierarchical clustering initializes all data points as part of the same cluster, while agglomerative clustering initially assigns all the data points to their own clusters [181]. For the visualization of the hierarchical clustering often a dendrogram such as the one in Fig. 4.32 is used.

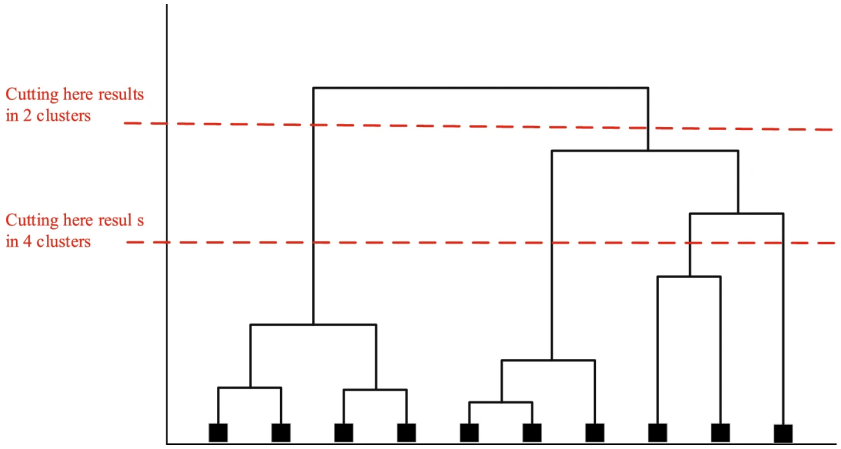


Figure 4.32: General dendrogram for hierarchical clustering [181].

The points at the very bottom level represent the data entries, and the horizontal lines above them show the clustering process. In case of divisive clustering, the process goes from top to bottom, while for agglomorative clustering it goes from bottom to top. At any point the clustering can be stopped, and a new horizontal line can be drawn (such as in red). The number of crossings with vertical black lines represents the number of clusters.

Ward's hierarchical clustering is a type of agglomerative clustering. Agglomerative clustering methods are further subdivided into many subtypes, but focus is only kept on the type of methods that Ward's method belongs to, which are the methods using distance-based similarity measured as classified by Ran et al. in [181]. This subset of methods uses the distance between the data points - depending on the particular method, it can be the shortest distance between two clusters, the longest distance, the average distance among others. In the case of Ward's linkage method, the Eucledean distance between the data points is used to determine the clusters.

Ward's hierarchical clustering can be described in four steps [182]:

1. Initialize the clusters - each data entry is assigned to its own cluster
2. For each combination of two cluster merge calculate the sum-of-squared-errors (SSE), which is based on the Eucledean distance.
3. Merge the two clusters with the smallest SSE
4. Repeat steps 2 and 3 till only one cluster is left

After completion of the four steps, the SSE for each number of clusters is acquired. There is a trade-off between the deviation from reality and the computational cost. The smaller the number of representative days, the faster the optimization will converge, yet the result will contain a higher error than the actually optimal result. There is no universal method that gives the optimal number of clusters, as each use case has different requirements for accuracy and computational cost.

A commonly used method to acquire the initial estimate is the elbow-based method, introduced by Thorndike in [183]. Fig. 4.33 shows the SSE depending on the number of clusters for the use case later introduced in Chapter 6.

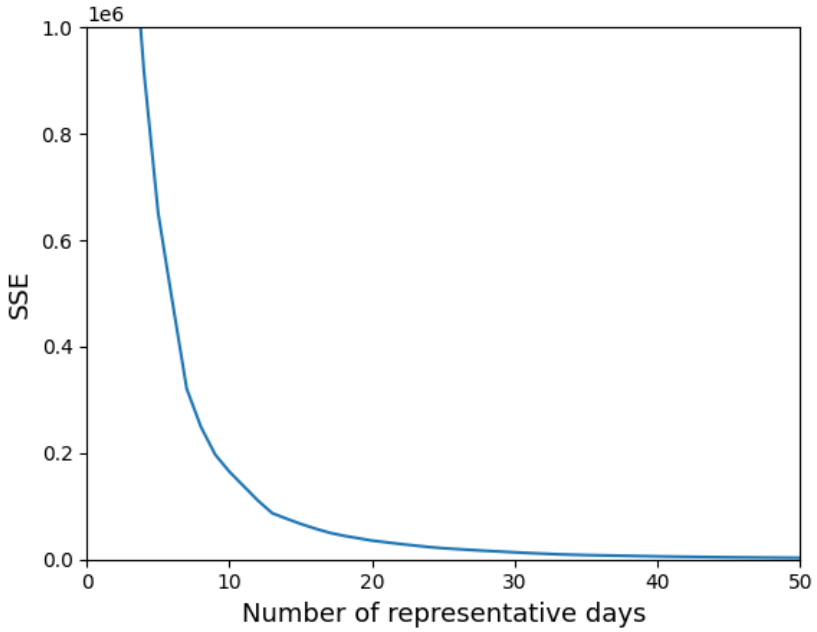


Figure 4.33: SSE as a function of representative days for the Samionta use-case.

It can be seen that around 15 days the curve reaches a knee after which the SSE continues decreasing significantly slower. The number of clusters around the elbow region provides a good compromise between accuracy and computational cost. In this thesis, it has been decided to value the accuracy higher than the computational cost, and hence 40 days has been chosen, which is a point after the elbow and provides an additional margin of safety. Having a buffer in the number of selected representative days also circumvents some of the criticisms expressed on the validity of the method, as, for example, shown in the paper by Erich Shubert in [184]. They show that different toy data sets and different noise data sets produce similar elbow-like plots when SSE is plotted against the number of clusters. However, it should be noted that they consider the k-means clustering and not hierarchical clustering. However, both types of clustering have the same challenge of choosing the right number of clusters. They present the problem of finding the ”elbow” rooted in the fact that the y-axis of the SSE has an entirely different scale than the x-axis of the number of clusters.

4.2.2 Weather Curve Generation

The temperature, irradiation and corresponding solar power generation curves have been extracted from Renewables.ninjaportal developed by Stefan Pfenninger and Iain Staffell [185]. The portal is based on the methods described in [186] and [187]. The weather data is based on NASA MERRA-2 and CM-SAF’s SARAH datasets. The data provided by Renewables.ninja has a resolution of one hour, and the portal allows to select any location on Earth.

Renewables.ninja has already been used as an input for weather curves in rural microgrid optimization problems in academic research. For example, Stevanato et al. in [29] used the portal to acquire data on natural resource availability as input to the MicrogridsPy-MYCE model. Another example is the paper by Rousis et al. [101] where an AC/DC microgrid sizing optimization was performed by using a genetic algorithm.

4.2.3 Battery Degradation Models

The work of this thesis considers two battery degradation models - an energy throughput model and a semi-empirical degradation model.

Energy Throughput Model

The modeling of the energy throughput model is done as described in Section 3.4. For ease of access, equations (3.3) and (3.4) are repeated here, where the energy flowing through the battery is calculated as:

$$E_{\text{th}}(d_t) = \sum_{d=1}^{d_t} \sum_{h=1}^{24} (p_{\text{dis}}(d,h) + p_{\text{ch}}(d,h)), \tag{4.8}$$

and the corresponding battery capacity degradation is calculated as:

$$Q_{\text{bss,deg}}(d_t) = Q_{\text{bss}} - k_{\text{deg}} E_{\text{th}}(d_t), \tag{4.9}$$

In this case a linear energy throughput model is considered, hence, k_{deg} is calculated as $\frac{1}{E_{\text{total}}}$, where E_{total} is the total energy available throughout the lifetime of the battery. E_{total} is calculated as the area of a trapezoid where the x-axis denotes the full equivalent cycles (FEC) and the y-axis denotes the battery capacity. The capacity is updated every full cycle. Hence, the lifetime energy can be calculated as:

$$E_{\text{total}} = Q_{\text{end}} \cdot N_{\text{life}} + 0.5 \cdot (Q_{\text{new}} - Q_{\text{end}}) \cdot N_{\text{life}} \tag{4.10}$$

where Q_{end} is equal to $Q_{\text{end}} = 0.8 \cdot Q_{\text{new}}$. The concept has been visualized in Fig. 4.34.

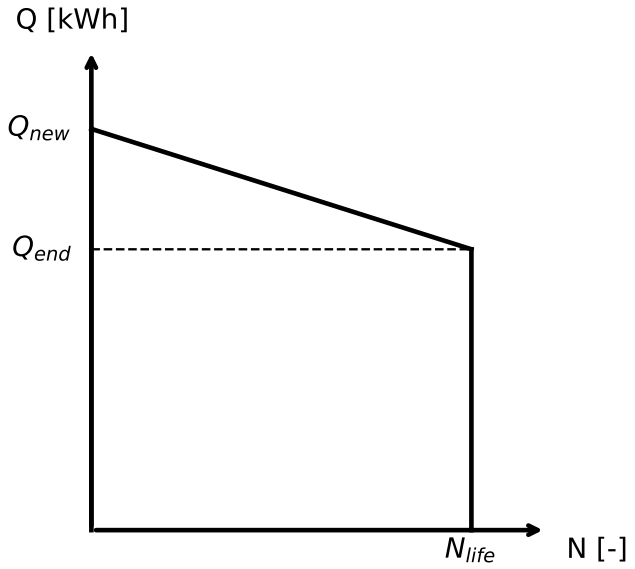


Figure 4.34: Energy throughput calculation for a simple degradation model.

Semi-empirical Model

In the case of the semi-empirical battery degradation model, the model derived by Schimpe et al. in [188] has been used. The capacity degradation in the model is described by four components:

- Calendar degradation
- Cyclic degradation at high temperatures

- Cyclic degradation at low temperature
- Cyclic degradation at low temperatures and high SOC

In the model, the border between low and high temperatures is drawn at 25 °C, while high SOC is denoted to start at the point when constant voltage charging mode starts. Battery charging typically consists of two stages - constant-current (CC) charging and constant-voltage (CCCV) charging. As the name suggests, during the constant current charging, the charging current to the battery is constant while the voltage slowly increases. When a specific threshold voltage is reached, it is advised to switch to constant-voltage charging during which the voltage is kept constant, and the magnitude of the current decreases as the SOC of the battery increases. The two charging stages are depicted in Fig. 4.35.

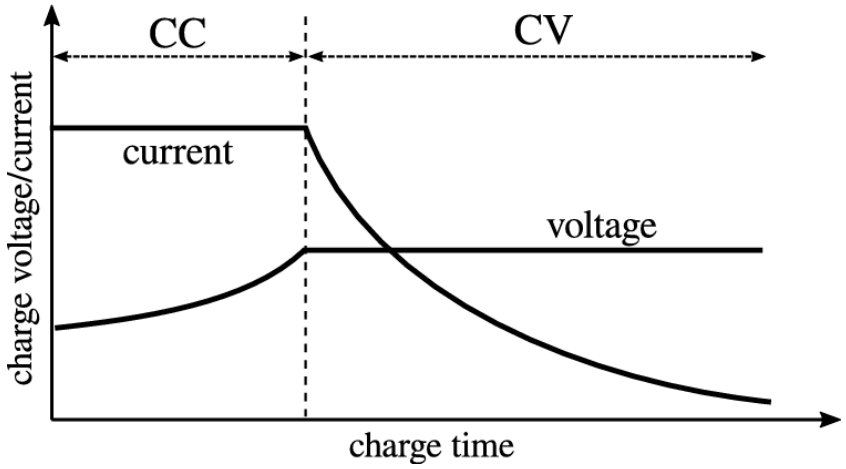


Figure 4.35: CC and CV charging stages of a battery [189].

Mathematically, the model is described as follows:

$$\begin{aligned} Q_{\text{Loss}}\,(T, SOC, I_{\text{Ch}}, Q_{\text{Tot}}, Q_{\text{Ch}}, t) = \\ = Q_{\text{L,Cal}}(T, SOC, t) + Q_{\text{L,Cyc,High T}}\,(T, Q_{\text{Tot}}) \\ + Q_{\text{L,Cyc,Low T}}\;(T, I_{\text{Ch}}, Q_{\text{Ch}}) \\ + Q_{\text{L,Cyc, Low T High SoC}}\;(T, I_{\text{Ch}}, SOC, Q_{\text{Ch}}) \end{aligned} \tag{4.11}$$

It is assumed that the battery is cycled between 20% and 85%. The reference SOC for the start of the CV stage in the model has been set as 82% [188].Therefore, to simplify the model, the high SOC component is emitted. It would increase both the computational cost and the complexity of the algorithm, while providing a marginal increase in accuracy. Therefore, the degradation equation is simplified to:

$$Q_{\text{Loss}}\,(T, SOC, I_{\text{Ch}}, Q_{\text{Ch}}, t) = Q_{\text{L,Cal}}(T, SOC, t) + Q_{\text{L,Cyc,Low T}}\;(T, I_{\text{Ch}}, Q_{\text{Ch}}) + Q_{\text{L,Cyc,High T}}\,(T, Q_{\text{Tot}}) \tag{4.12}$$

The calendar aging of the battery Q_{cal} has been derived to have a square root dependence with time.

$$Q_{\text{L,cal}}(T, SOC, t) = k_{\text{cal}}(T, SOC)\sqrt{t} \tag{4.13}$$

The stress factor k_{cal} is a function of the temperature and idling SOC and is expressed as:

$$k_{\text{cal}}(T, SOC) = k_{\text{cal,ref}} f(T) f(SOC), \tag{4.14}$$

where $k_{\text{cal,ref}}$ is the calendar reference stress factor modeled for $T = 25°C$ and $SOC = 50\%$. In the study by Schimpe et al. , the value of $k_{cal,ref}$ has been found to be equal to $3.694 \cdot 10^{-4}\ h^{-0.5}$ This notation shows that the effects of the temperature and idling SOC can be modeled as independent from each other. Temperature dependence has been modeled by using the Arhenius equation:

$$k_{\text{cal}}(T, SOC = 50\%) = k_{\text{cal,ref}} \cdot e^{\frac{-E_{\text{a,cal}}}{R_g}\left(\frac{1}{T} - \frac{1}{T_{\text{Ref}}}\right)}, \tag{4.15}$$

where R_g is the universal gas constant equal to $R_g = 8.314\ J/(mol \cdot K)$, reference temperature is equal to $T_{\text{Ref}} = 298.15\ K$ and the parameter activation energy is equal to $E_{\text{a,cal}} = 20592\ J/mol$ [188].

The dependence on the SOC is based on the Tafel equation, and the final expression for the SOC stress factor is:

$$k_{\text{cal}}(T = 298.15, SOC) = k_{\text{cal,ref}} \cdot \exp\left(\frac{\alpha F}{R_g}\left(\frac{U_{\text{a,ref}} - U_a(SOC)}{T_{\text{ref}}}\right)\right) + k_0, \tag{4.16}$$

where $U_{\text{a,ref}}$ is the anode reference potential set to $U_{\text{a,ref}} = 0.123\ V$ for an $SOC = 50\%$, F is the Faraday constant equal to $F = 96485\ C/mol$ and α and k_0 are parameters resulting from the fitting of the equation done by Safari et al. in [190], where $\alpha = 0.384$ and $k_0 = 0.142$.

Hence, the final expression for the calendar aging stress factor can be written as the combination of both stress factors:

$$k_{\text{cal}}(T, SOC) = k_{\text{cal,ref}} \cdot \exp\left(\frac{-E_{\text{a,cal}}}{R_g}\left(\frac{1}{T} - \frac{1}{T_{\text{ref}}}\right)\right) \cdot \left(\exp\left(\frac{\alpha F}{R_g} \cdot \frac{U_{\text{a,ref}} - U_a(SOC)}{T_{\text{ref}}}\right)\right) \tag{4.17}$$

The general expression of the cyclic loss at low temperatures has been denoted in [188] as:

$$Q_{\text{L,cyc,low T}}(T, I_{\text{ch}}, Q_{\text{ch}}) = k_{\text{cyc,low T}}(T, I_{\text{ch}})\sqrt{Q_{\text{ch}}}, \tag{4.18}$$

where the reference stress factor $k_{\text{cyc,low T}}$ is equal to $k_{\text{cyc,low T}} = 4.009 \cdot 10^{-4}\ Ah^{-0.5}$ and I_{ch} and Q_{ch} refer only to the part of the cycle where the battery is being charged.

Similarly as with calendar aging, the dependence on temperature and charging current is decomposed into two separate stress factors [188]:

$$k_{\text{cyc,low T}}(T, I_{\text{ch}}) = k_{\text{cal,ref}} f(T) f(I_{\text{ch}}), \tag{4.19}$$

The dependence on the temperature is once again expressed by using the Arhenius equation resulting in:

$$k_{\text{cyc, low T}}(T, I_{\text{ch}} = 1C) = k_{\text{cal,ref}} \cdot \exp\left(\frac{-E_{\text{a,cal}}}{R_g}\left(\frac{1}{T} - \frac{1}{T_{\text{Ref}}}\right)\right), \tag{4.20}$$

The dependence on the charging current has been modeled through an exponential relationship:

$$k_{\text{cyc,low T}}(T, I_{\text{ch}}) = k_{\text{cyc, low T, ref}} \cdot \exp\left(\beta_{\text{low T}} \frac{I_{\text{ch}} - I_{\text{ch, ref}}}{C_0}\right), \tag{4.21}$$

where C_0 is the nominal cell capacity of 3 Ah and the reference charging current is equal to $I_{\text{ch}} = 3\ A$. The fitting parameter $\beta_{\text{low T}}$ is equal to $\beta_{\text{low T}} = 2.64\ h$.

Therefore, the cyclic stress factor $k_{\text{cyc, low T}}(T, I_{\text{ch}})$ can be expressed as:

$$k_{\text{cyc, low T}}(T, I_{\text{ch}}) = k_{\text{cyc,low T, ref}} \cdot \exp\left(\frac{E_{\text{a,cyc,low}}}{R_g}\left(\frac{1}{T} - \frac{1}{T_{\text{Ref}}}\right)\right) \cdot \exp\left(\beta_{\text{low T}} \frac{I_{\text{ch}} - I_{\text{ch, ref}}}{C_0}\right) \tag{4.22}$$

The cyclic stress factor for high temperatures has a similar form as the one for low temperatures except for the dependence on the cycling current, which there is no direct dependence on at high temperatures. The final expression for $k_{\text{cyc,highT}}$ is:

$$k_{\text{high, low T}}(T) = k_{\text{cyc,high T, ref}} \cdot \exp\left(\frac{-E_{\text{a,cyc,high}}}{R_g}\left(\frac{1}{T} - \frac{1}{T_{\text{Ref}}}\right)\right) \tag{4.23}$$

where $k_{\text{cyc,high T, ref}} = 1.456 \cdot 10^{-4}\ Ah^{-0.5}$ and $E_{\text{a,cyc,high}} = 32699\ J/mol$

4.2.4 Proposed Optimization Algorithm

This section provides an overview of the proposed microgrid sizing optimization algorithm. First, the motivation for the chosen optimization approach is provided. It is followed by a detailed explanation of the two nested optimization stages. Finally, a discussion on the choices made to reduce computational speed is provided.

The choice of the optimization approach

As explained in Section 3.2, there is no clear best option when it comes to choosing the optimization algorithm, as each choice brings its own advantages and disadvantages. Therefore, the choice was made for the option that best fits the user and was easiest to implement without sacrificing performance.

The aim of the thesis is to produce an algorithm that can be used by anyone with open-source software. Since to run mathematical optimization algorithms such as LP or MILP one needs to use an external solver, the choice was made for the use of metaheuristics. In principle it is possible to use open source solvers, however, as mentioned by the developers of MicroGridsPy, the difference in performance between a commercial solver such as Gurobi and an open source solver, for example, GLPK, can be between several times to the orders of magnitude [89].

With the choice of metaheuristics, there are still many options available as shown in Section 3.2. Given that the author of the thesis did not have prior experience in implementing metaheuristic algorithm, a choice was made for algorithms that were extensively covered in literature and actively used for specifically microgrid sizing and EMS optimization. The two optimization approaches that stand out are genetic algorithms and particle swarm optimization. Both approaches have been used in large amount of research papers for rural microgrid optimization as was shown in Table 3.2. The final decision was made for the use of PSO due to the simpler implementation. However, GA would have been just as reasonable a choice.

Working principles of PSO

Originally introduced by Kennedy and Eberhart, particle swarm optimization is inspired by the behaviour of bird flocks. Each bird performs a search taking into account not only the area that they have explored on their own but also communicates with the other birds about the conditions of other areas. In such a way, bird flocks manage to effectively look for food, find a location for rest, and reform a flock after a disturbance [82]. Even though the paper refers to previously made models with a similar goal of recreating the behaviour of flocks, it presents the classical formulation of PSO that is still used novadays in different fields of research. Improvements in the algorithm have been made since then, but most of them are still based on the original model introduced by Kennedy and Eberhart.

In this paper, a modified version of the original PSO formulation created by Shi and Eberhart in [191] is used. The general concept of the PSO consists of a swarm of particles (a flock of birds), which represent the decision variables of the optimization problem. Each particle is attributed with a position and a velocity. The position changes over time as

$$x_{t+1} = x_t + v_{t+1} \tag{4.24}$$

where v_t is the velocity and changes over time according to:

$$v_{t+1} = w \cdot v_t + c_1 \cdot r_1 \cdot (p_{\text{best}} - x_t) + c_2 \cdot r_2 \cdot (g_{\text{best}} - x_t), \tag{4.25}$$

where w is the inertia of the particle, c_1 and c_2 are the cognitive and social coefficients, r_1 and r_2 are randomly generated numbers in the range between 0 and 1, p_{best} is the best position of the specific particle and g_{best} is the best position between all the particles in the swarm. p_{best} and g_{best} are updated every time step according to (4.26) in which $f(x)$ is the cost function of the optimization that is being

minimized.

$$
\begin{aligned}
&\textbf{if } f(x_t) < f(g_{\text{best}}) \textbf{ then} \\
&\quad g_{\text{best}} = x_t \\
&\quad p_{\text{best}} = x_t \\
&\textbf{else if } f(x_t) < f(p_{\text{best}}) \textbf{ then} \\
&\quad g_{\text{best}} = g_{\text{best}} \\
&\quad p_{\text{best}} = x_t \\
&\textbf{else} \\
&\quad g_{\text{best}} = g_{\text{best}} \\
&\quad p_{\text{best}} = p_{\text{best}}
\end{aligned}
\tag{4.26}
$$

The $w \cdot v_t$ term in (4.25) determines to what extent will the same velocity be maintained in the subsequent time moment. The term $c_1 \cdot r_1 \cdot (p_{\text{best}} - x_t)$ determines to what extent the performance of the particle itself will influence its velocity in the next time step. Finally, the term $c_2 \cdot r_2 \cdot (g_{\text{best}} - x_t)$ determines to what extent the performance of the entire swarm influences the velocity of the particle. By correctly choosing the coefficients c_1 and c_2 it is possible to reach a situation where the particles balance between exploration and exploitation - exploring the solution space sufficiently while converging as fast as possible.

Typically, two types of stopping criteria are used to determine when to halt the optimization - the maximum number of iterations and the number of iterations without improvement [192]. The criteria can be used separately or together to determine when the optimization should end.

Fig. 4.36 shows a visualization of a PSO in two dimensions.

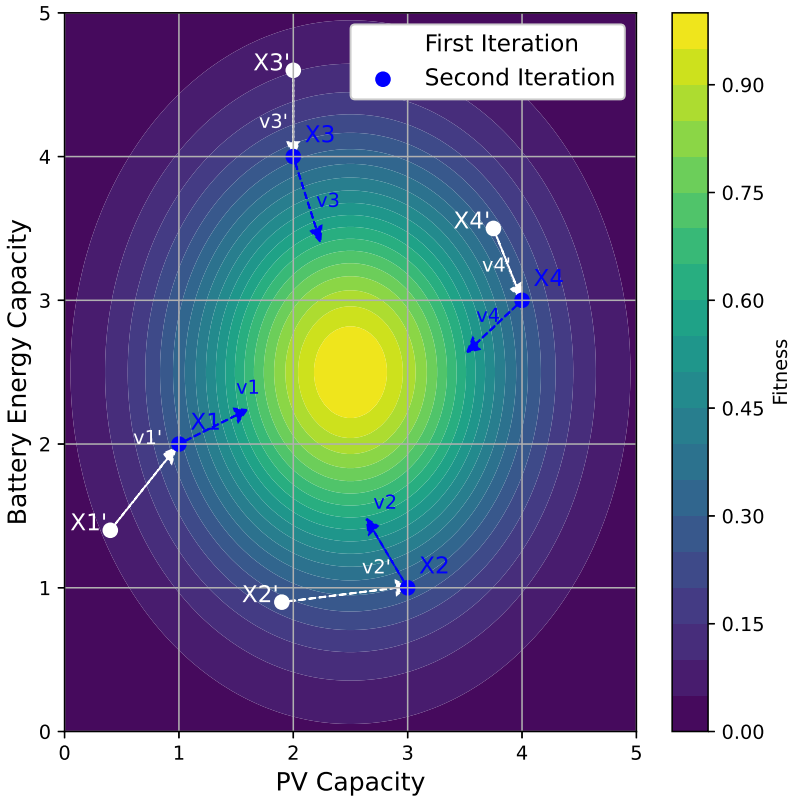


Figure 4.36: Visualization of the particle swarm consisting of four particles. The positions and velocities of the first iteration are in white while the ones of the second iteration are in blue.

On the horizontal and vertical axes, the decision variables are denoted. In the context of microgrid sizing optimization, the x axis is the PV array capacity, while the y axis represents the battery energy capacity. The particles have been denoted with their velocity vectors as arrows. At each position, the fitness function is evaluated. With each iteration, the position of the particle changes depending on the velocity of the previous iteration, while the velocity itself changes depending on the cost function evaluations of all the particles. It can be seen how the particles gradually go closer to the global optimum in yellow (the figure portrays a maximization problem, but the same can be implemented with minimization). In the figure a fitness function with a single global optimum in the center has been shown, however, fitness functions can often have several global optimums and local optimums making the search process significantly more complex.

Structure of the Algorithm

The general form of the nested PSO sizing optimization is similar to some that can be found in the literature, for example [114] or [118]. Nevertheless, the exact details on how these algorithms are implemented in code are rarely revealed (at least in the context of rural microgrid optimization). The proposed nested sizing / EMS PSO algorithm is shown in Fig. 4.37.

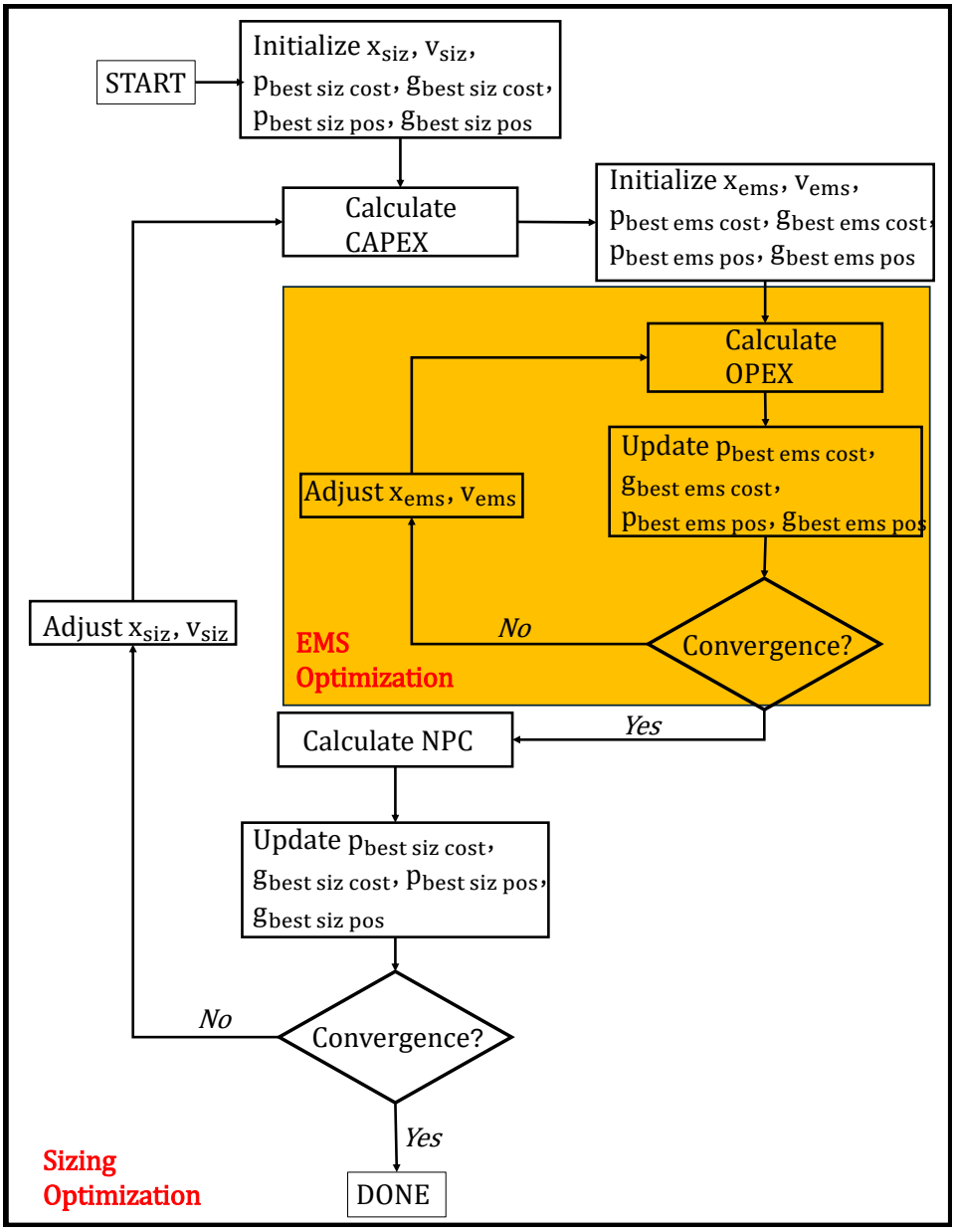


Figure 4.37: Overview of the nested sizing/EMS PSO algorithm.

The flowchart shows the general microgrid sizing optimization within which another PSO is performed to do the optimization of the EMS. The algorithm starts with a similar situation as has been denoted in Fig. 4.36 with two-dimensional particles, where the first dimension is the capacity of the solar panel array and the second dimension is the energy capacity of the battery. The particles are initialized in a grid pattern, meaning that the initial positions of the particles inside the swarm are evenly spread across the solutions space. The vector of particles in the sizing PSO have the following format:

$$x_{\text{siz}} = \begin{bmatrix} x_{\text{siz,p1}} \\ x_{\text{siz,p2}} \\ \dots \\ x_{\text{siz,pN}} \end{bmatrix}, \tag{4.27}$$

with N being the number of particles. Each particle has a vector form of:

$$x_{\text{siz,pn}} = \begin{bmatrix} x_{\text{n,pv}} \\ x_{\text{n,batt}} \end{bmatrix}. \tag{4.28}$$

The velocity array of the particles has the same form as the position array in (4.27) and the velocity vector of each particle is the same as the one for the position in (4.28).

After the initialization of the particles, the CAPEX for each particles is calculated. CAPEX in this optimization problem contains the cost of the solar panel array and the battery. Therefore, CAPEX is calculated as:

$$CAPEX = x_{\text{siz, pv}} \cdot c_{\text{pv, kWp}} + x_{\text{siz, batt}} \cdot c_{\text{batt, kWh}}, \tag{4.29}$$

where $x_{\text{siz,pv}}$ is a vector that contains the capacities of the solar panel array of each particle while $x_{\text{siz,batt}}$ contains the capacities of the battery for each particle. $c_{\text{pv,kWp}}$ and $c_{\text{batt,kWh}}$ are the costs of the solar panel array per kilowatt peak (kWp) and the battery per kWh respectively.

For each particle within the sizing optimization another PSO is performed to calculate the dispatch and correspondingly the OPEX. There is a difference, however, in the setup of the PSO done to find the optimum dispatch. The arrays containing the positions and velocities of the EMS particles have 72 dimensions, since each particle contains 24 time steps for three components being dispatched - solar power, battery storage, and generator power. The EMS position vector can therefore be expressed as:

$$x_{\text{ems}} = \begin{bmatrix} x_{\text{ems,p1}} \\ x_{\text{ems,p2}} \\ \dots \\ x_{\text{ems,pM}} \end{bmatrix}, \tag{4.30}$$

where M denotes the number of particles in the EMS optimization swarm.

Each EMS particle has the following form:

$$x_{\text{ems,pm}} = \begin{bmatrix} x_{\text{m,t1-pv}} & x_{\text{m,t1-batt}} & x_{\text{m,t1-gen}} \\ x_{\text{m,t2-pv}} & x_{\text{m,t2-batt}} & x_{\text{m,t2-gen}} \\ \dots & \dots & \dots \\ x_{\text{m,t24-pv}} & x_{\text{m,t24-batt}} & x_{\text{m,t24-gen}} \end{bmatrix}. \tag{4.31}$$

The velocity array for the EMS swarm has the same format as the position array.

The first step after the initialization of the EMS swarm is the calculation of the OPEX for each particle. The OPEX consists of five terms and is calculated as:

$$OPEX = c_{\text{fuel}} + c_{\text{degr,batt}} + c_{\text{degr,sw}} + c_{\text{pen,pb}} + c_{\text{pen,soc}}\ , \tag{4.32}$$

where c_{fuel} is the fuel cost, $c_{\text{degr, batt}}$ and $c_{\text{degr, sw}}$ are the degradation costs of the battery and the switch, respectively, and finally $c_{\text{pen, pb}}$ and $c_{\text{pen,soc}}$ are the penalties for deviating from the power balance and the SOC limits. Fuel cost is calculated as:

$$c_{\text{fuel}} = \left(\sum_{t=1}^{24} x_{\text{t-gen}} c_{\text{gen}}(x_{\text{t-gen}}) \right), \tag{4.33}$$

where $x_{\text{t-gen}}$ corresponds to dispatched generator power at each hour and $c_{\text{gen}}(x_{\text{t-gen}})$ is the cost of the dispatched energy, which depends on the dispatched power. The dependency is present due to the fact that the generator has a significantly higher efficiency when it operates at full power than when operating at partial power. An example of a fuel efficiency curve can has been shown in Fig. 4.38.

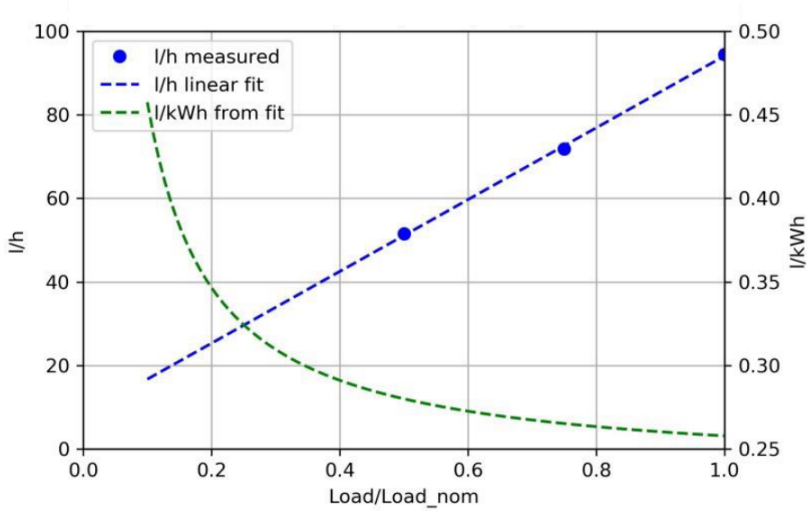


Figure 4.38: Example diesel consumption of a diesel generator [193]

The example curve depicting the fuel consumption per kWh depending on the loading level has been normalized and scaled corresponding to the chosen generator size. The cost per kWh is then interpolated from a curve fit of the cost curve.

The degradation of the battery is calculated as described in Section 4.2. In the case of the energy-throughput degradation model, the degradation cost per day is calculated as follows:

$$c_{\text{degr,batt}} = \Delta SOH \cdot c_{\text{batt}}, \tag{4.34}$$

where ΔSOH is the absolute decrease in SOH in the battery calculated as:

$$\begin{aligned} \Delta SOH &= \Delta E_{\text{rel}} \cdot SOH_{\text{useable}} \\ \Delta E_{\text{reg}} &= \frac{\Delta E}{E_{\text{total}}}, \end{aligned} \tag{4.35}$$

where SOH_{useable} is the useable SOH expressed as the difference between the SOH at the start and end of the battery lifetime and ΔE_{reg} is the relative energy throughput to the lifetime energy. The calculation of E_{total} can be found in (4.10). c_{batt} can be calculated as :

$$c_{\text{batt}} = x_{\text{siz,batt}} \cdot c_{\text{batt,kWh}}, \tag{4.36}$$

where $c_{\text{batt,kWh}}$ is the battery price per kWh.

In the case of a semi-empirical battery degradation model the degradation cost calculation is more involved. An approach literature suggests for the semi-empirical battery degradation models expresses the degradation cost based on the degradation rate as:

$$\begin{aligned} Degr.\ rate &= \frac{SOH_{\text{useable}}}{RUL_t} \\ Degr.\ cost &= \sum_{t=1}^{24} c_{\text{batt}} \end{aligned} \tag{4.37}$$

where RUL_t is the remaining useful lifetime determined by using the specific battery degradation model [194]. The implication of this model is that the degradation cost increases over the lifetime of the battery, which discourages the use of the battery later in the system lifetime. This was deemed undesired for the application of rural microgrids, and hence an alternative approach is proposed.

After the calculation of the calendar and cycling capacity loss of the battery, a projection is made for the battery degradation for the next ten years if the battery was used in the same manner. A derivative

of the projection is made to see the degradation rate over time. The median degradation rate is taken as the representative degradation of the specific dispatch of the battery. This approach therefore linearizes the semi-empirical degradation model when it comes to the calculation of the degradation cost. Nevertheless, the degradation of the battery itself over time however is still updated according to the semi-empirical model without any linearization and taken into account when calculating NPC.

The switch degradation cost $c_{\text{degr,sw}}$ is calculated similarly as for the battery energy throughput model and is as follows:

$$c_{\text{degr,sw}} = Degr_{\text{sw}} \cdot c_{\text{inv}} \tag{4.38}$$

where the switch degradation is determined by using the same method as done in [102], namely by using the rainflow-counting method to determine the heating cycles based on the dispatch, which is used as an input in the Bayerer model and consequently Miner's rule. c_{inv} is calculated as the product of solar panel capacity and inverter cost per kWp in the same way as done in (4.36) for the battery. During the optimization two cases are considered - one case takes into account switch degradation while other case does not. In the former case the inverter cost is part of the OPEX as degradation cost while in the latter case inverter cost is part of CAPEX as part of $c_{\text{pv,kWp}}$. This comparison is not fully fair since when considered as OPEX the cost of the inverter is split over the years and influenced by the inflation and discount rates, while when considered as CAPEX it has to be paid all at once. However, this disparity has been taken into account when comparing the final results.

Finally, there are two penalty terms in the calculation of OPEX: $c_{\text{pen, pb}}$ and $c_{\text{pen, soc}}$. These penalty terms are necessary for the particle swarm to maintain the power balance and keep within the chosen SOC limits. The penalties serve as soft constraints to encourage solutions to adhere to the power balance and SOC limits. However, there may be circumstances where a solution with a very low fuel expenditure is chosen at the expense of deviating from these constraints. The extent to which the swarm is capable to deviate from the soft constraints can be adjusted by tuning the penalties, which is explained in detail in the following subsection. Therefore, the penalty costs are calculated as:

$$\begin{aligned} c_{\text{pen,pb}} &= p_{\text{pen,pb}} \cdot \Delta pb \\ c_{\text{pen,soc}} &= p_{\text{pen,soc}} \cdot \Delta SOC \end{aligned} \tag{4.39}$$

where $p_{\text{pen,pb}}$ and $p_{\text{pen,soc}}$ are the penalty terms and Δpb and ΔSOC are the deviations from the power balance and the SOC limits (20% and 85%), respectively.

It should be noted that some of the costs have been excluded. It is assumed that the solar panel array and battery operation costs are negligible. Operation costs include, for example, maintenance costs or solar panel cleaning costs.

After the OPEX has been calculated for each particle, the personal best solutions of each specific particle and the global best solution of the entire swarm are updated if applicable. The global best solution is then checked against the convergence criteria. If any of the criteria have been passed, the EMS optimization has been concluded. Otherwise, the velocities and positions are then updated according to (4.25) and (4.24) respectively, and the process is repeated. There are two convergence criteria used in both EMS and sizing optimization. The first criterion is the maximum number of iterations. The number of iterations of the optimizations is kept track of, and if the limit is reached the optimizations are stopped even if better solutions are continuously being found. The second criterion is the number of iterations without improvement. Since for the PSO it is not possible to know whether a global optimum has been reached, a convergence threshold is set. If the global best position of the swarm has not been improved for a certain number of iterations set by the user, then the optimization is stopped.

Following the completion of the EMS optimization, the next step of sizing optimization can be proceeded with, which is the calculation of the NPC. NPC is often used as the fitness function in the literature. Some alternatives include NPV or LCoE. The NPC is calculated as:

$$NPC = CAPEX + OPEX_{\text{life,no-pen}} \tag{4.40}$$

where $OPEX_{\text{life,no-pen}}$ is the total OPEX over the lifetime of the microgrid. The penalties from the original OPEX calculated are excluded, since they do not have a financial meaning and they are only used to influence the behaviour of the swarm such that it abides by certain constraints.

For the calculation of lifetime OPEX a distinction is made between the fuel cost and degradation costs as the former is adjusted by the inflation while the latter is not. Both terms are adjusted with the discount rate over the years. Hence, the total lifetime OPEX is calculated as:

$$OPEX_{\text{life, no-pen}} = \sum_{y=1}^{\text{lifetime}} \left(c_{\text{fuel}} \cdot \frac{r_{\text{inflation}}^{y} \cdot (1 + 0.01t)}{(1 + r_{\text{discount}})^{y}} + OPEX_{\text{degr}} \cdot \frac{1}{(1 + r_{\text{discount}})^{y}} \right) \tag{4.41}$$

where $r_{\text{inflation}}$ is the inflation rate while r_{discount} is the discount rate. It can also be seen that c_{fuel} is increased by 1% per year in addition to the inflation rate. This term was added to address the fact that the energy produced by the generator would theoretically increase over the years if the battery is not oversized, as the degradation of the battery reduces the amount of energy that can be stored every year. However, the factor was not chosen to be added as proportional to the total loss of the battery because the increase in OPEX would be related to the component sizes, and this relationship is not easy to define. Therefore, the increase by 1% is added to acknowledge the fact that OPEX would often increase, but it is kept in mind that it could also not change over time for certain component sizes. Similar considerations could be made for the inverter degradation cost.

After the calculation of NPC the personal best and global best positions are updated and similarly as for the EMS convergence criteria are checked against the global optimum. If any of the criteria are satisfied, then the optimization is done otherwise, the positions and velocities of the sizing particle swarm are updated, and the next iteration can start in the same manner as was shown for EMS optimization.

Particle Neighborhoods

Previously, the swarm's performance as a whole was referred to as the global best position. However, there are different methods for acquiring the globally best result. The most straight-forward method and the one used in the original paper by Kennedy and Eberhard [82] extracts the global optimum by checking every particle in the swarm and adjusting the velocities based on this optimum. Such an approach can however lead to a convergence to a local optimum since the particles start converging to specific region before properly exploring the entire solution space [195]. Therefore, particle neighborhoods are a good alternative where every particle is connected to some other particles and its velocity is adjusted based on the neighborhood to which the particle belongs. Such an approach allows to explore the solution space better [195]. The convergence criteria are still checked with the global best position of all the neighborhoods. Once the optimization is stopped, the global optimum is taken as the solution.

Some examples of PSO neighborhood have been shown in Fig. 4.39. Subfigure (d) shows the topology where all of the particles are interconnected. Options include the Von Neumann topology, where every particle is connected to exactly four particles, or the ring, where every particle is connected to two other particles.

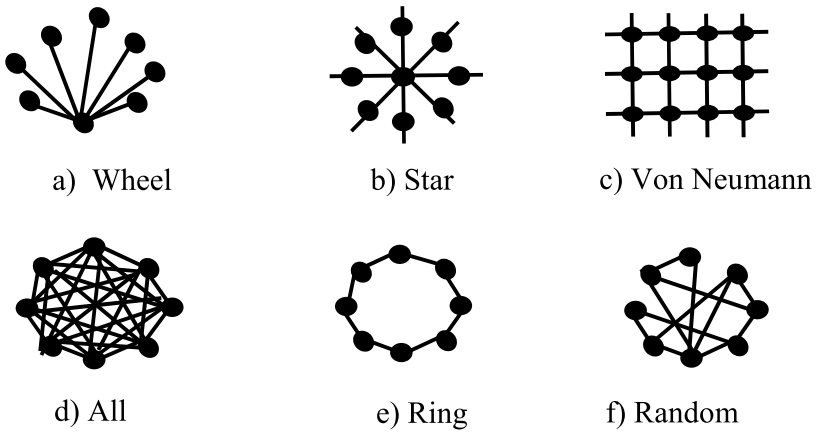


Figure 4.39: Different types of PSO Neighbourhood Topologies [196].

One of the main drawbacks of particle neighborhood is the decrease in computation speed. The decrease is due to two reasons. First, the convergence speed is decreased as the particles explore the solution more. Secondly, it is needed to track how each neighborhood performs and extract the best solutions from each neighborhood separately to then update each particle's velocity based on the performance of their corresponding neighborhood.

There is also a distinction between dynamic neighborhoods (based on distance) and static neighborhoods (based on the initialization). Dynamic neighborhoods change their members based on the closest particles in a particular region, however, this approach is even more computationally costly as the neighborhoods need to be frequently recomputed. Static neighborhoods keep the same members throughout the optimization, hence the neighbors are not necessarily the closest particles. To keep the optimization simple and computationally cheap in the context of this thesis, it was chosen to use a static neighborhood with randomly chosen neighbors. The tuning of the the number of neighbors is explained in the subsequent subsection.

Tuning of the PSO parameters

This part of the subsection addresses the tuning of different parameters of the PSO. Those are parameters that define how the swarm approaches the solving of the optimization problem but cannot be determined analytically. This is why tuning is necessary, which often relies on trial-and-error. A general note for the tuning process is to use test cases with known solutions as much as possible while keeping the structure of the problem as close to the actual optimization problem as possible.

The three main parameters of PSO are inertia w, cognitive coefficient c_1, and social coefficient c_2. Since there are two nested PSO algorithms, two sets of the three hyperparameters are needed. The final values for the EMS PSO algorithms are $w = 0.8$, $c_1 = 2.6$ and $c_2 = 2.0$ while for the sizing PSO they are $w = 1.0$, $c_1 = 2.0$ and $c_2 = 2.0$. The three parameters should not be too sensitive since otherwise it would indicate that the solution is falling into local optimum or that the implementation is not generalizable. For the tuning of the parameters, literature indicates that it is a good start to initially fix the values around $w = 1.0$, $c_1 = 2.0$ and $c_2 = 2.0$ and then perform a grid search to find the values that on average lead to better results [82]. The approach was used in this work and grid-search with a step of 0.2 for c_1 and c_2 in the range between 1.0 and 3.0 and a step of 0.1 for w in the range between 0.5 and 1.5 was used to tune the parameters. Three optimization runs were performed on each setting, after which the setting with the smallest cost function was chosen.

Next, the penalty terms are described that have been previously introduced in the context of OPEX calculations. The penalty terms are only present in the EMS PSO.

In general, constraint handling techniques can be divided into soft and hard constraints [195]. Soft constraints are often implemented into a form of penalties when a certain constraint has been breached. Hence, the cost of breaching a constraint is increased. Soft constraints allow the swarm to explore the solution space better, and sometimes it can be okay to slightly breach the constraint in exchange for a noticeably better solution.

Hard constraints, on the other hand, do not allow for the breach of the constraints. One method of implementing a hard constraint is to ignore a particle if it does not comply with the constraints. However, this can lead to problems with exploration if many particles have breached a constraint. Another method for implementing a hard constraint is the so-called *preserving feasibility* technique, which stops the particle at the boundary of the feasible solution space if it tries to breach a constraint, but this approach once again relies on the fact that initial particles are already located inside a feasible solution space [195]. Hence, it was chosen to apply the approach that makes use of soft constraints as it provides more flexibility in the implementation.

As described in [197], penalties can be split into static penalties and dynamic penalties. Static penalties are predefined constants that do not change during the optimization process, whereas dynamic penalties can change based on optimization variables, such as the number of elapsed iterations or the global best solution. This project makes use of dynamic penalties.

As previously explained, the algorithm implements two penalties - a power balance penalty and an SOC penalty to keep the power balance between generated power and consumed power and to make

sure that the battery keeps within the defined boundary SOC values. To preserve battery life, the battery is limited to operate between the SOC values of 20% and 85% as cycling at very high and very low SOC values exhibits the fastest degradation [198]. Since the algorithm considers hourly dispatch it is expected that the microgrid would be able to deal with some imbalance between the predicted generation and consumption, since forecasts and scheduled power flows are not always a 100% match. The compensation mechanisms are not part of this research, hence it is not considered in further detail, but it is assumed that a total power imbalance of up to 5% can be tolerated.

The power balance penalty and the SOC penalty are calculated as:

$$\begin{aligned} p_{\text{pb}} &= m_{\text{pb,pv}} \cdot m_{\text{batt}} \cdot m_{\text{load}} \\ p_{\text{soc}} &= 0.035 \cdot m_{\text{soc,pv}} \cdot m_{\text{batt}} \cdot m_{\text{load}}, \end{aligned} \tag{4.42}$$

where $m_{\text{pb,pv}}$, $m_{\text{soc,pv}}$, m_{batt}, and m_{load} are empirically found multipliers. The multipliers are necessary because as the capacities of the components change, the fraction between the penalty terms, fuel cost, and degradation cost in (4.32) changes. Therefore, for different component sizes the algorithm would favour the penalty terms or the fuel/degradation costs differently, which would be undesirable.

To determine the values of the multipliers, the pv growth and battery growth values need to be defined based on a reference value:

$$\begin{aligned} g_{\text{pv}} &= \frac{P_{\text{pv}}}{P_{\text{pv,ref}}} \\ g_{\text{batt}} &= \frac{E_{\text{batt}}}{E_{\text{batt,ref}}} \end{aligned} \tag{4.43}$$

where g_{pv} and g_{batt} are the solar growth and battery growth respectively and $P_{\text{pv,ref}}$ and $E_{\text{batt,ref}}$ are the solar and battery power/energy reference values equal to 5kWp and 10kWh respectively in this project. The reference values are simply the settings at which the tuning process has been started. At the reference values, the multiplier values would be equal to 1.

The solar multiplier has been tuned as follows:

$$\begin{aligned} &\textbf{if } g_{\text{pv}} > 1.8: \\ &\qquad m_{\text{pv,pb}} = 0.85 \\ &\qquad m_{\text{pv,soc}} = 0.95 \\ &\textbf{else if } g_{pv} > 0.2: \\ &\qquad m_{\text{pv,pb}} = 1.00 \\ &\qquad m_{\text{pv,soc}} = 1.00 \\ &\textbf{else}: \\ &\qquad m_{\text{pv,pb}} = 10.0 \\ &\qquad m_{\text{pv,soc}} = 10.0 \end{aligned} \tag{4.44}$$

It can be seen that penalty multipliers are very large at solar capacities below 20% of the reference value or 1kWp. This is because at such low solar capacity, it is not possible to satisfy the electrical demand during the day, hence it is needed to use the generator at low powers, which is very inefficient and hence very expensive. Therefore, the fuel cost dominates the OPEX over the power balance and the SOC penalties. Without large multipliers, power balance and SOC limits are no longer taken into account.

An opposite effect but to a lower extent can be seen at very large solar panel capacities. At large solar power capacities, fuel consumption decreases and the penalties start to take more importance leading to sub-optimal dispatch decisions. However, this effect is limited since during the night there is no solar power and generator still needs to be used unless there is a complementary large battery storage unit. Hence, the current implementation of the dispatch algorithm does not work well for heavily over-sized systems. Upper limits of 25kWp for the solar panel array and 60kWh for the battery storage unit have

been set, which gives a large enough of a reserve in the context of this optimization problem and its load levels.

The tuning was done similarly as for the tuning of w, c_1 and c_2. Steps of 0.025 for both the $m_{\text{pv,pb}}$ and $m_{\text{pv,soc}}$ were used and it was checked whether the total power imbalance was below 5% and the SOC is still kept between 20% and 85%.

The battery penalty multiplier has been set as inversely proportional to the battery energy growth:

$$m_{\text{batt}} = \frac{1}{g_{\text{batt}}} \tag{4.45}$$

Similarly as with the solar panel multiplier, higher battery capacities allow for more energy storage which can be used during the night. It both allows to store excess generated solar power and the generator to work at higher loading levels, increasing its efficiency and thus reducing the necessary amount of fuel. Therefore, the total fuel cost decreases, increasing the dominance of the penalties. The inverese relationship helps counter the imbalance between the penalties and the fuel/degradation costs. This relationship was found empirically and might not work for drastically different use cases.

Finally, m_{load} is simply the load growth in comparison to a reference value. This multiplier is present to implement the functionality of the multi-year optimization with load growth.

The last three parameters to tune are the number of particles in a swarm, the velocity limits, and the number of particles per neighborhood. Velocity limits are necessary for the particles to avoid jumping from one end of the solution space to the other in a single step and causing a very chaotic behavior. Since this project utilizes large number of particles the velocity limit is kept low such that the particles focus on the exploration around their initial position instead of jumping around close to other particles.

The velocity limits for the implementation of this algorithm have been tuned simultaneously with the number of particles. The general principle applied was that the velocity limit is in the range of the distance between the initial positions of the particles. In such a manner, they are forced to explore their initial surroundings before entering proximity of other particles. The number of particles was chosen such that a sufficient convergence is reached in combination with a satisfactory computation time. In the end the number of particles for the sizing optimization was chosen as 49 and for the EMS optimization - 1000 particles. EMS optimization contains significantly more particles since each particle has 72 dimensions.

However, since it was noticed that the low velocity limit often caused issues in reaching a suitable power level for the generator, the velocity limit was increased for the generator specifically. This is due to the fuel efficiency curve. If a particle is located at a low efficiency point, the velocity limit can effect it finding a much better solution at higher efficiency which can be located relatively far away. Therefore, increasing the velocity limit for the generator produced a great improvement in finding the solution to the optimizaiton problem.

The number of particles per neighbourhood was tuned the last and done by trial-and-error by checking with a step size of 5 particles. Hence, the number of particles per neighbourhood in the EMS optimization was chosen to be 35.

Computation Speed

Computational speed has been one of the driving constraints in the development of the nested PSO algorithm. One of the reasons why many of the existing optimization algorithms do not use detailed degradation models for electrical components is because of the significantly increased computation time that comes with the implementation of these models.

The programming of the algorithm has been done by using Python programming language. Below, the three main steps taken to keep the computational time as low as possible are described:

- The code has been primarily coded by using the NumPy library. NumPy library is a very computationally efficient library for performing matrix calculations. The reason for its high computational efficiency is that it translates the code directly into a well-optimized C-code [199]. Moreover, the

use of other libraries has been kept to a minimum, since usually the libraries offer flexibility for different operational settings which causes large overheads. Therefore, even well-established functions were usually written from scratch using NumPy if needed, for example, in the case of the rainflow counting algorithm.

- Numba library has been used to further increase the computation speed. Numba is just-in-time (JIT) compiler, which allows to avoid the step of converting the Python code into byte-code before translating it into the machine code. By using Numba library, it is possible to compile the code directly into machine code thus significantly decreasing the computation time. The drawback of using Numba is that it makes the debugging process more difficult, since the code is no longer compiled line by line. The most used functions in the code were rewritten so that it is compatible with Numba.
- Wherever possible precomputed arrays were used and imported at the start of the code such that they do not need to be imported from csv files or computed during the optimization itself. Examples include PV curves of MPPT tracking or voltage-SOC curve of the battery.

The goal set at the start of the thesis project was to keep the full nested optimization to finish in 24 hours. This is an arbitrary goal, which aims to keep the balance between feasibility in realization and usability. This goal is comparable with the computation times of similar MILP algorithms [24], [114].

Environmental Cost

The thesis project has been done in collaboration with the company OnePower, which operates microgrids in Lesotho and Benin and has provided data on one of their microgrids to be used as a use case. During the interaction with the company it has been stated by the company that they aim to provide 95% of the total electricity from renewable energy sources, thus minimizing the dependence on fuel deliveries and minimizing the impact on climate and the environment. However, this goal cannot be achieved by cost optimization alone, as it is possible that the cheapest solutions include larger proportions of the electricity generated by the diesel generator.

Due to the time constraints of the thesis project it was not possible to design a multi-objective optimization algorithm which would consider the carbon emissions. Instead, an analysis is performed by performing a sweep of optimizations with different fuel prices. The increased fuel prices could be considered as a ”carbon tax”, which theoretically should discourage the algorithm from using the generator. It can then be seen whether there is a knee-point, which usually is found when doing a multi-objective optimization of weighted aggregation. Weighted aggregation places a weight on each cost function and investigates at which point the combination of both cost functions is most optimal, which can be called a knee point [200]. In the context of this project the knee point would be the point where increasing the fuel price further would bring significantly less decrease in carbon emissions in comparison to the decreases leading that set point point.

4.2.5 Performance Evaluation

Rule-Based Dispatch

The performance of the nested PSO algorithm introduced in the previous subsection is compared with the existing dispatch algorithm utilized by OnePower. For the planning of their microgrids OnePower uses uGrid software in combination with uGridNet, which is introduced in [124]. uGrid is used to determine the optimal sizing of the microgrid, while uGridNet is used to optimize the geographical placements of the electrical components and the distribution grid. The remainder of this subsection focuses only on uGrid.

uGrid is an optimization algorithm based on PSO, while dispatch has been implemented with a rule-based method. The flowchart of the rule-based method is provided in Fig. 4.40.

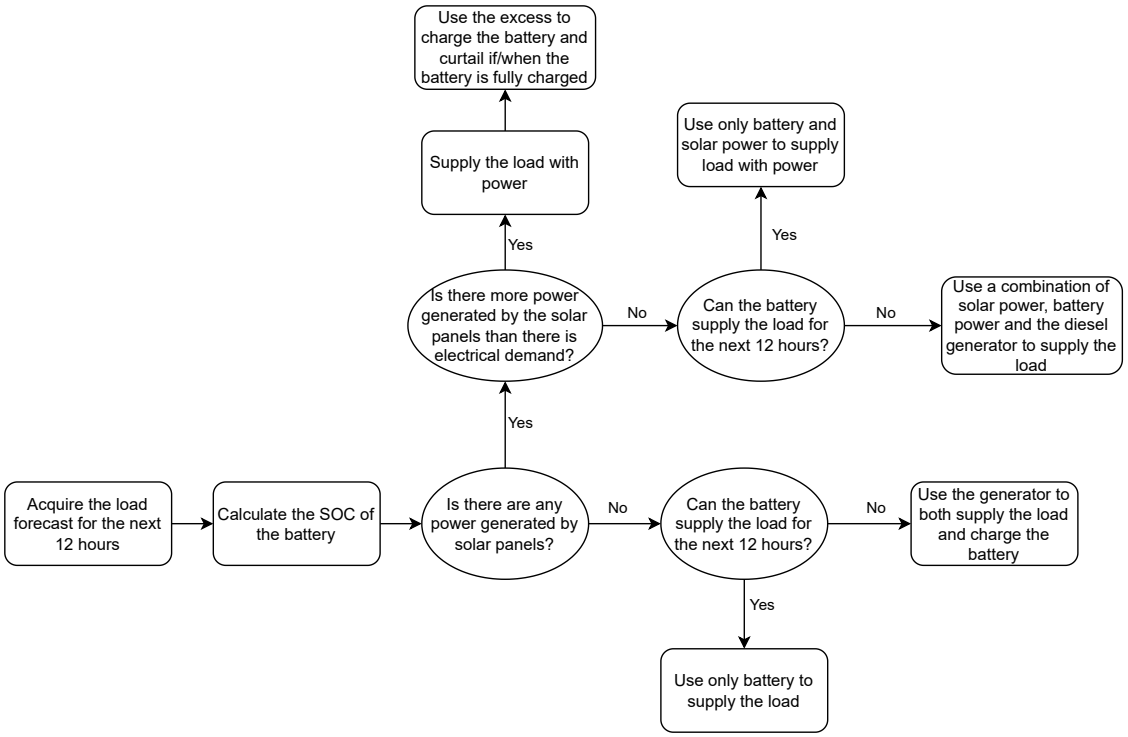


Figure 4.40: High-level flowchart of the dispatch algorithm introduced in [124].

The utilized rule-based method is more advanced than the typically used Load-Following or Cyclic Charging methods. The dispatch algorithm relies on a 12-hour load forecast based on a similar tool to RAMP [124]. At each time instant, it is checked whether the battery has enough energy to supply the remainder of the necessary electricity after the solar energy has been dispatched. If there is more energy from the solar panels available than electrical demand, then the battery is charged if possible. Finally, there is also a logic that maximizes the power dispatched by the generator during the moments when there is no solar power. During those moments, generators are run at as high a power as possible to supply the load and charge the battery because higher loading levels increase the efficiency of the generator, as previously discussed.

Performance Indicators

The propsed nested-PSO algorithm is compared across different cases where different combinations of degradation models are considered. Furthermore the solutions of the nested-PSO are cmpared with the sizing optimization where the PSO dispatch is replaced with RB dispatch introduced in this section. These combinations of different settings for optimization are compared by using multiple performance criteria:

- PV and battery capacities
- NPC
- CAPEX
- Daily OPEX
- Daily curtailed energy
- Battery degradation after 10 years
- Switch degradation after 10 years
- Daily energy throughput of the generator and the battery

In summary, Section 4.2 has provided an elaborate explanation of the proposed nested-PSO sizing optimization. It was first, motivated why PSO has been chosen after which the general structure of the algorithm was explained. It has been shown how to include the degradation cost of non-linear battery and switch degradation models into the final calculation of the OPEX. It was also shown that particle neighborhoods are used to improve the convergence of the algorithm. Finally, an elaborate explanation of the tuning of the PSO hyperparameters and the penalties has been provided, which is rarely done in the literature in the context of microgrid optimization if done at all. Finally, an alternative version of the algorithm has been introduced which uses RB dispatch instead of PSO dispatch similarly as is done by the software that the company uses currently (uGrid). The solutions of the two algorithms will be presented and compared in detail in Chapter 6.

The scientific contributions include a nested PSO optimization algorithm with two detailed degradation models, which to the author's knowledge has not been done before. In addition, the algorithm performs a day-ahead dispatch, which is known to be very computationally expensive. Many comparable algorithms instead use real-time dispatch, where each time step is optimized separately. Finally, a structured way to tuning the empirical parameters of the algorithm has been provided, which also to the author's knowledge has been missing so far in the context of rural microgrid optimization.

The next chapter describes the results of the experimental investigation of the switch degradation to see whether it is a valid assumption to use the switch degradation inside the algorithm at all.

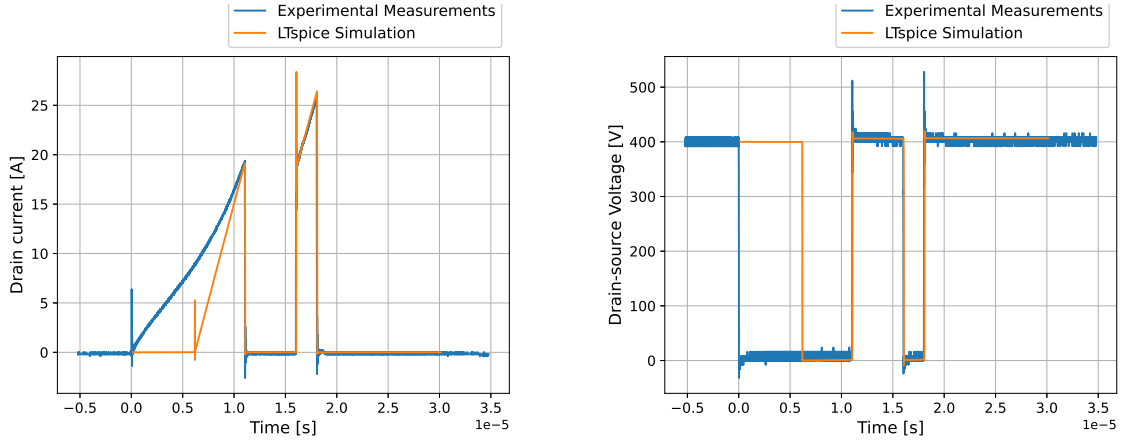
Chapter 5

Experimental Results of Switch Lifetime Testing

This chapter presents the experimental results of the switch lifetime testing, which has been performed according to the methods explained in Section 4.1. First, Section 5.1 shows the results of the double-pulse test performed and provides a comparison with the simulated waveforms. The measured and simulated switching losses is compared with the reference values from the datasheet. Secondly, Section 5.2 shows the results of the $R_{\text{ds-on}}$ measurements extracted from different operating points of the Boost converter. The measured $R_{\text{ds-on}}$ waveforms are translated to junction temperature by using the datasheet of the switch. The generated junction temperature curves are then used to calculate the switch degradation at different curtailment thresholds for the mission profile presented in [102] by Alpízar-Castillo et al.

5.1 Double-Pulse Test

Fig. 5.1 shows the simulated and experimentally measured waveforms of the drain current waveform and the drain-source voltage waveform during the execution of the DPT.



(a) Simulated and measured drain current waveforms of the DPT.

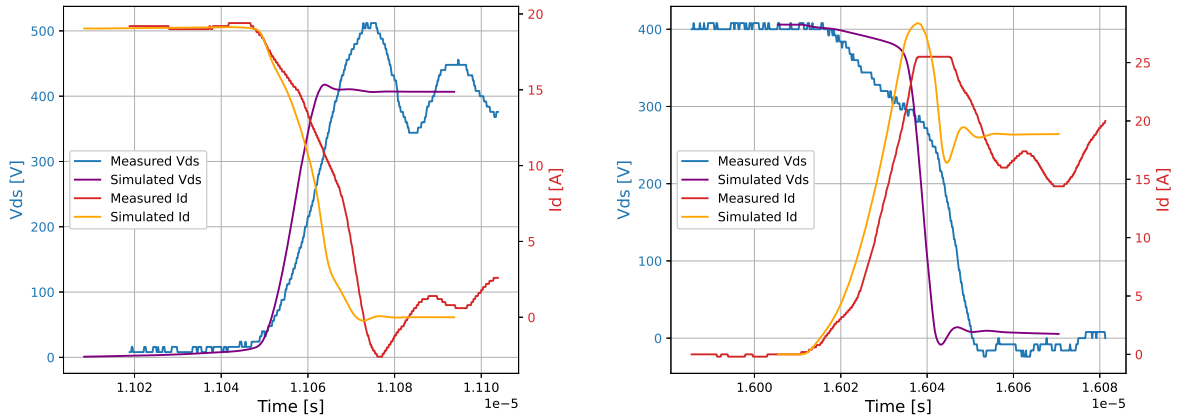
(b) Simulated and measured drain-source voltage waveforms of the DPT.

Figure 5.1: Simulated and measured drain current and drain-source voltage waveforms of the DPT.

It can be seen that there is a noticeable difference between $\frac{di}{dt}$ of the simulated and experimental DPT during the first pulse shown in Fig. 5.1a. However, at the end of the first pulse and during the second

pulse the current rise slopes match significantly closer. One of the reasons for the mismatch at the start of the first pulse could be the parasitic capacitances of the evaluation board that are being charged during the first pulse. It can be seen that there is visually identifiable noise in the measured voltage waveforms in Fig.5.1b. The noise reaches around 10-15 V. Additionally, there are voltage overshoots of over 100 V for the measured waveform, while it stays within 10-15 V for the simulated waveform. The most likely reason for the large overshoots in the measurements is the parasitic inductances of the circuit, as the stored charge can act as a current source during the turn-off [168]. Finally, the intention was to reach a current in the range of 17.5 to 18.0 A in order to have a close match with the setting of the datasheet, however, the current reached during the test was around 19.0 A, due to the first pulse being set slightly too long. Instead of 10.5 μs, it was set to 11 μs. Additional simulations have been performed to still be able to make proper comparisons between the measurements and the datasheet.

The comparison between the simulated current and voltage waveforms during the turn-off and turn-on can be seen in Fig. 5.2.



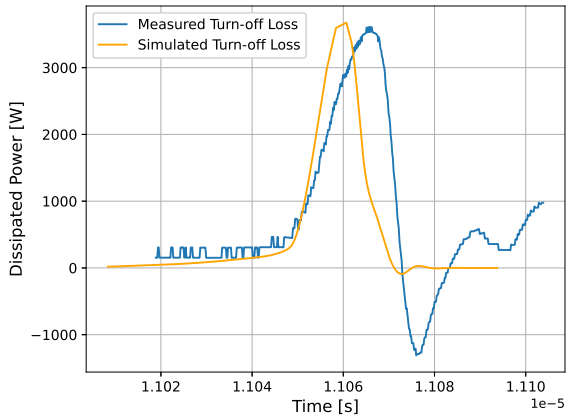
(a) Simulated and measured drain current and drain-source voltage waveforms during the turn-off.

(b) Simulated and measured drain current and drain-source voltage waveforms during the turn-on.

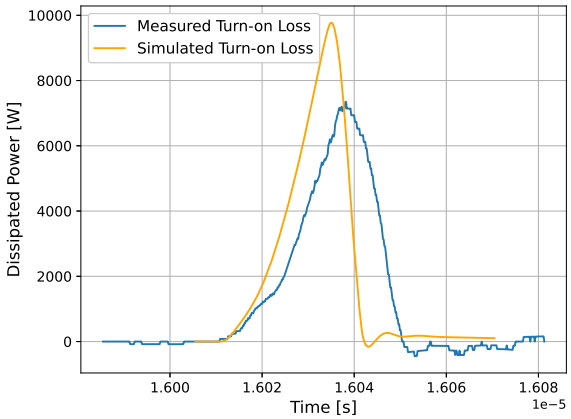
Figure 5.2: Simulated and measured drain current and drain-source voltage waveforms during turn-off and turn-on of the SiC MOSFET.

For the turn-off event in Fig. 5.2a both the measured current and voltage waveforms show a large resonance, which is significantly less visible in the simulated waveforms. Fig. 5.2b shows the turn-on event. Although there is a visibly good match between the slopes of the rising parts of the current waveforms, it can be seen that the measured current waveform has a cutoff at 25 A. Unfortunately, the cut-off was caused by mistakenly set oscilloscope range for the current channel, which was noticed only much later during the post-processing of the data. There is also a noticeable difference in the voltage waveforms, as the measured voltage has an extended period of a slow $\frac{dv}{dt}$. This period is the period right after the gate-source voltage has reached the threshold voltage and the device starts conducting. During the initial conduction stage parasitic inductances play a great role in how long the period with the reduced $\frac{dv}{dt}$ persists and correspondingly influence the turn-on switching loss [168].

The power dissipated during turn-off and turn-on is depicted in Fig. 5.3.



(a) Simulated and measured dissipated power of the switch during the turn-off.



(b) Simulated and measured dissipated power of the switch during the turn-off.

Figure 5.3: Simulated and measured dissipated power of the switch during the turn-off and turn-on.

It can be seen that both during turn-on and turn-off the power waveforms are wider for the measured waveforms than for the simulated ones. It depicts a relatively slower switching. The simulated power waveform during the turn-on has a higher peak than the measured one, however, it can partially be explained by the measured current waveform which was cut-off.

A summary of the estimated turn-off and turn-on losses for different test is provided in Table 5.1. Simulation 1 corresponds to the current setting of 17.7 A which corresponds to the setting of the datasheet. The second simulation corresponds to the current setting of 19.0 A, which corresponds to the current achieved during the experimental DPT measurement.

Table 5.1: Summary of the simulations and experimental measurements of the DPT.

	I_d [A]	V_{ds} [V]	E_{off} $[\mu J]$	E_{on} $[\mu J]$	E_{tot} $[\mu J]$
Datasheet	17.7	400	44	115	159
Simulation 1	17.7	400	34	113	147
Simulation 2	19.0	400	38	120	158
Experimental Measurements	19.0	400	52	126	178

It can be seen that both the simulations and the measurements have turn-on loss estimates within 10% of the datasheet value. The overestimates for the measurements at 19.0 A are expected, since at higher currents the switching loss increases. However, the cut-off of the current has to be taken into account for the experimental measurements. Hence, the actual turn-on loss for the measurements is expected to be higher.

Accounting for the increased testing current the turn-off loss of the experimental measurements would be close to 10 to 15% range of the datasheet value. However, there is a larger mismatch in the simulated turn-off loss. This could be explained by the parasitic inductances inside the circuit that can increase the voltage peaks upon turn-off. Since it is difficult to estimate parasitic inductances of a specific circuit, the simulation assumes no parasitic inductance. However, when a 10 nH parasitic bus inductance is added the voltage peaks increase by 4% and the turn-off loss is increased by roughly 10% (from 34 to 38 μJ in the 17.7A simulation). Another parasitic effect to consider is the parasitic stray capacitance inside the load inductor. A stray capacitance of 0.1 nF can increase the current peaks and the turn-on loss by around 10-15 %.

Despite some differences between the datasheet data, simulations and the experimental measurements, it has still been shown that the simulation can achieve a satisfactory accuracy for the purposes of

the project. The relative difference in the total switching loss between the simulation and the datasheet is below 10% and the relative difference between the simulation and the measurements remains below 15%. Some difference is expected in most experiments, not only because of the parasitics introduced by the circuit itself but also by the measurement equipment. For example, there are errors introduced by probes and power supplies. Depending on which probe is used the relative error can change. Similarly, power supplies do not necessarily provide a voltage, which perfectly matches the selection. Therefore, the simulation can be used as a tool to get the sense of the switching losses which can then be used as an input to the Foster/Cauer model while the adressed differences have to be kept in mind.

5.2 Junction Temperature Experiments

An example of the relative $R_{\text{ds-on}}$ increase upon different sustained currents at a duty cycle of $D = 0.65$ corresponding to an output voltage of 100 V and an input voltage of 35 V can be seen in Fig.5.4. It can be seen that the relative $R_{\text{ds-on}}$ steadily increases with an increase in the RMS current, and the slope becomes steeper at higher currents. Only currents starting from 10 A have been depicted since little heating was observed up to that point the data on the $R_{\text{ds-on}}$ was very noisy for low currents.

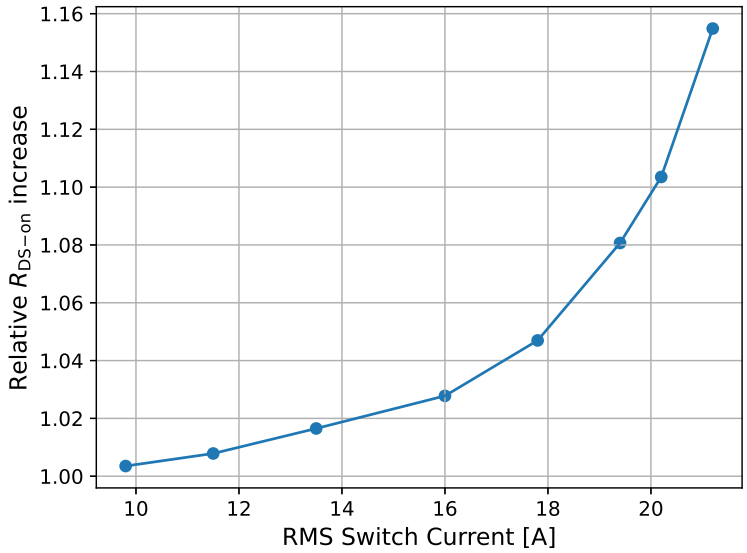


Figure 5.4: Relative $R_{\text{DS-on}}$ increase depending on the RMS current flowing through the switch for a duty cycle of 0.65.

Due to the limitations of the available power resistors, it was not possible to test the entire range of currents at a single duty cycle. Hence, a range of duty cycles was tested to cover a larger current range by combining them all together. The combination of the curves of measurements at different duty cycles can be seen Fig. 5.5.

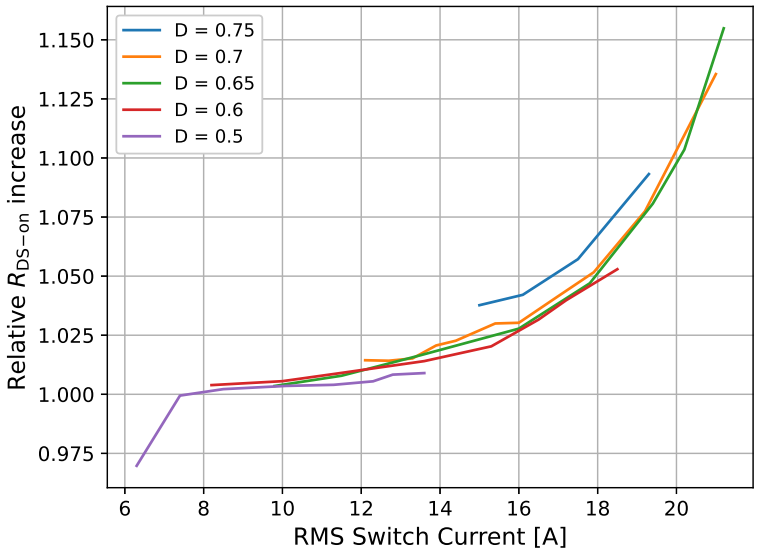


Figure 5.5: Relative $R_{\text{DS-on}}$ curves depending on the RMS current for different duty cycles.

It can be seen that most of the curves closely overlap in the regions where the same currents have been tested, which shows that the method works consistently. Additionally, it can be seen that there is a positive offset with an increasing duty cycle. This can be explained by the increasing thermal impedance at higher duty cycles as was shown in Fig. 4.10. At high duty cycles however the thermal impedance changes more slowly upon an increase in the duty cycle than it is at low duty cycles. Due to the difference in the thermal impedance, one would need to have a separate lookup table for each duty cycle, but to keep the method simple and due to the lack of complete curves it was decided to create a fit from the combination of all the curves, which approximates the average behaviour. Therefore, the plot was transformed into a scatter plot and a second-order polynomial fit was created as shown in Fig. 5.6.

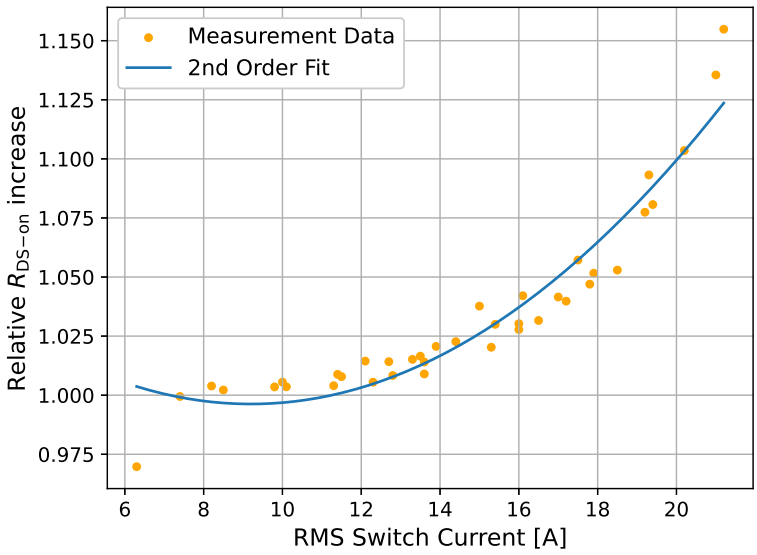


Figure 5.6: A second-order polynomial fit of the stacked $R_{\text{DS-on}}$ curves.

The fitted curve at currents under 10 A has a visually worse fit than for the higher currents. As mentioned previously, the $R_{\text{ds-on}}$ values at the lower range of currents are very close to unity indicating little sensitivity, which makes it difficult to filter the values out from noise. Therefore, it was decided to use the final fit only starting from 12.5 A.

Fig. 5.7 shows the final correlation curve between the RMS current of the switch and the junction temperature. The curve was created by combining the extrapolated curve from the measurements in Fig. 5.6 with the $R_{\text{ds-on}}$ curve at different junction temperatures from the datasheet depicted in the previous chapter in Fig. 4.25. The lower range of currents (currents up to 12.5 A) is assumed to have a linear correlation between the current and the junction temperature. Such an assumption possibly does not fit well with the reality, however, switch degradation is mainly influenced by the high temperatures and therefore this assumption should not affect the estimation of switch degradation.

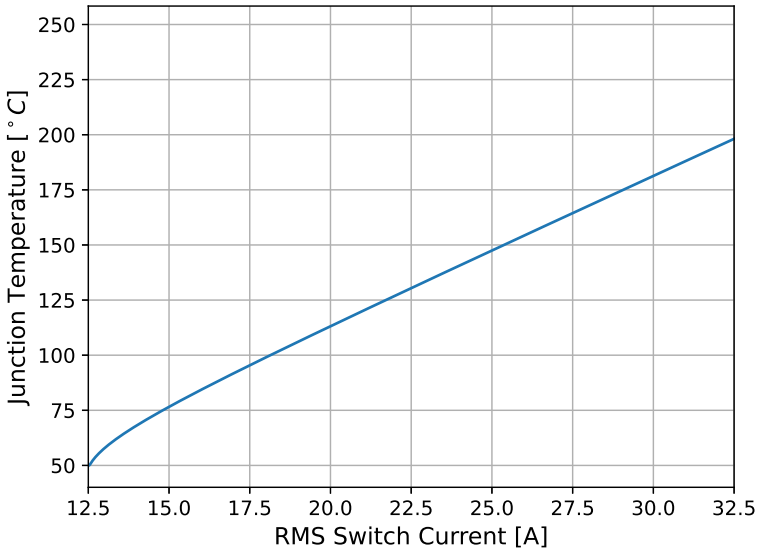


Figure 5.7: Junction temperature dependence on the RMS switch current extracted by combining the junction temperature calibration curve and the polynomial fit of the R_{DS-on} curves.

To compare the obtained current-temperature curve with the reference model a fit of the reference model has been extrapolated from the data points for the threshold value of -1.1 kW as shown in Fig. 5.8.

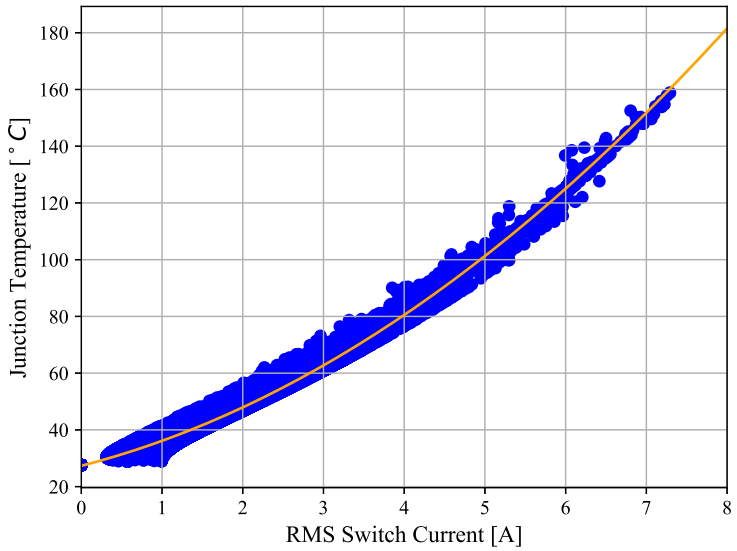


Figure 5.8: Extrapolated fit of the current-temperature curve from the current data points from the reference mission profile with a curtailment threshold of -1.1 kW.

The reason why there is a spread of points instead of a clear line is because the mission profiles account for the ambient temperature. Hence, at different temperatures the environment can either cool or heat the switch. The ambient temperature for the considered mission profile varies between -4 $°C$ and 28 $°$ C. The curve slightly differs for different curtailment thresholds as shown in Fig. 5.9.

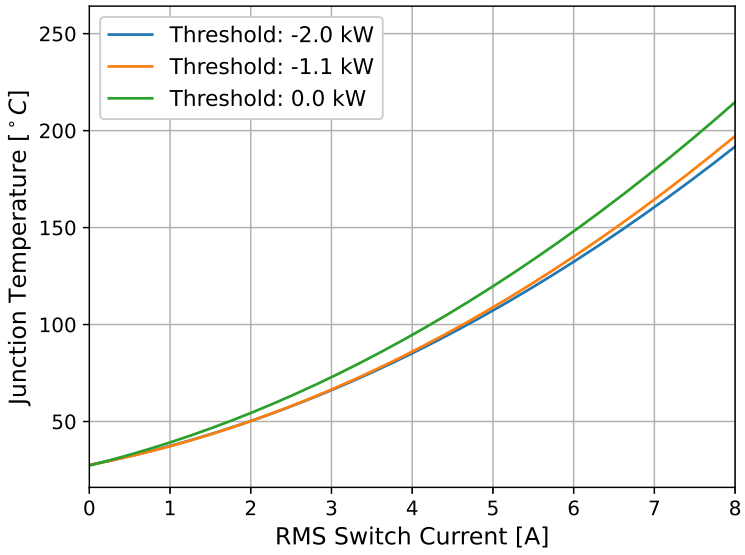


Figure 5.9: Junction temperature fits for three different thresholds in the reference model.

This is caused by the redistribution of the number of operating points at each current setting and correspondingly some adjustments in the resulting fitted lines. It is also influenced by the fact that usually more curtailment takes place in summer when there is more generated solar energy. Therefore, high currents are accompanied with high ambient temperature causing higher junction temperatures and

correspondingly a positive shift in the temperature fit line.

The current-temperature curve for the simulation was extracted by directly simulating temperatures at different current settings by using the Cauer model. Comparison between the reference model, the experimental measurements and the simualtion can be seen in Fig. 5.10. The current temperature curve for the threshold of -2.0 kW has been chosen as it is based on data points that cover the entire spectrum of possible currents.

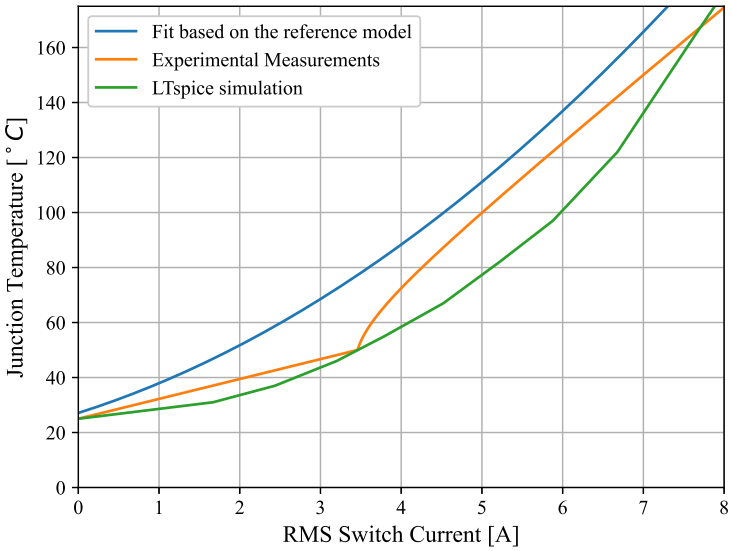


Figure 5.10: Current-temperature lookup-curves corresponding to the three results - reference model (threshold of -2.0 kW), experimental results and the simulation.

The curve derived from the experimental results has two sections as mentioned earlier. The first part is the linear part up to 12.5 A while the second part is extracted from the calibration curve from the datasheet. It is theoretically possible to create another fit which would connect the two sections of the curve, however, it was decided to leave it in two stages since the accuracy at higher currents is valued more than the discontinuity of the overall curve.

An important aspect which has to be mentioned when comparing different degradation models (reference model, simulation and experiments) is the alignment of the temperature curves. Firstly, there is a difference between the range of experimentally tested currents and the range of the currents in the reference model, since the switch used in the experimental tests has a different current rating that the one of the reference model. Secondly, depending on the chosen cooling system - the size of the heatsink or the use of a fan/cooling liquid - the junction temperature is different for the same current. Therefore, the current curves are aligned when calculating the degradation. The alignment is done by scaling the currents of the experimental data and simulations to a common temperature point with the reference model. In this case, the temperature of 175 °C is taken as a reference and the scaling is done based on that point. The current at 175 °C for the reference model is 8.0 A while for the experimental data it corresponds to a current of 29 A (the switch has a current rating of 35 A at 175 °C). Therefore, the scaling factor for the experimental data is $\frac{8}{29}$, which is used to derive a comparable current-temperature curve which can be used to calculate the degradation for the reference mission profile at different curtailment thresholds. The same is done for the simulation data.

It can be noticed that the simulation has a shape that resembles a second-order polynomial similarly to that of the reference model. The offset could be explained by the different switch technologies, since the reference model is based on a Si IGBT, while the simulation is done for the SiC MOSFET. Both switches have different thermal impedance curves. Specifically, the thermal impedance of the Si IGBT

is generally higher than the one for SiC MOSFET, which could at least partially explain the positive offset.

Although the simulated curve of the SiC is closer to the experimental measurements of the SiC switch, as for the reference model, both curves have different shapes. The exact reasons for the difference could not be investigated due to the time constraints, however, one possible explanation could include the fact that the simulation does not account for the changes in $R_{\text{ds-on}}$ when calculating the losses. Another reason could be related to the way the evaluation board is built, where the switch is cooled with a fan. Before reaching the switch, the air flow passes through the power diode, which is also heating up, which could influence the measurements, especially at low temperatures. The relative difference between the simulation and the experimental results in the current-temperature curves reaches up to 20% with the highest difference being at the current setting of 5.0 A.

Finally, it should be noted that during the experimental measurements the output voltage changes slightly depending on the operating point. As the output power of the boost converter is increased (decreasing resistance) the inductor, diode and switch currents increase and hence the voltage drops across the circuit increase as well. Within the range of testing conditions a difference of around 5% at the output voltage was observed. The output voltage has an influence on the switching loss. In a real-world setting the output bus voltage is kept at a near-constant value as the contrary would cause stability issues. Therefore, the duty cycle would have to be adjusted. However, to avoid influencing the thermal impedance of the switch which is dependent on the duty cycle the changes in the output voltage were kept. Hence, possibly the junction temperature curve of the measurement data has a higher slope in reality which would cause higher degradation and would result in a closer match with the curve derived by Alpízar-Castillo et al.

The current-temperature curves of the different models can finally be used to extract the junction temperatures for the mission profiles with different curtailment thresholds. Afterward, rainflow-counting algorithm and Miner's rule is used to determine the switch degradation at different curtailment thresholds the same as was done in [102]. The switch lifetime curve from the study and the lifetime curves derived from the experimental measurements and the simulation are shown in Fig. 5.11.

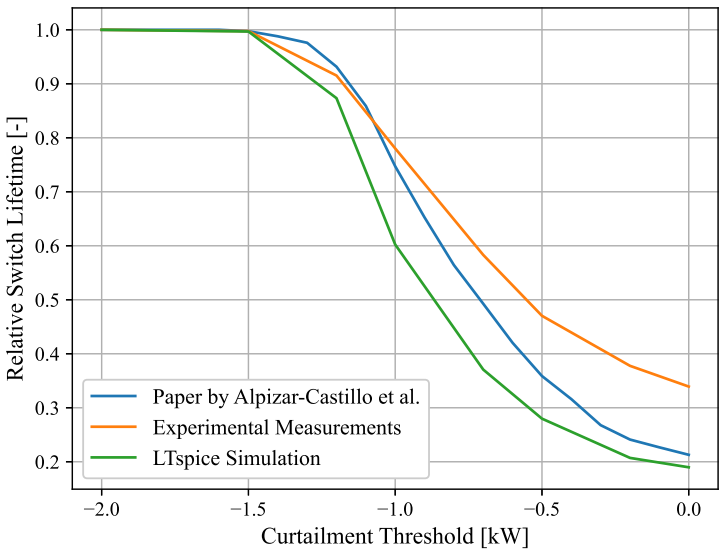


Figure 5.11: Degradation curves at different curtailment thresholds - the original curve from the paper by Alpizar-Castilo et al. in [102], the curve produced from the junction temperatures of the measurements, and the simulation of the performed measurements.

It can be seen that the simulation portrays generally more degradation for all curtailment thresholds than the in the reference model. At the same time, experimental measurements have resulted in rel-

atively more degradation at curtailment thresholds between -1.5 kW and -1.0 kW, while in the range between -1.0 kW and 0.0 kW there is relatively less degradation than it is for the reference model and the simulation. The differences between the three curves are directly related to the slopes of the current-temperature curves in Fig. 5.10. Higher slope in the current-temperature curves correlates with a higher degradation of the switch since the temperature swing is therefore higher for a certain increase in current. The simulation has the highest slope throughout most of the current-temperature curve and hence it also shows higher degradation at all thresholds. On the other hand, the slope of the experimental results is relatively lower for most of the current-temperature curves and hence the degradation is also lower. An exception is the current range between 3 and 5 A where the slope of the experimental result curve is higher and hence the degradation is higher for the threshold range of -1.5 to -1.0 kW.

To better understand the differeces between the relative lifetime curves current histogram curves for two threshold are provided in Fig. 5.12. It is possible to confirm that the higher current ranges are the deciding factor in the decrease in the relative switch lifetime. As the curtailment threshold is decreased in absolute value time instances with higher RMS switch current increases and higher RMS currents are encountered as has been shown in the histograms. The histogram shows the two extremes of the curtailment threshold to showcase the full range. The histogram excludes data of the currents up to 0.5 A to better show the details of the changes at high currents as they are the determining factor in degradation.

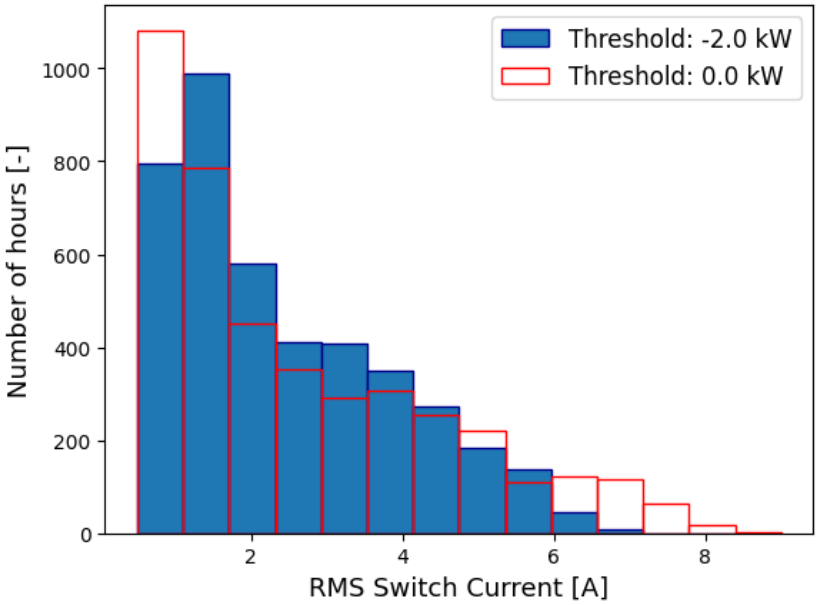


Figure 5.12: Histogram of the encountered RMS currents durin a mission profile for two different curtailment thresholds.

In conclusion, it has been shown that the experimental measurements portray a similar behaviour in the switch relative lifetime dependency on the RMS current mission profile. It has been shown that switch lifetime can reduce by over 60% if not enough care is taken in the decisions made by the energy management system. It was also shown that there are noticeable differences between the experimental measurements, reference model and the simulations. However, the goal of the experimental tests was not to validate but to investigate the switch degradation depending on the current mission profile as the availability of the lab equipment would not allow to closely replicate the reference model. Therefore, an exact match between the curves was never the goal of the research but rather to see whether the overall behaviour is comparable and where do the differences could potentially originate from.

This chapter has therefore shown that the dispatch strategy can have a great effect on the degradation of the switch and hence the degradation of the inverter. Next chapter shows and analyses the results

of microgrid optimization while considering different battery degradation models and the swithc degradation model. The implications of the switch degradation in the context of the optimal component sizing configuration and the final cost of the system are shown.

Chapter 6

Results of Microgrid Sizing Optimization

In this chapter, the results of the proposed optimization algorithm when considering different degradation models have been presented. In addition comparisons between PSO dispatch and RB dispatch have been done to explore the advantages and disadvantages of both. First, the use case of the Samionta microgrid operated by the company OnePower is introduced in Section 6.1. Next, Section 6.2 and Section 6.3 provide an overview of the impact of the battery and switch degradation on the optimization problem solutions. Section 6.4 compares the proposed PSO dispatch optimization with the RB dispatch by using the performance parameters discussed in Section 4.2.5. Section 6.5 compare the sizing optimization results for different combinations of battery and switch degradation models to understand the influence of the inclusion of different models. Finally, Section 6.6 shows possible configurations of the microgrid when different rates of ”carbon tax” have been applied as described in Section 4.2.4.

6.1 Use Case: Samionta Microgrid

OnePower is a company whose mission is to contribute to the mission of rural electrificaion in sub-Saharan Africa. OnePower has two branches - one in Lesotho with a portfolio of 10 microgrids and one in Benin with a planned portfolio of over 70 microgrids [201]. In the context of the thesis the microgrid located in Samionta village in Benin has been selected as a use case (Fig. 6.1)



Figure 6.1: Solar Panel Array built in Samionta.

Samionta village comprises 537 households. Of the 537 households, 30 were connected to the microgrid at the beginning of 2024 and are experiencing a consistent growth in new connections [202]. Typical appliances powered by electricity in the village include lighting, phones, radios, and TVs. In addition, there are two income-generating activities (ice cream shops), two churches and a public lighting system, which use the electricity provided by the microgrid [202].

By using the RAMP model as described in Subsection 4.2.1 a load profile for the Samionta was extracted, which has been shown in Fig. 6.2.

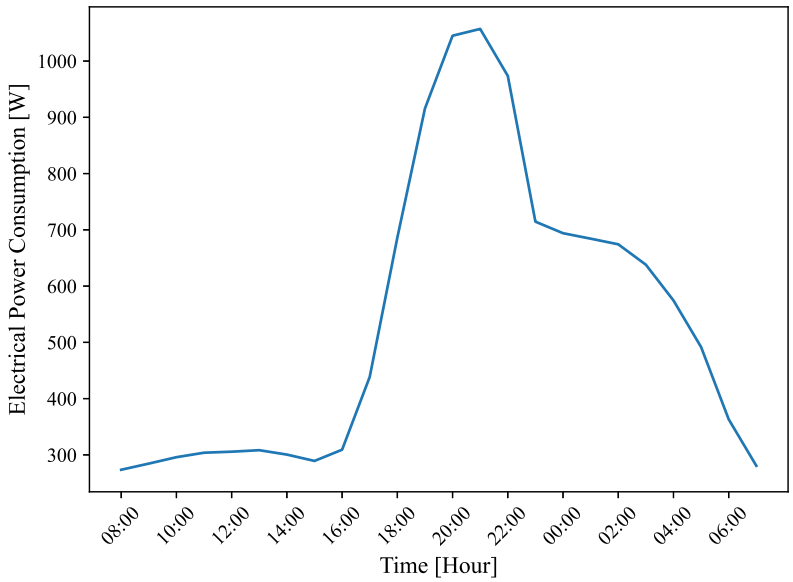


Figure 6.2: Base load curve, which has been generated by using RAMP model.

In addition, the newly proposed multi-year feature in Section 4.2.1 has been used to generate load curves for 20 years. The resulting evolution of the average load profile for a specfic day can be seen in Fig. 6.3.

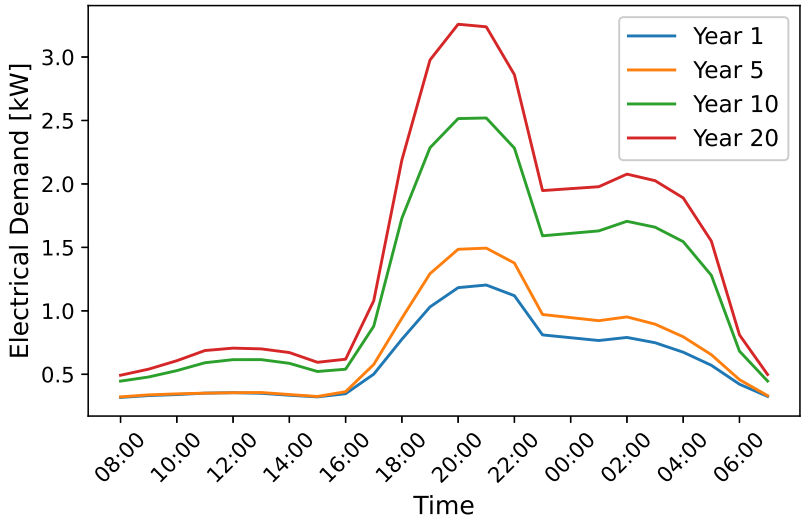


Figure 6.3: Modeled load profile of electrical consumption in Samionta village by using the newly-introduce multi-year feature of RAMP.

Although due to the time constraints it was not possible to fully implement multi-year optimization, multi-year feature of RAMP can serve as a starting point for future work if load growth influence on the optimization problem solutions is desired to be studied.

The extracted load profile is similar to the one generated in [202] in Fig. 6.2 as it uses the same information about the consumer appliance profile. The profile however is scaled in magnitude in comparison to [202] in order to represent the microgrid demand in its more likely levels, since the profile in [202] analyses the load in the first year of the implementation of the microgrid and the number of connections keeps growing every month. It is the shape of the load profile and how it evolves over time which is of the most importance since the algorithm works in the same manner for any magnitude.

The microgrid in Samionta has the same topology as considered in this thesis project, namely having the four main components of a solar panel array, battery electrical storage system, inverter, and diesel generator. An overview of the specific models of the components used in the microgrid as well as their capacities have been provided in Table 6.1.

Table 6.1: Microgrid components used in Samionta.

Component	Model	Capacity
Solar Panels	JA Solar JAM72S20	17.7 kWp
Battery	BYD Battery-box LV Flex	55 kWh
Inverter	Deye SUN-12K-SG04LP3-EU	12kVA
Diesel Generator	CGM 20P	20kVA

However, component capacities should not be compared with the results of the proposed optimization algorithm, as they have been chosen with the thought that the number of connections will continue to increase, and hence the expected load profile will be larger in magnitude than the one currently observed and reported in [202].

The component and fuel costs used in the optimization problem have been provided in Table 6.2. The costs have been set based on common values found in the literature for similar studies [203],[204], by analyzing the costs found on the Internet for specific components and by consulting with OnePower.

Table 6.2: Modeled costs of the components in Samionta microgrid.

Component	Modeled Cost [-]
Solar Panels	400 EUR/kWp
Battery	500 EUR/kWh
Inverter	500 EUR/kWp
Diesel Generator	1.2 EUR/l

6.2 Impact of Battery Degradation Models

Throughout the chapter, four cases of the optimization problem have been considered, which have differences in the modeling of the battery and switch degradation. The cases are summarized in Table 6.3, where ET stands for energy-throughput model, SE stands for semi-empirical model, NSD stands for ”No Switch Degradation” and SD stands for ”Switch Degradation”. The difference between the last two is that in the former case switch degradation cost is not considered in optimization and inverter cost is part of the CAPEX. When switch degradation is considered, the cost of the inverter is part of OPEX and CAPEX only contains the solar panel cost.

Table 6.3: Overview of the cases studied for the microgrid sizing optimization.

Case	Battery Degradation	Switch Degradation
1	ET	NSD
2	SE	NSD
3	ET	SD
4	SE	SD

An important input parameter for the energy throughput models is the number of cycles, as it determines the degradation of the battery and consequently the total cost of the system. Manufacturers sometimes depict a range for the expected number of cycles, however, the lifetime of the battery depends on many additional factors, such as the operation temperature, charge/discharge current, depth of discharge and many more factors as have been explained in Section 2.2. Therefore, it is not possible to predict the total number of cycles the battery would undergo without knowing the cycling profile and without making a detailed model. Fig. 6.4 illustrates the impact of the chosen number of cycles on total degradation over the years when the RB sizing optimization is performed while considering switch degradation. Three realistic number of cycles (3000 cycles, 4500 cycles and 6000 cycles) have been selected and provided in the figure and the semi-empirical model has been added for a reference.

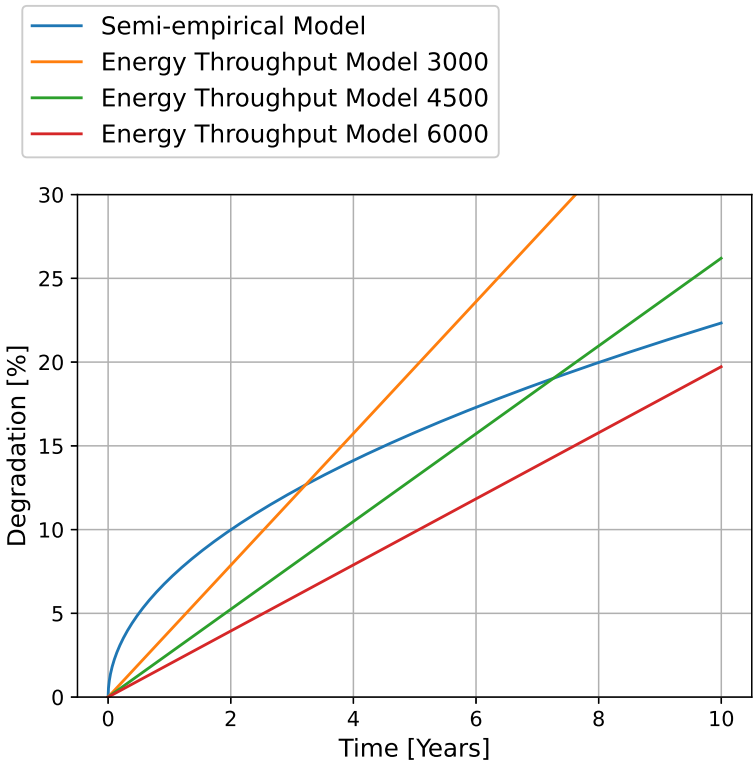
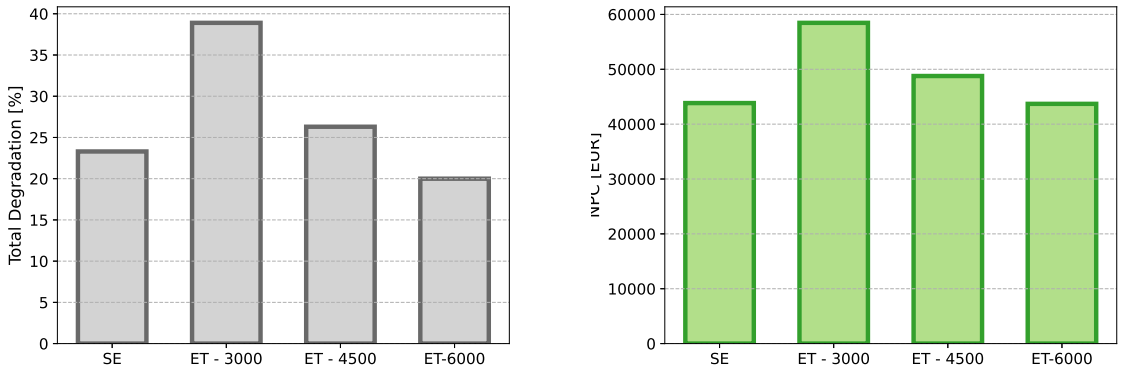


Figure 6.4: Comparison of the semi-empirical battery degradation with the energy-throughput model by considering different number of cycles.

It can be seen that the number of cycles determines the slope of the degradation curve- the larger the number of cycles, the slower the degradation takes place. When using the semi-empirical model, the estimated total degradation is between the one of the energy throughput model of 4500 cycles and that of 6000 cycles. In addition, it can be seen that semi-empirical model degrades significantly more rapidly in the first two years in comparison to the rest of the battery's lifetime.

A separate set of four optimization runs was performed to investigate the impact on the number of cycles on the total degradation and the NPC. RB dispatch has been considered while taking into account switch degradation. Fig. 6.5 shows how the total degradation and NPC change depending on how many cycles have been considered.



(a) Comparison of total degradation between different battery degradation models.

(b) Comparison of NPC between different battery degradation models.

Figure 6.5: Comparison of total degradation and NPC between different battery degradation models while using RB dispatch and considering switch degradation.

The total degradation values correspond with the ones in Fig. 6.4, to which a degradation of 10 years has been modeled. It can be noticed that there is a direct correlation in the relative changes in the total degradation with the relative changes in NPC between the four cases. The difference in the NPC between the energy throughput model considering 3000 cycles and the one considering 6000 cycles reaches 25%. In the next section it will be shown that the battery degradation model does not have a great influence on the configuration of the component sizing, however, the difference in NPC can be very crucial when considering the feasibility of a specific project or planning the budget.

Therefore, since the necessary analysis would be too extensive to consider different number of cycles for the energy throughput model it was decided to use a fixed value of 4500 cycles when performing the optimization runs. However, it is important to be aware of the influence of the choice made when using the energy-throughput model.

As introduced in Section 4.2.3 the chosen degradation model distinguishes between calendar and cyclic ageing for the semi-empirical degradation model. Fig. 6.6 shows a decomposition of the cyclic and calendar ageing of the span of ten years in the context of the use case.

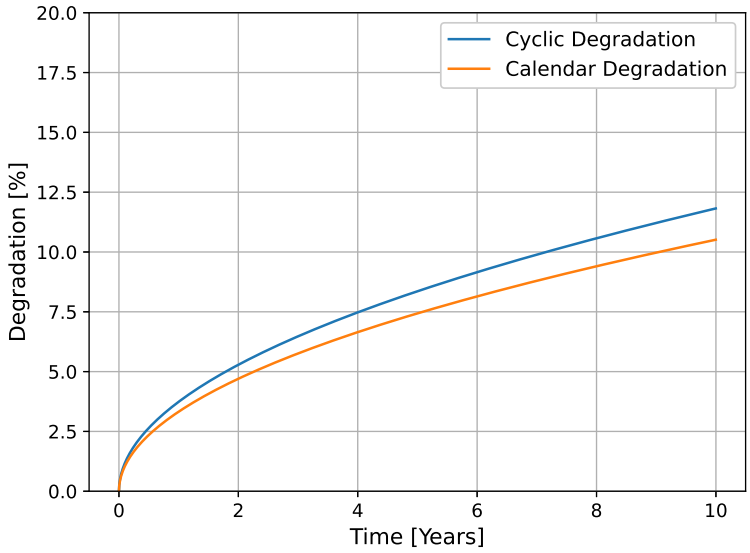


Figure 6.6: Calendar and cyclic degradation for the SE-SD case.

It can be seen that the cyclic and calendar ageing contribute roughly equally to the total degradation with the difference in year 10 of around 1% in absolute value (10% in the relative value). This figure is presented to show the general behaviour, however, the figure would change for every optimization run. In the cases when the optimal battery size is slightly oversized it has been observed that calendar ageing can contribute more than cyclic ageing since the SOC limits are often not reached.

6.3 Impact of switch degradation

To illustrate the difference between the sizing and dispatch between the cases when switch degradation is considered in comparison to when it is not Fig. 6.7 shows the PV dispatch of both cases. The PV capacities are sized according to the results of the sizing optimization. Semi-empirical battery degradation model has been considered.

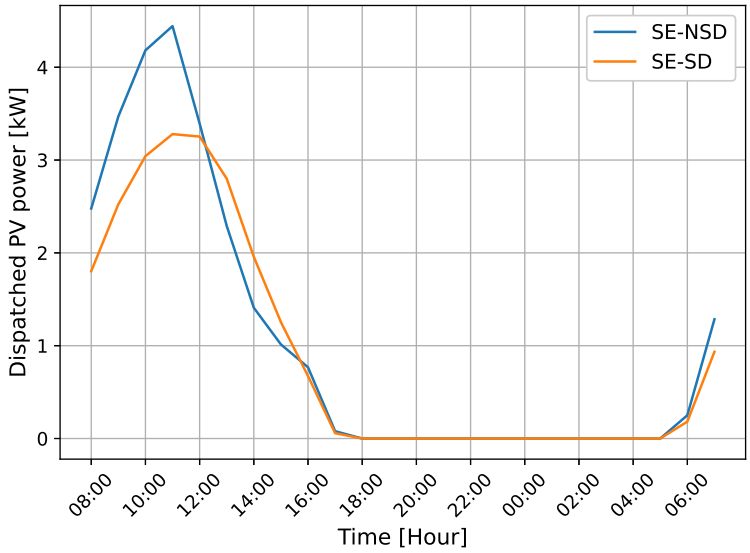
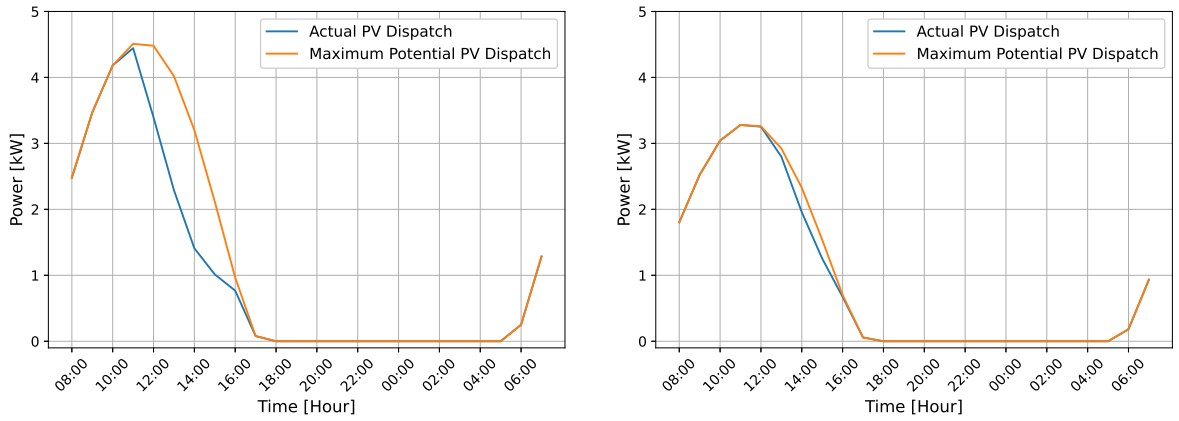


Figure 6.7: PV dispatch comparison between the cases when switch degradation has not been considered and when it has been considered.

It can be seen that the dispatched PV curve of SE-SD case is smoother than in SE-NSD case. This is because in SE-SD case the dispatch curve closely follows the maximum PV curve whereas in SE-NSD case there is a steep drop around 13:00 at which point the PV power has been curtailed. This is further illustrated in Fig. 6.8 where both cases have bee plotted against the maximum dispatchable PV power.



(a) Dispatched PV power and the maximum potential dispatchable PV power in SE-NSD case.

(b) Dispatched PV power and the maximum potential dispatchable PV power in SE-SD case.

Figure 6.8: Dispatched and maximum possible dispatchable PV power in SE-NSD and SE-SD cases.

It can be seen that the capacity of the solar panel array in the SE-NSD case in Fig. 6.8a is larger as the maximum dispatchable power is higher. However, since the load is the same for both cases it results in large curtailment once the battery is fully charged. In contrast in Fig. 6.8b it can be seen that the capacity of the solar panel array has been opimized to minimize the curtailment and fully use the generated solar power.

The average SOC of the battery over the representative days in both cases has been shown in Fig. 6.9.

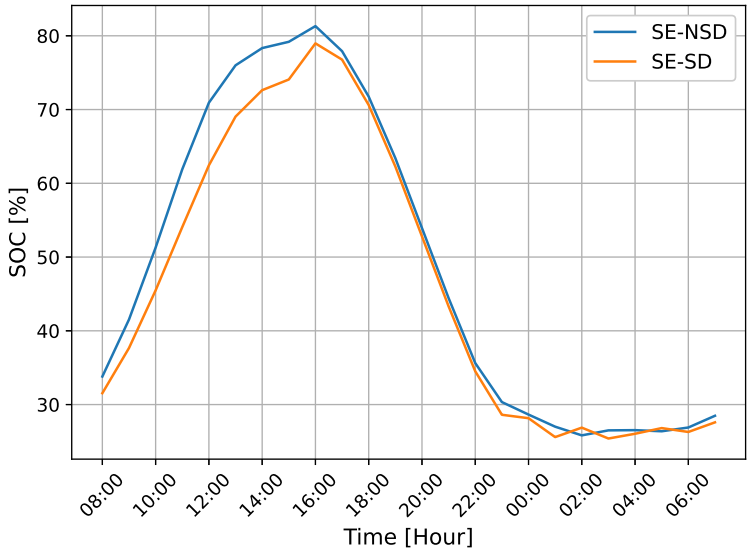


Figure 6.9: Battery SOC for the SE-NSD and SE-SD cases of RB dispatch optimization.

It can be seen that the average SOC of the battery in the SE-SD case is lower than in the SE-NSD case, since the solar panel array has a lower capacity. At the same time, the capacity of the battery is almost unchanged since it is needed to store the excess energy produced by the generator such that it can work at full capacity and hence higher efficiency.

Finally, Fig. 6.10 shows the difference in the switch temperature profile over the day when compared between both cases.

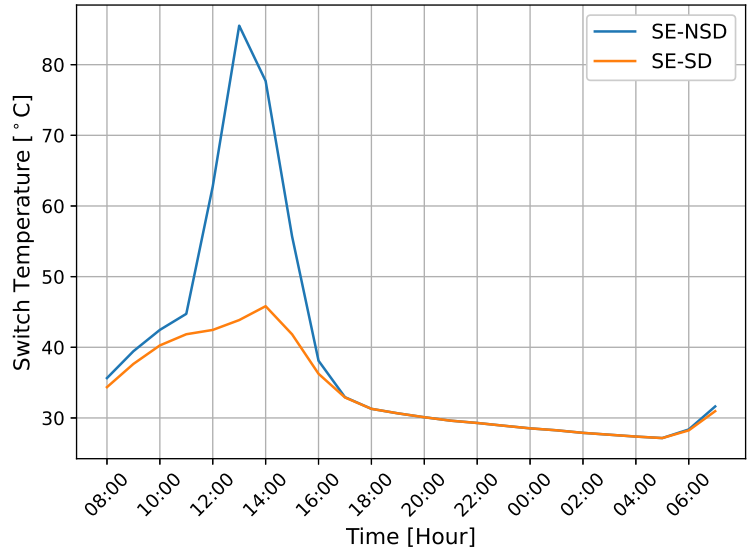


Figure 6.10: Switch temperature comparison between the cases when switch degradation has not been considered and when it has been considered.

In the SE-NSD case the temperature rises significantly higher than in the SE-SD - maximum temperatures of 85 °C and 45 °C respectively. The larger maximum switch temperature in the SE-NSD case leads to more severe degradation and ultimately requires the inverter to be replaced sooner than in the SE-SD case. The resulting switch degradation for the SE-NSD case and the SE-SD case is 65% and

2%, respectively. It is important to note however that these percentages do not reflect the actual degradation of the switch as there are too many variables, which cannot be accounted for by using Bayerer's degradation model. For example, the choice of the heatsink and the cooling system of the switches can influence the lifetime since better cooling systems will keep the switch temperature lower and hence reduce the degradation. Instead, the percentages are meant for relative comparison to indicate that in one case the degradation would take place more and hence reduce the lifetime of the switch. This is connected back to the results of Chapter 5 where the comparison of degradation depending on the current profile was relatively and not in absolute values.

6.4 Dispatch Optimization

This section first provides a comparison between the PSO and RB dispatch in Subsection 6.4.1. Afterward, in Subsection 6.4.2 results of an optimization run done on 20 years of load by using RB dispatch are presented.

6.4.1 Comparison between RB and PSO dispatch optimization

Given the random nature of the PSO the resulting optimum solutions when using PSO differ from one run to another. If the PSO produced the same result every time it could indicate that it is overfitted or that it is falling into a local optimum. Even for very simple problems there is usually a difference between the solutions in the order of a fraction of the percent. However, this difference rises as the complexity of the problem is increased. If the resulting solution for the dispatch optimization differs too much between the runs it has a direct influence on the sizing optimization problem as well. In addition, it makes it more difficult to compare between different cases and other algorithms (in this case RB).

To explore the variability of PSO solutions a dispatch optimization problem was set up with the component capacities, which were deemed optimal in the case of RB dispatch when considering semi-empirical degradation and switch degradation. The capacity of the solar panel array in the dispatch was set to 6.7 kW while the battery capacity was set to 29.5 kW. Five runs of the PSO algorithm were done to determine the optimal dispatch and correspondingly the daily average OPEX. The results have been summarized in Table 6.4.

Table 6.4: Dispatch optimization results for a run of a rule-based optimization and for five runs of the PSO-based optimization for the SE-SD case.

Type of optimization	Number of the run	Daily OPEX [EUR]
RB	1	2.56
PSO	1	2.27
PSO	2	2.93
PSO	3	2.36
PSO	4	2.57
PSO	5	2.66

It can be seen that there is a spread of the resulting OPEX for the PSO optimization values with the difference between the maximum and minimum being in the range of 20%. Coincidentaly the average daily OPEX of the five runs of PSO matches with the daily OPEX value of 2.56 EUR evaluated by the RB dispatch optimization. Whether a 20% difference in the optimization results is satisfactory depends on the needs of the user, however, for the purposes of this project the difference is larger than aimed for. It makes it more difficult to do comparisons between different models. However, this applies only to the dispatch optimization and not sizing optimization. During the sizing optimization there are many particles exploring the component capacities. Since the solutions of the dispatch optimization for nearby particles in the sizing swarm should result in similar OPEX, it is expected that it would compensate for the shown challenge and still would be able to look for the cheapest sizing configuration effectively.

Next, a comparison between RB and PSO dispatch optimization is done for three different sizing configurations - optimal configuration (based on RB optimization); configuration with an oversized solar panel array; configuration with and undersized solar panel array. The configurations have been selected in the range that matches the results in Section 6.5. The overview of the results can be seen in Table 6.5, Table 6.6 and Table 6.7. The rows corresponding to the PSO present results based on the average of three consecutive runs to consider the possible differences from one run to another.

Table 6.5: Comparison of the optimization solutions between RB and PSO dispatch for PV capacity of 6.5 kWp and battery capacity of 30.0 kWh.

Optimizaiton Algorithm	Daily OPEX [EUR]	Daily Battery Throughput [kWh]	Daily Generator Throughput [kWh]	Total Battery Degradation [%]	Total Switch Degradation [%]
RB	2.6	42.2	12.3	17.7	2.2
PSO	2.9	35.7	11.0	18.3	66

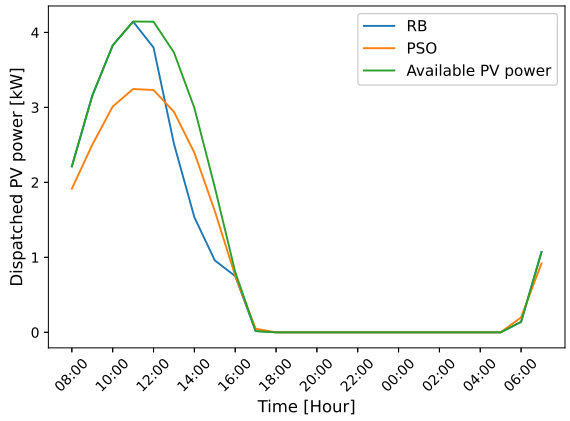
Table 6.6: Comparison of the optimization solutions between RB and PSO dispatch for PV capacity of 7.8 kWp and battery capacity of 30.0 kWh.

Optimizaiton Algorithm	Daily OPEX [EUR]	Daily Battery Throughput [kWh]	Daily Generator Throughput [kWh]	Total Battery Degradation [%]	Total Switch Degradation [%]
RB	3.9	43.2	10.1	18.2	44
PSO	3.0	38.9	8.9	17.6	74

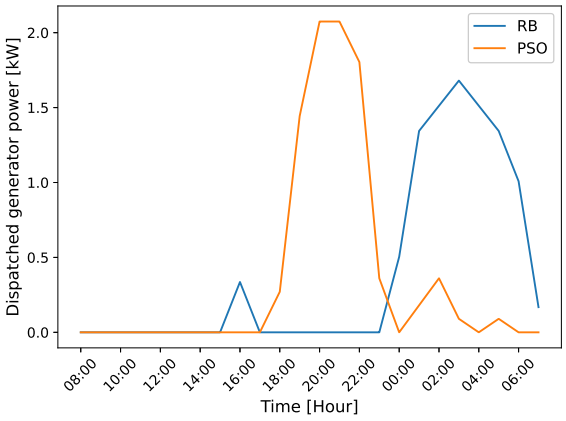
Table 6.7: Comparison of the optimization solutions between RB and PSO dispatch for PV capacity of 5.2 kWp and battery capacity of 30.0 kWh.

Optimizaiton Algorithm	Daily OPEX [EUR]	Daily Battery Throughput [kWh]	Daily Generator Throughput [kWh]	Total Battery Degradation [%]	Total Switch Degradation [%]
RB	3.1	41.0	15.8	17	0.5
PSO	2.8	33.4	13.6	18.2	15.9

It can be seen from the tables that RB optimization is capable of finding a cheaper solution for dispatch if the sizing is chosen accordingly to the intention of the RB dispatch design. It means that the solar panel and the battery capacities are sized such that all the excess PV power can be stored in the battery. On the other hand, if the solar panel array is oversized then the curtailment does not take place in a smart matter and the switch degradation is enhanced. An example of the dispatched PV power for the oversized case can be seen in Fig. 6.11a.



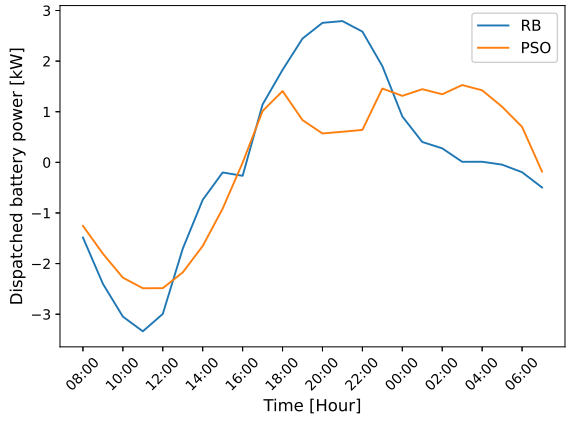
(a) Dispatched PV power for RB and PSO optimization .



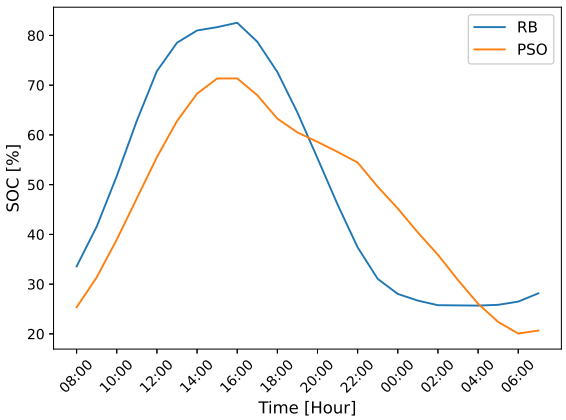
(b) Dispatched generator power for RB and PSO optimization .

Figure 6.11: PV and diesel generator dispatch for RB and PSO optimization for SE-SD case with oversized solar panel array.

It can be observed that the RB method attempts to follow the maximum PV curve as long as possible until it has to curtail the power rapidly since the battery is fully charged. PSO instead curtails the power more evenly. It can be seen that the switch degradation is still higher for PSO optimization, however, comparitively between the optimal size and the oversized configurations, switch degradation has increased significantly more for the RB dispatch than for PSO. Fig. 6.11b shows the power supplied by the diesel generator. It can be noticed that the RB dispatch performs most of the dispatch starting from 00:00 until 06:00 while the peak for the PSO takes place at 20:00. In Fig. 6.2, it can be seen that the peak load takes place between 18:00 and 22:00, which corresponds to the dispatch of the diesel generator in the PSO algorithm. Such an approach is better than the one utilized by the RB dispatch because in such a manner less cycling of the battery takes place. RB dispatch uses the generator when the electrical load levels are lower, which means that the battery has to be charged to maintain high efficiency. After an hour or two of charging, the dispatch algorithm lets the battery discharge the power that has been stored, and the pattern repeats. PSO instead dispatches the generator when there is peak load, which means that the battery does not have to be used much. Then later during the night the battery is steadily discharged to supply the lower load levels. This also corresponds with the battery dispatch profile and the corresponding SOC depicted in Fig. 6.12.



(a) Dispatched battery power for RB and PSO optimization.



(b) SOC curve for RB and PSO optimization.

Figure 6.12: Dispatched battery power and the corresponding SOC curves for RB and PSO optimization.

Finally, it can be observed in Table 6.7 that in the case of an undersized PV array the curtailment has been reduced due to the smaller size of the solar panel array, which means that most of the power is used to supply the electrical demand or charge the battery. The daily OPEX is by 10% lower for the PSO dispatch largerly due to the previously explained difference in the timing of the diesel generator dispatch.

6.4.2 OPEX changes over the years

In this Subsection it is inspected how the OPEX and other performance variables change if dispatch is performed for a load data of 20 years. In this case RB dispatch optimization is used with a constant yearly load which has been extracted by using RAMP. This section only aims to support the reasoning for the method chosen to evaluate OPEX over the years and correspondingly NPC as introduced in Section 4.2.4. Fig. 6.13 and Fig. 6.14 show how the OPEX and the energy throughput of the generator and battery linearly change over the years as the battery degrades in capacity. The curves have been normalized with the values of the first year.

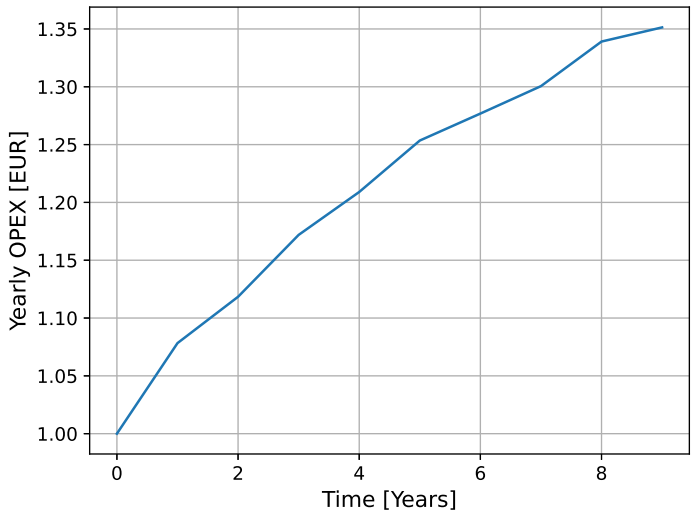
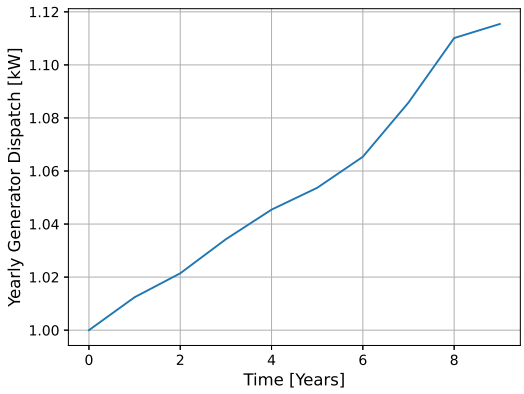
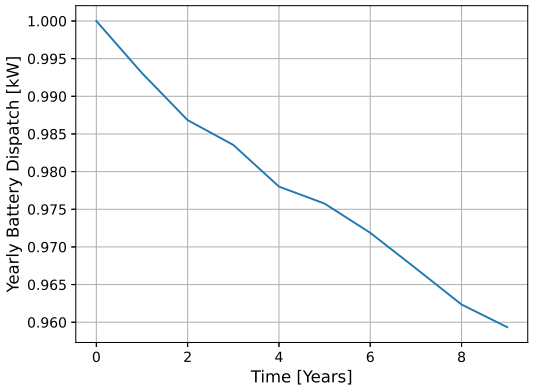


Figure 6.13: Yearly normalized OPEX changes over 10 years.



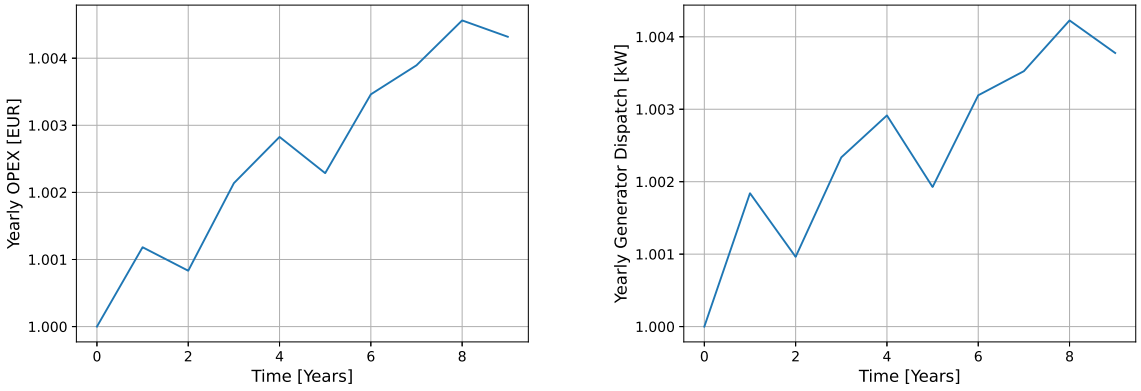
(a) Yearly normalized generator throughput changes over 10 years.



(b) Yearly normalized battery throughput changes over 10 years.

Figure 6.14: Yearly normalized changes in generator and battery throughput.

The generator energy throughput increases while the battery throughput decreases, which follows the expectations. As the battery degrades it can be expected that less energy can be cycled through and correspondingly it has to be compensated by the generator. However, this would be the case only for an optimized sizing. Fig. 6.15 depicts a situation with oversized components where it can be seen that the OPEX and the yearly generator throughput changes marginally.



(a) Yearly normalized OPEX changes for a second optimization example.

(b) Yearly normalized generator throughput changes for a second optimization example.

Figure 6.15: Yearly normalized changes in OPEX and generator throughput for another optimization case.

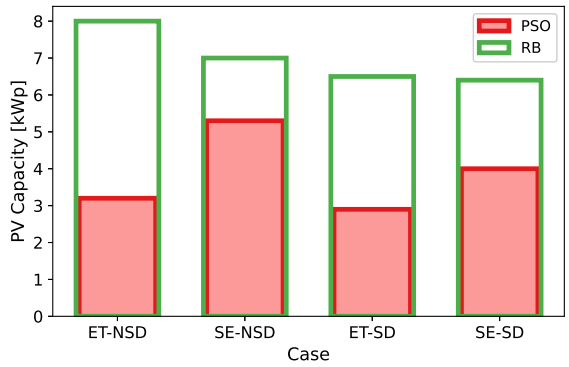
Hence, it has been shown why it is difficult to accurately estimate the OPEX changes over the years, and more research is needed to come up with a cost function which takes the component capacity into account to determine the OPEX changes over the years. The situation becomes even more complex to analyze as the load changes and the degradation of the solar panel array is taken into account.

6.5 Sizing Optimization Results

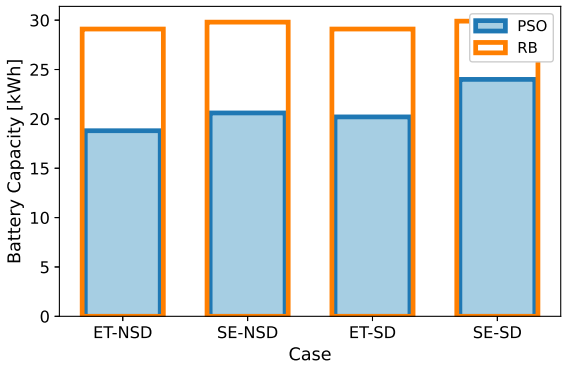
The sizing optimization was performed for both the RB method presented in Section 4.2.5 and with the nested PSO algorithm presented in Section 4.2.4. It has to be noted that due to a lately found error in the calculation of the NPC it was not possible to run the PSO algorithm for the full range of representative days due to the large computation times. Instead 6 representative days were taken. The impact of this has been analysed at the end of the section.

Both optimizations were performed for the four cases listed in Table 6.3. The four cases have been compared based on the performance parameters listed in Subsection 4.2.5. Namely, the component capacities, daily curtailment, battery and switch degradation as well as CAPEX, OPEX and NPC have been compared and analysed between the four cases.

The final sizing capacities for different cases for the solar panel array and the battery electricity storage can be seen in Fig. 6.16.



(a) PV capacity for different cases of PSO and RB sizing optimization.



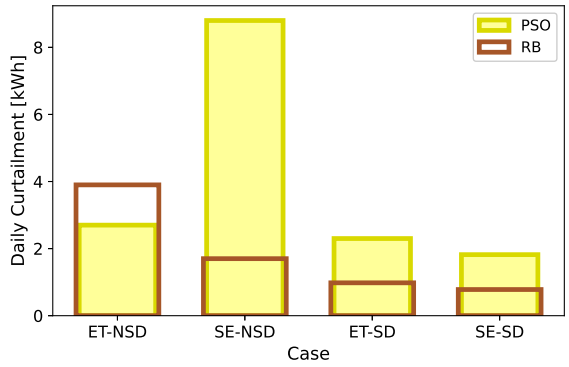
(b) Battery capacity for different cases of PSO and RB sizing optimization.

Figure 6.16: PV and battery capacities for different cases of PSO and RB sizing optimization

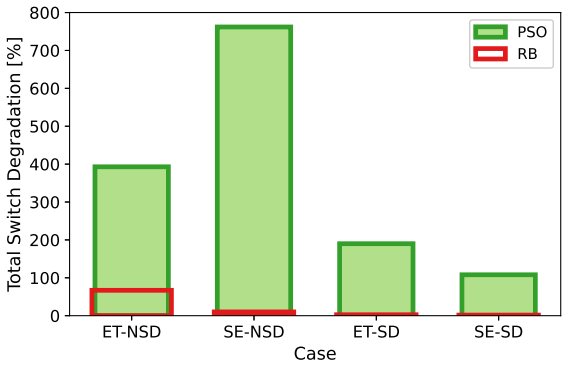
It can be seen in Fig. 6.16a that there is a decrease in the solar panel capacity for the cases when switch degradation cost is considered in the optimization. There is a drop in PV capacity between the cases ET-NSD and ET-SD as well as between the cases SE-NSD and SE-SD. For the RB dispatch the decreases correspond to 19% and 10% respectively while for the PSO dispatch the correspond to 10% and 30 % respectively. There does not seem to be a clear correlation between changes in the battery degradation model and the PV capacity as the capacity is lower for the semi-empirical model in case of RB and higher in the case of PSO .

In Fig. 6.16b it is visible that the battery capacity stays very stable for different cases. A slight exception can be seen for SE-SD case for PSO optimization where the battery capacity is by roughly 25% higher than for the rest of the cases. Overall the capacity of the battery is slightly higher in the cases when semiempirical model is used.

Daily energy curtailment and the total switch degradation after 10 years of operation can be seen in Fig. 6.17. Since the switch degradation for both optimization algorithms covers a large range an overview with the magnitudes of switch degradation for each case have been provided in Table 6.8.



(a) Daily energy curtailment for different cases of PSO and RB sizing optimization.



(b) The extent of switch degradation after 10 years for different cases of PSO and RB sizing optimization.

Figure 6.17: Daily curtailment and the switch degradation for different cases of PSO and RB optimization

Table 6.8: Overview of switch degradation for RB and PSO optimization for the four considered cases.

	ET-NSD	SE-NSD	ET-SD	SE-SD
RB	67 %	10 %	2.5 %	1.6 %
PSO	393 %	762 %	190 %	108 %

It can be seen that the curtailment and switch degradation are directly correlated as expected based on the conclusions of Chapter 5. Both the curtailment and switch degradation decrease by more that half when switch degradation cost is considered inside the optimization. The only exception is between the case ET-NSD and ET-SD for the PSO optimization where the decrease is 15%. The consistent decrease in curtailment when switch degradation is considered indicates that switch degradation cost is comparable in the amplitude with the battery degradation cost and the fuel cost since optimization algorithm takes it into account and correspondingly adjusts the size of the solar panel array and the dispatch. It can be that the drop in PV capacity was also lower between ET-NSD and ET-SD cases for PSO optimization.

Fig. 6.18 depicts the battery degradation after ten years for the four cases when both optimization approaches are performed.

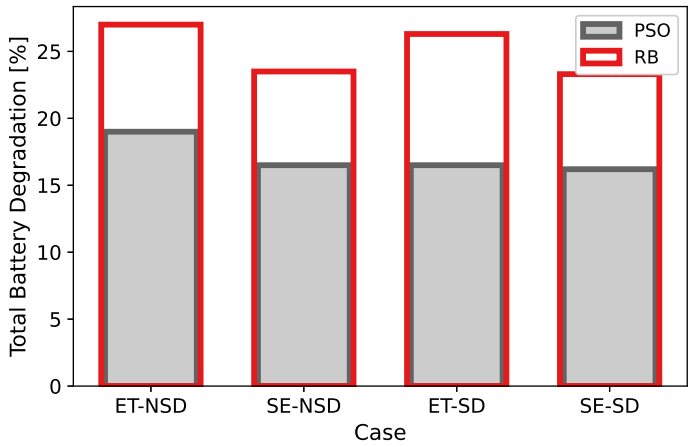
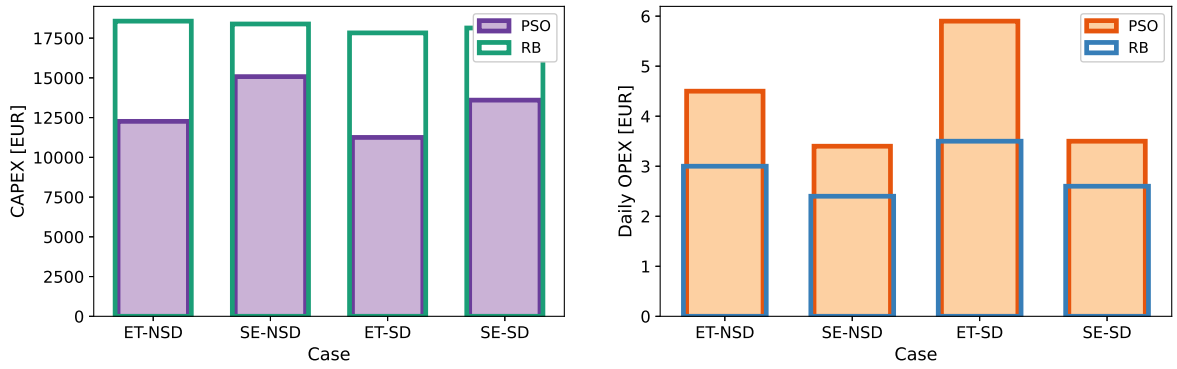


Figure 6.18: Battery degradation after 10 years for different cases of PSO and RB sizing optimization.

It can be seen that the total degradation is lower in the case of the semi-empirical model. For the RB dispatch there is a decrease between 10% and 15% for both switch degradation cases. Similarly there is a decrease of 15% between the ET-NSD and SE-NSD cases for the PSO dispatch. However, the difference between ET-SD and SE-SD for PSO dispatch is only 2%. Nevertheless, the overal behaviour matches with Fig. 6.4 where it was shown that semi-empirical degradation model overal estimates lower degradation after 10 years when compared with the energy throughput model of 4500 cycles. It can also be seen that PSO algorithm results in an overall lower battery degradation than the RB dispatch. This matches with the discussion in Subsection 6.4.1 where it was shown that RB dispatch cycles battery more due to the different time window of diesel generator dispatch.

The comparison of CAPEX and daily OPEX has been provided in Fig. 6.19.



(a) CAPEX for different cases of PSO optimization.

(b) OPEX for different cases of PSO optimization.

Figure 6.19: CAPEX and daily OPEX for different cases of RB and PSO sizing optimization.

Since the battery capacity is relatively stable across different cases, CAPEX is mostly affected by changes in PV capacity. Something that has to be reminded is that the CAPEX calculation changes depending on whether or not the switch degradation is considered. If not considered, the inverter cost is part of CAPEX while if not considered, then the inverter cost is part of OPEX. This is an aspect that should be improved in future versions of the algorithm, as it can influence comparisons. It can therefore be seen that there is a slight decrease between the NSD and SD cases for both dispatch algorithms. It is caused by the shift of the inverter cost from CAPEX to OPEX. Nevertheless, there can be seen a clear correlation between the PV capacities in Fig. 6.16a and the CAPEX.

Correspondingly an opposite behaviour can be seen in the OPEX chart where there is an increase in OPEX between NSD and SD cases as the switch degradation is moved from CAPEX to OPEX. There is a drop in OPEX between the ET and SE cases, which can partially be explained by the decrease in the total battery degradation shown in Fig. 6.16b. However, mainly OPEX is related to the energy generated by the diesel generator as it constitues the largest share of OPEX. The generator energy throughput comparison between the cases can be see in Fig. 6.20.

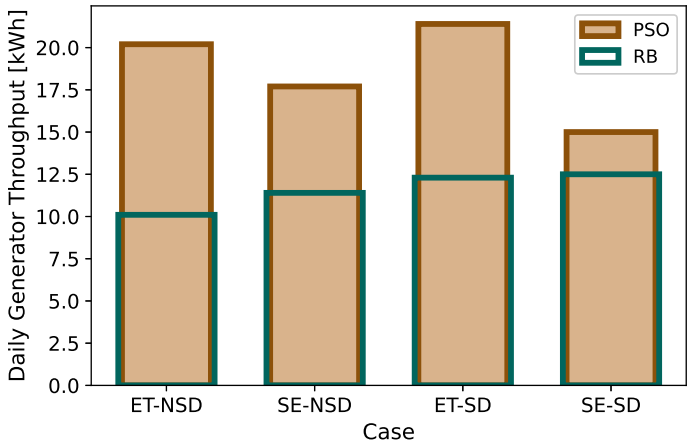


Figure 6.20: Daily energy throughput for different cases of RB and PSO dispatch algorithms inside sizing optimization.

There can be seen a clear correlation between the generator energy throughput and the OPEX in the case of PSO dispatch. However, the correlation is not present for the RB dispatch algorithm. The most likely reason for the mismatch is the fact that RB likely operates in suboptimal efficiency points of the generator, therefore, it would be better to compare the OPEX with fuel consumption. Unfortunately,

due to time constraints, the fuel consumption plot was not made, as the fuel consumption has to be extracted back from the fuel efficiency curve presented in Section 4.2. However, it can also be noticed that the sizing optimization utilizing PSO ends up with between 25% and 100% more energy generated by the generator than the RB. This makes sense as the optimization is only based on the NPC. On the other hand, the RB method was specifically designed to reduce fuel consumption [124].

Finally, the NPC of the sizing optimization for both dispatch approaches for the four cases can be seen in 6.21.

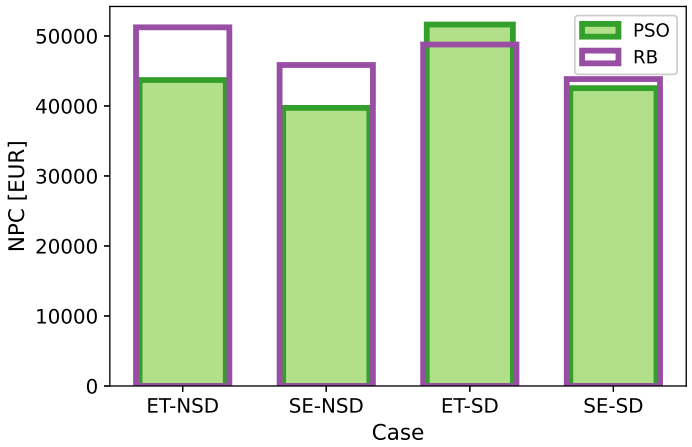


Figure 6.21: NPC for different cases of PSO and RB sizing optimization.

Since NPC is calculated from CAPEX and OPEX the differences between the cases can be correlated with the differences in the previously covered CAPEX and OPEX. To observe the general behaviour it can be seen that SE cases generally result in lower NPC than ET cases. At the same time, SD cases result in higer NPC than NSD cases for the nested PSO sizing and lower NPC for RB-based optimization. Finally, it can be seen that the sizing algorithm utilizing PSO has resulted in cheaper solution in three out of four cases. However, it has to be returned to the fact that only 6 representative days were used instead of 40. To see the possible differences that it could have cause the dispatch has been rerun for the found capacities with 40 representative days instead of 6 and the results are summarized in Table 6.9. Once again the average of three consecutive runs is taken for the dispatch optimization runs of 40 representative days.

Table 6.9: Comparison between the OPEX of 6 representative days and 40 representative days.

	ET-NSD	**SE-NSD**	**ET-SD**	**SE-SD**
6 representative days	4.5 EUR	3.4 EUR	5.9 EUR	3.5 EUR
40 representative days	5.2 EUR	3.5 EUR	5.4 EUR	4.1 EUR

It can be seen that there is a maximum difference of 15% between the OPEX values of 6 and 40 representative days. Given that the analysis of the results only aims to find correlations and patterns between different parameters, the difference range is acceptable. However, it can only be concluded that nested PSO sizing optimization can only find cheaper solutions when switch degradation is not considered, while it is not possible to say the same for the cases when switch degradation is considered. It has to finally be mentioned that Fig. 6.21 shows that the total cost of the system varies depending on the models of degradation of the components considered. The difference in NPC when considering different battery or switch degradation models can reach 10- 15%. However, more importantly, it was shown that the PV capacity varies greatly depending on the degradation models considered. Therefore, the analysis has shown that the type of degradation models used can have a great influence on the final portfolio of the chosen component capacities and correspondingly the dispatch.

To conclude the section computation times have been provided for different cases and both dispatch optimization algorithms as shown in Table 6.10. The dispatch runs have been done with 40 representative days and for both algorithms 3 consecutive runs are done from which the average computation time has been taken. The model of the computer on which the algorithms have been run is Lenovo Thinkpad P1 (2019) with 16GB of installed RAM and Intel Core i7 2.2GHz processor. It has to be noted once again that the sizing optimization for PSO dispatch was done for 6 representative days instead of 40. Therefore, it is expected that the nested PSO optimization would take noticeably longer than shown in the table. Nevertheless, it can be seen that nested-PSO optimization with 6 representative days takes more than 1000 times longer than the sizing optimization when using RB dispatch. This illustrates the greatest disadvantage of using nested optimization.

Table 6.10: Comparison of computation time for different cases for RB and PSO dispatch and sizing.

	RB Dispatch	**RB Sizing**	**PSO Dispatch**	**PSO Sizing**
ET-NSD	4 s	22 s	175 s	8 h
SE-NSD	6 s	27 s	214 s	10.1 h
ET-SD	11 s	32 s	223 s	9.4 h
SE-SD	14 s	42 s	244 s	10.7 h

It can also be seen that the increase in the computation time between the simplest case of ET-NSD to the most complex case in SE-SD is 250% for RB dispatch, 90% for RB sizing, 40% for the PSO dispatch and 25% for PSO sizing optimization. The large slowdown for RB dispatch is largely due to the overhead of calling Numba functions, which have been designed to make the PSO optimization faster, however, do not work well for RB dispatch. However, given that the RB optimization is relatively much faster, there was not much focus during the thesis project on improving the speed of the RB dispatch algorithm.

By comparing the computation times between the cases of both battery degradation models, it can be derived that the increase in computational times for the RB dispatch and sizing optimization varies between 20% and 50%. For the PSO-based dispatch optimization and sizing the increase varies between 10% and 25%. In comparison, the introduction of the switch degradation model causes an increase in computational time of around 250% for RB dispatch and 40% for RB-based sizing. The increase in computational time for the PSO dispatch optimization is roughly 20%. The increase for nested PSO sizing optimization is between roughly 10%.

6.6 Environmental Cost

To find the configurations of component capacity that would allow to reduce the dependency on the diesel generator a ”carbon tax” was introduced as explained in Subsection 4.2.4. The optimization runs for different rates of the ”carbon tax” have been performed on the RB model with semi-empirical battery degradation model and switch degradation in consideration. Since the PSO algorithm takes significantly more time to run it was not possible to repeat the analysis for the proposed algorithm. Fig. 6.22 shows a graph showing the fraction of energy provided by the diesel generator as a function of the ”carbon tax”. ”Carbon tax” is expressed as a relative percentage of increase to the base price of diesel.

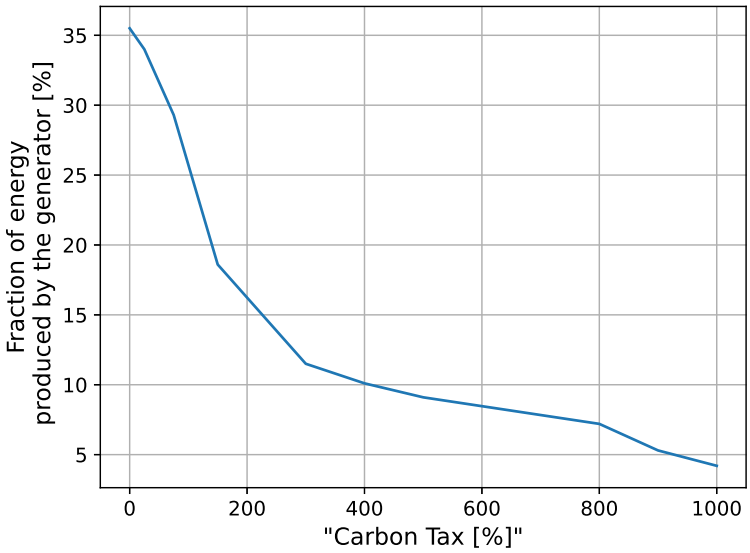


Figure 6.22: Sizing by introducing a ”carbon tax” in case of RB dispatch, semi-empirical battery degradation model and switch degradation considered.

It can be seen that there is knee point around a value of 300% after which the gain in reduced fuel consumption as opposed to the increase in fuel price decreases. Nevertheless it is still possible to find configurations of component sizing where very low fuel consumption is reached. An overview of component capacities for every setting of the ”carbon tax” as well as the resulting NPC values have been provided in Table 6.11. The resulting NPC is by 90% higher than the base case for a configuration, which complies with the goal of OnePower of having less than 5% of the electricity be generated by the diesel generator.

Table 6.11: Sizing and fuel fraction for different applied carbon tax amounts.

”Carbon tax” [%]	PV Capacity [kWp]	Battery Capacity [kWh]	Generator Energy Fraction [%]	NPC [EUR]
0	6.7	29.3	35.5	41,472
25	6.9	30.0	34.0	44,380
75	7.3	32.7	29.3	50,056
150	8.4	39.3	18.6	54,865
300	9.1	46.0	11.5	61,607
500	9.6	46.6	9.1	67,553
800	9.7	54.8	7.2	75,086
1000	10.4	58.0	4.2	78,006

To conclude the chapter the main takeaways have been summarized based on the results from the various runs and comparison of the different cases for both dispatch and sizing optimization:

- The choice of the number of cycles for the energy throughput battery degradation has a great influence on the final cost estimation.
- Switch degradation has a direct correlation with the amount of curtailed power, which is consistent with the results presented in Chapter 5.
- The selected PV capacity and the dispatch algorithm has a direct impact on the amount of curtailed power and hence the inverter lifetime.

- The proposed PSO dispatch algorithm has a larger variability between different runs than hoped, nevertheless, it shows higher flexibility in finding optimal dispatch strategies for different component configurations than RB dispatch does.
- Although the final battery capacity is not influenced much by the change in component degradation models, there are significant changes in the optimal PV array capacity.
- Nested-PSO sizing optimization has a bottleneck in keeping the computation time low, however, it has been shown that it can potentially lead to cheaper solutions.

Chapter 7

Conclusions and Suggested Future Improvements

7.1 Conclusions

In Chapter 1 four research questions were derived to answer the the main research question of: **How to optimally size a microgrid in sub-Saharan Africa under dry climate with high irradiation while considering consumer behaviour uncertainty and component degradation?** The main research question was answered by designing a nested sizing-dispatch algorithm based on particle swarm optimization, which models the battery degradation model through a semi-empirical model proposed by Schimpe et al. [188] and models the switch degradation based on the work of Alpízar-Castillo et al. [102]. In addition, the switch degradation model was investigated in a practical setup, and it was shown that switch degradation is indeed dependent on dispatch decisions, which can reduce its lifetime by more than half.

By using the designed algorithm together with a second sizing algorithm, which makes use of the rule-based dispatch presented in [124] by Cicilio et al. investigation of the effects of component degradation and optimization approach was done. Furthermore, by adjusting the fuel price, it was also shown that it is possible to design the microgrid in which less than 5% of the generated energy comes from the diesel generator, although the NPC of this microgrid increases by almost 100%.

The three proposed research questions are repeated below with the corresponding answers based on the results of the thesis project.

1. How does the inclusion of the battery and solar panel inverter switch degradation influence the solution of the sizing and EMS optimization problem(s) and the computation time?

It has been shown that battery and inverter degradation models have a great influence on the PV capacity, the dispatch decisions, as well as the final cost of the system. The results also indicate that the influence on battery capacity is less noticeable. The results indicate that the optimal PV capacity can change by up to 30% depending on the battery and switch degradation models chosen. It was also shown that when switch degradation was considered the amount of curtailed PV power could reduce by up to 75% showing that when switch degradation is considered the dispatch strategy has to be adjusted to minimize the degradation and hence the final cost of the system. Finally, the net present cost was shown to change depending on the chosen degradation models, with differences of up to 15%.

A comparison between the computation times revealed that the time needed to solve the optimization problem upon the introduction of the semi-empirical battery degradation model increases by 25% to 50% in comparison to when energy throughput model is used. The increase in computation time upon the introduction of the switch degradation model is around 50% for the RB-based optimization and between 15% and 25% for the PSO-based optimization.

2. How do the results of the microgrid sizing optimization compare between a nested microgrid sizing-dispatch optimization with a non-nested optimization?

It has been shown that the PSO dispatch optimization algorithm is more flexible than the rule-based dispatch as it can find cheaper dispatch strategies at different component sizing configurations. However, PSO has also presented challenges with consistency between different runs, which should be improved if it is desired to use the algorithm for future research. The nested PSO optimization algorithm has been able to find cheaper microgrid sizing configurations when switch degradation is not considered by using the diesel generator more actively and smarter. The differences in the final cost between the nested PSO and RB optimization still need to be investigated once the consistency of the PSO dispatch algorithm is improved. Finally, the nested PSO sizing optimization algorithm has a computation time which is more than 1000 times longer than the RB dispatch-based optimization algorithm, which in certain contexts might not be practical. Therefore, a trade-off between the accuracy in the solution and the computation time has clearly been shown.

3. How to experimentally test the influence of the solar power curtailment strategy on switch degradation inside the inverter without the need of doing long-term power cycling experiments?

The thesis project has come up with a design of a two-stage testing setup, which allows to compare the experimental results of switch degradation with circuit-based simulation software. The first stage involves the estimation of the switching losses, which allows to validate that the simulation can estimate the selected real-world circuit. The double-pulse testing setup was created by making use of the evaluation board produced by Wolfspeed, which allowed to measure the switching losses. The losses were used as an input for the simulation model to model the junction temperature inside the switches, which allowed to consequently model the degradation. The second stage of the experimental testing setup contained a boost converter to test the junction temperature of the switches under different current settings according to the work by Alpízar et al. On-resistance of the switch was used as a temperature-sensitive electrical parameter for the estimation of the junction temperature. The measurement data was used to create a lookup curve between different current amplitudes and the corresponding switch junction temperature. Finally, the results between the reference model, the experimental measurements and simulation were compared, showing that the current mission profile of the switch has indeed a great influence on the degradation of the switch. Unsuitable control strategies were shown to reduce the lifetime of the switch by more than 60% relative to a base mission profile. The use of the current-temperature curves allowed to avoid performing long power cycling tests as the curves could be directly used together with the mission profile provided in the reference model.

7.2 Future Improvements

The research during this project has also shown that there is room for improvement in the model to improve the accuracy of the results. Some of the suggestions on how to improve the model and the experimental setup have been provided below.

Microgrid sizing optimization algorithm:

- Validation of the battery degradation model - even if it might be too computationally costly to include a physics-based battery degradation model inside the optimization algorithm validation and comparison of the battery degradation can still be validated with it. The battery dispatch decisions can be extracted from the final solution and run through the physics-based model and the resulting battery degradation can be compared. LiiBRA package written with Julia programming language is an example of a package which could be used to achieve this task [205].
- Multi-objective optimization - the provided analysis of the decrease in the fraction of energy generated by the generator by increasing the fuel price provides insights into how it is possible to penalize the use of fossil fuels. Nevertheless, the analysis does not replace a full multi-objective optimization. A multi-objective optimization would be a more accurate approach since it would allow to more rigorously explore the solution space and to create a pareto-front of optimal solutions.

- Multi-year optimization - one of the objectives of the thesis project was to investigate the impact of the load growth on the solution of the optimzation problem. Due to the time constraints it was not possible to finish the investigation. Given that a multi-year RAMP feature has been developed during this project to facilitate this investigation a natural next step of this research is to investigate the impact of the assumptions about load growth on the solutions of the optimization problem.
- Distributions system losses and capacity limits - while originally the investigation of distribution system losses and capacity limits was part of the research questions of the project it was soon deemed to be unfeasible to implement in the proposed algorithm. To accurately determine the losses and the loading of the lines, power flow analysis would have to be done, which is very computationaly heavy tasks. It would likely be possible to implement the power flow calculations inside the dispatch optimization, but when implemented inside the sizing optimization it would not be possible to reach reasonable computational times.
- Reliability - in the context of the thesis it was assumed that the generator capacity is sized according to the maximum encountered load as is currently done by OnePower. This design choice has been made to make sure that everyone in the village is always supplied with electricity in case of ongoing periods without sun or in case there are technical problems with the solar panel array or the battery. Although this approach can provide a very high reliability it can result in an oversized system and suboptimal dispatch decisions as the generator might be forced to operate at low efficiencies. A study by Soto et al. explored the tradeoff between the system size and the unserved energy in [20]. A similar analysis could be done in this use case. In addition, it could be interesting to explore the option of replacing the diesel generator with two generators of half the capacity to potentially increase the operating point efficiencies.
- Weather uncertainty - in this thesis project a deterministic weather profile was used. Although the weather in Benin is relatively stable it still varies over the years. The use of typical meteorological year can be used, however, it still provides a fixed weather curve, albeit a more representative one. Ideally a stochastic weather profile model should be used or a Monte Carlo analysis could be performed with different weather profile scenarios.
- Socio-economical factors for the RAMP multi-year feature - The current version of the RAMP multi-year feature uses dummy parameters to project the load changes over time in such a manner showing a proof of concept. It would be desired to however replace these parameters with ones based on socio-economical studies about projections of the economical development of the studied regions.

Experimental Testing Setup:

- Fan placement - as mentioned in the discussion on the differences between the simulated and acquired current-temperature curves one of the influential factors could be the fan placement. If a further studies are done on the existing setup it is necessary to change the placement of the fan such that warm air is not blown on the switch.
- Testing Si IGBTs - to fully replicate the study done by Alp'izar-Castillo et al. in [102] it is necessary to build a setup which matches the conditions assumed in the study by using Si IGBT switches instead of SiC switches and by matching the values of the components used in the modeled Boost converter.
- Power Cycling Tests - to investigate how accurate the Bayerer model in combination with Miner's rule is, it is possible to perform power cycling tests. Since it would take too long (years) to degrade the switch to a failure point by directly applying the mission profile it could be possible to observe real-time degradation via TSEPs. $R_{\text{ds-on}}$ changes over time as an indicator for degradation is an active field of research [206].

References

[1] United Nations, *The 17 Goals*, 2015. [Online]. Available: https://sdgs.un.org/goals.

[2] "Sustainable development High-level political forum on sustainable development, convened under the auspices of the Economic and Social Council Progress towards the Sustainable Development Goals," Tech. Rep., 2023.

[3] L. Pellegrini and L. Tasciotti, "Rural electrification now and then: Comparing contemporary challenges in developing countries to the USA's experience in retrospect," *Forum for Development Studies*, vol. 40, no. 1, pp. 153–176, Mar. 2013, ISSN: 08039410. DOI: 10.1080/08039410.2012.732108.

[4] World Bank, *Access to electricity*, 2023. [Online]. Available: https://data.worldbank.org/indicator/EG.ELC.ACCS.ZS?view=chart.

[5] K. Nyarko, J. Whale, and T. Urmee, *Drivers and challenges of off-grid renewable energy-based projects in West Africa: A review*, Jun. 2023. DOI: 10.1016/j.heliyon.2023.e16710.

[6] O. Omole and P. Olatunde, "Challenges and Successes in Rural Electrification: a Review of Global Policies and Case Studies," *Engineering Science & Technology Journal*, vol. 5, no. 3, pp. 1031–1046, 2024, ISSN: 2708-8952. DOI: 10.51594/estj/v5i3.956. [Online]. Available: www.fepbl.com/index.php/estj.

[7] Our World in Data, *Population Density*, 2025. [Online]. Available: https://ourworldindata.org/grapher/population-density.

[8] D. Mentis, M. Howells, H. Rogner, *et al.*, "Lighting the World: the first application of an open source, spatial electrification tool (OnSSET) on Sub-Saharan Africa," *Environmental Research Letters*, vol. 12, no. 8, Jul. 2017, ISSN: 17489326. DOI: 10.1088/1748-9326/aa7b29.

[9] D. Palit and K. R. Bandyopadhyay, *Rural electricity access in South Asia: Is grid extension the remedy? A critical review*, Jul. 2016. DOI: 10.1016/j.rser.2016.03.034.

[10] A. S. Duran and F. G. Sahinyazan, "An analysis of renewable mini-grid projects for rural electrification," *Socio-Economic Planning Sciences*, vol. 77, Oct. 2021, ISSN: 00380121. DOI: 10.1016/j.seps.2020.100999.

[11] M. Torero, "The Impact of Rural Electrification: Challenges and Ways Forward," *Revue d'économie du développement*, vol. 23, no. HS, pp. 49–75, 2015. DOI: 10.3917/edd.hs03.0049.

[12] F. Adusah-Poku and K. Takeuchi, "Determinants and welfare impacts of rural electrification in Ghana," *Energy for Sustainable Development*, vol. 52, pp. 52–62, Oct. 2019, ISSN: 23524669. DOI: 10.1016/j.esd.2019.07.004.

[13] J. ; Peters and Sievert, "Impacts of rural electrification revisited - the african context," *Journal of Development Effectiveness*, vol. 8, pp. 327–345, 2016. DOI: 10.4419/86788637. [Online]. Available: https://doi.org/10.4419/86788637.

[14] E. L. Litzow, S. K. Pattanayak, and T. Thinley, "Returns to rural electrification: Evidence from Bhutan," *World Development*, vol. 121, pp. 75–96, Sep. 2019, ISSN: 18735991. DOI: 10.1016/j.worlddev.2019.04.002.

[15] F. Burlig and L. Preonas, "Out of the Darkness and into the Light? Development Effects of Rural Electrification," *Journal of Political Economy*, vol. 132, no. 9, pp. 2937–2971, Sep. 2024, ISSN: 0022-3808. DOI: 10.1086/730204.

[16] A. González-García, P. Ciller, S. Lee, R. Palacios, F. de Cuadra García, and J. I. Pérez-Arriaga, "A Rising Role for Decentralized Solar Minigrids in Integrated Rural Electrification Planning? Large-Scale, Least-Cost and Customer-Wise Design of Grid and Off-Grid Supply Systems in Uganda," *Energies*, vol. 15, no. 13, Jul. 2022, ISSN: 19961073. DOI: 10.3390/en15134517.

[17] K. Cabana-Jiménez, J. E. Candelo-Becerra, and V. S. Santos, "Comprehensive Analysis of Microgrids Configurations and Topologies," *Sustainability (Switzerland)*, vol. 14, no. 3, Feb. 2022, ISSN: 20711050. DOI: 10.3390/su14031056.

[18] S. Mandelli, J. Barbieri, R. Mereu, and E. Colombo, *Off-grid systems for rural electrification in developing countries: Definitions, classification and a comprehensive literature review*, May 2016. DOI: 10.1016/j.rser.2015.12.338.

[19] M. Jafari, G. B. Gharehpetian, and A. Anvari-Moghaddam, *On the Role of Virtual Inertia Units in Modern Power Systems: A Review of Control Strategies, Applications and Recent Developments*, Aug. 2024. DOI: 10.1016/j.ijepes.2024.110067.

[20] A. Soto, S. Balderrama, E. Cardozo, F. Miguel, Z. Jaime, and S. Qouilin, "Exploring the Trade-off between Installed Capacity and Unserved Energy in Rural Electrification," in *ECOS 2021 - 34th International Conference on Efficency, Cost, Optimization, Simulation and Environmental Impact of Energy Systems*, ECOS 2021 Program Organizer, 2021, pp. 994–1004, ISBN: 9781713843986. DOI: 10.52202/062738-0088.

[21] I. Fuchs, S. Balderrama, S. Quoilin, P. C. del Granado, and J. Rajasekharan, "Swarm electrification: Harnessing surplus energy in off-grid solar home systems for universal electricity access," *Energy for Sustainable Development*, vol. 77, Dec. 2023, ISSN: 23524669. DOI: 10.1016/j.esd.2023.101342.

[22] K. Watkins, "Lights, Power, Action: Electrifying Africa," Geneva, Switzerland, Tech. Rep., 2016. [Online]. Available: https://www.africa50.com/fileadmin/uploads/africa50/Documents/Knowledge_Center/APP_Lights_Power_Action_2016__PDF.pdf.

[23] Elsevier, *Scopus*, 2025. [Online]. Available: https://www.scopus.com.

[24] D. Fioriti, D. Poli, P. Duenas-Martinez, and I. Perez-Arriaga, "Multi-year stochastic planning of off-grid microgrids subject to significant load growth uncertainty: overcoming single-year methodologies," *Electric Power Systems Research*, vol. 194, May 2021, ISSN: 03787796. DOI: 10.1016/j.epsr.2021.107053.

[25] K. Anoune, M. Bouya, A. Astito, and A. B. Abdellah, *Sizing methods and optimization techniques for PV-wind based hybrid renewable energy system: A review*, Oct. 2018. DOI: 10.1016/j.rser.2018.05.032.

[26] Fioriti D., G. Lutzemberger, Poli D., and Micangeli A., "Optimal sizing and operation of isolated microgrids for developing countries hedging uncertainties with Monte Carlo techniques," in *IEEE PES Innovative Smart Grid Technologies Europe (ISGT-Europe)*, The Hague, Netherlands: IEEE, 2020, pp. 744–748, ISBN: 9781728171005.

[27] M. S. Drame, D. Diop, K. Talla, M. Diallo, B. D. Ngom, and B. Nebon, "Structural and physicochemical properties of dust collected on PV panels surfaces and their potential influence on these solar modules efficiency in Dakar, Senegal, West Africa," *Scientific African*, vol. 12, Jul. 2021, ISSN: 24682276. DOI: 10.1016/j.sciaf.2021.e00810.

[28] C. Blodgett, P. Dauenhauer, H. Louie, and L. Kickham, "Accuracy of energy-use surveys in predicting rural mini-grid user consumption," *Energy for Sustainable Development*, vol. 41, pp. 88–105, Dec. 2017, ISSN: 09730826. DOI: 10.1016/j.esd.2017.08.002.

[29] N. Stevanato, F. Lombardi, G. Guidicini, *et al.*, "Long-term sizing of rural microgrids: Accounting for load evolution through multi-step investment plan and stochastic optimization," *Energy for Sustainable Development*, vol. 58, pp. 16–29, Oct. 2020, ISSN: 23524669. DOI: 10.1016/j.esd.2020.07.002.

[30] Y. Zheng, B. M. Jenkins, K. Kornbluth, and C. Træholt, "Optimization under uncertainty of a biomass-integrated renewable energy microgrid with energy storage," *Renewable Energy*, vol. 123, pp. 204–217, Aug. 2018, ISSN: 18790682. DOI: 10.1016/j.renene.2018.01.120.

[31] A. Micangeli, R. Del Citto, I. N. Kiva, *et al.*, "Energy production analysis and optimization of mini-grid in remote areas: The case study of Habaswein, Kenya," *Energies*, vol. 10, no. 12, Dec. 2017, ISSN: 19961073. DOI: 10.3390/en10122041.

[32] S. Balderrama, F. Lombardi, F. Riva, W. Canedo, E. Colombo, and S. Quoilin, "A two-stage linear programming optimization framework for isolated hybrid microgrids in a rural context: The case study of the "El Espino" community," *Energy*, vol. 188, Dec. 2019, ISSN: 03605442. DOI: 10.1016/j.energy.2019.116073.

[33] M. Prilliman, J. S. Stein, D. Riley, and G. Tamizhmani, "Transient Weighted Moving-Average Model of Photovoltaic Module Back-Surface Temperature," *IEEE Journal of Photovoltaics*, vol. 10, no. 4, pp. 1053–1060, Jul. 2020, ISSN: 21563403. DOI: 10.1109/JPHOTOV.2020.2992351.

[34] S. Wang, D. Guo, X. Han, *et al.*, "Impact of battery degradation models on energy management of a grid-connected DC microgrid," *Energy*, vol. 207, Sep. 2020, ISSN: 03605442. DOI: 10.1016/j.energy.2020.118228.

[35] S. Dakir and B. Cornelusse, "Combining optimization and simulation for microgrid sizing," in *2021 IEEE Madrid PowerTech, PowerTech 2021 - Conference Proceedings*, Institute of Electrical and Electronics Engineers Inc., Jun. 2021, ISBN: 9781665435970. DOI: 10.1109/PowerTech46648.2021.9494788.

[36] S. G. R. P. U.S. Department of Energy Office of Electricity Delivery Energy Reliability, "DOE Microgrid Workshop Report," San Diego, CA, USA, Tech. Rep., Aug. 2011. [Online]. Available: https://www.energy.gov/sites/prod/files/Microgrid%20Workshop%20Report%20August%202011.pdf.

[37] International Energy Agency (IEA), "Unlocking the Potential of Distributed Energy Resources Power system opportunities and best practices," Paris, France, Tech. Rep., 2022. [Online]. Available: www.iea.org/t&c/.

[38] Y. Zhou and C. N.-M. Ho, "A review on microgrid architectures and control methods," in *IEEE 8th International Power Electronics and Motion Control Conference (IPEMC-ECCE Asia)*, Hefei: IEEE, 2016, pp. 3149–3156, ISBN: 9781509012107. DOI: 10.1109/IPEMC.2016.7512799.

[39] L. Ahmethodzic and M. Music, "Comprehensive review of trends in microgrid control," *Renewable Energy Focus*, vol. 38, pp. 84–96, Sep. 2021, ISSN: 17550084. DOI: 10.1016/j.ref.2021.07.003.

[40] K. Zuo and L. Wu, "A review of decentralized and distributed control approaches for islanded microgrids: Novel designs, current trends, and emerging challenges," *Electricity Journal*, vol. 35, no. 5, Jun. 2022, ISSN: 10406190. DOI: 10.1016/j.tej.2022.107138.

[41] N. Altin and S. E. Eyimaya, "A Review of Microgrid Control Strategies," in *10th IEEE International Conference on Renewable Energy Research and Applications, ICRERA 2021*, Institute of Electrical and Electronics Engineers Inc., 2021, pp. 412–417, ISBN: 9781665445245. DOI: 10.1109/ICRERA52334.2021.9598699.

[42] T. M. Gür, "Review of electrical energy storage technologies, materials and systems: Challenges and prospects for large-scale grid storage," *Energy and Environmental Science*, vol. 11, no. 10, pp. 2696–2767, Oct. 2018, ISSN: 17545706. DOI: 10.1039/c8ee01419a.

[43] M. Mohsen and I. Abd El-Rahman, "Optimization of Renewable Energy-Based Smart Micro-Grid System," in *Modeling, Simulation and Optimization of Wind Farms and Hybrid Systems*, K. Y. Maalawi, Ed., IntechOpen, 2020. DOI: 10.5772/intechopen.87093. [Online]. Available: www.intechopen.com.

[44] A. Berrueta, I. San Martín, P. Sanchis, and A. Ursúa, "Lithium-ion batteries as distributed energy storage systems for microgrids," in *Distributed Energy Resources in Microgrids: Integration, Challenges and Optimization*, Elsevier, Jan. 2019, pp. 143–183, ISBN: 9780128177747. DOI: 10.1016/B978-0-12-817774-7.00006-5.

[45] M. M. Kabir and D. E. Demirocak, "Degradation mechanisms in Li-ion batteries: a state-of-the-art review," *International Journal of Energy Research*, vol. 41, no. 14, pp. 1963–1986, Nov. 2017, ISSN: 1099114X. DOI: 10.1002/er.3762.

[46] D. Choi, N. Shamim, A. Crawford, *et al.*, "Li-ion battery technology for grid application," *Journal of Power Sources*, vol. 511, Nov. 2021, ISSN: 03787753. DOI: 10.1016/j.jpowsour.2021.230419.

[47] S. S. Zhang and T. R. Jow, "Aluminum corrosion in electrolyte of Li-ion battery," *Journal of Power Sources*, vol. 109, no. 2, pp. 458–464, 2022, ISSN: 0378-7753. DOI: 10.1016/S0378-7753(02)00110-6.

[48] N. Collath, B. Tepe, S. Englberger, A. Jossen, and H. Hesse, "Aging aware operation of lithium-ion battery energy storage systems: A review," *Journal of Energy Storage*, vol. 55, 2022. DOI: 10.14459/2022m. [Online]. Available: http://creativecommons.org/licenses/by/4.0/.

[49] C. Strange and G. dos Reis, "Prediction of future capacity and internal resistance of Li-ion cells from one cycle of input data," *Energy and AI*, vol. 5, Sep. 2021, ISSN: 26665468. DOI: 10.1016/j.egyai.2021.100097.

[50] M. F. Zia, E. Elbouchikhi, and M. Benbouzid, "Optimal operational planning of scalable DC microgrid with demand response, islanding, and battery degradation cost considerations," *Applied Energy*, vol. 237, pp. 695–707, Mar. 2019, ISSN: 03062619. DOI: 10.1016/j.apenergy.2019.01.040.

[51] M. Ecker, N. Nieto, S. Käbitz, *et al.*, "Calendar and cycle life study of Li(NiMnCo)O2-based 18650 lithium-ion batteries," *Journal of Power Sources*, vol. 248, pp. 839–851, 2014, ISSN: 03787753. DOI: 10.1016/j.jpowsour.2013.09.143.

[52] S. Pu, F. Yang, B. T. Vankayalapati, and B. Akin, "Aging Mechanisms and Accelerated Lifetime Tests for SiC MOSFETs: An Overview," *IEEE Journal of Emerging and Selected Topics in Power Electronics*, vol. 10, no. 1, pp. 1232–1254, Feb. 2022, ISSN: 21686785. DOI: 10.1109/JESTPE.2021.3110476.

[53] A. Abuelnaga, M. Narimani, and A. S. Bahman, "A review on IGBT module failure modes and lifetime testing," *IEEE Access*, vol. 9, pp. 9643–9663, 2021, ISSN: 21693536. DOI: 10.1109/ACCESS.2021.3049738.

[54] Y. Chen, H. Z. Huang, Y. Rao, *et al.*, "Degradation assessment of 1.2-kV SiC MOSFETs and comparative study with 1.2-kV Si IGBTs under power cycling," *Microelectronics Reliability*, vol. 132, May 2022, ISSN: 00262714. DOI: 10.1016/j.microrel.2022.114528.

[55] M. Held, P. Jacob, G. Nicoletti, P. Scacco, and M.-H. Poech, "Fast Power Cycling Test for IGBT Modules in Traction Application," in *Proceedings of Second International Conference on Power Electronics and Drive Systems*, Singapore, 1997, pp. 425–430. DOI: 10.1109/PEDS.1997.618742.

[56] F. Hoffmann and N. Kaminski, "Power cycling capability and lifetime estimation of discrete silicon carbide power devices," in *Materials Science Forum*, vol. 1004 MSF, Trans Tech Publications Ltd, 2020, pp. 977–984, ISBN: 9783035715798. DOI: 10.4028/www.scientific.net/MSF.1004.977.

[57] R. Bayerer, J. Lutz, and M. Feller, "Model for Power Cycling lifetime of IGBT Modules-various factors influencing lifetime," in *5th International Conference on Integrated Power Electronics Systems*, Nuremberg, Germany: VDE, 2008, pp. 1–6.

[58] Infineon Technologies, "PC and TC Diagrams – Application Note AN2019-05," Infineon Technologies, Tech. Rep., 2019. [Online]. Available: https://www.infineon.com/assets/row/public/documents/60/42/infineon-an2019-05-pc-and-tc-diagrams-applicationnotes-en.pdf.

[59] S. Peyghami, H. Wang, P. Davari, and F. Blaabjerg, "Mission-Profile-Based System-Level Reliability Analysis in DC Microgrids," *IEEE Transactions on Industry Applications*, vol. 55, no. 5, pp. 5055–5067, Sep. 2019, ISSN: 19399367. DOI: 10.1109/TIA.2019.2920470.

[60] Semikron Danfoss, "Power Cycle Model for IGBT Product Lines," Semikron Danfoss, Tech. Rep., 2021. [Online]. Available: https://www.semikron-danfoss.com/dl/service-support/downloads/download/semikron-danfoss-application-note-an-21-001-power-cycle-model-for-igbt-product-lines.pdf.

[61] F. Lombardi, S. Balderrama, S. Quoilin, and E. Colombo, “Generating high-resolution multi-energy load profiles for remote areas with an open-source stochastic model,” *Energy*, vol. 177, pp. 433–444, Jun. 2019, ISSN: 03605442. DOI: 10.1016/j.energy.2019.04.097.

[62] M. Turowski, B. Heidrich, L. Weingärtner, *et al.*, “Generating synthetic energy time series: A review,” *Renewable and Sustainable Energy Reviews*, vol. 206, Dec. 2024, ISSN: 18790690. DOI: 10.1016/j.rser.2024.114842.

[63] C. Kuster, Y. Rezgui, and M. Mourshed, “Electrical load forecasting models: A critical systematic review,” *Sustainable Cities and Society*, vol. 35, pp. 257–270, Nov. 2017, ISSN: 22106707. DOI: 10.1016/j.scs.2017.08.009.

[64] S. Mandelli, M. Merlo, and E. Colombo, “Novel procedure to formulate load profiles for off-grid rural areas,” *Energy for Sustainable Development*, vol. 31, pp. 130–142, Apr. 2016, ISSN: 23524669. DOI: 10.1016/j.esd.2016.01.005.

[65] S. Mandelli, C. Brivio, E. Colombo, and M. Merlo, “Effect of load profile uncertainty on the optimum sizing of off-grid PV systems for rural electrification,” *Sustainable Energy Technologies and Assessments*, vol. 18, pp. 34–47, Dec. 2016, ISSN: 22131388. DOI: 10.1016/j.seta.2016.09.010.

[66] Llanos. J., D. Saez, R. Palma-Behnke, A. Nunez, and G. Jimenez-Estevez, “Load profile generator and load forecasting for a renewable based microgrid using Self Organizing Maps and neural networks,” in *The 2012 International Joint Conference on Neural Networks (IJCNN)*, Brisbane, QLD, Australia, 2012, pp. 1–8. DOI: 10.1109/IJCNN.2012.6252648.

[67] V. Caquilpan, D. Saez, R. Hernandez, J. Llanos, T. Roje, and A. Nunez, “Load estimation based on self-organizing maps and bayesian networks for microgrids design in rural zones,” in *2017 IEEE PES Innovative Smart Grid Technologies Conference - Latin America (ISGT Latin America)*, Quito, Ecuador: IEEE, 2017, pp. 1–6, ISBN: 9781538633120. DOI: 10.1109/ISGT-LA.2017.8126709.

[68] J. Llanos, R. Morales, A. Núñez, *et al.*, “Load estimation for microgrid planning based on a self-organizing map methodology,” *Applied Soft Computing*, vol. 53, pp. 323–335, Apr. 2017, ISSN: 15684946. DOI: 10.1016/j.asoc.2016.12.054.

[69] E. Mele, C. Elias, and A. Ktena, “Electricity use profiling and forecasting at microgrid level,” in *2018 IEEE 59th International Scientific Conference on Power and Electrical Engineering of Riga Technical University (RTUCON)*, Riga, Latvia, 2018, pp. 1–6. DOI: 10.1109/RTUCON.2018.8659866.

[70] R. Takalani and B. Bekker, “Load and load growth models for rural microgrids, and how to future-proof designs,” in *2020 International SAUPEC/RobMech/PRASA Conference*, Cape Town, South Africa: IEEE, 2020, pp. -6, ISBN: 9781728141626. DOI: 10.1109/SAUPEC/RobMech/PRASA48453.2020.9041001.

[71] P. Yuan, L. Duanmu, Z. Wang, *et al.*, “Electricity consumption and load prediction method for Chinese rural residences based on the randomness and seasonality in electricity usage behavior,” *Energy and Buildings*, vol. 279, Jan. 2023, ISSN: 03787788. DOI: 10.1016/j.enbuild.2022.112647.

[72] A. A. Ashetehe, F. Shewarega, B. B. Gessesse, G. Biru, and S. Lakeou, “A stochastic approach to determine the energy consumption and synthetic load profiles of different customer types of rural communities,” *Scientific African*, vol. 24, Jun. 2024, ISSN: 24682276. DOI: 10.1016/j.sciaf.2024.e02172.

[73] Narayan, “Solar home systems for improving electricity access An off-grid solar perspective towards achieving universal electrification,” DOI: 10.4233/uuid:aa29b04f-4cd7-41fa-b48b-5edc75fef104. [Online]. Available: https://doi.org/10.4233/uuid:aa29b04f-4cd7-41fa-b48b-5edc75fef104.

[74] F. Riva, H. Ahlborg, E. Hartvigsson, S. Pachauri, and E. Colombo, *Electricity access and rural development: Review of complex socio-economic dynamics and causal diagrams for more appropriate energy modelling*, Apr. 2018. DOI: 10.1016/j.esd.2018.02.003.

[75] E. Hartvigsson, M. Stadler, and G. Cardoso, “Rural electrification and capacity expansion with an integrated modeling approach,” *Renewable Energy*, vol. 115, pp. 509–520, 2018, ISSN: 18790682. DOI: 10.1016/j.renene.2017.08.049.

[76] F. Riva, F. D. Sanvito, F. Tonini, and E. Colombo, “Modelling long-term electricity load demand for rural electrification planning,” Milan, Italy, 2019, pp. 1–6. DOI: 10.1109/PTC.2019.8810727.

[77] F. Riva, A. Tognollo, F. Gardumi, and E. Colombo, *Long-term energy planning and demand forecast in remote areas of developing countries: Classification of case studies and insights from a modelling perspective*, Apr. 2018. DOI: 10.1016/j.esr.2018.02.006.

[78] M. Ban, J. Yu, M. Shahidehpour, and D. Guo, “Optimal sizing of PV and battery-based energy storage in an off-grid nanogrid supplying batteries to a battery swapping station,” *Journal of Modern Power Systems and Clean Energy*, vol. 7, no. 2, pp. 309–320, Mar. 2019, ISSN: 21965420. DOI: 10.1007/s40565-018-0428-y.

[79] J. Yang and C. Su, “Robust optimization of microgrid based on renewable distributed power generation and load demand uncertainty,” *Energy*, vol. 223, May 2021, ISSN: 03605442. DOI: 10.1016/j.energy.2021.120043.

[80] Z. A. Arfeen, U. U. Sheikh, M. K. Azam, *et al.*, “A comprehensive review of modern trends in optimization techniques applied to hybrid microgrid systems,” *Concurrency and Computation: Practice and Experience*, vol. 33, no. 10, May 2021, ISSN: 15320634. DOI: 10.1002/cpe.6165.

[81] O. Erdinc and M. Uzunoglu, “Optimum design of hybrid renewable energy systems: Overview of different approaches,” *Renewable and Sustainable Energy Reviews*, vol. 16, no. 3, pp. 1412–1425, Apr. 2012, ISSN: 13640321. DOI: 10.1016/j.rser.2011.11.011.

[82] J. Kennedy, R. Eberhart, and b. gov bls, “Particle Swarm Optimization,” in *IEEE International Conference on Neural Networks*, Perth, WA, Australia, 1995, pp. 1942–1948. DOI: 10.1109/ICNN.1995.488968.

[83] K. Gao, T. Wang, C. Han, J. Xie, Y. Ma, and R. Peng, “A review of optimization of microgrid operation,” *Energies*, vol. 14, no. 10, May 2021, ISSN: 19961073. DOI: 10.3390/en14102842.

[84] S. Mirjalili, S. M. Mirjalili, and A. Lewis, “Grey Wolf Optimizer,” *Advances in Engineering Software*, vol. 69, pp. 46–61, 2014, ISSN: 09659978. DOI: 10.1016/j.advengsoft.2013.12.007.

[85] HOMER Energy, *HOMER PRO*, 2025. [Online]. Available: https://www.homerenergy.com/products/pro/index.html.

[86] Grid Integration Group Berkeley Lab, *DER-CAM: Distributed Energy Resources Customer Adoption Model*, 2025. [Online]. Available: https://gridintegration.lbl.gov/der-cam.

[87] J. Jung and M. Villaran, “Optimal planning and design of hybrid renewable energy systems for microgrids,” *Renewable and Sustainable Energy Reviews*, vol. 75, pp. 180–191, 2017, ISSN: 18790690. DOI: 10.1016/j.rser.2016.10.061.

[88] W. Kang, Y. Guan, F. Danang Wijaya, *et al.*, “Community microgrid planning in Lombok Island: an Indonesian case study,” *Frontiers in Energy Research*, vol. 11, 2023, ISSN: 2296598X. DOI: 10.3389/fenrg.2023.1209875.

[89] Nicolo Stevanato, *MicrogridsPy*, 2025. [Online]. Available: https://github.com/SESAM-Polimi/MicroGridsPy-SESAM.

[90] R. Dufour, *iHOGA: Hybrid Optimization by Genetic Algorithms*, 2025. [Online]. Available: https://ihoga.unizar.es/en/descarga/.

[91] I. C. Hoarcă, N. Bizon, I. S. □orlei, and P. Thounthong, “Sizing Design for a Hybrid Renewable Power System Using HOMER and iHOGA Simulators,” *Energies*, vol. 16, no. 4, Feb. 2023, ISSN: 19961073. DOI: 10.3390/en16041926.

[92] H. Shamachurn, “Optimization of an off-grid domestic Hybrid Energy System in suburban Paris using iHOGA software,” *Renewable Energy Focus*, vol. 37, pp. 36–49, Jun. 2021, ISSN: 17550084. DOI: 10.1016/j.ref.2021.02.004.

[93] D. Höffner and S. Glombik, “Energy system planning and analysis software—A comprehensive meta-review with special attention to urban energy systems and district heating,” *Energy*, vol. 307, Oct. 2024, ISSN: 18736785. DOI: 10.1016/j.energy.2024.132542.

[94] D. Connolly, H. Lund, B. V. Mathiesen, and M. Leahy, “A review of computer tools for analysing the integration of renewable energy into various energy systems,” *Applied Energy*, vol. 87, no. 4, pp. 1059–1082, 2010, ISSN: 03062619. DOI: 10.1016/j.apenergy.2009.09.026.

[95] B. Akbas, A. S. Kocaman, D. Nock, and P. A. Trotter, “Rural electrification: An overview of optimization methods,” *Renewable and Sustainable Energy Reviews*, vol. 156, Mar. 2022, ISSN: 18790690. DOI: 10.1016/j.rser.2021.111935.

[96] S. Mohseni and A. C. Brent, “Long-term planning optimisation of sustainable energy systems: A systematic review and meta-analysis of trends, drivers, barriers, and prospects,” *Energy Strategy Reviews*, vol. 57, Jan. 2025, ISSN: 2211467X. DOI: 10.1016/j.esr.2025.101640.

[97] R. Siddaiah and R. P. Saini, *A review on planning, configurations, modeling and optimization techniques of hybrid renewable energy systems for off grid applications*, May 2016. DOI: 10.1016/j.rser.2015.12.281.

[98] Gurobi Optimization, *Mixed-Integer Programming (MIP) – A Primer on the Basics*, 2025. [Online]. Available: https://www.gurobi.com/resources/mixed-integer-programming-mip-a-primer-on-the-basics/.

[99] D. Fioriti, D. Poli, P. Cherubini, G. Lutzemberger, A. Micangeli, and P. Duenas-Martinez, “Comparison among deterministic methods to design rural mini-grids: effect of operating strategies,” in *2019 IEEE Milan PowerTech*, Milan, Italy, 2019, pp. 1–6. DOI: 10.1109/PTC.2019.8810717.

[100] S. Mashayekh, M. Stadler, G. Cardoso, and M. Heleno, “A mixed integer linear programming approach for optimal DER portfolio, sizing, and placement in multi-energy microgrids,” *Applied Energy*, vol. 187, pp. 154–168, Feb. 2017, ISSN: 03062619. DOI: 10.1016/j.apenergy.2016.11.020.

[101] A. O. Rousis, I. Konstantelos, and G. Strbac, “A Planning Model for a Hybrid AC-DC Microgrid Using a Novel GA/AC OPF Algorithm,” *IEEE Transactions on Power Systems*, vol. 35, no. 1, pp. 227–237, Jan. 2020, ISSN: 15580679. DOI: 10.1109/TPWRS.2019.2924137.

[102] J. Alpízar-Castillo, J. J. A. Nl, C. Engström, L. Ramírez-Elizondo, and P. Bauer, “Investigating the Effect of Power Curtailment on the Switch of a Solar Boost Converter Under Residential Loads,” in *2024 IEEE 21st International Power Electronics and Motion Control Conference (PEMC)*, Pilsen, Czech Republic, 2024, pp. 1–6. DOI: 10.1109/PEMC61721.2024.10726347.

[103] R. Mallol-Poyato, S. Jiménez-Fernández, P. Díaz-Villar, and S. Salcedo-Sanz, “Adaptive nesting of evolutionary algorithms for the optimization of Microgrid’s sizing and operation scheduling,” *Soft Computing*, vol. 21, no. 17, pp. 4845–4857, Sep. 2017, ISSN: 14337479. DOI: 10.1007/s00500-016-2373-x.

[104] D. R. Prathapaneni and K. P. Detroja, “An integrated framework for optimal planning and operation schedule of microgrid under uncertainty,” *Sustainable Energy, Grids and Networks*, vol. 19, Sep. 2019, ISSN: 23524677. DOI: 10.1016/j.segan.2019.100232.

[105] A. Malheiro, P. M. Castro, R. M. Lima, and A. Estanqueiro, “Integrated sizing and scheduling of wind/PV/diesel/battery isolated systems,” *Renewable Energy*, vol. 83, pp. 646–657, Nov. 2015, ISSN: 18790682. DOI: 10.1016/j.renene.2015.04.066.

[106] F. Boutros, M. Doumiati, J. C. Olivier, I. Mougharbel, and H. Kanaan, “New modelling approach for the optimal sizing of an islanded microgrid considering economic and environmental challenges,” *Energy Conversion and Management*, vol. 277, Feb. 2023, ISSN: 01968904. DOI: 10.1016/j.enconman.2022.116636.

[107] F. A. Kassab, B. Celik, F. Locment, M. Sechilariu, S. Liaquat, and T. M. Hansen, “Optimal sizing and energy management of a microgrid: A joint MILP approach for minimization of energy cost and carbon emission,” *Renewable Energy*, vol. 224, Apr. 2024, ISSN: 18790682. DOI: 10.1016/j.renene.2024.120186.

[108] M. Sugimura, M. M. Gamil, H. Akter, *et al.*, “Optimal sizing and operation for microgrid with renewable energy considering two types demand response,” *Journal of Renewable and Sustainable Energy*, vol. 12, no. 6, Nov. 2020, ISSN: 19417012. DOI: 10.1063/5.0008065.

[109] P. Benalcazar, A. Suski, and J. K. Nski, "Optimal Sizing and Scheduling of Hybrid Energy Systems: The Cases of Morona Santiago and the Galapagos Islands," *Energies*, vol. 13, no. 15, Aug. 2020, ISSN: 19961073. DOI: 10.3390/en13153933.

[110] J. Chen, W. Zhang, J. Li, *et al.*, "Optimal sizing for grid-tied microgrids with consideration of joint optimization of planning and operation," *IEEE Transactions on Sustainable Energy*, vol. 9, no. 1, pp. 237–248, Jan. 2018, ISSN: 19493029. DOI: 10.1109/TSTE.2017.2724583.

[111] M. Cao, Q. Xu, J. Cai, and B. Yang, "Optimal sizing strategy for energy storage system considering correlated forecast uncertainties of dispatchable resources," *International Journal of Electrical Power and Energy Systems*, vol. 108, pp. 336–346, Jun. 2019, ISSN: 01420615. DOI: 10.1016/j.ijepes.2019.01.019.

[112] R. Atia and N. Yamada, "Sizing and Analysis of Renewable Energy and Battery Systems in Residential Microgrids," *IEEE Transactions on Smart Grid*, vol. 7, no. 3, pp. 1204–1213, May 2016, ISSN: 19493053. DOI: 10.1109/TSG.2016.2519541.

[113] M. Petrelli, D. Fioriti, A. Berizzi, and D. Poli, "Multi-Year Planning of a Rural Microgrid Considering Storage Degradation," *IEEE Transactions on Power Systems*, vol. 36, no. 2, pp. 1459–1469, Mar. 2021, ISSN: 15580679. DOI: 10.1109/TPWRS.2020.3020219.

[114] D. Fioriti, R. Giglioli, D. Poli, *et al.*, "Stochastic sizing of isolated rural mini-grids, including effects of fuel procurement and operational strategies," *Electric Power Systems Research*, vol. 160, pp. 419–428, Jul. 2018, ISSN: 03787796. DOI: 10.1016/j.epsr.2018.03.020.

[115] P. V. Seger, R. Rigo-Mariani, P. X. Thivel, and D. Riu, "A storage degradation model of Li-ion batteries to integrate ageing effects in the optimal management and design of an isolated microgrid," *Applied Energy*, vol. 333, Mar. 2023, ISSN: 03062619. DOI: 10.1016/j.apenergy.2022.120584.

[116] M. K. Kiptoo, O. B. Adewuyi, M. Furukakoi, P. Mandal, and T. Senjyu, "Integrated Multi-Criteria Planning for Resilient Renewable Energy-Based Microgrid Considering Advanced Demand Response and Uncertainty," *Energies*, vol. 16, no. 19, Oct. 2023, ISSN: 19961073. DOI: 10.3390/en16196838.

[117] R. Mallol-Poyato, S. Jiménez-Fernández, P. Díaz-Villar, and S. Salcedo-Sanz, "Joint optimization of a Microgrid's structure design and its operation using a two-steps evolutionary algorithm," *Energy*, vol. 94, pp. 775–785, Jan. 2016, ISSN: 03605442. DOI: 10.1016/j.energy.2015.11.030.

[118] B. Li, R. Roche, and A. Miraoui, "Microgrid sizing with combined evolutionary algorithm and MILP unit commitment," *Applied Energy*, vol. 188, pp. 547–562, Feb. 2017, ISSN: 03062619. DOI: 10.1016/j.apenergy.2016.12.038.

[119] N. E. Koltsaklis, M. Giannakakis, and M. C. Georgiadis, "Optimal energy planning and scheduling of microgrids," *Chemical Engineering Research and Design*, vol. 131, pp. 318–332, Mar. 2018, ISSN: 02638762. DOI: 10.1016/j.cherd.2017.07.030.

[120] D. Fioriti, G. Lutzemberger, D. Poli, P. Duenas-Martinez, and A. Micangeli, "Coupling economic multi-objective optimization and multiple design options: A business-oriented approach to size an off-grid hybrid microgrid," *International Journal of Electrical Power and Energy Systems*, vol. 127, May 2021, ISSN: 01420615. DOI: 10.1016/j.ijepes.2020.106686.

[121] P. V. Krishna, P. C. Sekhar, and T. R. Behera, "A robust optimal sizing of renewable-rich multi-source microgrid under uncertainties with multi-storage options," *Electrical Engineering*, vol. 106, pp. 6547–6563, 2024, ISSN: 14320487. DOI: 10.1007/s00202-024-02331-w.

[122] H. R. Bouchekara, Y. A. Sha'aban, M. S. Shahriar, S. M. Abdullah, and M. A. Ramli, "Sizing of Hybrid PV/Battery/Wind/Diesel Microgrid System Using an Improved Decomposition Multi-Objective Evolutionary Algorithm Considering Uncertainties and Battery Degradation," *Sustainability (Switzerland)*, vol. 15, no. 14, Jul. 2023, ISSN: 20711050. DOI: 10.3390/su151411073.

[123] S. Mohseni, A. C. Brent, D. Burmester, W. N. Browne, and S. Kelly, "Adding a Computationally-Tractable Probabilistic Dimension to Meta-Heuristic-Based Microgrid Sizing," in *IEEE Region 10 Annual International Conference, Proceedings/TENCON*, vol. 2021-December, Institute of Electrical and Electronics Engineers Inc., 2021, pp. 464–469, ISBN: 9781665495325. DOI: 10.1109/TENCON54134.2021.9707310.

[124] P. Cicilio, M. Orosz, A. Mueller, and E. Cotilla-Sanchez, “UGrid: Reliable Minigrid Design and Planning Toolset for Rural Electrification,” *IEEE Access*, vol. 7, pp. 163 988–163 999, 2019, ISSN: 21693536. DOI: 10.1109/ACCESS.2019.2952896.

[125] D. P. Mishra, B. Routray, N. Pattanayak, P. Shekhar, P. R. Behera, and S. R. Salkuti, “Cost optimization of electricity in energy storage system by dynamic programming,” *International Journal of Applied Power Engineering*, vol. 13, no. 2, pp. 343–350, Jun. 2024, ISSN: 27222624. DOI: 10.11591/ijape.v13.i2.pp343-350.

[126] K. S. Joshal and N. Gupta, “Microgrids with Model Predictive Control: A Critical Review,” *Energies*, vol. 16, no. 13, Jul. 2023, ISSN: 19961073. DOI: 10.3390/en16134851.

[127] F. J. Vivas, F. Segura, J. M. Andújar, *et al.*, “Multi-objective fuzzy logic-based energy management system for microgrids with battery and hydrogen energy storage system,” *Electronics (Switzerland)*, vol. 9, no. 7, pp. 1–25, Jul. 2020, ISSN: 20799292. DOI: 10.3390/electronics9071074.

[128] O. Abdel-Raouf, M. A. Elsisy, and E. F. Kelash, “A Survey of Game Theory Applications in Electrical Power Micro-Grid Systems,” *International Journal of Computer Applications*, vol. 177, no. 37, pp. 975–8887, 2020.

[129] G. S. Thirunavukkarasu, M. Seyedmahmoudian, E. Jamei, B. Horan, S. Mekhilef, and A. Stojcevski, “Role of optimization techniques in microgrid energy management systems—A review,” *Energy Strategy Reviews*, vol. 43, Sep. 2022, ISSN: 2211467X. DOI: 10.1016/j.esr.2022.100899.

[130] H. V. Priyadarshana, M. A. Sandaru, K. T. Hemapala, and W. D. Wijayapala, “A review on multi-agent system based energy management systems for micro grids,” *AIMS Energy*, vol. 7, no. 6, 2019, ISSN: 23338334. DOI: 10.3934/ENERGY.2019.6.924.

[131] N. Shamarova, K. Suslov, P. Ilyushin, and I. Shushpanov, “Review of Battery Energy Storage Systems Modeling in Microgrids with Renewables Considering Battery Degradation,” *Energies*, vol. 15, no. 19, Oct. 2022, ISSN: 19961073. DOI: 10.3390/en15196967.

[132] P. V. Seger, P. X. Thivel, and D. Riu, “A second life Li-ion battery ageing model with uncertainties: From cell to pack analysis,” *Journal of Power Sources*, vol. 541, Sep. 2022, ISSN: 03787753. DOI: 10.1016/j.jpowsour.2022.231663.

[133] B. Xu, A. Oudalov, A. Ulbig, G. Andersson, and D. S. Kirschen, “Modeling of lithium-ion battery degradation for cell life assessment,” *IEEE Transactions on Smart Grid*, vol. 9, no. 2, pp. 1131–1140, 2018, ISSN: 19493053. DOI: 10.1109/TSG.2016.2578950.

[134] C. Boennec, L. Albuquerque, B. Sareni, F. Lacressonnière, and S. U. Ngueveu, “Comparison of Battery Models Integrating Energy Efficiency and Aging for the Design of Microgrids,” *Smart Grids and Sustainable Energy*, vol. 9, no. 1, Mar. 2024, ISSN: 27318087. DOI: 10.1007/s40866-023-00174-1.

[135] S. Totaro, I. Boukas, A. Jonsson, and B. Cornélusse, “Lifelong control of off-grid microgrid with model-based reinforcement learning,” *Energy*, vol. 232, Oct. 2021, ISSN: 03605442. DOI: 10.1016/j.energy.2021.121035.

[136] W. M. Witharama, K. M. Bandara, M. I. Azeez, K. Bandara, V. Logeeshan, and C. Wanigasekara, “Advanced Genetic Algorithm for Optimal Microgrid Scheduling Considering Solar and Load Forecasting, Battery Degradation, and Demand Response Dynamics,” *IEEE Access*, vol. 12, pp. 83 269–83 284, 2024, ISSN: 21693536. DOI: 10.1109/ACCESS.2024.3412914.

[137] A. Ahsan, Q. Zhao, A. M. Khamabadkone, and M. H. Chia, “Dynamic Battery Operational Cost Modeling for Energy Dispatch,” Milwaukee, WI, USA: IEEE, 2016, pp. 1–5, ISBN: 9781509007370. [Online]. Available: 10.1109/ECCE.2016.7855055.

[138] M. Amini, M. B. Sanjareh, M. H. Nazari, G. B. Gharehpetian, and S. H. Hosseinian, “A Novel Model for Battery Optimal Sizing in Microgrid Planning Considering Battery Capacity Degradation Process and Thermal Impact,” *IEEE Transactions on Sustainable Energy*, vol. 15, no. 3, pp. 1435–1449, Jul. 2024, ISSN: 19493037. DOI: 10.1109/TSTE.2024.3349391.

[139] M. Swierczynski, D. I. Stroe, A. I. Stan, R. Teodorescu, and S. K. Kær, "Lifetime Estimation of the Nanophosphate LiFePO4/C Battery Chemistry Used in Fully Electric Vehicles," *IEEE Transactions on Industry Applications*, vol. 51, no. 4, pp. 3453–3461, Jul. 2015, ISSN: 00939994. DOI: 10.1109/TIA.2015.2405500.

[140] T. M. Masaud and E. F. El-Saadany, "Correlating Optimal Size, Cycle Life Estimation, and Technology Selection of Batteries: A Two-Stage Approach for Microgrid Applications," *IEEE Transactions on Sustainable Energy*, vol. 11, no. 3, pp. 1257–1267, Jul. 2020, ISSN: 19493037. DOI: 10.1109/TSTE.2019.2921804.

[141] Y. Wang, Z. Zhou, A. Botterud, K. Zhang, and Q. Ding, "Stochastic coordinated operation of wind and battery energy storage system considering battery degradation," *Journal of Modern Power Systems and Clean Energy*, vol. 4, no. 4, pp. 581–592, Oct. 2016, ISSN: 21965420. DOI: 10.1007/s40565-016-0238-z.

[142] R. Fallahifar and M. Kalantar, "Optimal planning of lithium ion battery energy storage for microgrid applications: Considering capacity degradation," *Journal of Energy Storage*, vol. 57, Jan. 2023, ISSN: 2352152X. DOI: 10.1016/j.est.2022.106103.

[143] J. Wang, P. Liu, J. Hicks-Garner, *et al.*, "Cycle-life model for graphite-LiFePO4 cells," *Journal of Power Sources*, vol. 196, no. 8, pp. 3942–3948, Apr. 2011, ISSN: 03787753. DOI: 10.1016/j.jpowsour.2010.11.134.

[144] Y. Wei, T. Han, S. Wang, *et al.*, "An efficient data-driven optimal sizing framework for photovoltaics-battery-based electric vehicle charging microgrid," *Journal of Energy Storage*, vol. 55, Nov. 2022, ISSN: 2352152X. DOI: 10.1016/j.est.2022.105670.

[145] E. M. Brito, A. F. Cupertino, P. D. Reigosa, Y. Yang, V. F. Mendes, and H. A. Pereira, "Impact of meteorological variations on the lifetime of grid-connected PV inverters," *Microelectronics Reliability*, vol. 88-90, pp. 1019–1024, Sep. 2018, ISSN: 00262714. DOI: 10.1016/j.microrel.2018.07.066.

[146] S. S. Kshatri, J. Dhillon, and S. Mishra, "Impact of solar irradiance and ambient temperature on PV inverter reliability considering geographical locations," *International Journal of Heat and Technology*, vol. 39, no. 1, pp. 292–298, Feb. 2021, ISSN: 03928764. DOI: 10.18280/ijht.390132.

[147] L. R. GopiReddy, L. M. Tolbert, B. Ozpineci, and J. O. Pinto, "Rainflow Algorithm-Based Lifetime Estimation of Power Semiconductors in Utility Applications," *IEEE Transactions on Industry Applications*, vol. 51, no. 4, pp. 3368–3375, Jul. 2015, ISSN: 00939994. DOI: 10.1109/TIA.2015.2407055.

[148] M. Matsuishi and T. Endo, "Fatigue of metals subjected to varying stress," in *Japan Society of Mechanical Engineers*, Fukuoka, 1968.

[149] Y. L. Lee and T. Tjhung, "Rainflow Cycle Counting Techniques," in *Metal Fatigue Analysis Handbook*, Elsevier Inc., 2012, pp. 89–114, ISBN: 9780123852045. DOI: 10.1016/B978-0-12-385204-5.00003-3.

[150] B. A. Milton Miner and S. Monica, "Cumulative Damage in Fatigue," *Journal of Applied Mechanics*, vol. 12, pp. 159–164, 1945. [Online]. Available: http://asmedigitalcollection.asme.org/appliedmechanics/article-pdf/12/3/A159/6745060/a159_1.pdf.

[151] Wolfspeed, "C3M0045065K: 650 V, 45 mΩ, Discrete SiC MOSFET," Tech. Rep., 2023. [Online]. Available: https://assets.wolfspeed.com/uploads/2024/01/Wolfspeed_C3M0045065K_data_sheet.pdf?utm_source=chatgpt.com.

[152] "Online Monitoring Method for Junction Temperature of SiC MOSFETs based on Temperature Sensitive Electrical Parameter," *CSEE Journal of Power and Energy Systems*, 2024, ISSN: 20960042. DOI: 10.17775/CSEEJPES.2021.04840. [Online]. Available: https://xplorestaging.ieee.org/ielx7/7054730/10631812/09862545.pdf?arnumber=9862545.

[153] Nexperia BV, "AN11261 RC Thermal Models Rev. 4.0-11 May 2020 application note Document information Information Content," Tech. Rep., 2020. [Online]. Available: https://assets.nexperia.com/documents/application-note/AN11261.pdf.

[154] Wolfspeed and Inc, “PRD-08376: Thermal Characterization Methods and Applications | Wolfspeed,” Tech. Rep., 2024. [Online]. Available: www.wolfspeed.com..

[155] L. Ceccarelli, R. M. Kotecha, A. S. Bahman, F. Iannuzzo, and H. A. Mantooth, “Mission-Profile-Based Lifetime Prediction for a SiC mosfet Power Module Using a Multi-Step Condition-Mapping Simulation Strategy,” *IEEE Transactions on Power Electronics*, vol. 34, no. 10, pp. 9698–9708, Oct. 2019, ISSN: 19410107. DOI: 10.1109/TPEL.2019.2893636.

[156] J. N. Davidson, D. A. Stone, and M. P. Foster, “Required Cauer network order for modelling of thermal transfer impedance,” *Electronics Letters*, vol. 50, no. 4, pp. 260–262, Feb. 2014, ISSN: 00135194. DOI: 10.1049/el.2013.3426.

[157] B. ’Ufnalski, *Foster and Cauer equivalent networks*, 2025. [Online]. Available: https://nl.mathworks.com/matlabcentral/fileexchange/48042-foster-and-cauer-equivalent-networks.

[158] JEDEC Solid State Technology Association, “JESD51□14: Transient Dual Interface Method for Measurement of the Thermal Resistance Junction-to-Case (RθJC) of Semiconductor Devices with a Heat Flow Path Through a Single Surface,” Tech. Rep., 2015. [Online]. Available: https://www.jedec.org/standards-documents/docs/jesd51-14.

[159] Infineon Technologies, “IGBT Power Losses Calculation using the Data Sheet Parameters,” Tech. Rep., 2007. [Online]. Available: https://www.infineon.com/assets/row/public/documents/faq/igbt-power-losses-calculation-using-the-data-sheet-parameters.pdf.

[160] S. Baba, G. Palesa, J. Wiśniewski, and F. Mańka, “Considerations on SiC MOSFET TSEP-based junction temperature measurement routines in practical use,” *Przeglad Elektrotechniczny*, vol. 5, pp. 31–37, 2024, ISSN: 24499544. DOI: 10.15199/48.2024.05.06.

[161] T. Kim and T. Funaki, “Thermal measurement and analysis of packaged SiC MOSFETs,” *Thermochimica Acta*, vol. 633, pp. 31–36, Jun. 2016, ISSN: 00406031. DOI: 10.1016/j.tca.2016.03.004.

[162] S. Chen, Y. Zhu, and G. Konstantinou, “Dependencies of Temperature Sensitive Electrical Parameters and Influence of Degradation in Silicon Carbide MOSFETs: A Review,” in *2024 IEEE 34th Australasian Universities Power Engineering Conference, AUPEC 2024*, Institute of Electrical and Electronics Engineers Inc., 2024, ISBN: 9798350377941. DOI: 10.1109/AUPEC62273.2024.10807630.

[163] H. Yu, X. Jiang, J. Chen, Z. J. Shen, and J. Wang, “Comparative Study of Temperature Sensitive Electrical Parameters for Junction Temperature Monitoring in SiC MOSFET and Si IGBT,” in *2020 IEEE 9th International Power Electronics and Motion Control Conference, IPEMC 2020 ECCE Asia*, Institute of Electrical and Electronics Engineers Inc., Nov. 2020, pp. 905–909, ISBN: 9781728153018. DOI: 10.1109/IPEMC-ECCEAsia48364.2020.9367830.

[164] M. H. M. Sathik, J. Pou, S. Prasanth, V. Muthu, R. Simanjorang, and A. K. Gupta, “Comparison of IGBT Junction Temperature Measurement and Estimation Methods - A Review,” Singapore: IEEE, Oct. 2017, ISBN: 9781538609712. DOI: 10.1109/ACEPT.2017.8168600.

[165] F. Simjanoski, A. Shekhar, R. Poelma, G. Q. Zhang, and W. van Driel, “Towards Health Monitoring of SiC MOSFETs by Precise Junction Temperature Profiling,” in *Proceedings - 2025 26th International Conference on Thermal, Mechanical and Multi-Physics Simulation and Experiments in Microelectronics and Microsystems, EuroSimE 2025*, Institute of Electrical and Electronics Engineers Inc., 2025, ISBN: 9798350393002. DOI: 10.1109/EuroSimE65125.2025.11006628.

[166] N. Mohan, T. M. Undeland, and W. P. Robbins, “Component Temperature Control and Heat Sinks,” in *Power Electronics: Converters, Applications and Design*, 3rd ed., John Wiley & Sons, Inc, 2002, ch. 29, pp. 730–744.

[167] M. I. Masoud, W. Issa, and W. Yates, “A Tutorial on Double Pulse Test of Silicon and Silicon Carbide MOSFETs,” Tech. Rep.

[168] J. Schweickhardt and K. Hermanns, “Application Note: Tips and Tricks on Double Pulse Testing,” R&S, Tech. Rep., 2021. [Online]. Available: https://scdn.rohde-schwarz.com/ur/pws/dl_downloads/dl_application/application_notes/gfm347/GFM347_1e_Double_Pulse_Testing.pdf.

[169] W. Inc, “SpeedVal Kit™ Half-Bridge Motherboard User Guide MOD-MB-HB-0900V-40A SpeedVal Kit™ Half-Bridge Motherboard User Guide,” Tech. Rep., 2023. [Online]. Available: https://www.wolfspeed.com/products/power/evaluation-kits/speedval-.

[170] W. Inc, “SpeedVal Kit TO-247-4 Power Daughter Card User Guide | Wolfspeed,” Tech. Rep., 2024. [Online]. Available: https://forum.wolfspeed.com/.

[171] Z. Zhang, B. Guo, F. F. Wang, E. A. Jones, L. M. Tolbert, and B. J. Blalock, “Methodology for Wide Band-Gap Device Dynamic Characterization,” *IEEE Transactions on Power Electronics*, vol. 32, no. 12, pp. 9307–9318, Dec. 2017, ISSN: 08858993. DOI: 10.1109/TPEL.2017.2655491.

[172] Shubha B., *A New Software Deskew Approach Accelerates Double Pulse Testing*, 2025. [Online]. Available: https://www.tek.com/en/blog/a-new-software-deskew-approach-accelerates-double-pulse-testing.

[173] W. Inc, “MOD-ACC-BUCKBOOST-xxxuH SpeedVal Kit™ Buck/Boost Filter Board User Guide User Guide Wolfspeed Power Applications,” Tech. Rep., 2022.

[174] “CoolSiC ™ Schottky diode 2000 V G5 datasheet,” Tech. Rep., 2021. [Online]. Available: www.infineon.com.

[175] S. Pfenninger, “Dealing with multiple decades of hourly wind and PV time series in energy models: A comparison of methods to reduce time resolution and the planning implications of inter-annual variability,” *Applied Energy*, vol. 197, pp. 1–13, 2017, ISSN: 03062619. DOI: 10.1016/j.apenergy.2017.03.051.

[176] P. Nahmmacher, E. Schmid, L. Hirth, and B. Knopf, “Carpe diem: A novel approach to select representative days for long-term power system modeling,” *Energy*, vol. 112, pp. 430–442, Oct. 2016, ISSN: 03605442. DOI: 10.1016/j.energy.2016.06.081.

[177] M. Geraedts, J. Alpizar-Castillo, L. Ramirez-Elizondo, and P. Bauer, “Optimal Sizing of a Community Level Thermal Energy Storage System,” in *MELECON 2022 - IEEE Mediterranean Electrotechnical Conference, Proceedings*, Institute of Electrical and Electronics Engineers Inc., 2022, pp. 52–57, ISBN: 9781665442800. DOI: 10.1109/MELECON53508.2022.9842945.

[178] Q. Chen, M. Xia, Y. Zhou, H. Cai, J. Wu, and H. Zhang, “Optimal planning for partially self-sufficient microgrid with limited annual electricity exchange with distribution grid,” *IEEE Access*, vol. 7, pp. 123 505–123 520, 2019, ISSN: 21693536. DOI: 10.1109/ACCESS.2019.2936762.

[179] K. Poncelet, H. Hoschle, E. Delarue, A. Virag, and W. Drhaeseleer, “Selecting representative days for capturing the implications of integrating intermittent renewables in generation expansion planning problems,” *IEEE Transactions on Power Systems*, vol. 32, no. 3, pp. 1936–1948, May 2017, ISSN: 08858950. DOI: 10.1109/TPWRS.2016.2596803.

[180] M. S. ElNozahy, M. M. A. Salama, and R. Seethapathy, “A probabilistic load modelling approach using clustering algorithms,” in *2013 IEEE Power & Energy Society General Meeting*, Vancouver, BC, Canada: IEEE, 2013, pp. 1–5, ISBN: 9781479913039. DOI: 10.1109/PESMG.2013.6672073.

[181] X. Ran, Y. Xi, Y. Lu, X. Wang, and Z. Lu, “Comprehensive survey on hierarchical clustering algorithms and the recent developments,” *Artificial Intelligence Review*, vol. 56, no. 8, pp. 8219–8264, Aug. 2023, ISSN: 15737462. DOI: 10.1007/s10462-022-10366-3.

[182] J. H. Ward, “Hierarchical Grouping to Optimize an Objective Function,” *Journal of the American Statistical Association*, vol. 58, no. 301, pp. 236–244, 1963, ISSN: 1537274X. DOI: 10.1080/01621459.1963.10500845.

[183] R. L. Thorndike, “WHO BELONGS IN THE FAMILY?*,” vol. 18, no. 4, 1953.

[184] E. Schubert, “Stop using the elbow criterion for k-means and how to choose the number of clusters instead,” TU Dortmund University, Dortmund, Germany, Tech. Rep., 2022. [Online]. Available: https://arxiv.org/abs/2212.12189.

[185] S. Pfenninger and I. Staffell, *Renewables.ninja*, 2025. [Online]. Available: https://renewables.ninja/.

[186] S. Pfenninger and I. Staffell, "Long-term patterns of European PV output using 30 years of validated hourly reanalysis and satellite data," *Energy*, vol. 114, pp. 1251–1265, Nov. 2016, ISSN: 03605442. DOI: 10.1016/j.energy.2016.08.060.

[187] I. Staffell and S. Pfenninger, "Using bias-corrected reanalysis to simulate current and future wind power output," *Energy*, vol. 114, pp. 1224–1239, Nov. 2016, ISSN: 03605442. DOI: 10.1016/j.energy.2016.08.068.

[188] M. Schimpe, M. E. von Kuepach, M. Naumann, H. C. Hesse, K. Smith, and A. Jossen, "Comprehensive Modeling of Temperature-Dependent Degradation Mechanisms in Lithium Iron Phosphate Batteries," *Journal of The Electrochemical Society*, vol. 165, no. 2, A181–A193, 2018, ISSN: 0013-4651. DOI: 10.1149/2.1181714jes.

[189] W. Maranda, "Capacity degradation of lead-acid batteries under variable-depth cycling operation in photovoltaic system," in *Proceedings of the 22nd International Conference Mixed Design of Integrated Circuits and Systems, MIXDES 2015*, Institute of Electrical and Electronics Engineers Inc., Aug. 2015, pp. 552–555, ISBN: 9788363578060. DOI: 10.1109/MIXDES.2015.7208584.

[190] M. Safari and C. Delacourt, "Modeling of a Commercial Graphite/LiFePO4 Cell," *Journal of The Electrochemical Society*, vol. 158, no. 5, A562, 2011, ISSN: 00134651. DOI: 10.1149/1.3567007.

[191] Y. Shi and R. Eberhart, "A Modified Particle Swarm Optimizer," in *1998 IEEE International Conference on Evolutionary Computation Proceedings*, Anchorage, AK, USA: IEEE World Congress on Computational Intelligence, 1998, pp. 69–73. DOI: 10.1109/ICEC.1998.699146.

[192] S. Phommixay, M. L. Doumbia, and D. Lupien St-Pierre, "Review on the cost optimization of microgrids via particle swarm optimization," *International Journal of Energy and Environmental Engineering*, vol. 11, no. 1, pp. 73–89, Mar. 2020, ISSN: 22516832. DOI: 10.1007/s40095-019-00332-1.

[193] J. Wüllner, "IEA PVPS Task 9 Optimal Integration of Photovoltaics in Micro-Grids that are dominated by Diesel Power Plants," IEA, Tech. Rep., 2019. [Online]. Available: https://iea-pvps.org/wp-content/uploads/2020/02/IEA-PVPS_T09-19-2019-REPORT_Integration_of_PV_in_Diesel_Micro-grids.pdf.

[194] V. Safavi, A. M. Vaniar, N. Bazmohammadi, J. C. Vasquez, O. Keysan, and J. M. Guerrero, "A battery degradation-aware energy management system for agricultural microgrids," *Journal of Energy Storage*, vol. 108, Feb. 2025, ISSN: 2352152X. DOI: 10.1016/j.est.2024.115059.

[195] M. S. Innocente and J. Sienz, "Constraint-Handling Techniques for Particle Swarm Optimization Algorithms," in *7th ASMO UK Conference on Engineering Design Optimization*, 2021. DOI: https://doi.org/10.48550/arXiv.2101.10933.

[196] K. Kassoul, N. Zufferey, N. Cheikhrouhou, and S. Brahim Belhaouari, "Exponential Particle Swarm Optimization for Global Optimization," *IEEE Access*, vol. 10, pp. 78 320–78 344, 2022, ISSN: 21693536. DOI: 10.1109/ACCESS.2022.3193396.

[197] A. R. Jordehi, "A review on constraint handling strategies in particle swarm optimisation," *Neural Computing and Applications*, vol. 26, no. 6, pp. 1265–1275, Aug. 2015, ISSN: 09410643. DOI: 10.1007/s00521-014-1808-5.

[198] N. R. Chowdhury, A. J. Smith, K. Frenander, A. Mikheenkova, R. W. Lindström, and T. Thiringer, "Influence of state of charge window on the degradation of Tesla lithium-ion battery cells," *Journal of Energy Storage*, vol. 76, Jan. 2024, ISSN: 2352152X. DOI: 10.1016/j.est.2023.110001.

[199] C. R. Harris, K. J. Millman, S. van der Walt, *et al.*, "Array programming with NumPy," *Nature*, vol. 585, pp. 357–362, 2020. DOI: 10.1038/s41586-020-2649-2.

[200] R. Yang and L. Wang, "Multi-objective optimization for decision-making of energy and comfort management in building automation and control," *Sustainable Cities and Society*, vol. 2, no. 1, pp. 1–7, Feb. 2012, ISSN: 22106707. DOI: 10.1016/j.scs.2011.09.001.

[201] *OnePower Benin*. [Online]. Available: https://onepowerbenin.com/en/home/.

[202] S. Sossou, A. K. Tossa, S. Vodounnou, *et al.*, "Calibration and Extrapolation of a Stochastic Model for Electricity Demand Forecasting in RUral Communities: The Case of Samionta, Benin," in *The 38th International Conference on Efficiency, Cost, Optimization, Simulation and Environmental Impact of Energy Systems*, Paris, France, 2025.

[203] N. Rangel, H. Li, and P. Aristidou, "An optimisation tool for minimising fuel consumption, costs and emissions from Diesel-PV-Battery hybrid microgrids," *Applied Energy*, vol. 335, Apr. 2023, ISSN: 03062619. DOI: 10.1016/j.apenergy.2023.120748.

[204] M. A. Gelchu, J. Ehnberg, D. Shiferaw, and E. O. Ahlgren, "Exploring the advantages of a multi-year-adaptive approach on cost-optimal long-term mini-grid design under different demand evolution scenarios," *Smart Energy*, vol. 18, May 2025, ISSN: 26669552. DOI: 10.1016/j.segy.2025.100178.

[205] *LiiBRA*. [Online]. Available: https://juliapackages.com/p/liibra.

[206] E. Ugur, F. Yang, S. Pu, S. Zhao, and B. Akin, "Degradation Assessment and Precursor Identification for SiC MOSFETs under High Temp Cycling," in *IEEE Transactions on Industry Applications*, vol. 55, Institute of Electrical and Electronics Engineers Inc., May 2019, pp. 2858–2867. DOI: 10.1109/TIA.2019.2891214.